University of Wollongong
Research Online

University of Wollongong Thesis Collection

University of Wollongong Thesis Collections

2013

Bio-inks for drop-on-demand cell printing

Cameron Ferris
University of Wollongong, cjf146@uowmail.edu.au

Recommended Citation

Ferris, Cameron, Bio-inks for drop-on-demand cell printing, Doctor of Philosophy thesis, School of Chemistry, University of Wollongong, 2013. http://ro.uow.edu.au/theses/3875

Research Online is the open access institutional repository for the University of Wollongong. For further information contact the UOW Library: research-pubs@uow.edu.au

UNIVERSITY OF WOLLONGONG

COPYRIGHT WARNING

You may print or download ONE copy of this document for the purpose of your own research or study. The University does not authorise you to copy, communicate or otherwise make available electronically to any other person any copyright material contained on this site. You are reminded of the following:

Copyright owners are entitled to take legal action against persons who infringe their copyright. A reproduction of material that is protected by copyright may be a copyright infringement. A court may impose penalties and award damages in relation to offences and infringements relating to copyright material. Higher penalties may apply, and higher damages may be awarded, for offences and infringements involving the conversion of material into digital or electronic form.

Intelligent Polymer Research Institute, ARC Centre of Excellence for Electromaterials Science
&
Soft Materials Group, School of Chemistry

Bio-inks for drop-on-demand cell printing

Cameron Ferris
B Nanotech. (Adv)(Hon, Class I)

This thesis is presented as part of the requirements for the award of the Degree of Doctor of Philosophy of the

University of Wollongong

March 2013

CERTIFICATION

I, Cameron J. Ferris, declare that this thesis, submitted in partial fulfilment of the requirements for the award of Doctor of Philosophy, in the School of Chemistry, University of Wollongong, is wholly my own work unless otherwise referenced or acknowledged. The document has not been submitted for qualifications at any other academic institutions.

Cameron J. Ferris

ABSTRACT

A rapidly growing synergy between biological science and engineering technology is currently re-shaping the way we view the challenge of treating injury and disease. In particular, emerging biofabrication techniques that allow the precise construction of complex biological structures have reinvigorated the effort to engineer replacement tissues and organs. In addition to the potential for direct therapeutic approaches, advanced engineered tissues promise to significantly improve *in vitro* studies of fundamental cell biology and disease processes, and expedite drug development.

Drop-on-demand cell printing technologies are at the forefront of these advances in biofabrication. These approaches offer the ability to place living cells, biomaterials and other factors in defined arrangements in two or three dimensions in order to reproduce the complex spatial interplay that regulates tissue function. Significant progress towards this goal has been made over the last decade, but the design of bio-inks remains a key challenge due to the need to simultaneously satisfy disparate engineering and biological requirements. The aim of this thesis was to develop bio-inks for drop-on-demand cell printing that enable the robust deposition of living cells. Specifically, a suitable bio-ink should be non-cytotoxic, prevent cell settling and aggregation, possess optimal fluid properties (i.e. viscosity and surface tension) for drop-on-demand printing and contain minimal dry mass.

Bio-inks were developed by forming gellan gum (GG) microgel suspensions in cell culture media by applying shear during gelation. At a low polymer concentration (0.05% w/v) the bio-ink showed a yield stress (~ 43 mPa), while exhibiting a low viscosity (~ 1.7 mPa.s) at high shear rates (10^3 s^{-1}). These properties were shown to prevent cell settling and aggregation without affecting printability. Surfactants were added to the formulation to achieve surface tension reduction for inkjet printing. Addition of the fluorosurfactant, Novec FC-4430, allowed a suitable surface tension (~ 30 mN/m at 0.05% v/v) to be achieved, while Poloxamer 188 (P188) was included (0.1% v/v) for its reported cell-protecting qualities. Neither surfactant significantly affected the bio-ink structure or rheology, and C2C12 (skeletal muscle) and PC12 (pheocromocytoma) cells exposed to the surfactant-containing bio-ink for 2 hr exhibited normal viability, proliferation and differentiation.

The bio-ink formulations, with and without surfactants, proved suitable for cell deposition by microvalve and inkjet printing, respectively. The bio-ink enabled reproducible cell output over 1 hr printing periods from both a microvalve printer (Deerac Equator GX1) and multiple-nozzle piezoelectric inkjet print heads (Xaar-126). Printed cells exhibited phenotypic responses that were comparable to controls. It was also demonstrated that P188 had a protective effect on cells during inkjet printing.

Inkjet cell printing using the bio-ink was applied to the fabrication of two dimensional cell constructs. Cell microarrays were printed on glass slides and subsequently analysed by a novel surface-sampling mass spectrometry technique. The combination of the two techniques allowed the detection of characteristic lipid profile 'fingerprints' from single printed C2C12, PC12 and L929 (fibroblast) cells. The bio-ink also enabled simultaneous printing of two cells types (C2C12 and PC12) from two inkjet print heads to create patterned co-cultures of viable cells on collagen substrates.

Both cell printing techniques were applied in approaches to fabricate cell-laden hydrogel constructs. In a novel method, a microvalve printer tip dispensed cell-laden solutions while immersed in GG solutions. In another approach, cell-laden bio-ink and GG solutions were printed simultaneously from separate inkjet print heads. In both cases, cell-encapsulating hydrogels were formed through ionic crosslinking of GG by the cell solution. Encapsulated cells did not interact with the hydrogel matrix, however, and this observation was repeated in standard culture. Modification strategies to impart biofunctionality to GG hydrogels were therefore explored. Covalent conjugation of the peptide G_4RGDSY to purified GG was optimised. The peptide conferred significant improvement in the attachment, proliferation and differentiation of surface-seeded and encapsulated C2C12 cells, which was attributed to specific binding with the RGD domain.

The work in this thesis shows that smarter design of bio-ink materials can yield important advances in drop-on-demand cell printing approaches. The bio-inks address some of the key challenges in the continuing evolution of these techniques towards becoming clinically relevant biofabrication tools.

ACKNOWLEDGEMENTS

I would like to gratefully acknowledge my supervisory team, A/Prof Marc in het Panhuis, Dr. Kerry Gilmore and Prof. Gordon Wallace, for their support and guidance. Marc, it has been a privilege working with you for the last 6 years. I really appreciate the way you have constantly sought to encourage and back me, which opened up great opportunities in research and beyond. Kerry, thank you for your kindness and your willingness to always listen and provide assistance; I would not have survived in the lab without it. Gordon, your inspirational leadership has created a world-class environment in which to do research. Thank you for your genuine interest in the betterment of your students, and the opportunities you have provided for me to follow my passions.

I am thankful for the excellent research teams within the Intelligent Polymer Research Institute and the School of Chemistry. While there are too many to name individually, I acknowledge the many people who gave assistance in the labs, engaged in useful discussions and provided administrative support. I would particularly like to thank Stephen Beirne, Don McCallum, Shane Ellis, Todd Mitchell and Stephen Blanksby for fruitful and enjoyable research partnerships.

It was a pleasure to work with several fantastic external collaborators: Eskender Mume, Ivan Greguric, Paul Pellegrini, Grant Griffiths, Naomi Wyatt and Suzanne Smith from the Australian Nuclear Science and Technology Organisation; Danielle Taylor, Patrice Castignolles and Marion Gaborieau from the University of Western Sydney; Jeffrey Keisler and Roger Blake from the University of Massachusetts (Boston); and Ross Clarke and Phil Jackson from CP Kelco.

I gratefully acknowledge the financial support provided by the Australian Research Council, the University of Wollongong, the Australian Institute of Nuclear Science and Engineering and the Australian National Fabrication Facility.

My friends and colleagues at IPRI, past and present, are an amazing bunch of people. It has been a lot of fun working with you all! To my family at Camden Uniting Church, thank you for your love and support. It is all of these friends who have made the journey worthwhile. I couldn't list you all, but thank you. I'm incredibly grateful for those close friends – you know who you are – who have loved, laughed, cried,

celebrated and persevered... and taught me more than any amount of research could have done.

I could never express enough thanks to my family. I am always blown away by your unconditional love and support. Thank you for being amazing, for lifting me up when it was tough and for cheering me on. To Kristy Lee... you have always been and continue to be the love and joy of my life. Thank you especially for your support during this thesis. I can't wait for the rest of the journey!

Finally, I want to honour God who saved me, sustains me and leads me home. *"Now to him who is able to do immeasurably more than all we ask or imagine, according to his power that is at work within us, to him be glory in the church and in Christ Jesus throughout all generations, for ever and ever! Amen." (Ephesians 3:20-21)*

TABLE OF CONTENTS

LIST OF FIGURES

LIST OF TABLES

ABBREVIATIONS

§	Section
2D	Two-dimensional
3D	Three-dimensional
AAS	Atomic absorption spectroscopy
AFA-LIFT	Absorbing film assisted laser induced forward transfer
AM	Additive manufacturing
ANOVA	Analysis of variance
ASCs	Adipose-derived stem cells
ATCC	American Type Culture Collection
BACs	Bovine articular chondrocytes
BAECs	Bovine aortic endothelial cells
BioLP	Biological laser printing
BSA	Bovine serum albumin
BSC	Bio-safety cabinet
CCM	Cell culture medium
CDM	Cell differentiation media
CHO	Chinese hamster ovary
CIJ	Continuous inkjet
CPM	Cell proliferation media
DAPI	4,6-diamidino-2-phenylindole
DMEM	Dulbecco's Modified Eagles Medium
DMSO	Dimethyl sulfoxide
DOD	Drop-on-demand
DRIP	Drop-on-demand Reactive In-solution Plotting
ECFCs	Endothelial colony-forming cells
ECM	Extra-cellular matrix
EDTA	Ethylenediaminetetraacetic acid
EPCs	Endothelial progenitor cells
FBS	Foetal bovine serum
GG	Gellan gum
HA	Hyaluronic acid
HP	Hewlett-Packard
HPLC	High-performance liquid chromatography
HS	Horse serum

HSFs	Human skin fibroblasts
HUVSMCs	Human umbilical vein smooth muscle cells
LAB	Laser-assisted bioprinting
LESA	Liquid extraction surface analysis
LIFT	Laser-induced forward transfer
MAPLE-DW	Matrix-assisted pulse laser evaporation – direct write
MFC	Magnetic Feedback-Controlled
MPSCs	Multi-potent stromal cells
MRI	Magnetic resonance imaging
MS	Mass spectrometry
MSCs	Mesenchymal stem cells
MTS	3-(4,5-dimethylthiazol-2-yl)-5-(3-carboxymethoxyphenyl)-2-(4-sulfophenyl)-2H-tetrazolium
MWCO	Molecular weight cut-off
NGF	Nerve growth factor
nHAp	Nano-particulate hydroxyapatite
OTF	On-the-fly
P188	Poloxamer 188 surfactant
PBS	Phosphate buffered saline
PC	Phosphatidyl choline
PCL	Polycaprolactone
PDMS	Polydimethylsiloxane
PEG	Polyethylene glycol
pen/strep	Penicillin/streptomycin
PES	Phenazine ethosulfate
PF	Paraformaldehyde
PLL	Poly-L-lysine
RT	Room temperature
SCs	Schwann cells
SE	Standard error
SM	Sphingomyelin
TCPS	Tissue culture polystyrene
TE	Tissue engineering

PUBLICATIONS

The following is a list of peer-reviewed publications by this author:

Journal articles

- *__C.J. Ferris__, K.J. Gilmore, G.G. Wallace and M. in het Panhuis (2013), *Modified gellan gum hydrogels for tissue engineering applications*, Soft Matter 9:3705-3711
- *__C.J. Ferris__, K.J. Gilmore, G.G. Wallace and M. in het Panhuis (2013), *Biofabrication: an overview of the approaches used for printing living cells*, Applied Microbiology and Biotechnology, 97:4243-58
- **C.J. Ferris**, K.J. Gilmore, S. Beirne, D. McCallum, G.G. Wallace and M. in het Panhuis (2013), *Bio-ink for on-demand printing of living cells*, Biomaterials Science 1:224-230
  - Highlighted in *Chemistry World* (Royal Society of Chemistry), 7 Nov 2012
  - Featured on front cover
- S.R. Ellis, **C.J. Ferris**, K.J. Gilmore, T.W. Mitchell, S.J. Blanksby and M. in het Panhuis (2012), *Direct Lipid Profiling of Single Cells from Inkjet Printed Microarrays*, Analytical Chemistry 84:9679-9683
- **D.L. Taylor, **C.J. Ferris**, A.R. Maniego, P. Castignolles, M. in het Panhuis and M. Gaborieau (2012), *Characterization of Gellan Gum by Capillary Electrophoresis*, Australian Journal of Chemistry 65:1156-1164
- ****C.J. Ferris** and M. in het Panhuis (2009), *Gel-carbon nanotube composites: the effect of carbon nanotubes on gelation and conductivity behaviour*, Soft Matter 5:1466-1473.
- ****C.J. Ferris** and M. in het Panhuis (2009), *Conducting bio-materials based on gellan gum hydrogels*, Soft Matter 5:3430-3437
  - Highlighted in *Highlights in Chemical Biology* 4:B68
  - Selected for inside cover image

Conference proceedings

- ****C.J. Ferris** and M. in het Panhuis (2010), *Diffusion of vitamin B_{12} in Gellan Gum-Carbon Nanotube Hydrogels*, IEEE, 2010 International Conference on Nanoscience and Nanotechnology (ICONN), 234-236
- **D. McCallum, **C.J. Ferris**, P. Calvert, G.G. Wallace and M. in het Panhuis (2010), *Printed hydrogel materials*, IEEE, 2010 International Conference on Nanoscience and Nanotechnology (ICONN), 257-260
- **D. McCallum, **C.J. Ferris**, P. Calvert, M. in het Panhuis and G.G. Wallace (2010), *Rapid deposition of hydrogel layers by inkjet printing*, NIP26: International Conference on Digital Printing Technologies and Digital Fabrication 2010 (NIP26 and DF2010), Society for Imaging Society and Technology Conference Proceedings, Austin (TX), September 2010, 554-557.

**Review articles. **publications not directly related to work presented in this thesis.*

DISCLAIMER

This thesis, at times, utilises active voice ("We found that...") instead of passive voice ("It was found that..."). This was a stylistic choice with the intention of enhancing the readability of this thesis, and is not a reflection of contribution made to the work by anyone other than the author. Rather, 'we' is intended to refer to tasks undertaken by the author under the guidance of the supervisory team. Where significant contributions were made by others, this is clearly indicated in the main text.

1 INTRODUCTION

The human body is composed of more than 50 trillion cells, classified into over 200 different types, each with a specific and important role in their respective anatomic sites. These multiple cell types are organised in a complex and heterogeneous extra-cellular matrix (ECM), and their function is dictated and regulated by a plethora of spatiotemporal cues from their microenvironment, neighbouring cells, soluble factors and physical forces. Throughout the history of scientific progress, we have sought to understand this biological complexity in the search for answers to the challenges of healing damaged bodies. This pursuit continues to escalate rapidly. Advances in biological science, matched by those in engineering and technology, are creating a revolution in our understanding and treatment of injury and disease. Tissue engineering is one pursuit at the forefront of these advances.

1.1 Tissue engineering

Tissue engineering (TE) is a multidisciplinary field that draws primarily on principles from the engineering and life sciences to develop biological substitutes that restore, maintain or improve tissue function *(1)*. Typically, this is achieved through some combination of living cells with synthetic or natural biomaterials. These biomaterials act as a surrogate for the natural ECM, with the primary aim of engineering functional constructs that reflect the complex characteristics of natural tissues and organs. The term TE is often used interchangeably with ‘regenerative medicine’, which is reflective of the growing synergy between the fundamental principles of TE and stem cell technology. Engineered tissues with functionality that approaches that of their *in vivo* counterparts have two principle areas of application. The first is in therapeutic approaches for the treatment of injury and disease, and the second is in the development of constructs for *in vitro* studies.

1.1.1 Tissue engineering of replacement body parts

Over the last century, advances in medical device technology and our ability to transplant tissues and organs from one patient to another have substantially improved the quality and longevity of life, but these approaches are fundamentally limited. Artificial devices are often short-lived and are unlikely to fully achieve the function of living tissue, while organ transplants are hindered by potential immunological

rejection of allogeneic tissues and a critical shortage of donors. The possibility of engineering tissue or organ replacements 'on-demand', using an autologous cell source (Figure 1.1A), has the potential for profound therapeutic and economic impact. The disparity between the number of patients awaiting an organ transplant and the number of transplant operations actually performed is vast (Figure 1.1B). Waiting times for a transplant are long; in the year 2005 (the last for which a full data set is available) the median time to transplant in the US varied from 131 days for a heart to 1269 days for a kidney *(2)*. Incidences of acute rejection by 3 years post-transplantation are on average 32%, and as high as ~ 50% for heart and lung transplants *(3)*. The economic cost of procedures is staggering, with the average total cost of a single transplant totalling ~ US$ 800,000 (2011 data) and requiring ~ 30 days in hospital (2008 data) *(2)*. The US spends an incredible ~1% of its GDP on organ replacement therapies *(4)*. Clearly, the therapeutic and economic impact that could be realised by the provision of tissue and organ replacements through TE cannot be overstated.

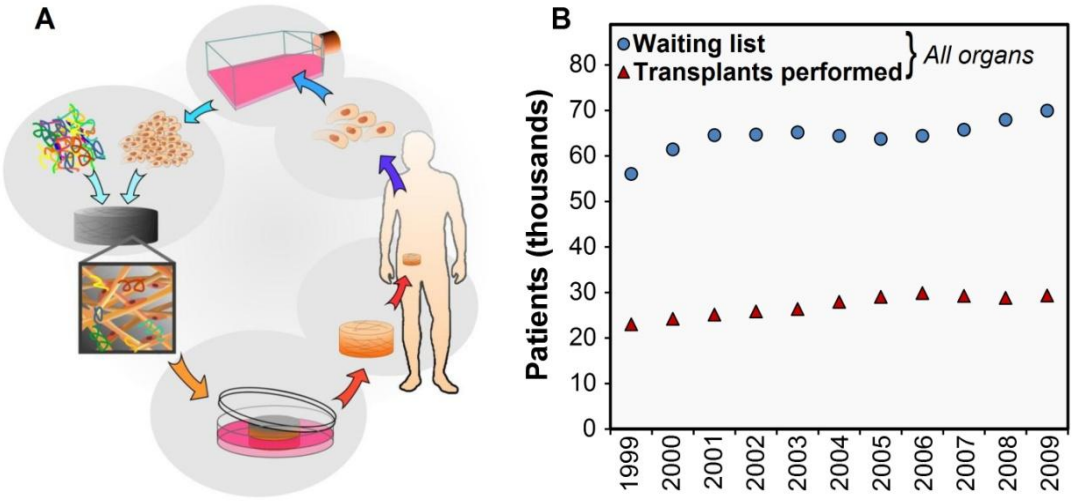

Figure 1.1: (A) Schematic representation of the general tissue engineering concept. Autologous cells are expanded *in vitro*, combined with biomaterials and cultured to produce a tissue or organ replacement that is then implanted. Adapted from reference *(5)*. **(B)** The number of patients awaiting transplant (all organs) compared to the number of transplant operations performed in the US between 1999 and 2009. Data from reference *(3)*.

1.1.2 Tissue engineering for *in vitro* studies

Engineered tissues offer enormous potential in improving *in vitro* studies of fundamental cell biology, the investigation of disease processes, and the evaluation of therapeutic candidates in drug development *(6)*. The advent of traditional cell culture at the end of the 19th century triggered growth in our understanding of complex biological phenomena through the study of monolayers of cells growing in two-dimensional (2D) plates and dishes. However, it is now well-established that the behaviour of cells is very different in 2D cultures in comparison to 3D cultures *(7–9)*. There has consequently been a significant push to study cellular responses in 3D cultures that are more reflective of the physiological microenvironment *(9, 10)*. This is no more important than in drug screening and development *(11)*. The cost of bringing a new drug to market is immense; estimates reach up to $1.3 billion for a single product *(12, 13)*. While expenditure in research and development continues to escalate, this is not reflected in new drug outcomes with still only a handful of products successfully brought to market each year (Figure 1.2). These trends reflect both the challenge of treating increasingly complex conditions, and the difficulty in identifying new therapeutic candidates. A large portion of this expenditure is associated with the costs of unsuccessful projects, particularly late-phase failures which may arise, for example, due to discrepancies between drug efficacy in animal and human trials *(14)*. High-throughput *in vitro* models using human cells in a physiologically relevant engineered tissue environment could significantly enhance the efficiency of drug screening and development processes.

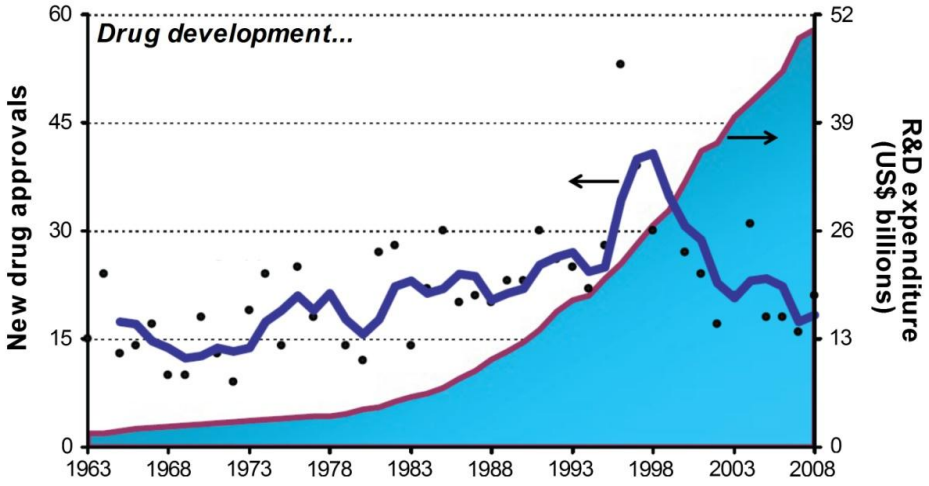

Figure 1.2: The number of new drug approvals (dots, left axis) and pharmaceutical expenditure in research and development (shaded area, right axis) in the US between 1963 and 2008. The trend line is a 3-year moving average. Adapted from reference *(13)*

1.1.3 Current progress in tissue engineering

The term 'tissue engineering' was first coined at a National Science Foundation committee meeting in 1987 *(15)*. TE then emerged as a recognised scientific field in the 1990's, largely due to the pioneering work of researchers such as Langer and Vacanti *(1)*. The first tissue engineering society was founded in 1995, and the journal 'Tissue Engineering' was launched in 1996. Since then, the field has seen rapid escalation in publication trends (Figure 1.3A), and has attracted over US$4 billion in research funding *(15)*. Several comprehensive reviews have outlined the progress in TE research during that time *(1, 16–21)*.

Unlike many burgeoning scientific fields, TE also stimulated significant activity in the private sector from the outset. Early on, government-funded academic research in TE only constituted ~10% of the total activity *(22)*. Commercial activity in TE since its inception has been monitored and documented by Lysaght and others *(20–25)*. Considerable scientific expectation and hype in the mass media accompanied initial developments: a US Business Week report in 1998 estimated that TE would constitute an $80 billion per year industry in the US alone *(17)*; in 1999 a Good Morning America report described TE as the greatest scientific accomplishment of the 20th century *(21)*; and in 2000 Time Magazine highlighted tissue engineering at the top of a list of ten hottest jobs for the 21st century *(15)*. Despite a significant downturn at the start of the millennium *(22)*, the TE industry has recovered and continues to progress strongly today (Figure 1.3B) *(21)*.

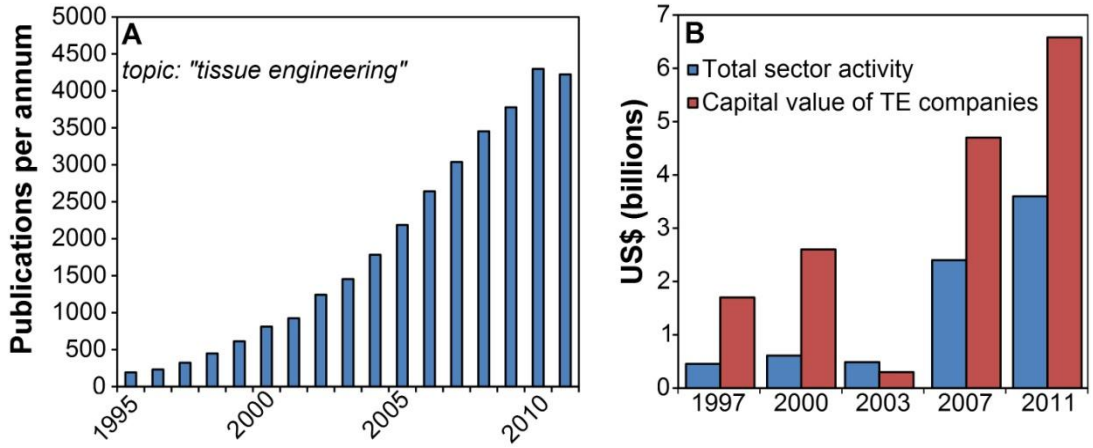

Figure 1.3: (A) Publications per year in tissue engineering. Data from Web of Knowledge (topic = "tissue engineering"). **(B)** Total annual sector activity (spending on products and services), and the capital value of TE companies, for specified years between 1997 and 2011. Data from reference *(20)* (data up to 2007) and reference *(21)* (2011 data).

On the whole, however, progress in TE has struggled to live up to the promise of its early beginnings. Currently, the only TE products with clinical success are simple tissues such as skin and bone *(26, 27)*. Engineering more complex functional tissues represents a considerable scientific and technical challenge in the future of TE *(28)*. This can be attributed to a range of key challenges, including an on-going search for reliable cell sources *(29–31)*, the continued development of suitable biomaterials *(32, 33)*, challenges in securing regulatory approval for TE products *(15, 21)*, and limitations of current fabrication approaches. While each of the aforementioned challenges is significant, this thesis will focus on developing fabrication approaches for the engineering of complex tissues.

1.2 Biofabrication

It has been argued that biofabrication is the key to bridging the gap between the promise of TE and the current reality *(15)*. Biofabrication is generally defined as the production of complex living and non-living biological products from living cells, biomolecules and biomaterials *(34)*. An interdisciplinary technological field drawing from cell and developmental biology, mechanical engineering and materials sciences (Figure 1.4A), it encompasses a broad range of fabrication approaches that are summarised within this section. Proponents have suggested that biofabrication has the potential to become the leading manufacturing paradigm of the 21st century *(34)*. While some biofabrication techniques have been applied to TE since its inception, a growing realisation of the importance of developing more sophisticated fabrication approaches has been reflected in the rapidly growing interest in the field.

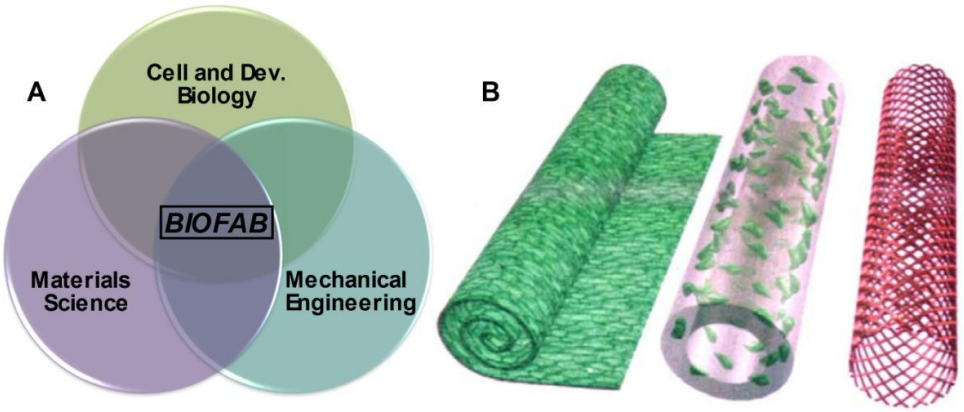

Figure 1.4: (A) The interdisciplinary nature of biofabrication. **(B)** Schematic representation of cylindrical structures produced by different biofabrication processes. Left to right; cell sheet engineering, cell-laden hydrogels and solid scaffolds. Adapted from reference *(34)*.

1.2.1 Conventional approaches

To understand the need for advanced biofabrication techniques, it is first important to outline the limitations of conventional approaches. The traditional approach to the fabrication of TE constructs has been to seed a solid, pre-formed, biodegradable polymeric scaffold with a cell suspension (Figure 1.1A). The scaffold is typically highly porous to facilitate mass transfer and cell incorporation through the bulk. Initially, conventional manufacturing processes including solution casting, particulate leaching, gas foaming, phase separation, melt molding and freeze drying were employed to fabricate these scaffolds *(35, 36)*. Electrospinning has also been widely adopted as a means to create porous scaffolds with nanoscale fibrous architecture *(37)*. However these methods provide little control over pore size, geometry, interconnectivity and spatial distribution. Furthermore, the nature of this approach means that placement of cells within scaffolds is essentially random.

There remain two key challenges in TE of functional constructs resulting from these limitations. Firstly, mass transfer and the development of vascular networks within constructs are significant issues *(38–40)*. *In vivo*, cells reside no more than 200 µm from a blood vessel or capillary that supplies the cells with oxygen and nutrients, and this supply must be reproduced in engineered constructs if cell viability and function is to be maintained long term *(41)*. Secondly, seeding a scaffold does not facilitate control over cell-cell contact and tissue architecture, which are primary determinants of cell behaviour and tissue function *(42)*. In order to address these challenges, biofabrication techniques must provide the means to accurately control cell position and tissue architecture in 3D constructs with microscale precision.

1.2.2 Additive manufacturing

More recently, the *modus operandi* for solid scaffold biofabrication has shifted significantly as a result of the increasing capabilities of additive manufacturing (AM). Often referred to as rapid prototyping or solid free-form fabrication, AM refers to a suite of techniques capable of layer-by-layer fabrication of 3D objects through computer-aided design (CAD) and/or computer-aided manufacturing (CAM). These techniques represent a dramatic paradigm shift from ‘top-down’ manufacturing principles to a ‘bottom-up’ approach that has been so widely

pervasive that AM has been described as "a third industrial revolution" *(43)*. AM techniques including 3D printing, selective laser sintering, fused-deposition modelling and stereolithography have all been applied extensively to the biofabrication of solid scaffolds for TE applications, as highlighted in several thorough review papers *(35, 36, 44–46)*. The advantage of these approaches is that they provide precise control over both the external macrostructure and internal microstructure of scaffolds. Programmable micro-porosity can therefore be designed to aid in mass transfer and the development of vascular networks throughout constructs *(47)*. Also, the possibility of integration between CAD principles and 3D medical imaging (magnetic resonance imaging, computer tomography) means that scaffolds can potentially be designed to suit an individual patient *(48)*. Although solid scaffolds can be fabricated with added complexity through these AM techniques, they are still secondarily seeded with cells. As such, many of the problems associated with traditional solid scaffolds, particularly the inability to produce complex multi-cellular architectures, are not alleviated through the use of solid scaffolds produced by AM *(34)*.

1.2.2.1 Cell sheet engineering

One alternative to bypass the limitations of the solid scaffold approach is to remove the need for a scaffold completely. Cell sheet engineering (Figure 1.4B) is a technology where cells are grown to confluency in a monolayer culture on a thermo-responsive polymer and allowed to produce their own ECM. Cell sheets are then detached from the substrate via a temperature change *(49)*, and can be manipulated by stacking multiple sheets or rolling to form thin or tubular functional tissue structures *(50)*. It is also possible to produce multi-cellular constructs by first patterning the growth surface with different cell types using soft lithography techniques *(51)*. While this is more reflective of an additive approach to TE, the scope of tissue architectures that can be realised through manipulation of cell sheets is limited.

1.2.2.2 Hydrogels

The most popular alternative to the use of solid scaffolds is the encapsulation of cells within hydrogel biomaterials. Hydrogels, by virtue of their high water content, are generally biocompatible, and often utilise gentle crosslinking/gelation mechanisms

that facilitate cell encapsulation with minimal adverse effects on cell viability. The hydrogel can act as a surrogate ECM until the encapsulated cells mature and produce their own. The design of hydrogel biomaterials for TE applications *(52)* is a broad area of research that will not be covered extensively here. Several recent reviews thoroughly cover progress in this field to date *(52–59)*. Hydrogel biomaterials can be synthetic or natural in origin *(53, 54, 56)*, and are selected based on a range of criteria including crosslinking/gelation mechanism, mechanical properties, degradation rate and mass transport properties *(53, 55)*. Common synthetic materials *(60)* include poly(acrylic acid) (PAA), poly(ethylene glycol) (PEG) and its copolymers, poly(vinyl acrylate) (PVA) and self-assembling polypeptides. Commonly employed natural materials *(61, 62)* include proteins or protein derivatives like collagen, gelatin and fibrin, as well as polysaccharides such as hyaluronic acid, alginate, agarose and chitosan. As well as finely tuning physical properties to guide cell responses, hydrogels can also be modified by the inclusion of cell-instructive biological cues (Figure 1.5) *(52, 58, 59, 63)*. This is particularly important for synthetic or polysaccharide materials where these cues are not already present. Modifications include the addition of growth factors, cell adhesion peptides like the RGD sequence, and/or oligopeptide crosslinkers that are susceptible to cleavage by cell-secreted colleganases *(64–66)*.

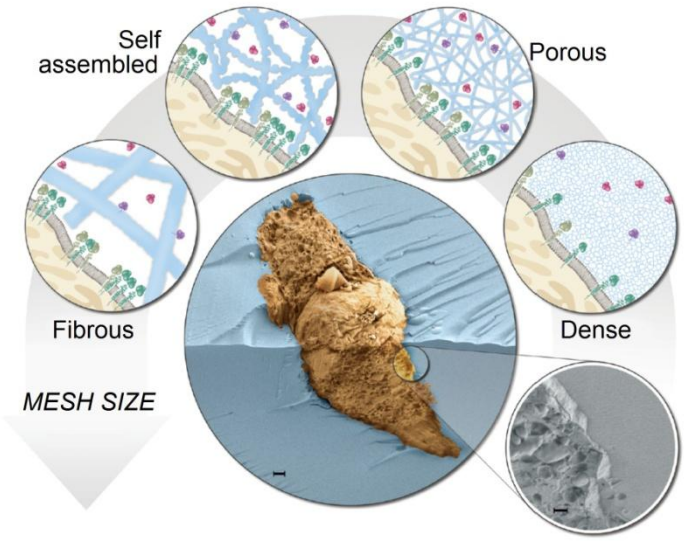

Figure 1.5: Cell-instructive hydrogels. Centre: cryogenic scanning electron micrograph of the interface (magnified bottom right) between a hydrogel (blue) and encapsulated cell (brown). Around: Schematic of the cell-gel interface in cell-instructive hydrogels with various network structures, and containing soluble (red) and tethered (purple) bioactive molecules that interact with receptors (green) on the cell membrane. Adapted from reference *(52)*.

Like solid polymeric scaffolds, hydrogels have also been implemented in conventional TE approaches. Cells can be uniformly suspended in a hydrogel precursor and cast into a mold prior to crosslinking/gelation, or photosensitive hydrogels can be fabricated into more complex shapes through stereolithography and subsequently seeded with cells *(67)*. However, the inclusion of cells in hydrogels also invites new possibilities with more advanced biofabrication approaches. In particular, a range of techniques are emerging that provide micro-scale control over the global architecture and cell composition within hydrogels *(27, 58, 63, 68, 69)*. For example, individual cell-laden microgel building blocks can be fabricated through emulsification, micromolding or photolithography and subsequently assembled into 3D constructs *(70)*. Microfluidic devices have also been used to produce micro-engineered hydrogel structures with spatial and temporal complexity mimicking native tissues *(71, 72)*. In a novel approach, electric forces can even be used to provide some control over the position of cells within a hydrogel prior to crosslinking/gelation *(73)*. These types of approaches are particularly useful in the biofabrication of constructs for *in vitro* applications *(6, 11)*. Cellular microarrays, for example, are of immense value in high throughput drug screening, toxicology studies and stem cell research *(74–78)* and even for the study of biological heterogeneity between single cells *(79)*. Typically, these arrays are formed by seeding cells onto 2D patterned protein arrays *(80)* or in micro-wells *(81)*. Microengineered hydrogels provide a route to produce microarrays where cells are positioned in microenvironments that more closely resemble natural physiology. Many of the additive manufacturing techniques applied to the fabrication of solid scaffolds have also been adapted to produce complex 3D hydrogel structures *(82)*, which are particularly attractive for the engineering of soft tissues.

The biofabrication techniques introduced thus far form part of a growing tool box in the production of functional tissue constructs for both *in vivo* and *in vitro* applications. All of them, however, are limited in their capacity to rapidly place cells and other biological components in defined locations within 3D constructs in order to reproduce the complex spatial interplay that regulates tissue function and vascularisation. One promising advance that offers the potential to overcome these limitations is cell printing technology.

1.3 Cell printing

Cell printing can be described as the use of material transfer processes to pattern and assemble cells and biomaterials with a defined organisation *(83)*. It is one of the most powerful combinations of TE with AM techniques that allows the production of 3D tissue constructs, where multiple cell types and biomaterials (usually hydrogels) can be directly placed in specific spatial arrangements; either in organotypic architectures to engineer functional tissues (Figure 1.6), or in cellular microarrays where individually addressable micro-cultures contain cells in physiologically relevant microenvironments.

The work of Klebe and co-workers *(84)* in 'cytoscribing' laid the foundation for the precise patterning of living cells on surfaces, but it was the more recent advances in AM and CAD/CAM that have seen the advent of several bioprinting technologies that can actually deposit living cells. Several recent reviews outline progress in cell printing to date *(27, 83, 85–92)*. Cell printing techniques are still in their infancy, having only been explored over the last decade, but are developing rapidly. Mironov, a significant contributor to cell printing research, has predicted that cell printers will one day become as common in academic, clinical and industrial laboratories as microscopes are today *(93)*.

Current cell printing technologies include extrusion printing of cell-laden hydrogels and cell aggregates, as well as drop-on-demand techniques including laser, microvalve and inkjet printing. This section contains a thorough description of the reports to date on applying each of these approaches to the deposition of living cells. Each sub-section will outline the general principle, current progress, advantages and challenges associated with the technique. Particular focus has been given to the bio-inks used to suspend cells for printing, and the methods employed for fabricating 3D structures.

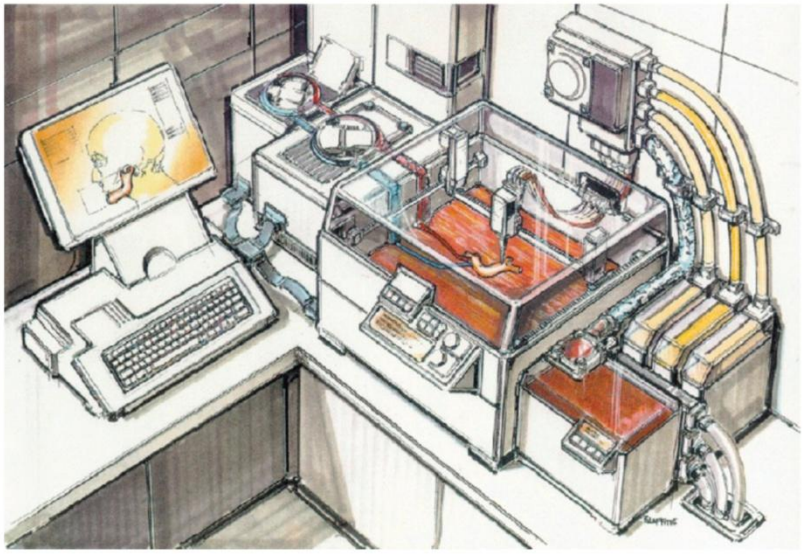

Figure 1.6: Cartoon representing the concept of cell printing technology. A patient-specific computer model of a jaw bone instructs the deposition of cells and biomaterials from a cell printer to fabricate a tissue engineered replacement construct. Reproduced from reference *(88)*.

1.3.1 Extrusion printing

Extrusion printing refers to techniques where continuous filaments of a material are forced through a nozzle in a controlled manner to construct a 3D structure. For extrusion printing of cells, the material usually consists of a highly viscous cell-laden hydrogel *(94)* that can flow from the nozzle without the need for high temperatures. Once deposited, solidification of the hydrogel through physical or chemical means provides sufficient mechanical integrity to fabricate 3D structures (Figure 1.7). The printer design is generally simple, consisting of a 3-axis robot that controls the movement of either pneumatically or volumetrically driven displacement pens or syringes with a typical nozzle diameter of 150-300 µm. Several reviews have highlighted the application of extrusion approaches to cell printing *(91, 94–96)*.

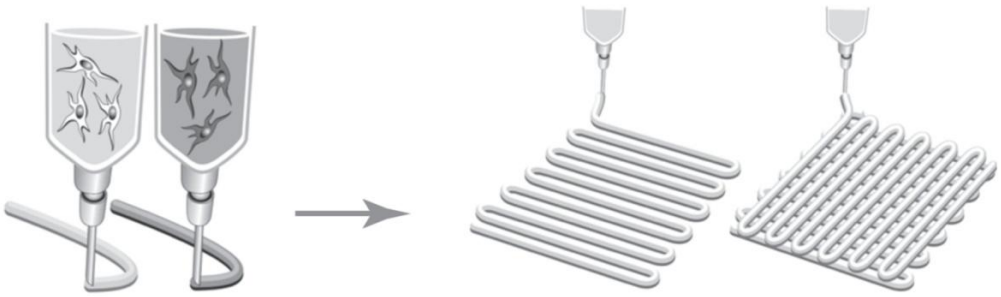

Figure 1.7: Schematic of the extrusion cell printing approach, adapted from reference *(97)*. Cells are encapsulated in hydrogels and printed in 3D structures through layer-by-layer deposition of continuous filaments.

The first report on the use of an extrusion printer to deposit living cells was from Williams' group at the University of Arizona (Tuscon, Arizona) *(98)*, using a Bio-Assembly Tool made by the company Sciperio (Orlando, Florida). This printer was used to deposit cold (2-10 °C) solutions of either human fibroblasts encapsulated in Pluronic-F127, or bovine aortic endothelial cells (BAECs) in type I collagen, onto heated substrates where solidification of the printed structures was induced by thermal gelation of the biopolymers. The low temperatures used in this work and problems with dehydration of printed filaments resulted in low cell viability, although BAECs printed in collagen from a 250 μm tip maintained 86% viability and were shown to proliferate over 24 hr. Importantly, this work showed that CAD/CAM technology could be used to deposit cell laden structures that mimicked an anatomical vascular structure. Further work from this group assessed the viability of rat microvascular cells printed in collagen as a function of several process parameters *(99)*.

Since this initial work, several groups have printed cells encapsulated in a range of hydrogels that are solidified through either thermal processes or by post-print crosslinking, to engineer diverse tissues ranging from liver to bone. For example, a group from Tsinghua University (Beijing, China) has been active in developing extrusion printing approaches to engineer biofabricated liver constructs *(100)*. Using a custom-made printing system, originally based on a computer numerical-control (CNC) milling machine as the positioning robot and using volumetric displacement pens, this group has printed primary rat hepatocytes encapsulated in materials including gelatin *(101)*, gelatin/chitosan *(102, 103)*, gelatin/alginate *(104)* and gelatin/fibrinogen *(105)*. Structures were deposited at low temperature (< 10 °C) onto a warmer stage, with the thermal gelation of gelatin providing initial structural support, and then stabilised by immersion of the construct in a solution containing a crosslinking agent or polymerising enzyme, specifically: glutaraldehyde for gelatin; sodium tripolyphosphate for chitosan; calcium chloride for alginate; thrombin for fibrinogen. These approaches showed good cell survival and retention of metabolic function, although the use of harsh crosslinking conditions was a concern, and vascularisation of the constructs remained a challenge *(96)*.

The group subsequently demonstrated that adipose-derived stem cells (ASCs) printed in gelatin/alginate/fibrinogen gels could be induced to differentiate into endothelial cells at the walls of printed channels *(106)*. With an upgraded printing system containing two separate dispensing heads, they were then able to simultaneously deposit hepatocytes in gelatin/alginate/chitosan and ASCs in gelatin/alginate/fibrinogen to fabricate a complex 3D structure mimicking the liver *(107)* (Figure 1.8). There was some evidence that the hepatocytes in these structures were metabolically active, and that the ASCs differentiated towards endothelial cells albeit without a typical morphology. There was little direct characterisation of the effects of printing and post-treatment on cell viability in this report.

While this group focussed their efforts on the application of extrusion printing to liver biofabrication, a group from Utrecht University in the Netherlands has sought to engineer bone and cartilage constructs *(97)*. This group utilised a pneumatic deposition tool that was first developed by Landers and co-workers at the Freiburg Materials Research Centre in Germany *(108)* to deposit hydrogel structures *(109)*, and subsequently commercialised by EnvisionTec (Gladbeck, Germany) *(110)*. Multi-potent stromal cells (MPSCs) from goat bone marrow were initially deposited in Lutrol F127 and alginate hydrogels, with gelation induced by thermal changes and ionic crosslinking with calcium chloride, respectively *(111)*. Cell viability was shown to be unaffected by the printing process, and in alginate constructs (but not Lutrol F127 constructs) cells survived in subsequent culture with some evidence of osteogenic differentiation. A further study of both human and goat MPSCs in printed alginate constructs showed that the enhanced diffusion of nutrients and oxygen to

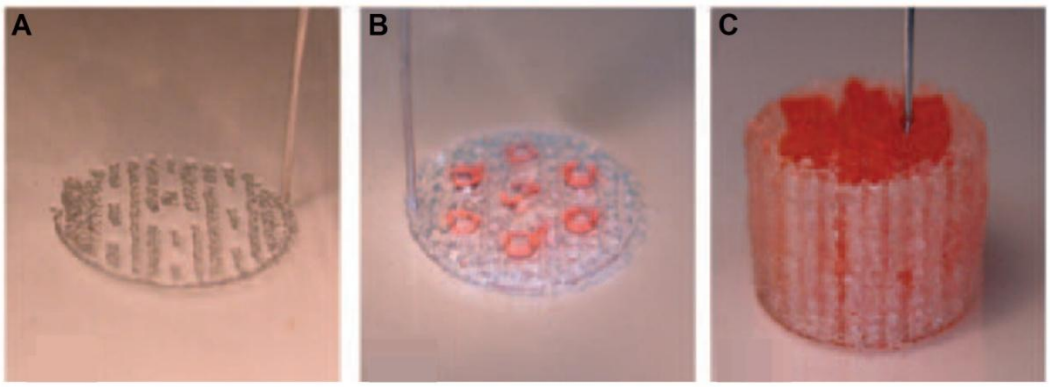

Figure 1.8: Sequential deposition of hepatocytes in gelatin/alginate/collagen (A, clear) and ASCs in gelatin/alginate/fibrinogen (B, red) to produce a 3D liver construct (C). Adapted from reference *(107)*.

encapsulated cells, afforded by the engineered porosity, enhanced cell viability and reduced apoptosis and hypoxia in comparison with cells in solid alginate constructs when assessed both *in vitro* and *in vivo (112)*. However, only a fraction of cells in either construct differentiated towards an osteogenic lineage.

In a similar manner to the group from Tsinghua University, multi-cell-type constructs were then fabricated to incorporate goat endothelial progenitor cells (EPCs) in an effort to improve the engineered bone grafts and encourage vascularisation *(113)*. This work utilised Matrigel™, a gelatinous mixture of natural ECM proteins. Both heterogeneous Matrigel/Matrigel constructs (EPCs and MPSCs both in Matrigel), and Matrigel/alginate constructs (EPCs in Matrigel, MPSCs in alginate) were fabricated and implanted *in vivo*. In each case, the alginate or Matrigel component containing MPSCs was supplemented with osteo-inductive biphasic calcium phosphate (BCP) particles. After 6 weeks *in vivo*, Matrigel/Matrigel constructs demonstrated considerable bone formation in the MPSC-laden Matrigel that was enhanced by the BCP particles, and vascularisation in the EPC-laden Matrigel. There was little bone formation or vascularisation in alginate constructs, however, which was attributed to the lack of cell interaction and migration in alginate. A similar lack of cell interaction and function was observed for human MSCs and articular chondrocytes encapsulated in alginate in multi-cell fabricated osteochondral grafts *(114)*. Functionalisation of alginate with cell-instructive moieties could potentially overcome this lack of interaction; for example a recent report gave some indication that the adhesion of cardiac progenitor cells in printed alginate constructs was enhanced by using alginate modified with the cell-adhesive peptide RGD *(115)*.

In all of the work summarised here, a common problem was a lack of mechanical integrity in the printed hydrogel constructs. This limited the scale and fidelity of the constructs, and also posed challenges for implantation and the retention of the fabricated structure *in vivo*. Recently, several reports have introduced approaches where extrusion printing of soft, cell-laden hydrogels is combined with extrusion printing of stiffer, structural synthetic polymers. For example, the group from Utrecht University demonstrated sequential printing of polycaprolactone (PCL) and cell-laden alginate *(116)* (Figure 1.9). The alginate component was crosslinked with

calcium chloride following deposition. Only a slight decrease in viability of a human chondrocyte cell line deposited in the alginate was observed after 24 hr, likely due to heat shock from the PCL printed adjacent to it (deposited at 160 °C). A very similar approach was adopted by a group from the Pohang University of Science and Technology (POSTECH, Korea), who used a custom multi-head dispensing system *(117)* to deposit hybrid constructs containing a PCL/PLGA blend as the structural polymer alongside collagen containing pre-osteoblast cells *(118)*. The group from Tsinghua University took a different approach to this problem with a 'cryo-printing' technique *(119)*. They had developed a method to print polyurethane at very low (-20 °C) temperatures, but these temperatures were detrimental to cell viability. Subsequently, they printed ASCs in gelatin/alginate/fibrinogen containing a cryo-preservant (DMSO or glycerol) alongside polyurethane in a cell-compatible organic solvent (tetraglycol), both at -20 °C. The constructs were then stored at -80 °C for one week before thawing and crosslinking the gel component. Cell viability as high as 75% could be reached and the cells proliferated over 14 days in culture.

A group at Cornell University developed a simple open-source extrusion printing tool, called Fab@Home, which contains syringe-based deposition pens *(120)*. This system was used to demonstrate a slightly different reactive bioprinting approach, where a delayed ionic crosslinking process was instigated prior to deposition *(121)*. Alginate solutions were mixed with calcium sulphate, whose partial solubility provided a ~15 min window in which to deposit the mixture before calcium-induced gelation occurred. This approach was used to encapsulate bovine articular chondrocytes (BACs) in a 3D geometry representing an ovine meniscus, with high

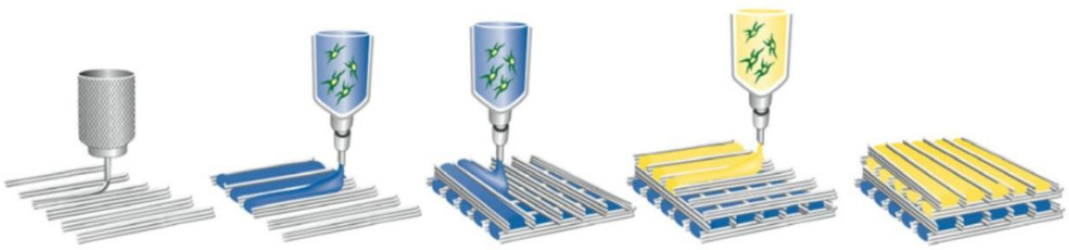

Figure 1.9: Schematic of the hybrid extrusion printing process, adapted from reference *(116)*. Alternating strips of structural polymer and cell-laden hydrogel and deposited layer-by-layer to form a hybrid construct.

viability (~ 95%) and ECM production. It was later shown that more thorough mixing of the two-components yielded improved construct fabrication via this approach *(122)*. The group also demonstrated that this tool, modified with a laser distance sensor, could be used to deposit alginate hydrogels *in situ* in an osteochondral defect, although cells were not incorporated in this process *(123)*. The Fab@Home system was also utilised by Prestwich's group at the University of Utah to print fibroblasts and hepatocytes encapsulated in novel hydrogel formulations *(124, 125)*. These included an extrudable gelatin/HA gel crosslinked by synthetic PEG derivatives *(124)*, and a photo-crosslinkable hydrogel formulation containing methacrylated gelatin and methacrylated HA *(125)*.

Wei Sun's group at Drexel University (Philadelphia, USA) developed a novel bioprinting tool comprising four separate nozzles, each with a different mode of deposition *(126)*. They used one of these, a pneumatic microvalve nozzle in extrusion mode, to fabricate constructs with rat heart endothelial cells encapsulated in alginate hydrogels by deposition of filaments directly into a thin layer of calcium chloride solution *(127, 128)*. This group's work has subsequently focussed on developing mathematical models of the forces experienced by cells during cell printing *(129)*, and probing their effect on the viability of extruded hepatocytes *(130)* and endothelial cells *(131)*.

1.3.2 Printing tissue fragments

The combination of bioprinting techniques with biological self-assembly is another approach to fabricating tissue structures that has been developed over the last decade. Founded on the dictum that 'nature knows best', and drawing from the principles of developmental biology, this approach exploits the intrinsic capacity of closely spaced tissue fragments to fuse together; otherwise known as 'tissue fluidity' *(132)*. Tissue fragments, often spheroids containing several thousand cells, are deposited in spatial organisations such that they fuse together to generate an organotypic structure (Figure 1.10). In many ways, this could be viewed as a distinct bioprinting concept, rather than just an alternate bioprinting method. It has been the subject of several topical reviews and opinion pieces *(83, 133–136)*.

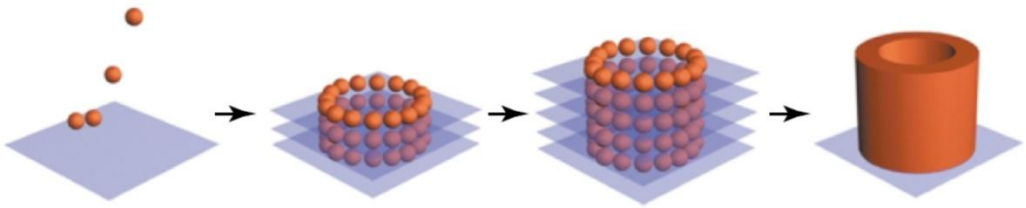

Figure 1.10: Schematic representation of the fabrication of a 3D tube by deposition and subsequent fusion of tissue spheroids. Reproduced from reference *(93)*.

This bioprinting approach has been driven by collaborative research between groups at the Medical University of South Carolina (South Carolina, USA) and the University of Missouri (Columbia, USA). The concept was initially proposed in 2003 *(93)* after initial results showed the fusion of aggregates of bovine aortic endothelial cells printed onto thermosensitive gels using the first cell printer developed by Wilson and Boland at Clemson University (South Carolina, USA) *(137)* (described further in §1.3.5). However, in this work, both the cellular aggregates and the printed structures lacked reproducibility. Subsequently, techniques were developed to obtain reproducible spherical aggregates of CHO cells (~ 500 µm in diameter) by controlled scission of tissue cylinders *(138)*, and the fusion of these CHO aggregates manually positioned within hydrogels was demonstrated *(138, 139)*.

Concomitantly, various bioprinting tools were being developed elsewhere for the extrusion printing of living cells (§1.3.1). It was shown that the CHO aggregates could be aspirated into a capillary and then printed into defined assemblies surrounded by collagen gel using a mechanical bio-assembly tool developed by nScrypt (Orlando, Florida), and this approach was also applied to the fabrication of cardiac constructs from aggregates of embryonic cardiac and endothelial cells *(140)*. The process was then refined further, through the development of a specifically designed bioprinter and alterations to printing methods *(141)*. Specifically, it was recognised that the use of collagen gels limited the fabrication of 3D structures due to premature gelation and unwanted integration with the fusing aggregates. Collagen was therefore replaced with bio-inert agarose gels, and a branched vascular structure was subsequently fabricated from spheroids of human skin fibroblasts (HSFs) (Figure 1.11A-C). Without suitable methods to upscale the fabrication of tissue spheroids and reproducibly aspirate them into a capillary, however, this approach was cumbersome and limited to small structures. Furthermore, the fusion of tissue

aggregates was a slow process and could lead to distortion of the printed constructs *(141)*. Consequently, an alternative approach was demonstrated where long cylindrical tissue aggregates were matured and strengthened in agarose moulds prior to aspiration into capillaries and deposition in 3D arrangements (Figure 1.11D-F). This approach was utilised to fabricate vascular tubes from human umbilical vein smooth muscle cells (HUVSMCs) and HSFs *(141)*. Preliminary results have also been reported on the fabrication of nerve grafts containing Schwann cells (SCs) *(136)*. In 2010, the company Organovo™ (California, USA) was founded, based on this technology, marketing a customised bioprinter and support materials.

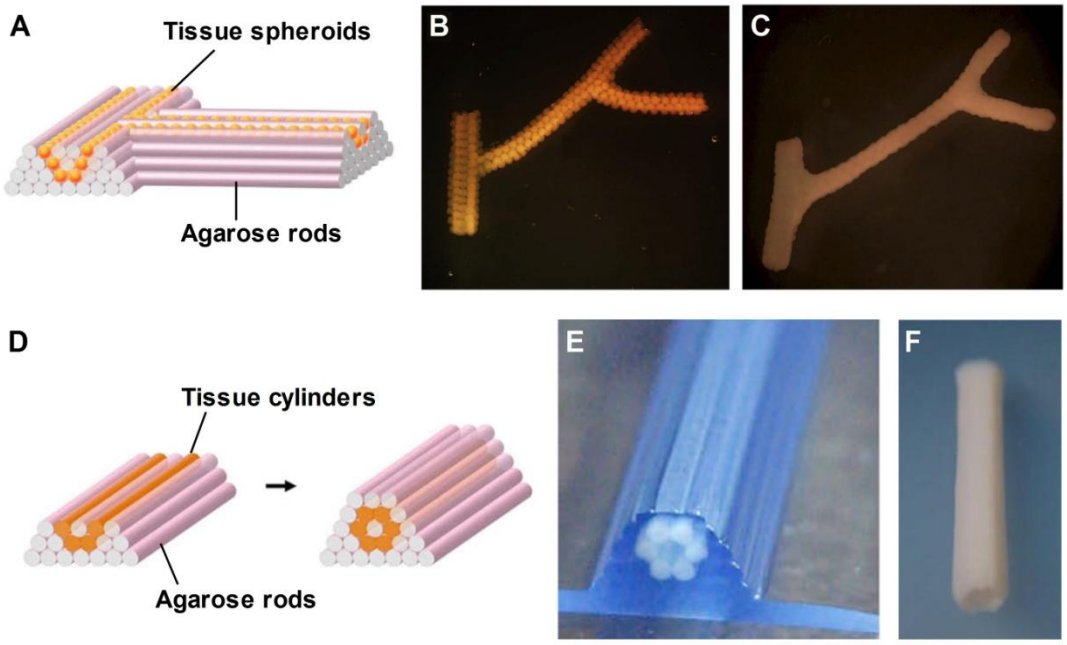

Figure 1.11: Representative structures printed from tissue fragments, adapted from reference *(141)*. **(A)** Deposition scheme for a branched vascular structure from tissue spheroids. **(B,C)** Branched structure built from 300 µm HSF spheroids initially (B), and fused 6 days after deposition (C). **(D)** Deposition scheme for tube fabrication using tissue cylinders. **(E,F)** Printed tubes from agarose cylinders and pig SMCs initially (E), and after fusion and removal from agarose 3 days after deposition (F).

1.3.3 Laser-assisted bioprinting (LAB)

Laser-based approaches were among the pioneering works in cell printing. A technique called laser guidance direct write (LG DW) *(142)*, where a weakly focussed laser beam acts as an optical trap that can control the movement of particles in a solution, was first employed in the year 2000 to pattern living cells on a substrate *(143)*. Since then, the technique has been explored for layering multiple cell types *(144)* and positioning of cells in microarrays *(145)*. However, it is limited by low throughput, low cell viability and a narrow scope of fabricated structures and thus has not been explored extensively as a biofabrication approach.

By far the most published application of laser-based printing techniques has been approaches based on the principle of laser-induced forward transfer (LIFT). This technique was initially developed for the direct writing of metal features using a high-energy pulsed laser to stimulate a metal film on an optically transparent support *(146)*. Modifications of the LIFT technique to deposit biological materials, including cells, have collectively been described as laser-assisted bioprinting (LAB) techniques *(147)*. The three key components of any LAB technique are a pulsed laser source, a target plate usually made of quartz and coated with the ink to be printed (the ribbon), and a receiving substrate that faces the ribbon (Figure 1.12A). There have been two widely employed variations of the LAB approach, which are distinguished by the nature of the ribbon. In matrix-assisted pulse laser evaporation – direct write (MAPLE-DW), the ribbon is coated with a sacrificial biopolymer hydrogel (Figure 1.12B) which acts as an attachment layer for cells and absorbs the laser, typically a low-powered pulsed laser in the UV or near-UV region. Volatilisation at the ribbon-biopolymer interface induces cavitation, which generates a high speed (20 - 100 ms^{-1}) jet that transfers a small volume of the biopolymer and cells to the substrate. In contrast, biological laser printing (BioLP™), which is also referred to as absorbing film assisted-LIFT (AFA-LIFT), uses a ribbon with a thin (1 - 100 nm) metal or metal oxide (usually Au, Ti or TiO_2) layer to absorb a high-powered laser pulse (Figure 1.12C). Due to rapid thermal expansion of this layer, a small volume of the ink is propelled to the substrate as before, but with little transfer of the laser energy to the ink solution. In this approach, cells can be coated onto the ribbon in either cell culture media or a biopolymer hydrogel.

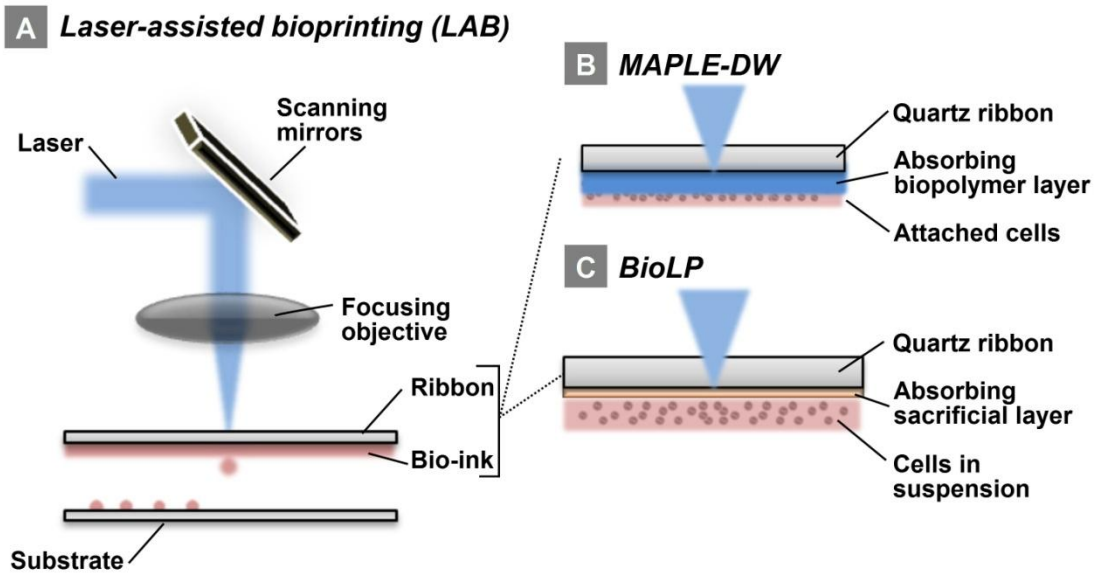

Figure 1.12: Schematic representation of the LAB approach (A), including the ribbon design utilised in both MAPLE-DW (B) and BioLP (C) variations.

Recent reviews provide both a broad overview of LAB in the context of other biofabrication technologies *(27, 148)*, as well as detailed summaries of the development of each of these LAB techniques *(147)*.

The origins of LAB can be traced to the development of MAPLE-DW at the Naval Research Laboratory (Washington, DC) *(149)*. Here, Chrisey's group first demonstrated this technique and its capability to pattern biomaterials including poly(ethylene glycol), enzymes and Chinese hamster ovary (CHO) cells *(150)*, as well as bacteria and proteins *(151)*. Further work enhanced the cell printing capabilities, showing that various cell types including human osteosarcoma and rat cardiac cells *(152)*, as well as pluripotent murine embryonal carcinoma cells *(153)*, could be printed with viability nearing 100% at close to single-cell resolution using Matrigel™ as the absorptive layer. At the same time, this group developed the improved BioLP™ approach in an attempt to limit direct interaction between the laser and sensitive biomaterials *(154)*. This technique also proved capable of depositing highly viable human osteosarcoma cells *(155)* and olfactory ensheathing cells *(156)* onto Matrigel™ substrates.

Since this initial work, both MAPLE-DW and BioLP™ approaches have been implemented with a range of ink materials and cell types, with increasing sophistication of printed constructs. The majority of work has utilised BioLP™, and

has been conducted by two key groups at either the French National Institute of Health and Medical Research (INSERM) in Bordeaux, France, or at Laser Zentrum Hannover (LZH) in Hannover, Germany. For example, Guillemot's group at INSERM demonstrated printing of human endothelial cells from an alginate ink as well as deposition of nano-particulate hydroxyapatite (nHAp) by BioLP™ *(157)*. They subsequently showed that sequential deposition of nHAp alongside human osteoprogenitors in alginate onto Matrigel™ substrates could be used to pattern these components in 2D and 3D with retention of cellular function for application in bone TE *(158)*. Deposition of nHAp alongside osteoblast-like cells has also been demonstrated by a MAPLE-DW approach *(159)*.

Chichkov's group at LZH have demonstrated that BioLP™ can be applied to reactive printing approaches. For example, both human adipose-derived stem cells (ASCs) and endothelial colony-forming cells (ECFCs) were printed sequentially from an ink mixture containing hyaluronic acid (HA) and fibrinogen, onto a substrate sprayed with thrombin to crosslink the printed material *(160)*. This process could be repeated to construct, layer-by-layer, 3D arrays of encapsulated cells for the study of cell-cell and cell-material interactions. Similarly, mesenchymal stem cells (MSCs) were encapsulated in hydrogels by printing them from an alginate ink onto substrates coated with $CaCl_2$, and the MSCs were subsequently differentiated towards osteogenic or chondrogenic lineages *(161)*. Sequential layer-by-layer printing of fibroblasts and keratinocytes from collagen or alginate based inks onto a Matriderm™ (dermal membrane) substrate with or without $CaCl_2$ was also shown to allow BioLP™ fabrication of skin-like 3D constructs *(162)* (Figure 1.13).

Several recent reports have also demonstrated BioLP™ of cells onto scaffolds pre-formed via other fabrication techniques. For example, Chichkov's group selectively seeded acrylated PEG scaffolds, formed by two-photon polymerisation, with ovine vascular smooth muscle cells and endothelial cells printed from alginate-based inks *(163)*. They also reported printing HUVEC and human MSCs onto polyester urethane urea cardiac patches which they implanted in infarcted rat hearts to yield functional improvement *(164)*. Another approach has been to deposit cells using BioLP™ onto thin bio-papers, which were subsequently stacked to form a3D structure. For example, at INSERM, osteosarcoma cells were printed from an

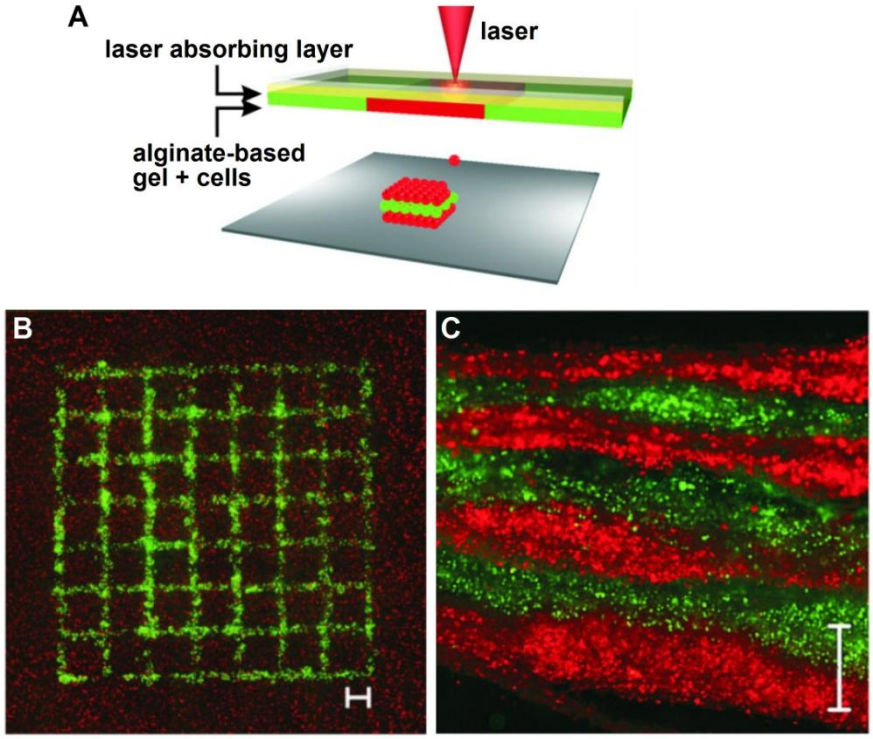

Figure 1.13: BioLP of 3D skin-like constructs, adapted from reference *(162)*. **(A)** Schematic representation of BioLP setup. **(B)** A printed grid containing fibroblasts (green) and keratinocytes (red). **(C)** Seven alternating layers of red and green stained keratinocytes, each layer comprising four sub-layers. Scale bars represent 500 µm.

alginate-based ink onto electrospun polycaprolactone (PCL) mats which were stacked together *(165)*. Similarly, a report from the Naval Research Laboratory outlined BioLP™ of HUVECs from a methyl cellulose ink onto porous poly-lactide-co-glycolide films filled with collagen or Matrigel, and subsequent stacking of cell-laden layers *(166)*. In a novel approach, Corr's group used a MAPLE-DW approach with a gelatin-based ink to print human dermal fibroblasts *(167)* as well as mouse embryonic stem cells that retained their pluripotency *(168)*. The advantage of the gelatin ink was that it melted and was removed during culture so that the printed cells then had access to an application-specific growth substrate, which in these reports was poly-L-lysine (PLL).

1.3.4 Microvalve printing

Microvalve printing is a simple droplet-based deposition mechanism where fluids under constant pneumatic pressure are dispensed from tips by opening and closing a small valve, which can be controlled mechanically, electrically or magnetically. This style of deposition has been implemented in extrusion-style printing as outlined

previously (§1.3.1), where the microvalve remains open for extended periods, but finds most application in drop-on-demand deposition by fast actuation of the microvalve (Figure 1.14). The tips are usually 100-200 µm in diameter, and are capable of dispensing droplets with volumes ranging from tens of nanolitres to several microlitres, from inks with relatively low viscosities (1-20 mPa.s).

The deposition of living cells using microvalve dispensing systems was first explored by Demirci and Yoo's groups at Harvard Medical School (Cambridge, USA) *(170)*. A custom printing tool was developed where four of these dispensers were mounted above a three-axis robotic stage for use in cell printing, and the fabrication of cell-laden collagen constructs by a modified reactive printing process was demonstrated *(171, 172)*. Two dispensers were used to print sequential layers of cells in culture media, and an acidic collagen solution. After printing each layer of collagen, gelation was induced through a pH change by spraying the construct with sodium bicarbonate using a nebuliser, before deposition of the cells onto the gelled collagen. In this manner, skin constructs containing human dermal fibroblasts and epidermal keratinocytes *(171)*, as well as neural constructs containing embryonic rat astrocytes and neurons *(172)*, were printed with high cell viability.

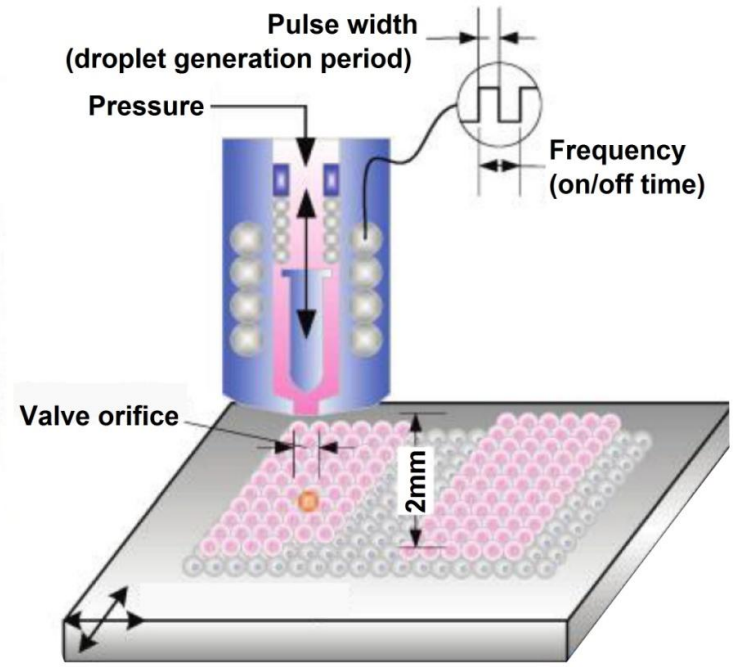

Figure 1.14: Schematic representation of microvalve printing, where droplets of a cell suspension in media or hydrogel are deposited through controlled opening of a microvalve, with constant applied pressure. Adapted from reference *(169)*.

It was also shown that channels suitable for media perfusion could be included in these constructs by printing sacrificial gelatin channels, and that perfusion enhanced the viability of encapsulated fibroblasts *(173)*. Since cells are suspended in culture medium in this approach, cell settling and aggregation led to variations in cell output and clogging of nozzles. In subsequent work, rat bladder smooth muscle cells were encapsulated in cold, pre-neutralised collagen solutions which could be microvalve printed and solidified by thermal gelation with only a slight decrease in cell viability *(174)*. Three-dimensional patches containing encapsulated cells could be fabricated in a layer-by-layer process, although 5 min equilibration at 37 °C was required after each printed layer to induce gelation *(169)*. Microvalve cell deposition has also been explored in the fabrication of constructs tailored for *in vitro* studies. For example, co-cultures were printed onto Matrigel surfaces to act as a model for the study of ovarian cancer *(175)*. Single mouse embryonic stem cells were also deposited in microarrays for RNA analysis *(176)*.

Robotic spotting technologies have been widely implemented in the fabrication of microarrays where antibodies, DNA, proteins or other biomaterials are typically deposited onto glass slides by contact pin-style printers *(177–179)*. While this style of printing can be used to print microarrays of fixed cells *(180)*, it is not suitable for live-cell deposition. Dordick's group at Rensselaer Polytechnic Institute (New York, USA) have used non-contact spotters, which utilise microvalve dispensing tips, to produce live cell microarray platforms *(74)*. Their approach is based on the deposition of individual droplets of cells suspended in a hydrogel matrix onto functionalised glass slides to create stable pseudo three-dimensional arrays of encapsulated cells *(181)* (Figure 1.15). Glass slides were first coated with poly(styrene-co-maleic anhydride) (PS-MA) to enhance hydrophobicity, and spots of poly-L-lysine (PLL) containing $BaCl_2$ were printed onto the surface and dried. Barium was used in place of the more common calcium crosslinker because it is stable in the presence of phosphate, which is a component of most cell culture media. Cells suspended in alginate were then deposited directly on these first spots; the PLL encourages adhesion of the alginate by ionic interactions, and the Ba^{2+} ions diffuse through the alginate solution to crosslink it, forming a cell-encapsulating hydrogel spot. In the first demonstration of this approach, breast cancer and human hepatoma cell lines were deposited in alginate spot microarrays and interrogated with a

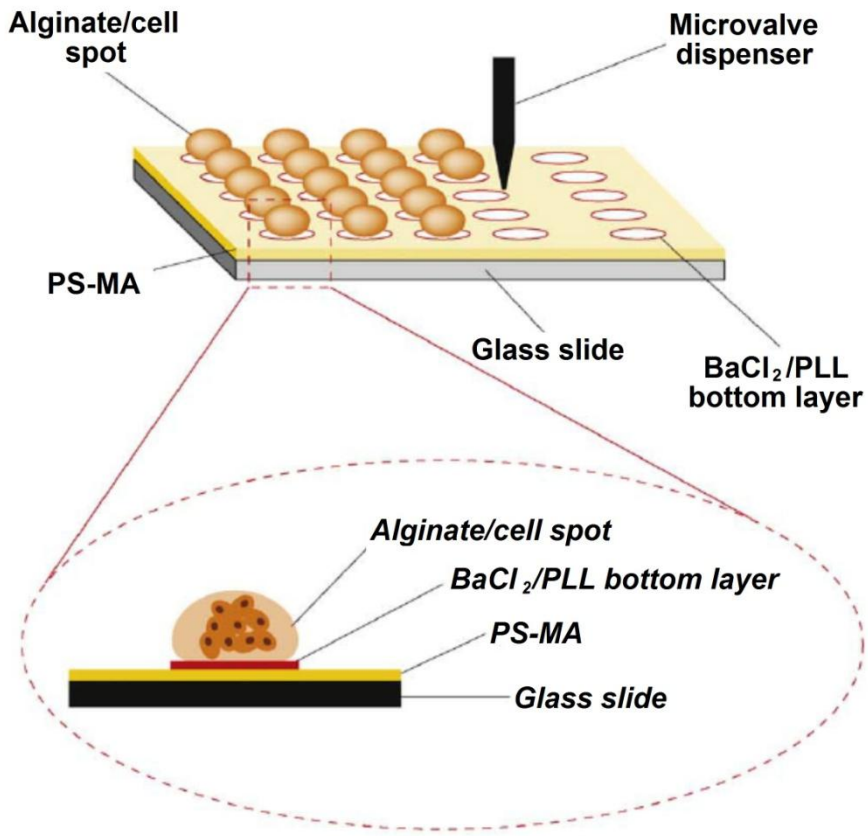

Figure 1.15: 3D cell microarrays produced by microvalve deposition of cell-laden alginate droplets onto pre-printed $BaCl_2$/PLL spots on PS-MA. Gelation of alginate droplets was mediated by Ba^{2+}, and adhesion to the PS-MA surface was enhanced using PLL coatings. Adapted from reference *(74)*.

complimentary array slide loaded with drugs or enzymes *(181)*. This method was also employed to develop an immunofluorescence-based array to investigate the response of alginate-encapsulated human pancreatic tumour cells to chemically-induced hypoxia *(182)*. In a subsequent demonstration, the microarrays were utilised to study the expansion and neural commitment of mouse embryonic stem cells *(183)*.

1.3.5 Inkjet printing

Inkjet printing is a non-contact technique capable of reproducing digital image data on a substrate using picolitre ink droplets. The origins of inkjet printing can be traced as far back as 1867, when Lord Kelvin was granted a patent for "Receiving or Recording Instruments for Electrical Telegraphers", which used electrostatic forces to eject ink droplets onto paper. More recently, ink jet technologies have progressed rapidly and are now ubiquitous in desktop consumer graphics printing, as well as

becoming increasingly important in industrial materials fabrication *(184)*. Inkjet printing can be divided into two broad categories: continuous inkjet (CIJ), where a steady stream of small droplets produced by fluid instability on passage through a nozzle are either deflected by an electrostatic field onto a substrate or not deflected and collected for reuse (Figure 1.16A); or drop-on-demand (DOD) inkjet, were ink droplets are only produced when required (Figure 1.16B-C). DOD inkjet is further categorised by the mechanism used to produce the ink droplets. In thermal inkjet printing, rapid local heating generates a bubble within the ink chamber that ejects a small droplet (Figure 1.16B). Conversely, in piezoelectric inkjet printing, the voltage-mediated actuation of a piezo-crystal is used to create a pressure pulse resulting in droplet ejection (Figure 1.16C). Static electricity actuated print heads comprise a third ejection mechanism but are far less common. CIJ requires electrically conducting ink formulations, and contamination concerns on ink re-circulation all but rule out the technique for cell printing. Consequently, only DOD inkjet has been investigated for cell printing to date

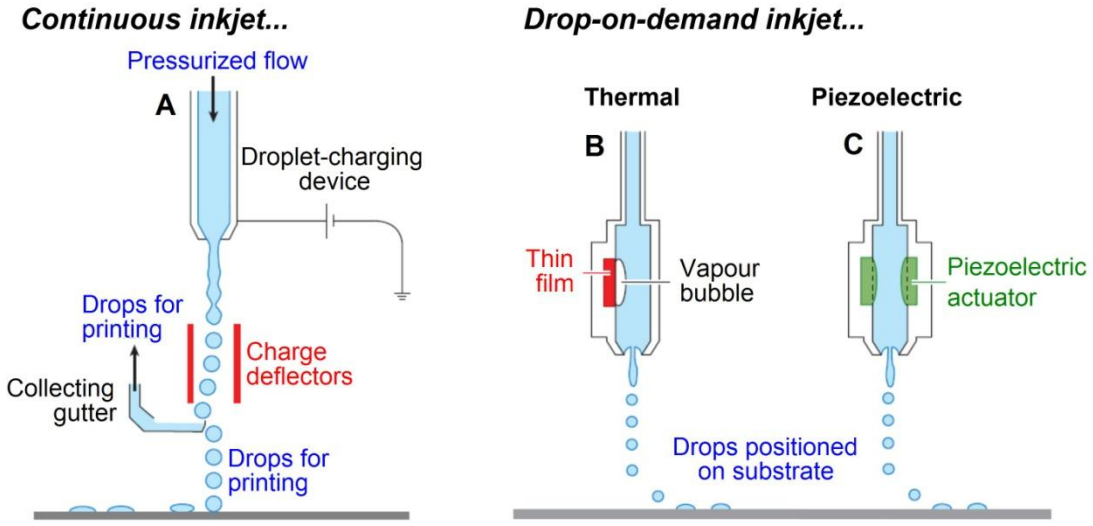

Figure 1.16: Schematic representation of inkjet printing mechanisms. **(A)** The principle of operation of a continuous inkjet (CIJ) printer. **(B,C)** Principles of operation of drop-on-demand (DOD) inkjet printers, where droplets are ejected based on thermal (B) or piezoelectric (C) mechanisms. Figures adapted from reference *(185)*.

As mentioned previously (§1.3), the foundational work of Klebe et al. *(84)* 'cytoscribing' with inkjet printers in 1988 could be considered the birth of bioprinting. Later, inkjet was introduced as a non-contact alternative to traditional contact pin systems for the deposition of biological materials in microarray fabrication *(186–188)*. These instruments were expensive and limited to commercial microarray fabrication. At the same time, however, the development of thermal inkjet technology by Hewlett-Packard and Canon enhanced the accessibility of the inkjet approach by producing cheap and readily available desktop printers. Research in cell printing has since utilised these readily available technologies, and several reviews have outlined the use of inkjet printing in tissue engineering and biofabrication applications *(86–88, 189–192)*.

The use of inkjet printing technology to deposit living cells was first explored by Wilson and Boland *(193)* at Clemson University (South Carolina, USA). Their printer was based on a standard Hewlett-Packard (HP) printer housing, but for cell deposition they utilised a specially designed print head containing 9 individual piezoelectric pumps connected to needles (~160 µm internal diameter) that deposited relatively large (~15 nL) droplets. It was demonstrated that bovine aortic endothelial cells (BAECs) and smooth muscle cells in cell culture media could be deposited onto collagen or Matrigel™ substrates *(193)*. In collaboration with Mironov and Markwald from the Medical University of South Carolina (South Carolina, USA), aggregates of BAECs were printed onto collagen and thermo-reversible gels in a layer-by-layer fashion, and closely-spaced aggregates showed evidence of fusion *(137)*. Although this approach lacked the resolution that true inkjet printing could offer, it became the foundation for the tissue fragment printing approach introduced previously (§1.3.2).

Boland's group, however, continued to work on adapting commercial thermal inkjet technology for bioprinting applications *(189)*. Using slightly modified commercial thermal inkjet print heads from both HP and Canon, they demonstrated patterned deposition of bacteria *(194)* and proteins *(195)* including collagen to guide cellular adhesion *(196)*. The group were the first to show that viable mammalian cells could be deposited from standard commercial thermal inkjet print heads *(197)*. Using print heads (HP26) with a relatively large nozzle size (~ 50 µm) and drop volume (~ 80

pL), CHO cells and embryonic rat motor neurons were deposited onto soy agar and collagen substrates. Primary neural cells printed onto collagen were subsequently shown to exhibit normal electrophysiology *(198)*. In these reports cells were suspended in a 3x concentrated PBS ink, which aided passage through the print head as a result of cell contraction, but also lysed a significant portion of cells (~15%). Later work investigated further the viability of CHO cells printed from a 1x PBS ink and indicated that relatively high cell viability was maintained (89%), with only a small percentage of apoptotic cells *(199)*. It was found that the thermal inkjet printing process generated small (~100 Å) transient pores in cell membranes that self-repaired within 2 hr of printing and this phenomenon could be applied to transfect plasmid DNA into CHO cells *(199)* and endothelial cells *(200)* during printing (Figure 1.17).

Boland's group also explored reactive printing approaches to encapsulate cells in 3D hydrogel structures, using both alginate/calcium and fibrin/thrombin reactive systems. Cell-containing fibrin channels that mimicked simple vasculature were fabricated by suspending human microvascular endothelial cells in PBS containing thrombin and calcium chloride, and printing onto thin layers of fibrinogen *(201)*.

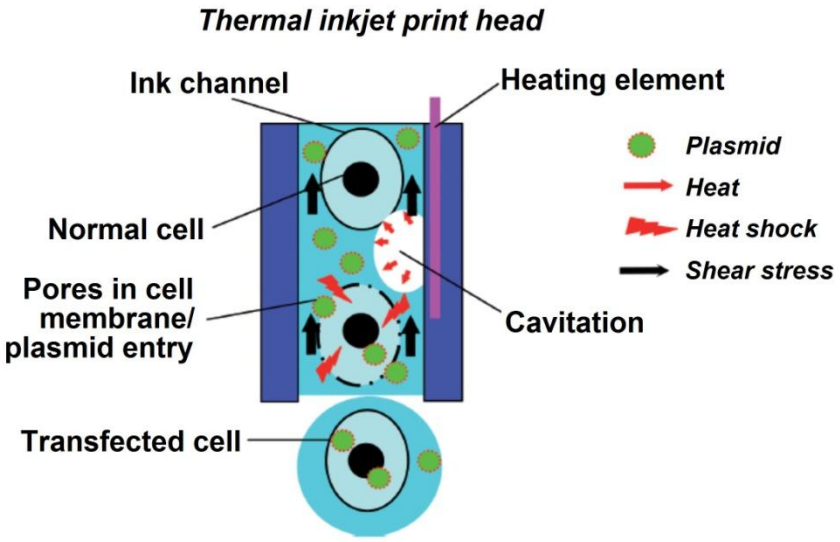

Figure 1.17: Cell deposition from thermal inkjet print heads created temporary pores in cell membranes, as a result of heat shock and shear stress, which allowed transfection of co-printed plasmids. Adapted from reference *(200)*.

While cells were not directly printed in the following approach, alginate solutions containing cells were also selectively cross-linked by the inkjet deposition of calcium chloride to create cell-encapsulating hydrogels with defined three-dimensional structure *(202, 203)*.

These reactive printing approaches were pursued further in Atala and Yoo's lab at Wake Forest University (North Carolina, USA), along with Xu who moved from Boland's group. The alginate/calcium reactive system was again utilised by suspending cells in a calcium chloride solution and printing them, with the same thermal inkjet setup, into an alginate/collagen mixture *(204, 205)* (Figure 1.18). In this way, hydrogels containing regions patterned with multiple cell types could be fabricated *(206)*. Printed cell-laden constructs were implanted into mice and monitored by magnetic-resonance imaging (MRI), revealing changes in tissue microvasculature. The reactive process was also reversed, with cells suspended in low viscosity alginate solutions and printed into a calcium receiving bath. This was used to create single droplets of alginate hydrogels encapsulating pancreatic islet cells that continued to produce insulin *(207)*.

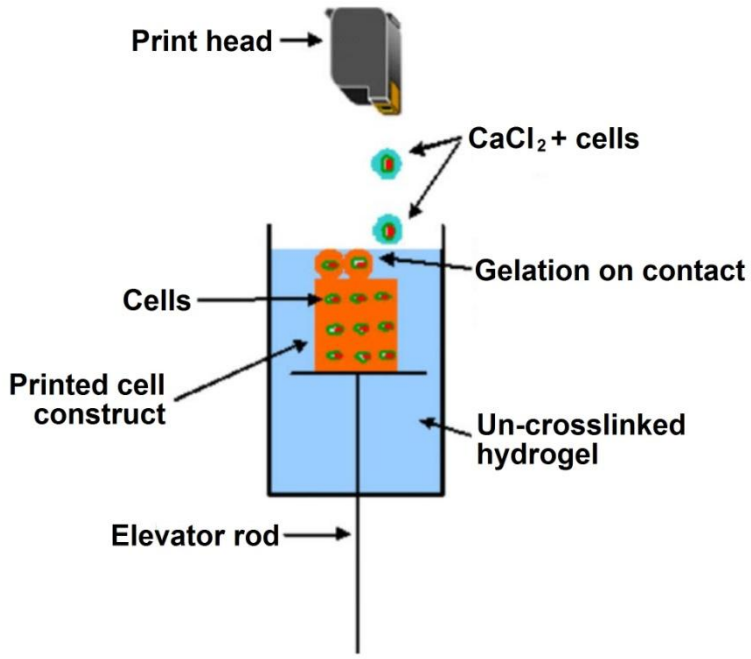

Figure 1.18: Inkjet printing cell-laden constructs by deposition of cells in crosslinking $CaCl_2$ solution into un-crosslinked hydrogel (alginate/collagen). 3D structures are built by sequential lowering of the construct on an elevator stage. Adapated from reference *(205)*.

The approach of printing low viscosity alginate solutions containing cells into calcium chloride receiving baths has also been investigated by Nakamura's group at the University of Toyama (Toyama, Japan), using a style of inkjet print heads that eject ink droplets by actuation of the ink chamber via static electricity (SEAjet™, Seiko EPSON). Having demonstrated that the print heads could deposit cells *(208)*, HeLa cells were subsequently encapsulated in 3D alginate hydrogels by this reactive printing approach *(209)*. In further work, the quality of the printed structures was improved by including viscosity enhancers such as PVA into the receiving bath and employing a high calcium chloride concentration (10%), although this came at the cost of cell viability (~70%) *(210)*. In a more recent report, this reactive printing approach was reproduced with a custom piezoelectric inkjet head containing four separate nozzles *(211)*, although cell viability was not thoroughly investigated.

There have been only a few other examples of cell deposition by piezoelectric inkjet printing, and all have used single nozzle systems. Derby's group at the University of Manchester (Manchester, UK) printed human fibroblast cells using a single nozzle (60 µm diameter) piezoelectric ejector from Microfab Inc. (Texas, USA) *(212)*. Importantly, this was the first comprehensive study on the viability of inkjet printed cells. Additionally, control over the actuation waveform used to drive the piezoelectric deposition allowed analysis of the effect of forces applied to cells on their response. Cell survival was high (> 90%) in all cases, with a slight reduction in viability with increasing actuation voltage (98% at 40V, 94% at 80V), and was indistinguishable from control cells under optimal printing conditions. This printer was also used to deposit cells into micro-well compartments pre-fabricated by inkjet printing of a novel ink material combining thermal and photo-initiated crosslinking mechanisms *(213)*. Derby has also been instrumental in highlighting to the cell printing community the requirements for printable inkjet fluids *(185)*, which will be outlined in the following section.

Two other groups have printed cells using a similar single piezoelectric nozzle ejector (60-100 µm diameters) from Microdrop Technologies (Norderstedt, Germany). Parsa and co-workers printed hepatocytes from a surfactant-containing ink and found similar high viability to that reported by Derby's group, although cell viability decreased after 7 days in culture *(214)*. It was not clear whether this was a

result of the printing process, the added surfactant, or other factors. This work also employed gentle agitation of the print head in an effort to reduce cell settling and aggregation, although this led to reduced cell viability. Liberski and co-workers also used the Microdrop system to fabricate living cell microarrays by combining deposition of cell-laden droplets with novel water-in-oil emulsion cell culture *(215)*.

Burg's group at Clemson University has recently taken the mantle of the research instigated by Boland and continued to explore cell deposition by thermal inkjet printing. With a renewed focus on developing *in vitro* tissue test systems for breast cancer research *(190)*, Burg's work has investigated some fundamental aspects of inkjet cell printing that are key checkpoints in the development of the technology towards becoming a clinically relevant biofabrication tool. Having recognised that printing salt-containing solutions through thermal inkjet heads can quickly lead to nozzle failure due to salt crystallisation, the chelating agent ethylenediaminetetraacetic acid (EDTA) was included in a culture media ink in an attempt to extend print head lifetime *(216)*. This approach was successful in enhancing throughput, although there was some evidence of reduced cell viability after longer (~30 min) exposure times to the EDTA-containing ink. The group has also thoroughly characterised the adverse effects of cell settling and aggregation on cell output during printing, noting that the consistency of cell deposition was affected after ~10 min *(217, 218)*. The group has developed novel methods to achieve alignment of multiple print heads *(190)*, retain printed pattern fidelity and viability through various post-processing methods *(219)*, and quantitatively analyse the fidelity of printed patterns *(220)*. These printing capabilities were utilised to deposit co-cultures of D1 murine mesenchymal stem cells and 4T07 murine mammary cancer cells on collagen hydrogel substrates (Figure 1.19) *(190)*.

1.3.6 Comparison of cell printing approaches

All of the cell printing techniques presented in this section provide alternative routes to controlled cell deposition, with individual advantages and challenges. The different approaches should be regarded as complimentary, rather than competing, technologies. It is likely that significant advances in cell printing will be made through synergistic combinations of these techniques in order to optimise resolution,

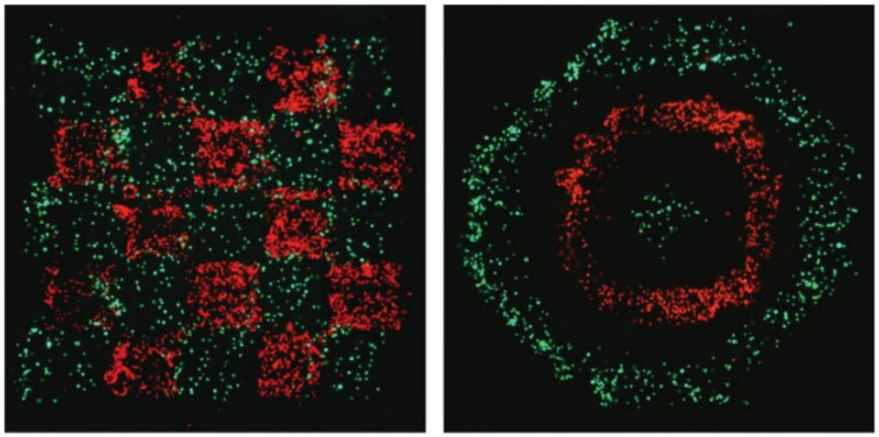

Figure 1.19: Patterns of D1 (green) and 4T07 (red) cells inkjet printed onto collagen substrates. Reproduced from reference *(190)*.

throughput and the overall complexity of printed constructs. For example, the use of printing approaches with different resolutions could be employed to mimic aspects of natural biological systems on different scales. Additionally, some of the work highlighted here has demonstrated the merging of cell printing with solid scaffolds produced via other biofabrication methods, and there is certainly scope to investigate these combinations further.

Extrusion printing could be considered the simplest of all the approaches introduced here, and is arguably the most amenable to the production of 3D hydrogels given that cells are encapsulated within a hydrogel ink prior to deposition. This could also be considered detrimental, however, because it means that cells must be confined to a printable matrix, and therefore cells cannot be deposited separately from the matrix. Reliance on contact with the substrate is not ideal and printing resolution is generally poor. The primary drawback is that deposition is restricted to continuous filaments, which limits the scope of fabricated structures. In contrast, drop-on-demand techniques employ digital fabrication, which is capable of reproducing essentially any pattern or structure.

Printing tissue fragments could be considered a drop-on-demand technique if cell spheroids are deposited. This approach is attractive because cells within the tissue fragments are in a physiologically relevant configuration with high density and cell-cell contact, and because it reflects the natural processes of developmental biology.

There remain, however, significant challenges. As previously discussed (§1.3.2), the formation and processing of tissue spheroids is cumbersome, and the alternative of extruding cylindrical tissue fragments limits fabrication flexibility; it is no longer a drop-on-demand approach. Removal of agarose supporting rods can also be difficult with more complex structures *(141)*. As with extrusion printing, resolution is generally poor. Cell aggregates are 300-500 µm in diameter, larger than the diffusion limit of oxygen (100-200 µm), and therefore hypoxia is a concern. Recent results have indicated some apoptotic cells within printed vascular tissue walls *(141)*.

The drop-on-demand techniques, including laser, microvalve and inkjet printing, boast good resolution and flexibility. They are amenable to deposition of cells directly onto a surface or, as demonstrated for each technique, 3D structures can be fabricated using reactive printing or layer-by-layer approaches. However each of these techniques engenders substantial technological hurdles.

The key advantage of LAB is that it is a nozzle-free approach, which allows printing of inks with a wide range of viscosities (1-300 mPa.s), at cell densities up to $1x10^8$ cells/mL, without issues associated with nozzle clogging *(27)*. High resolution is possible and only a very small amount of material is required. However, laser techniques are not as accessible or as well characterised as microvalve or inkjet printing. The process requires ribbon preparation prior to printing, non-uniform ink coating can cause inconsistent cell output, and the thin layer of ink can dry quickly on the ribbon surface *(147)*. Printing speed and throughput is also limited and scale-up is difficult *(27)*. The use of intense laser irradiation and its long term effect on cells is a concern, although BioLP™ addresses this somewhat with the absorptive interface layer. This layer presents additional problems, however, as cytotoxic metal and metal oxide particles can be transferred to the printed material *(27)*, although this could potentially be avoided by replacing the metal layer with a polyimide *(221)*.

Microvalve printing allows simple drop-on-demand deposition that, in comparison with inkjet printing, is not as dependent on the fluid properties of the ink. Importantly, control over microvalve actuation and the applied pressure means that the deposited droplet volume can be easily adjusted across a wide range, which is not possible for the other drop-on-demand techniques. The large minimum droplet size means that printing resolution is poor compared to laser and inkjet printing, and this

could prevent fabrication of some organotypic structures. In addition, although not as problematic as in inkjet printing, cell aggregation and settling within the printer can alter cell output and clog nozzles, especially when printing from cell culture medium (CCM).

Inkjet printing is arguably the bioprinting technique that is most amenable to positioning cells within engineered constructs, providing a combination of non-contact, high-throughput deposition with single cell resolution. Widespread implementation of inkjet in the consumer graphics printing market has led to rapid development of the technology, which is now well understood and highly accessible. Relationships between droplet generation and fluid properties or printing parameters are thus well understood *(185)*. Furthermore, the application of inkjet to colour printing, where several print heads are used to simultaneously deposit different coloured inks, should be easily transferrable to the deposition of multiple cell types, biomaterials and other biological factors. This has already been demonstrated to an extent *(190, 204)*. However, efficient inkjet printing is heavily reliant upon the ink meeting a relatively stringent set of fluid property requirements, which are elaborated later in this chapter (§1.4). Settling and aggregation of cells can easily clog the relatively small nozzles of inkjet print heads. Current strategies to alleviate this problem have proved largely inadequate, and thus allowable cell concentrations and printing times have been restricted. Furthermore, work to date has implemented thermal inkjet printheads, or single-nozzle piezoelectric print heads, while printing from multiple nozzle piezoelectric heads has not been achieved. Piezoelectric heads are the industry standard for high end printing applications and could provide advantages over thermal heads; primarily, a greater control over droplet formation parameters *(185, 212)*. Long-term cell viability could be an issue due to the high shear forces experienced during deposition, and further work is required to characterise this for both thermal and piezoelectric inkjet printing. One strategy for overcoming many of the technical difficulties associated with drop-on-demand printing of cells is the design of tailored bio-inks.

1.4 Bio-inks

Design of bio-inks for cell printing is challenging, due to the need to simultaneously satisfy often disparate engineering and biological requirements. A bio-ink must be easily printable and have some solidification mechanism to enable the fabrication of 3D structures. This must be achieved without causing cell damage, and the final structure should support the normal function of the printed cells. Currently, bio-inks have tended to satisfy either the engineering or biological requirements at the expense of the other. Real progress in bio-ink design is therefore needed to establish cell printing as a clinically relevant biofabrication tool. This has been reflected in calls from numerous workers in the field for the production of more sophisticated, intelligent bio-inks *(189, 208)*. To understand the need for new bio-inks, it is important to further elaborate on the limitations of current systems that have been described in detail in the previous sections. The following paragraphs seek to achieve this, and provide a framework for the approach taken to bio-ink design in this thesis.

One approach to bio-ink design is to suspend cells in a hydrogel matrix. This is necessary in extrusion printing, which requires a highly viscous ink, but has also been employed with other printing techniques. In this approach, bio-inks have to date been confined to the natural hydrogels gelatin, collagen, fibrin, Matrigel™ and alginate. Aside from alginate, these materials are natural ECM proteins and are chosen for their propensity to foster cell function. However, these systems either require temperature control to prevent premature gelation during printing or are dependent on harsh crosslinking mechanisms, both of which can pose a risk to cells. Alginate is widely available and offers a well defined ionic crosslinking mechanism. However, it is relatively bio-inert and is therefore only suitable as a matrix for anchorage-independent cells like chondrocytes. As outlined elsewhere in this chapter (§1.2.2.2), considerable research has investigated the modification of materials such as alginate, and the synthetic polymer PEG, to incorporate bio-functionality. To date, though, this work has not filtered down to widespread application in bio-ink formulations. Some novel ink formulations, including RGD-modified alginate *(115)* and PEG-based inks *(124)*, have recently been explored and hold promise to address some of these challenges.

The alternative approach is to use cell culture media or a similar low viscosity bio-ink. These have been applied mostly in microvalve and inkjet printing which are suited to these types of fluids. The advantage here is that cell deposition is separated from matrix deposition, which partially de-couples the need to simultaneously satisfy all demands of the system, and 3D cell-laden hydrogels can be fabricated through reactive printing or layer-by-layer approaches. The challenge here is preventing cell settling and aggregation, both of which can seriously hinder printing performance. Current attempts to address this problem have been either inefficient or detrimental to cell viability. In one recent report, a novel ink was designed to avoid cell settling by achieving neutral buoyancy of the suspended cells *(222)*. A sucrose copolymer, Ficoll PM400, was added to cell culture media at 10% (w/v) to increase the density of the solution. This enabled reliable deposition of cells from a piezoelectric dispenser over 90 min, with high viability.

Design of bio-inks for inkjet printing presents additional challenges as the ink must meet stringent fluid property requirements (e.g. viscosity and surface tension) for efficient deposition. While some reports have outlined the use of a surfactant to aid printability in inkjet printing of cells *(214, 222)*, these fluid properties have not been investigated thoroughly. The printability of inkjet inks is typically defined by a series of criteria that are largely dependent on their viscosity (η) and surface tension (γ); other important parameters include the ink density (ρ), nozzle radius (a) and drop velocity (v). An ink is deemed printable if $1 < Z < 10$, where Z is the reciprocal of the Ohnesorge number (*Oh*, Equation 1.1), a dimensionless grouping of these parameters obtained by combining the Weber number (*We*, Equation 1.2) and Reynolds number (*Re*, Equation 1.3). A value of $Z < 1$ will prevent droplet ejection while $Z > 10$ results in satellite droplets *(185)*. Additionally, the need to overcome surface tension barriers at the nozzle requires a $We > 4$, while to avoid splashing on droplet impact the criterion expressed in Equation 1.4 must be met where $f(R) \sim 50$ for smooth, flat surfaces *(185)*. The defined window of properties for a printable fluid created by these criteria is represented graphically in Figure 1.20.

$$Oh = \frac{\sqrt{We}}{Re} = \frac{\eta}{\sqrt{\gamma \rho a}}$$ **Equation 1.1**

$$We = \frac{v^2 \rho a}{\gamma}$$ **Equation 1.2**

$$Re = \frac{v \rho a}{\eta}$$ **Equation 1.3**

$$We^{1/2} Re^{1/4} < f(R)$$ **Equation 1.4**

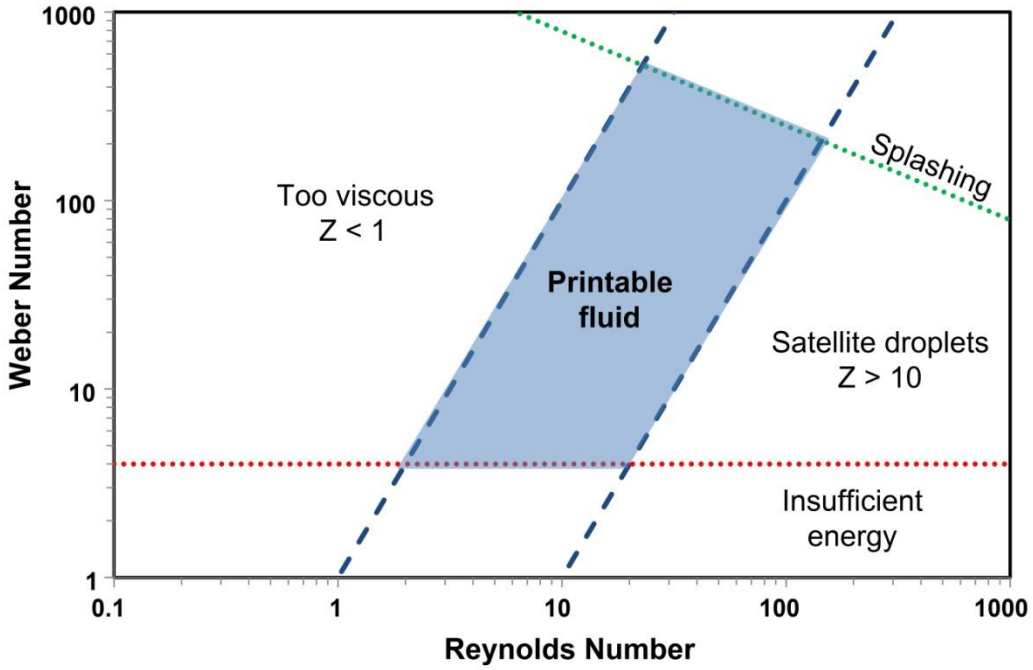

Figure 1.20: Graphical representation illustrating the regime of fluid properties amenable to DOD inkjet printing, where the multiple criteria outlined in Equations 1-4 are satisfied. Adapted from reference *(185)*.

1.4.1 Bio-ink design philosophy

Synergistic approaches that utilise numerous cell printing techniques, and bio-inks, will likely be required in order to fabricate multi-cellular tissue constructs that are truly organotypic. For example, cells could be deposited by inkjet printing, a gelatinous matrix by microvalve printing, and a structural polymer via extrusion printing. In this thesis, we have targeted the design of bio-inks for cell delivery by the drop-on-demand printing techniques, microvalve and inkjet printing. In light of the preceding discussion, our philosophy is that an ideal bio-ink for cell delivery

should have certain characteristics: it should achieve reliable and reproducible cell deposition by preventing cell settling and aggregation; it should also possess optimal fluid properties for drop-on-demand deposition, which is particularly important in the case of inkjet printing; these characteristics should be met without adding significant dry mass to the bio-ink, so that cells may be delivered without confinement in a particular polymer matrix; importantly, the bio-ink should have a physiological pH and ionic strength, and any additives should have no cytotoxic effect; and ideally, the bio-ink would be amenable to reactive printing approaches with polymer solutions delivered by another means. One material with the potential to be utilised in the formulation of a bio-ink that satisfies these criteria is gellan gum.

1.5 Gellan gum

Gellan gum (GG) is an anionic extracellular bacterial polysaccharide produced in high yield by the non-pathogenic strain *Sphingomonas elodea (223)* (ATCC 31461, formerly classified *Pseudomonas elodea*). It consists of a tetrasaccharide repeat unit containing β-D-glucose, β-D-glucuronic acid and α-L-rhamnose monomers in the molar ratio 2:1:1 *(224)*. In native GG, O-acetate and L-glycerate substituents are attached to one glucose residue, with an average of 1 glycerate and 0.5 acetate substituents per repeat unit *(225)*; this is called the 'high-acyl' form. In most commercial products however, these substituents are removed by alkali treatment to yield 'low-acyl' GG (Figure 1.21), which contains very few if any acyl groups. The average molecular mass of GG is ~ 2-5x10^5 Da. Throughout the rest of this thesis, GG refers to the low-acyl form. GG is sold commercially as Kelcogel (food grade) or Gelrite (non-food applications), as well as Gelzan which is extensively purified to removed any residual endotoxin material remaining after synthesis.

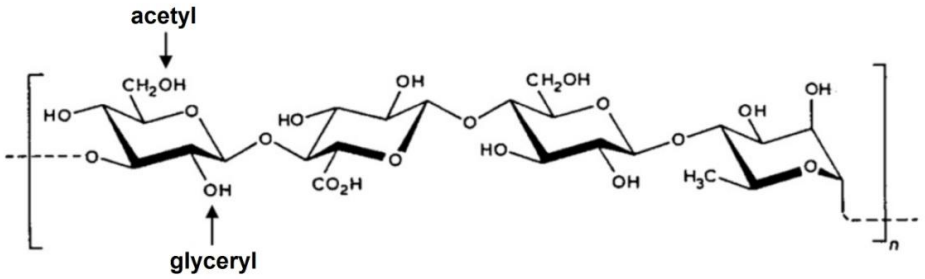

Figure 1.21: Structure of the tetrasaccharide repeat unit in low acyl gellan gum. The locations of glyceryl and acetyl substituents in the native high acyl gellan gum are indicated. Reproduced from reference *(226)*

GG was identified in 1978 by CP Kelco (San Diego, USA) during a large scale screening operation to identify polysaccharides with useful rheological properties from soil and water bacteria *(226)*. Since then GG has found wide application mainly as a multi-functional gelling, stabilising and suspending agent in a variety of foods and personal care products, and has received both US FDA and EU (E418) approval for these purposes. The usefulness of GG pertains largely to its gelation properties, which are discussed in detail in the following paragraph. Several review articles thoroughly describe these properties and the various applications of GG *(226–228)*.

GG dissolves readily in water, adopting a disordered conformation (random coil) at higher temperatures (> ~ 40 °C) which subsequently undergoes a disordered-to-ordered transition on cooling. X-ray diffraction studies on GG fibres have shown that the ordered conformation is a threefold, left-handed, parallel double helix *(229)*. This conformational transition has been observed and characterised extensively by techniques including rheology *(230, 231)*, light scattering *(232, 233)*, nuclear magnetic resonance (NMR) spectroscopy *(234, 235)*, and circular dichroism (CD) spectroscopy *(233)*. These studies have revealed that the conformational transition temperature is dependent on a number of factors including the concentration and molecular weight of the polymer *(236, 237)*, cation concentration *(238, 239)* and pH *(240)*. While helical ordering at low temperatures may impart weak gel characteristics, the formation of a true hydrogel network is achieved through cation-mediated association of helices *(241, 242)* (Figure 1.22). This association can be facilitated through either monovalent or divalent cations, although divalent cations produce a stronger gel. Divalent cations act as direct bridges by site binding between pairs of carboxyl groups, while monovalent cations induce aggregation by suppressing electrostatic repulsions *(243)*.

Aside from its widespread application in food and cosmetics, GG has also found use in the biomedical industry. The most common use has been as a versatile encapsulating agent and active ingredient in numerous controlled drug delivery systems for nasal, ocular, gastric and colonic drug delivery applications *(244–249)*. GG films have also been applied as implants for insulin delivery *(250)*. GG has also been used in plant tissue culture *(251)* and bacterial cell culture *(252)*, and in solid composite scaffold materials *(253, 254)*.

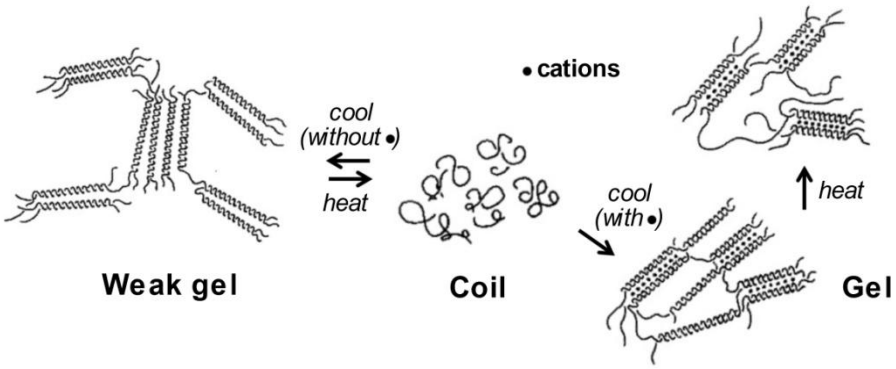

Figure 1.22: Schematic model of the conformational transitions and gelation of gellan gum through temperature changes with and without added cations. Adapted from reference *(226)*.

Recently, a number of groups have focussed on application of GG hydrogels in TE applications. Smith and co-workers were the first group to demonstrate that GG hydrogels could be used to encapsulate viable mammalian cells *(255)*. They showed that GG could be crosslinked by the addition of cell culture media alone, owing to the millimolar concentrations of divalent cations which are present in most media formulations, to form self-supporting hydrogels (Figure 1.23A). This enabled an extremely mild encapsulation of rat bone marrow cells (Figure 1.23B), which remained viable in the GG hydrogels for 21 days in culture.

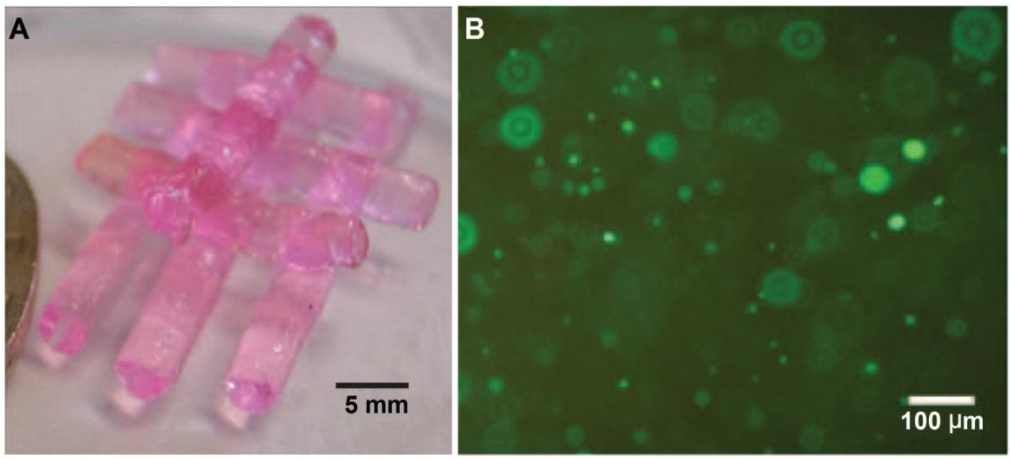

Figure 1.23: (A) GG hydrogel cylinders produced by extruding 1% w/v GG solution into culture medium. **(B)** Calcein-stained rat bone marrow cells in GG hydrogel after 10 days in culture. Figures adapted from reference *(255)*.

Reis and co-workers at the 3B's Research Group (University of Minho, Portugal) have explored the use of GG hydrogels in cartilage TE applications *(256)*. Chondrocytes were shown to remain viable when encapsulated in GG hydrogels *(256)* and exhibited ECM production when implanted subcutaneously in nude mice *(257)*. Injectable delivery of these chondrocyte-laden gels was also investigated, taking advantage of the ability of GG to form a gel under physiological conditions *(258)*. GG hydrogels were also used to encapsulate oligodendrocyte-like cells within the centre of a tubular structure fabricated by 3D extrusion printing of starch *(259)*. This group has demonstrated that GG can be methacrylated to introduce the possibility of photo-initiated crosslinking *(260)*, thus enhancing the range of mechanical and degradation properties that can be tailored into GG hydrogels. These materials have been studied as cellular or acellular artificial nucleus pulposus implants in the treatment of intervertebral disk degeneration *(261–263)*. Du and co-workers took an alternative route to chemical crosslinking by thiolation of GG to produce a stable injectable system *(264)*.

Wang's group at Nanyang Technological University (Singapore) have also utilised GG hydrogels in cartilage engineering. The gelation temperature of GG hydrogels was optimised (to 37.5 °C) by controlling the GG molecular weight through oxidative cleavage *(265)*. Chondrocytes encapsulated in these hydrogels showed expression of collagen that outperformed cells in the more commonly used agarose. Furthermore, rabbit mesenchymal stem cells encapsulated in GG hydrogels and cultured in chondrogenic medium were shown to express both chondrocytic genes and cartilaginous matrix *(266)*. Lee and co-workers also attempted to optimise physical parameters of GG hydrogels for cartilage applications by blending low-acyl and high-acyl GG *(267)*.

GG, like alginate, is a relatively bio-inert material. This has been demonstrated through the lack of cell infiltration and angiogenesis observed when implanting GG hydrogels *in vivo (262)* and in the morphological evaluation of anchorage dependent cells encapsulated in GG hydrogels *(255)*. Thus application has so far been largely limited to anchorage-independent cells such as chondrocytes *(266)*. Therefore, in order to function as a useful artificial ECM for anchorage-dependent cell types, GG must be modified (§1.2.2.2). Previously, GG microspheres produced by a water-in-

oil emulsion process have been covalently functionalised with gelatin through redox-mediated crosslinking to encourage the attachment of human dermal fibroblasts and human fetal osteoblasts *(268)*. Photo-crosslinkable variants of both GG and gelatin have been combined in a novel double-network hydrogel with enhanced mechanical properties *(269)*. However, there is only one very recent report on the functionalisation of GG hydrogels with biomolecules (i.e. adhesion peptides) that encourage the attachment and function of encapsulated anchorage-dependent cells; GG hydrogels were modified with RGD-containing peptides to enhance interaction with encapsulated neural stem/progenitor cells *(270)*.

Our group has been active in research with GG over the last 5-6 years. This research has focussed on utilising the unique suspending and rheological properties of GG in a range of applications. For example, we have used GG to suspend carbon nanotubes (CNTs) in aqueous suspensions which enabled subsequent processing into useful architectures by film casting *(271, 272)*, vacuum filtration *(273)*, inkjet printing *(274)* and extrusion printing *(275)*. Polyelectrolyte complexation between GG and chitosan has also been employed to produce wet-spun complex bio-fibres *(276)* and bi-layer films for wound healing applications *(277, 278)*. GG has also been used as a biocompatible dopant in the synthesis of polypyrrole electrode coatings tailored towards incorporation into neural devices *(279)* In our initial work on applications of GG for TE, hydrogels were produced with and without added CNTs and surface topographical features, and these were shown to support and guide the growth of L929 fibroblast cells *(280)* (Figure 1.24).

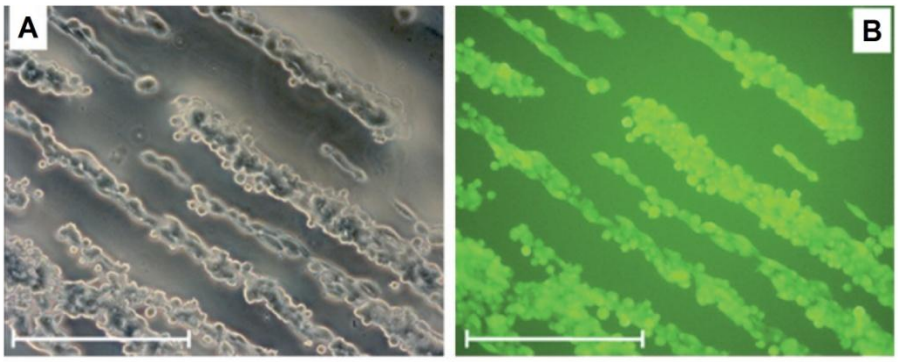

Figure 1.24: Bright field (A) and fluorescence (B) microscope images of calcein-stained L929 cells growing on the surface of moulded gellan gum hydrogels. Scale bars represent 100 µm. Reproduced from *(281)*.

We identified that GG could be a suitable material with which to develop bio-inks that meet the design philosophy previously outlined (§1.4.1). The choice to pursue GG as an alternative to widely employed polysaccharides such as alginate, was a carefully considered one. Alginate is also a linear anionic polysaccharide, containing alternating blocks of *β*-D-mannuronic acid (M) and *α*-L-guluronic acid (G), and is one of the most widely employed cell encapsulating hydrogel materials in TE to date *(65, 66, 282)*. However, GG could possess numerous advantages over alginate in these applications. The key difference between the two biopolymers is their gelation mechanism. Association of alginate chains during gelation occurs according to an 'egg-box' model *(283)*, where divalent cations bind pairs of polymer chains through the formation of stable junction zones, particularly due to the interactions between long stretches of G units and Ca^{2+} ions. Gelation of GG is different in that it is preceded by a conformational transition from coil to double helix, and association of these helices in junction zones is facilitated through either monovalent or divalent cations. Consequently, GG hydrogels may be formed at lower concentrations of divalent cations compared to those required for alginate *(284)*, or even in the presence of monovalent cations alone. This could be advantageous in TE and cell printing applications, in order to avoid the relatively high and potentially cytotoxic concentrations of Ca^{2+} usually employed to achieve gelation of cell-laden alginate. It has been shown, for example, that GG can be crosslinked to form self-supporting hydrogel structures simply by the addition of standard cell culture media with no added ions *(255)*. A direct comparison of GG and alginate as ophthalmic drug delivery vehicles highlighted this advantage of GG as it was able to form a gel on contact with tear fluid *(285)*. GG hydrogels are therefore also stable during long-term culture in standard media *(286)*, in comparison with alginate hydrogels which can undergo unwanted dissolution due to ionic exchange *(57)*.

In addition to these gelation properties, GG's superior optical clarity could prove advantageous in analysis of encapsulated cells *(227)*. Furthermore, GG appears not to inhibit polymerase chain reaction (PCR) analysis *(287)*, while there is evidence that alginate does so *(288)*. These properties of GG hydrogels make them an attractive cell-encapsulating matrix material. With respect to the formation of bio-inks for drop-on-demand cell printing, GG could also be useful due to its utility in the formation of fluid gels.

1.5.1 Gellan gum fluid gels

Gel forming polymers like GG are usually utilised in applications where gelation is allowed to occur under quiescent conditions, for example in order to encapsulate cells. However many of these polymers, including GG, can also be used to form fluid gels, otherwise known as 'structured liquids'. Here, constant shear is applied during the gelation process. Under conditions that would normally lead to the formation of strong, stable and homogenous gels, this shear disrupts the gelation process and hydrodynamic forces limit macromolecular aggregation *(289)*. This leads to the formation of an associated network of discrete microgel particles that imparts useful viscoelastic properties to the fluid *(290)*. The term 'fluid gel' is used to avoid confusion with other microgel particles or hydrogel microspheres that are produced by emulsion or other methods *(291, 292)*. Throughout the bulk of this thesis, the term 'microgel suspension' is used to refer to fluid gels in order to better reflect the nature of their structure. The formation of microgel suspensions (fluid gels) has been studied in biopolymers including gelatin *(293)*, agar *(294, 295)* and GG *(289, 296–298)*. The rheological properties of these systems, characterised by viscoelastic properties including a yield stress and shear-thinning behaviour, make them highly useful in the food industry *(299)*. Notably, they are capable of suspending dispersed materials such as herbs and spices in pourable dressings *(296, 300)*. That particular application is not too dissimilar from the need to suspend dispersed cells in a printable fluid.

The formation, structure and rheological properties of GG fluid gel systems has been studied extensively *(289, 296–298)*. Since GG forms strong quiescent gels at low polymer concentrations, useful fluid gels can also be formed at low concentrations provided adequate shear is applied during gelation *(297)*. Most commonly, these fluid gels are formed using the aforementioned approach of subjecting GG solutions to shear during thermal gelation in the presence of cations. However, it should be noted that quiescently cooled weak gels can also be converted to fluid gels by application of shear after gelation *(289)*, although the properties do not reproduce those of a shear cooled system *(298)*. The rheological properties of a fluid gel can also be achieved by quiescently cooling under certain ionic conditions *(296)*, although this is only possible at relatively high ionic strengths. GG fluid gels have

previously found application as low-concentration additives in the food industry, in paint formulations, and as ophthalmic drug delivery systems *(289)*. The formation of relatively strong quiescent GG gels using the cations present in CCM has been demonstrated previously by us *(280)* and others *(255)*, and therefore this ionic composition should also be sufficient for fluid gel formation. We therefore postulated that GG fluid gels in CCM could be an interesting system with which to explore the development of a bio-ink that could meet the criteria outlined in the bio-ink design philosophy section (§1.4.1).

1.6 Thesis aims and outline

It has been established that cell printing techniques will continue to have increasing impact in fabricating functional tissue constructs for both *in vivo* and *in vitro* applications. There remains, however, a need for more intelligent bio-inks that satisfy the demands imposed by both fabrication and biological requirements. This thesis aims to explore new strategies towards the development of bio-inks for the fabrication of cell constructs through drop-on-demand printing techniques.

Specifically, the objectives of this thesis were to:

- Develop bio-ink formulations that satisfied the design criteria (outlined in §1.4.1) for drop-on-demand printing through the formation of GG microgel suspensions in cell culture media and, in the case of inkjet printing, with the addition of suitable surfactants.

- Achieve robust and reproducible deposition of cells suspended in bio-inks through both microvalve printing and inkjet printing, and to use these techniques to fabricate both two-dimensional cell constructs and three-dimensional cell-encapsulating GG hydrogels.

- Modify GG hydrogels to enhance their biofunctionality and, as a result, enhance cellular interactions with these hydrogels.

A broad outline of each chapter is as follows:

- Chapter 2 provides a description of the materials and methods utilised in the work presented throughout all subsequent chapters.

- Chapter 3 outlines the formation and characterisation of the bio-inks, with and without added surfactants, including analysis of rheological properties and subsequent cell-suspending ability, surface tension and structure. The phenotypic responses of cells exposed to the formulations are also examined.

- Chapter 4 investigates microvalve printing of cells suspended in surfactant-free bio-ink, including the reproducibility of cell deposition and the phenotypic responses of cells to the printing process. A novel method whereby microvalve printing is used to fabricate cell-encapsulating GG hydrogels is also presented.

- Chapter 5 studies inkjet printing of cells suspended in surfactant-containing bio-ink, including the reproducibility of cell deposition and the phenotypic responses of cells to the printing process. Applications of inkjet cell printing are explored, including the fabrication of: cell microarrays for single cell analysis by surface-sampling mass spectrometry; patterned cell co-cultures on collagen substrates; and cell-encapsulating GG hydrogels.

- Chapter 6 examines in more detail the interaction of cells with GG hydrogels, with cells either seeded on the surface of hydrogels or encapsulated. Modification strategies aimed at enhancing favourable interactions are investigated, including the conjugation of cell-adhesion peptides to GG.

- Chapter 7 summaries the findings of this thesis, and suggests future work.

2 EXPERIMENTAL

2.1 General Cell Culture and Analysis

2.1.1 Cell culture

Three murine clonal cell lines, all obtained from the American Type Culture Collection (ATCC), were used in this thesis. C2C12 cells (ATCC CRL-1772) are a subclone, produced by Blau et al. *(301)*, of the mouse skeletal muscle myoblast cell line first established by Yaffe and Saxel *(302)*. The cells differentiate rapidly to form myotubes with concomitant expression of muscle-specific proteins. PC12 cells (ATCC CRL-1721) were derived from a transplantable rat adrenal pheochromocytoma by Greene and Tischler *(303)*. These cells respond to nerve growth factor (NGF) by ceasing to multiply and expressing a phenotype reminiscent of sympathetic neurons in primary culture, and are thus often used as a model of neuronal differentiation. L929 cells (CCL-1) were derived from mouse connective tissue by Sanford in 1948 *(304)* and were one of the first clonal cell lines to be established in continuous culture. Frozen cell stocks were stored under liquid nitrogen at a density of $1x10^6$ cells/mL in cell culture medium (CCM) containing 5% (v/v) dimethyl sulfoxide (DMSO, Sigma).

The CCM used to maintain these cells was high glucose Dulbecco's Modified Eagles Medium (DMEM, Gibco) supplemented with 3.7 g/L sodium bicarbonate (Sigma) and 10% (v/v) foetal bovine serum (FBS, Invitrogen) for C2C12 and L929 cells, or 10% (v/v) FBS and 5% (v/v) horse serum (HS, Sigma) for PC12 cells. Cells were cultured in standard tissue culture polystyrene (TCPS) flasks (Greiner) at 37°C in a humidified incubator with a 5% CO_2 environment, and sub-confluent cultures were passaged every 2-3 days. For C2C12 and L929 cells, CCM was removed from culture flasks, cells washed twice with phosphate buffered saline (PBS, Sigma) and trypsinised using 0.25% trypsin/EDTA (Gibco). Trypsinised cells were collected and pelleted by centrifugation (Heraeus Multifuge 1S-R, ThermoScientific) at 1500 rpm (500 *g*) for 5 min and seeded at 1:10 the original density in a new flask. For PC12 cells, the same protocol was followed however the floating cell population was retained by centrifugation along with the adherent cells that were collected using

0.05% trypsin/EDTA in order to maintain the entire culture in both growth phases. PC12 cells were re-seeded at 1:5 the original density in a new flask. Figure 2.1 displays representative images obtained from the ATCC showing the morphology of these three cell lines in culture on TCPS at low and high cell density.

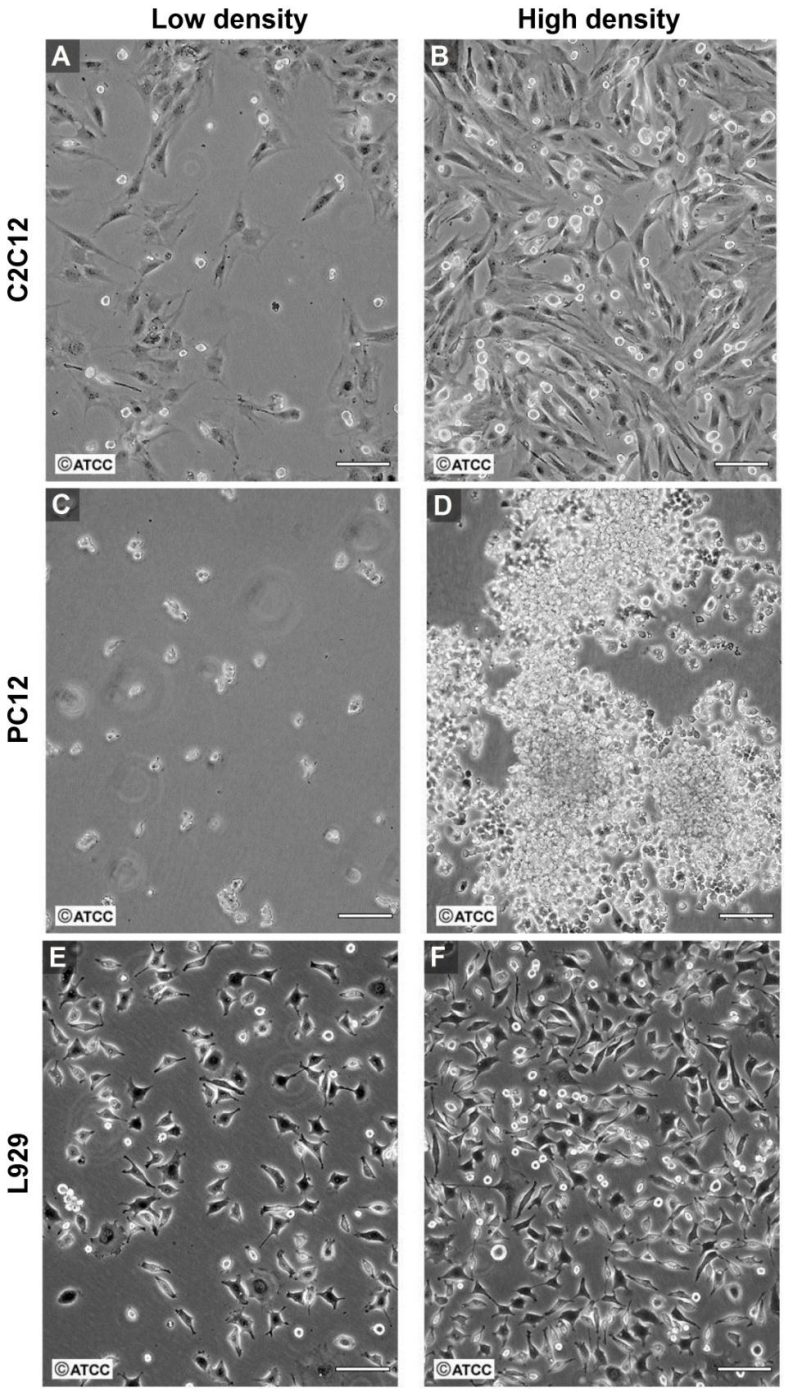

Figure 2.1: Representative images, supplied by the ATCC, of proliferative C2C12 (A, B), PC12 (C, D) and L929 (E, F) cells in culture at low density (A, C, E) and high density (B, D, F). Scale bars represent 100 µm.

In experiments where cells were maintained in a proliferative state, i.e. for analysis of cell viability (§2.1.5) or proliferation (§2.1.6), cells were cultured in cell proliferation media (CPM) consisting of their respective CCM formulation with the addition of 100 units/mL penicillin and 100 µg/mL streptomycin (pen/strep, Gibco) as an antibiotic/antimycotic agent. CPM in these experiments was replaced every two days, unless stated otherwise.

Cell differentiation was induced by serum starvation for C2C12 cells, and a combination of serum starvation and the addition of NGF in the case of PC12 cells. Cell differentiation media (CDM) for PC12 cells consisted of DMEM supplemented with 1% (v/v) HS, 50 ng/mL NGF (Invitrogen) and pen/strep. For C2C12 cells, CDM consisted of DMEM supplemented with 2% (v/v) HS and pen/strep. Unless stated otherwise, cells in these experiments were initially cultured in CPM for 24 hr before a changing to CDM to induce differentiation. In some experiments with C2C12 cells, the serum content was changed gradually, from 10% FBS (CPM conditions) to 5% FBS after 24 hr, 2% FBS after 48 hr, and finally to 2% HS (CDM conditions) after 72 hr. Previous work in our laboratory (unpublished) had suggested that this gradual serum change was more effective at inducing differentiation in C2C12 cells. Unless stated otherwise, final CDM was replaced every two days in these experiments. A complete summary of the various media compositions utilised in this thesis is provided in Table 2.1.

Table 2.1: Summary of the media compositions utilised in routine culture and in experiments under proliferation or differentiation conditions for C2C12, PC12 and L929 cells. The base of each media consisted of DMEM with 3.7 g/L sodium bicarbonate.

Cell line/condition	% FBS	% HS	Other
C2C12			
Culture (CCM)	10	-	-
Proliferation (CPM)	10	-	Pen/strep
Differentiation (CDM)	-	2	Pen/strep
PC12			
Culture (CCM)	10	5	-
Proliferation (CPM)	10	5	Pen/strep
Differentiation (CDM)	-	1	Pen/strep, NGF (50 ng/mL)
L929			
Culture (CCM)	10	-	-

2.1.2 Cell microscopy and imaging

Two microscopes were routinely used throughout this work for observation and imaging of cell cultures: a Zeiss AxioVert 40 CFL inverted microscope equipped with an AxioCam ICm1 camera and an HB050 mercury lamp; and a Zeiss AxioImager.A1m upright microscope equipped with an AxioCam MRm camera and an HB100 mercury lamp. Microscope control and image acquisition was facilitated by AxioVision software (release 4.8.1). The AxioVert microscope was used for routine observation of cell cultures and for cell counting, as well as for bright-field and fluorescence imaging (e.g. for cultures in well plates). The AxioImager microscope was used mainly for fluorescence imaging (e.g. for cover-slipped samples).

2.1.3 Cell counting

The density of cells in suspension was counted using a Bright-Line™ hemocytometer. A 10 µL aliquot of a well-mixed cell suspension was injected into the hemocytometer with cover-slip in place, and the number of cells in at least four separate grid regions was counted manually using the AxioVert microscope. For analysis of high cell concentrations, the suspension was first diluted 1/10 with fresh medium. Where a more accurate determination of the concentration of viable cells was required, cell suspensions were first mixed 1:1 with trypan blue solution (0.4%, Sigma). Trypan blue is excluded from viable cells with intact membranes, but is able to traverse the compromised membranes of dead cells, which are consequently stained blue.

For several experiments, it was necessary to count the number of cells within a given microscope image or region of interest within that image. This was required, for example, in the analysis of cell viability (§2.1.5), in cell settling experiments (§2.2.7), and when investigating cell output from both microvalve printing (§2.3.4) and inkjet printing (§2.4.4). Counting of very small cell numbers, for example when quantifying the number of cells in an individual inkjet droplet, was achieved by manual observation under the microscope. Otherwise, two software packages were utilised to assist cell counting. Image J, an open-source image processing program (available from http://rsbweb.nih.gov/ij), was used to aid manual counting of large numbers of cells from acquired microscope images using the ‘Cell Counter’ plug-in.

ImagePro software (MediaCybernetics, v. 6.0.0.260) was utilised when a large batch of images required automated counting. This program was used, for example, to count the number of C2C12 cells contained within inkjet printed square patterns (Figure 2.2A). Images were generally filtered using four passes of a 3x3 rank filter (25% threshold) and cells were counted with the 'histogram count' feature followed by application of a watershed split to separate any connected cells. Figure 2.2B shows results from both manual (aided by Image J software) and automated (ImagePro software) counts of C2C12 cells in triplicate squares at six different printed positions. In each case, both the average cell number and standard deviation show good agreement between counting methods. In some cases, where salt crystallisation in dried droplets obscured cell counting, printed slides were placed in a covered Petri dish containing a small amount of water; this effectively re-hydrated the printed patterns and aided cell visualisation.

2.1.4 Fluorescent staining

2.1.4.1 Live/dead staining

Fluorescent staining of live cells was achieved using calcein AM. The uncharged acetoxymethyl (AM) ester derivative of calcein is non-fluorescent and able to permeate cell membranes. Once inside live cells, ester hydrolysis by non-specific intracellular esterases results in conversion to the charged calcein, which exhibits a bright green fluorescence and is retained in cells much longer than its parent compound. Calcein staining was achieved by incubating cells in media containing

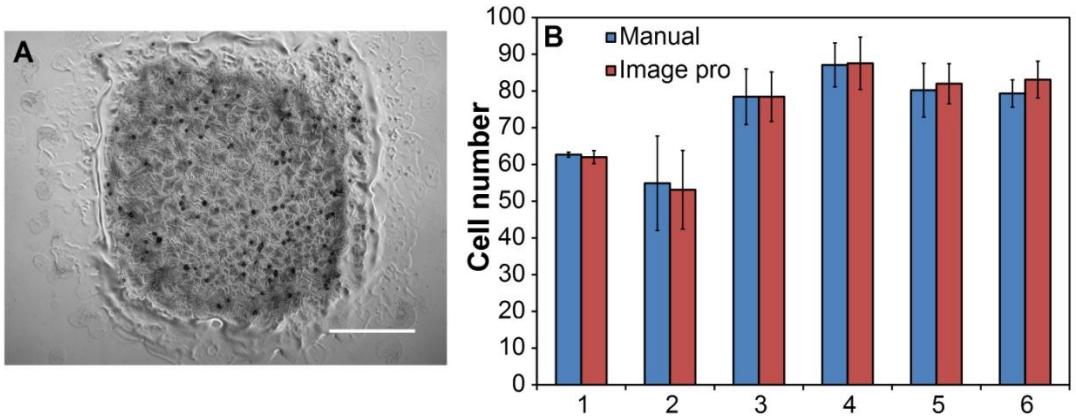

Figure 2.2: Comparison of manual (using Image J software) versus automated (using Image Pro software) counting of cell number. **(A)** A printed square containing C2C12 cells (black dots). Scale bar represents 500 µm. **(B)** Average cell number counted manually or using Image Pro software for triplicate cell-containing squares printed at six different spatial locations across an inkjet print head.

5 µg/mL calcein AM (Molecular Probes) at 37°C for 15 min in the dark. When cells were encapsulated within a hydrogel, incubation time was extended to 30 min and hydrogels were rinsed with fresh media prior to imaging to reduce background fluorescence.

Propidium iodide (PI) is a red-fluorescent dye that binds to cell nuclei by intercalating with DNA. Since it is membrane impermeant and excluded from live cells, it is commonly employed to identify dead cells in a population. The fluorescence of PI is enhanced 20-30x on binding to DNA. Staining of dead cells was achieved by addition of PI (Molecular Probes) at 1 µg/mL to media, followed by immediate imaging. PI is incorporated into dead cells quickly but is also taken up by cells with reduced membrane integrity (e.g. in the early stages of cell death), and so ensuring minimal time between addition of the dye and imaging reduces the likelihood of dye take-up by live or early apoptotic cells. The exception to this was staining of cells encapsulated in hydrogels, where incubation for 5 min at 37°C in the dark was employed to allow PI to diffuse through the hydrogel. To ensure the effectiveness of cell staining in hydrogels, control, dead-cell samples were treated with 70% (v/v) ethanol prior to staining with PI.

2.1.4.2 CellTracker™ staining

In some experiments, for example where both C2C12 and PC12 cells were patterned simultaneously by inkjet printing (§2.4.7), it was necessary to stain two live cell populations with different fluorescent markers in order to aid visualisation and to distinguish between the two cell types. For this purpose, we employed CellTracker™ dyes (Molecular Probes). These fluorescent probes pass freely through the membranes of live cells, where they are converted to membrane-impermeant products that, unlike calcein AM, have minimal effect on cellular function and are retained in living cells through several generations. In our experiments, C2C12 cells were stained with CellTracker™ Red CMPTX and PC12 cells were stained with CellTracker™ Green CMFDA. Lyophilised dye was dissolved in DMSO at a concentration of 10 mM, and this stock solution was diluted to a working concentration of 20 µM in DMEM and warmed to 37°C. The CCM from a near-confluent flask of cells was removed, and adherent cells were washed twice with PBS before addition of the dye working solution. For PC12 cells this step included

recovering cells in the culture supernatant, which were pelleted and re-suspended in the dye solution prior to addition to the adherent cells remaining in the culture flask. Cells were subsequently incubated in the dye solution for 45 min at 37°C. The dye solution was then replaced with fresh DMEM (again, for PC12 cells, this included recovering floating cells as previously) and cells were incubated for another 30 min at 37°C. Stained cells were then harvested as described previously (§2.1.1) for use in experiments.

2.1.4.3 Immunostaining

Immunostaining was used in this thesis to characterise the phenotype of differentiated C2C12 and PC12 cells. For C2C12 cells, staining targeted desmin; a sarcomeric intermediate filament protein expressed in differentiated skeletal muscle. For PC12 cells, staining targeted β-III tubulin; a globular microtubule protein expressed exclusively in neurons. In each case, cell nuclei were counter-stained using 4',6-diamidino-2-phenylindole (DAPI, 1 mg/mL), which binds strongly to DNA.

Differentiated cells were fixed with 3.7% (w/v) paraformaldehyde (PF, Fluka) in PBS for 10 min at room temperature, washed twice with PBS and, if required, stored in PBS at 4°C prior to staining. For staining of C2C12 mono-cultures, cells were permeabilised with 50:50 (v:v) methanol:acetone on ice for 5 min and washed with PBS before blocking in 10% (v/v) donkey serum (DS, Chemicon) with 0.05% (v/v) Tween-20 (Sigma) for 1 hr at room temperature (RT). Mouse monoclonal anti-desmin primary antibody (Novocastra, 45 mg/L) was diluted 1:100 in blocking solution and incubated at 4°C overnight. After two 10 min washes in PBS, cells were incubated for 1 hr at RT in the dark with the secondary antibody Alexa-546 donkey anti-mouse (Invitrogen, 2 mg/mL) diluted 1:1000 in blocking solution. After two 10 min washes in PBS, DAPI was added at 1:1000 in PBS for 5 min at RT, before replacing with PBS.

For differentiated PC12 and C2C12 co-cultures on collagen hydrogels (§2.4.7), the above protocol was used with cells incubated in a mixture of primary antibodies in blocking solution. C2C12 cells were labelled with rabbit monoclonal anti-desmin (Cell Signalling Technology) diluted 1:100, while PC12 cells were labelled with mouse anti-neuronal β-III tubulin (Covance, 1 mg/mL) diluted 1:1000. Secondary

antibodies were Alexa-488 donkey anti-rabbit (Invitrogen, 2 mg/mL) and Alexa-546 donkey anti-mouse (Invitrogen, 2 mg/mL), diluted 1:1000 in blocking solution.

2.1.4.4 Phalloidin staining

For differentiated PC12 cells on TCPS, cells were stained with fluorescently-labelled phalloidin to prevent lengthy immunostaining protocols that could have detached cells from the substrate. Phalloidin is a phallotoxin that binds strongly to F-actin filaments within the cell. Fixed cells were permeabilised with 0.1% Triton X-100 (Sigma) in PBS for 5 min at RT. After washing twice with PBS, cells were incubated for 20 min at RT in the dark with Alexa-488 phalloidin (Molecular Probes) at 165 mM in 1% (v/v) bovine serum albumin (BSA) in PBS. After two washes in PBS, cells were stained with DAPI as above.

Cells fixed and stained by either immunostaining or phalloidin staining were stored at 4°C in the dark in either sterile PBS, for short-term storage, or in ProLong® Gold anti-fade reagent (Invitrogen) for long term storage.

2.1.5 Cell viability

For quantitative analysis of cell viability, cells were seeded in 96-well plates (Greiner) at ~ 5000 cells/well. Live/dead staining was conducted as previously described (§2.1.4.1), and the number of live and dead cells counted by manual or automated methods (Figure 2.3) (§2.1.3). Unless stated otherwise, cells in three wells per condition were stained and live/dead cells were counted for three images acquired from random fields of view within each well to provide a robust measure of viability. Cells were allowed to incubate under culture conditions for 2 hr after challenge (i.e. printing, exposure to bio-ink) to allow cells to settle and equilibrate at the base of the well plate prior to staining. In some cases, viability measurements were repeated after 24 hr on a replicate set of wells. We found that live/dead staining in PC12 CPM led to high background staining, possibly due to interactions with the 5% HS content in this media, and so produced an un-reliable measure of cell viability. Consequently, assessment of PC12 viability was carried out with the cells in C2C12 CPM, which does not contain HS. Viability was only assessed after 2 hr in culture for PC12 cells, therefore the change in media conditions was not expected to have a significant effect on cell viability.

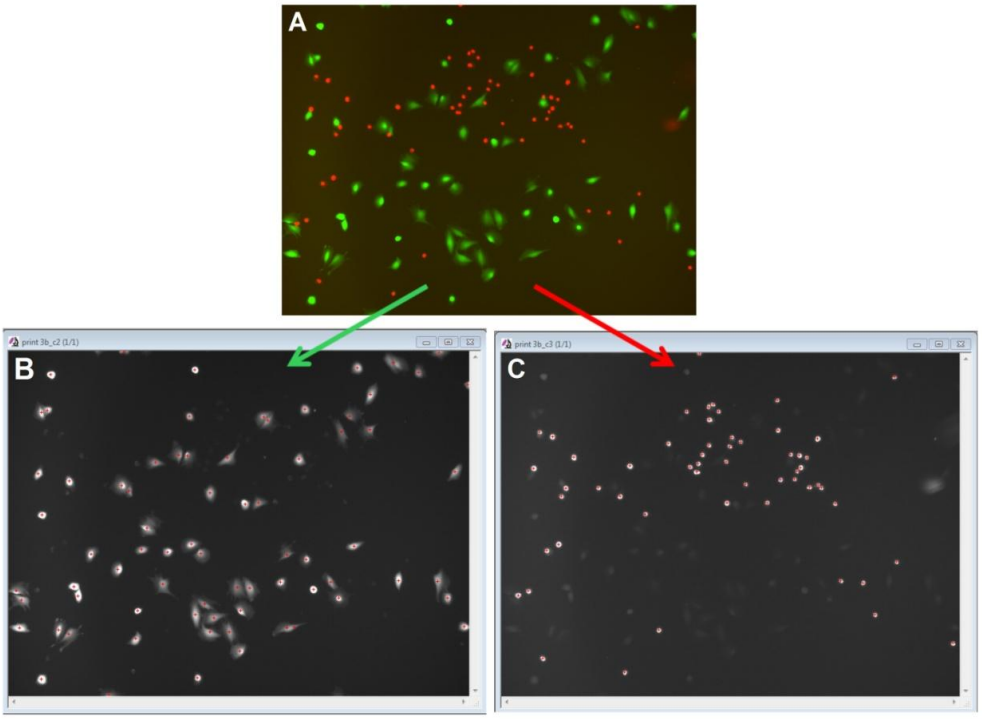

Figure 2.3: Live/dead stained image of C2C12 cells (A) split into the calcein (B) and PI (C) channels for automated counting by ImagePro software.

2.1.6 Cell proliferation

Cell proliferation over time was assessed using the CellTiter 96® AQ_{ueous} One Solution proliferation assay (Promega). This colorimetric method employs a reagent combining the tetrazolium compound MTS [3-(4,5-dimethylthiazol-2-yl)-5-(3-carboxymethoxyphenyl)-2-(4-sulfophenyl)-2H-tetrazolium] and an electron coupling reagent PES (phenazine ethosulfate) in a stable solution. The MTS compound is converted by metabolically active cells into a coloured formazan product (Figure 2.4) that is soluble is culture media, and can be quantified by measuring the absorbance at 490 nm. This absorbance level is directly proportional to the number of metabolically active cells.

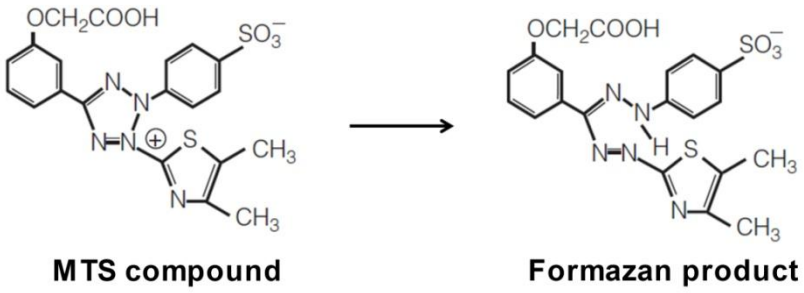

Figure 2.4: Structures of the MTS tetrazolium compound and the formazan product produced by bioreduction.

In cell proliferation experiments, cells were seeded in 96-well plates at ~5000 cells/mL in 100 µL CPM. Unless stated otherwise, three replicate plates designated for measurement after 2, 24, and 48 hr were seeded with triplicate wells for each condition under investigation. A set of wells with cell-free CPM was also included in each plate as a method blank. At each time point, 30 µL of warmed CellTiter 96® AQ_{ueous} One Solution reagent was added to each well and incubated under culture conditions in the dark for 90 min before reading absorbance on a plate reader (SpectraMax 190, Molecular Devices) at 490 nm (formazan product) and 650 nm (background). The absorbance at 650 nm was subtracted from that at 490 nm for each individual well, and then the average net absorbance for blank wells was subtracted from each cell-containing well. The final absorbance at the 24 and 48 hr time points was normalised to the 2 hr time point in order to account for differences in initial cell numbers between conditions. This approach has been adopted previously when reporting the viability of printed cells *(212)*. Standard curves for net absorbance as a function of the number of C2C12 or PC12 cells were prepared to ensure that the relationship of cell number to net absorbance was linear (Figure 2.5).

2.2 Bio-ink Formulation and Characterisation

2.2.1 Gellan gum

The gellan gum (GG) used throughout this thesis, Gelzan™ CM, was kindly donated by CP Kelco. Gelzan™ CM is a low-acyl form of GG that has been purified to remove endotoxins, and is commonly marketed as Gelrite®, a substitute for agar in microbiological media. It was received in powder form in 250 g batches, stored under cool dry conditions and replaced when the manufacturer's expiry date had been exceeded.

Stock solutions of 1% (w/v) GG in sterile Milli-Q water (≥ 18 MΩ) were prepared as follows. GG powder was mixed with hot (~80°C) stirring sterile Milli-Q water under aseptic conditions. The solution was stirred at ~ 80°C for 1-2 hr until completely clear. Stock solutions were stored at 4°C for up to ~ 2 months and used under aseptic conditions.

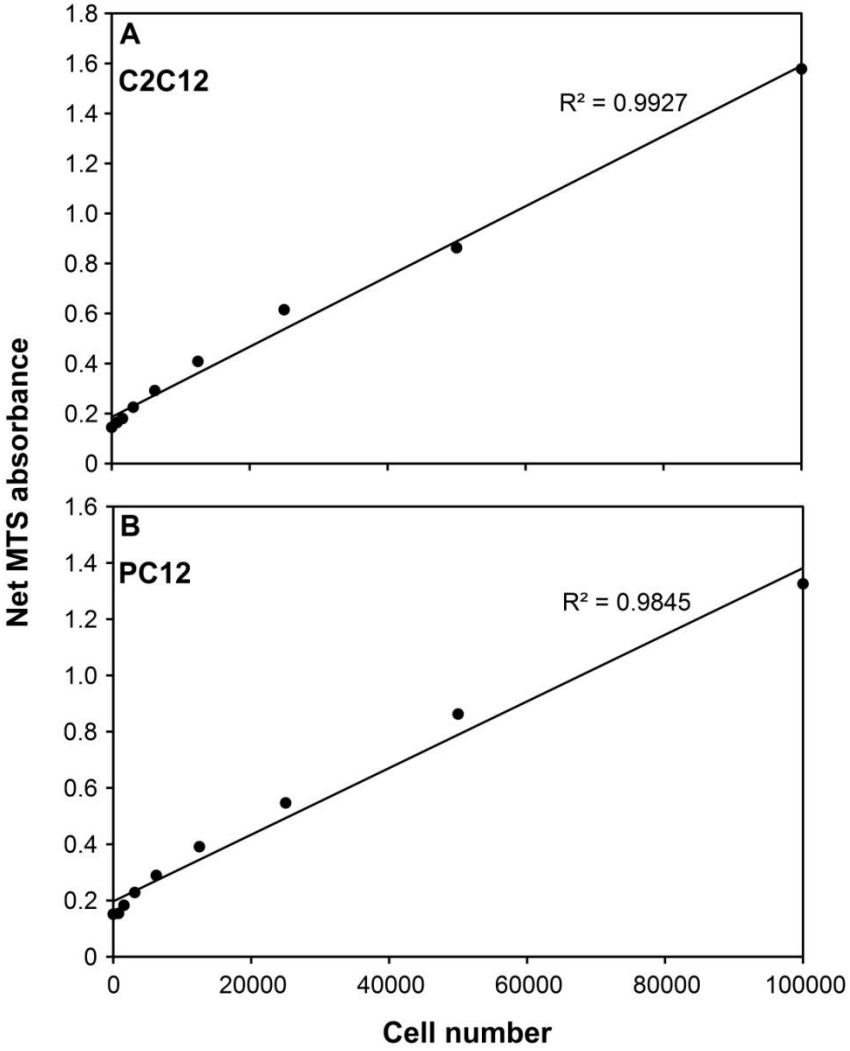

Figure 2.5: Standard curves for net absorbance (490 nm - 650 nm) as a function of C2C12 (A) and PC12 (B) cell concentration for the CellTiter 96® AQ_{ueous} One Solution proliferation assay. Results are for 30 µL reagent addition and an incubation time of 90 min.

2.2.2 Bio-ink preparation

This section outlines methods employed to form bio-ink solutions. In all cases where the bio-ink was subsequently used for experiments involving live cells, sterility was maintained through use under aseptic conditions.

2.2.2.1 Gellan gum microgel suspensions

In order to form microgel suspensions (fluid gels) of GG in DMEM, the precursor solutions needed to be combined while hot (i.e. above the GG gelation temperature) and then cooled with simultaneous application of a constant high shear rate to the solution. Stock 1% (w/v) GG solution, a 2x concentrated solution of DMEM, and

Milli-Q water were equilibrated in a hot water bath (~ 60°C) and combined in either 15 mL or 50 mL falcon tubes (Greiner) to yield a solution containing the desired GG concentration in 1x DMEM. Shear was applied immediately following combination by constant mixing using a laboratory vortex mixer (Jencons Julabo Miximatic) on the highest rotation speed, while the solutions were allowed to cool to RT over ~ 10 min.

Other methods investigated for the application of shear to cooling solutions were magnetic stirring and the use of an overhead homogeniser. Experiments where GG microgel suspensions were formed in situ in a rheometer are outlined later in this chapter (§2.2.6.2).

2.2.2.2 Surfactant addition

Four surfactants were investigated as additives in the bio-ink formulation: Triton X-100 (SigmaUltra), Tween 20 (Sigma), Poloxamer 188 (P188) which is marketed under the trade-name Lutrol® F68 (Sigma), and Novec® FC-4430 which was kindly donated by 3M. P188 was supplied as solid flakes, and so a stock solution was prepared by dissolution at 10% (w/v) in sterile Milli-Q water. All other surfactants were supplied as viscous liquids. Surfactant solutions were added to the bio-ink at RT following GG microgel formation and immediately mixed by vortex. Where two surfactants were included in the bio-ink, they were added sequentially with thorough mixing in between additions. All final surfactant concentrations are quoted as % (v/v).

2.2.3 Structure visualisation

We required a means to visualise the structure of the GG microgel particles in the bio-ink to ensure that their size was appropriate for passage through print nozzles and to assess any impact of surfactant addition on the microgel network structure. Two separate methods, fluorescent staining with the cell nuclear stain DAPI and negative staining with a black pigment ink, were utilised to this end. Attempts to stain cells encapsulated in GG hydrogels (§2.5) with DAPI produced high background staining that appeared to result from non-specific binding between DAPI and GG. The nature of the interaction between GG and DAPI is not clear, but is likely due to ionic binding. Fortuitously, this proved to present a useful route to stain GG microgel

particles. DAPI stock solution (1 mg/mL) was diluted 1:100 in Milli-Q water, and then added at 1:10 to the bio-ink and mixed thoroughly. A 20 µL aliquot was then placed on a glass slide and cover-slipped prior to imaging by fluorescence microscopy. To verify that these images provided an accurate reflection of the bio-ink structure and that the structure was not modified by the addition of DAPI, a second method was employed. A black pigmented calligraphy ink (Derivan Ink, http://www.derivan.com.au) was added at 1:5 to the bio-ink, and a 20 µL aliquot cover-slipped and imaged by bright-field microscopy. The black pigment particles diffuse through the bio-ink solution but are excluded from GG microgel particles, which consequently appeared light against the dark background.

2.2.4 Surface tension

Measurements of surface tension (specifically, the liquid-air interfacial surface tension) were made using a Dataphysics OCA goniometer, with SCA 20 software, by the pendant drop method *(305)*. Droplets were dispensed from a standard 1 mL syringe fitted with a 15-gauge (~1.8 mm outer diameter) needle to allow the formation of large hanging drops. The camera was rotated 90° in order to capture as large a drop as possible, and magnification was adjusted so that the hanging drop filled ~ 75% of the image width. SCA 20 software facilitated automated analysis of captured images of drop shape using the Young-Laplace equation *(306)* to return a value for the surface tension (Figure 2.6). The precise outer diameter of each needle used was measured using a digital micrometer and entered into the SCA 20 software to calibrate the measurements. At least four measurements were averaged for each sample. Intermittent measurements of the surface tension for a solution of Milli-Q water were conducted to ensure that it coincided with the expected value (72 mN/m), indicating that contamination of the syringe or tip did not influence the results.

2.2.5 Density

Characterisation of the bio-ink density was required to enable calculation of cell settling parameters (§3.1.4.1), and as a parameter in rheology measurements (§2.2.6). Bio-ink density was determined by weighing 100 µL aliquots of the solution, pipetted from a calibrated micropipette, on a six-figure analytical balance (Mettler Toledo AB204-S). At least five measurements were averaged, and density was calculated by dividing the measured mass (in grams) by the volume (in millilitres).

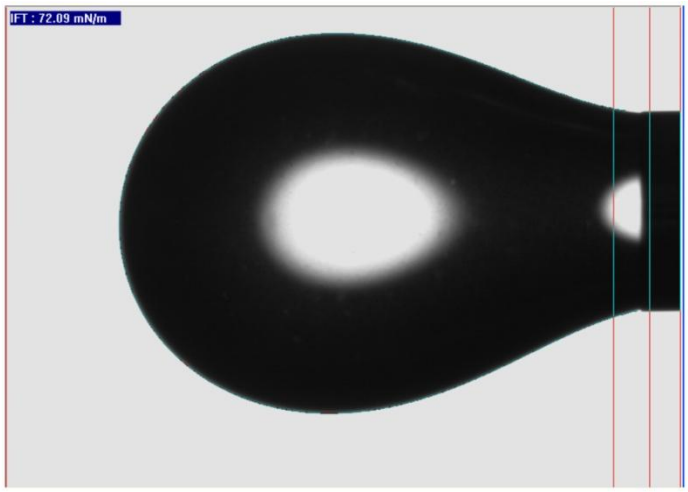

Figure 2.6: Representative image capture for pendant drop method, showing a drop of bio-ink without surfactants and drop-shape modelling using the Young-Laplace equation.

2.2.6 Rheology

2.2.6.1 Rheometer

All rheological measurements presented in this work were conducted with a TA Instruments AR-G2 controlled stress rheometer. In contrast to applied strain rheometers where the bottom plate applies a strain and the top plate measures the torsional forced produced, in controlled stress rheometers the bottom plate is fixed while the top plate simultaneously applies torque, through an induction motor, and measures the produced strain (Figure 2.7). The limit of low torque (stress) performance in controlled stress rheometers is the friction between stationary and rotating components. The AR-G2 instrument uses a magnetic bearing to limit this friction, allowing measurements at very low applied stresses. This renders the rheometer suitable for analysis of weak structures such as the GG microgel network in the bio-ink.

Rheology was used to characterise both the formation of GG microgel particles in situ, and the subsequent rheological properties of the formed microgel network, as described in the following sections. Data analysis and constitutive modelling were facilitated by Rheology Advantage software (TA Instruments).

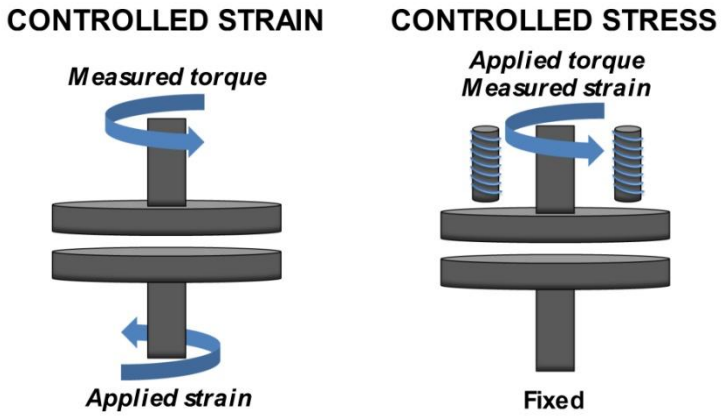

Figure 2.7: Schematic diagrams representing the operational principles of the two main types of rotational rheometers, controlled strain (left) and controlled stress (right).

2.2.6.2 In situ formation and measurement

To initially investigate the formation of GG microgel particles in DMEM, they were formed in situ in the rheometer in a similar approach to that employed by Sworn and co-workers to study GG microgels in NaCl and $CaCl_2$ solutions *(296)*. GG, 2x DMEM and Milli-Q water were combined at ~ 60 °C, as described previously (§2.2.2.1), and the hot solution was loaded onto the heated Peltier plate of the rheometer. The plate was initially held at 80 °C to ensure that the solution did not cool below the GG gelation temperature prematurely, and a solvent trap was utilised to minimise sample dehydration. Temperature ramps were conducted, with a constant shear rate of 500 s^{-1} applied to the solution using a 60 mm cone geometry (2° cone angle) while cooling to 25 °C at 1 °C/min using Peltier control. Calibration of the measurement gap over this temperature range had previously been conducted to account for thermal expansion/contraction. Measurement of viscosity during temperature ramps was used to determine the temperature at which microgel formation occurred. The shear rate was then held at 500 s^{-1} for a further 4 min, before flow behaviour was investigated using a stepped ramp of shear rate from 1-1000 s^{-1} (logarithmic ramp, 10 pts/decade). Each shear rate was held for 10 s and data was averaged over the last 5 s.

In situ microgel formation with a cup and vane geometry was also investigated as a means to fabricate microgel suspensions on a larger scale. After combining hot precursor solutions as described previously, samples were loaded into the heated cup (60 °C) and a constant shear rate of 750 s^{-1} was applied through the vane rotor while cooling to 25 °C at a rate of 2 °C/min.

2.2.6.3 Method validation

For thorough characterisation of the bio-ink rheology, we used a sand-blasted 40 mm parallel plate geometry. Although parallel plate geometries produce a less consistent shear field than cone and plate geometries, the presence of the GG microgel particles could cause jamming in the narrow (54 µm) gap between the cone apex and plate. The roughened sand-blasted surface helps to prevent slip between the plate and the sample. We were interested in characterising the rheological behaviour at both very high and very low shear rates. The viscosity at high shear rates is pertinent to printability, while the viscosity and yield behaviour at low shear rates defines the cell suspending ability of the bio-ink. To develop and validate the methods used to test these properties, we used polydimethylsiloxane (PDMS) viscosity standards (Scientific Polymer Products). These low molecular weight silicone fluids exhibit a Newtonian response and can be tailored to possess a wide range of viscosities. The two standards we employed had nominal viscosities of 1 and 10 cSt, which were converted to standard units of mPa.s using the fluid density (Table 2.2).

The measurement of high shear rate viscosity was investigated by performing continuous or stepped ramps of shear rate from 0.1-1000 s^{-1} with a plate gap of 0.5 or 1.0 mm at 25 °C with both standards. We were unable to measure at shear rates higher than 1000 s^{-1} as the sample would not remain between plates at very high shear. Continuous ramps were linear over 3 min with a sampling rate of 1 s^{-1}, while stepped ramps were logarithmic with 5-10 pts/decade and each shear rate was held for 10 s with data averaged over the last 5 s. Data for the high shear region of interest (100-1000 s^{-1}) is shown in Figure 2.8.

Table 2.2: Density and viscosity of silicone standards

Standard	Density (g/mL)	Viscosity (mPa.s)
1 cSt	0.82	0.82
10 cSt	0.93	9.3

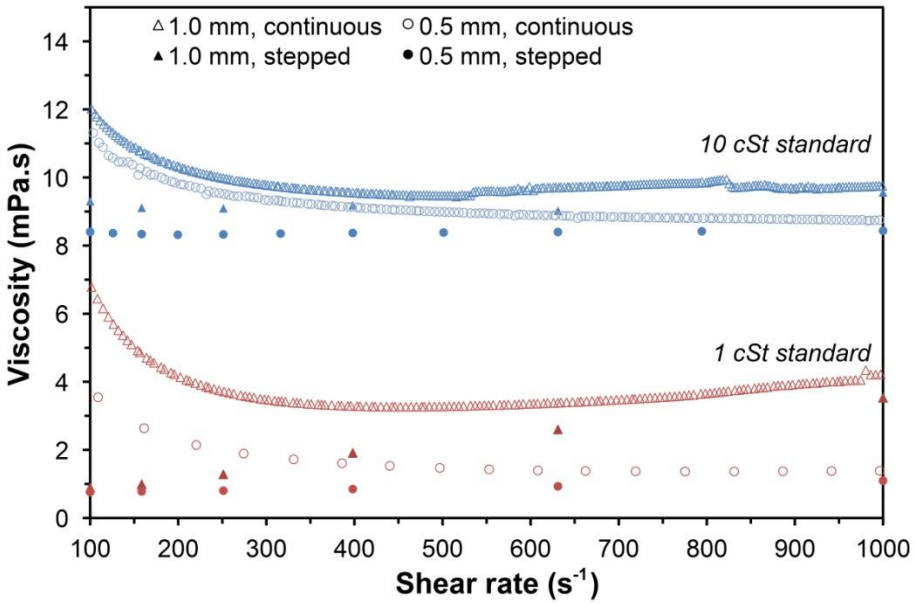

Figure 2.8: Viscosity at high shear rates for 1 cSt (red) and 10 cSt (blue) silicone standards measured using a 40 mm sand-blasted parallel plate geometry with a gap of 1.0 mm (triangles) or 0.5 mm (circles) by a continuous (empty symbols) or stepped (filled symbols) ramp of shear rate.

With a gap of 1 mm, artificial dilatency (increasing viscosity at high shear rate) was observed. This was likely a result of Taylor instabilities *(307)*, and was more pronounced with the lower viscosity standard. A gap of 0.5 mm gave more accurate high-shear data. Continuous ramps of shear rate introduced artificial pseudo-plasticity (shear-thinning), which was not introduced when performing stepped ramps. Therefore, stepped ramps with a gap of 0.5 mm gave good data for both standards in the shear rate range from 100-1000 s^{-1}, and hence this method was used for characterisation of the high shear behaviour of the bio-ink.

The yield behaviour and subsequent flow at very low shear rates was analysed by continuous ramps of shear stress from rest. The fine stress control provided by the AR-G2 instrument allowed accurate measurement of yield stress by increasing shear stress until shear strain was first recorded. Shear stress was increased from 0-2 Pa by a logarithmic ramp over 2 min, with data acquired at 50 pts/decade, to ensure that any yield point was captured. The measurements were conducted on the PDMS standards to ensure that they did not exhibit a yield stress via this method (Figure 2.9). Both standards flowed immediately on supplication of yield stress, as expected, and showed good agreement with a Newtonian model. The modelled viscosity for the 1 cSt standard was artificially high, as we had previously observed with continuous ramps of shear rate, which reinforced the need to use stepped ramps of shear rate to accurately characterise solution viscosities in the high-shear region.

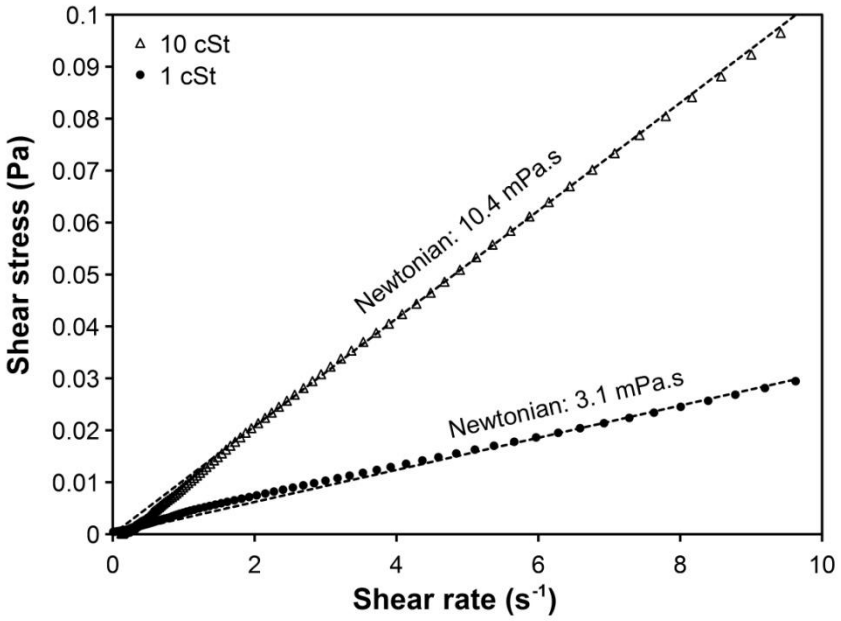

Figure 2.9: Shear stress as a function of shear rate for 1 cSt (circles) and 10 cSt (triangles) silicone standards measured using a 40 mm parallel plate geometry with a gap of 0.5 mm using a continuous ramp of shear stress. Dotted lines indicate Newtonian model with viscosity as indicated.

2.2.6.4 Bio-ink rheology

Rheological measurements were performed on bio-inks that had been prepared as described in §2.2.2. All measurements were conducted using a 40 mm sand-blasted parallel plate geometry with a measurement gap of 0.5 mm at 25 °C. The volume of sample required for each measurement was ~ 650 µL, which filled the measurement gap without bulging or depression at the perimeter. Shear history was kept consistent by applying a constant pre-shear of 500 s^{-1} for 30 s, followed by 1 min equilibration at rest, prior to each test. Both continuous ramps of shear stress and stepped ramps of shear rate were conducted as described in the previous section. At least three separate sets of tests were performed for each sample.

To assess the development of yield stress in the bio-ink over time, a single sample was subjected to a series of yield stress measurements with varying equilibration times. A constant pre-shear of 500 s^{-1} for 30 s was applied and samples were allowed to equilibrate at rest for time periods ranging from 1 min to 2 hr before measurement of yield stress by continuous stress ramps as described previously. After equilibration for 2 hr and yield stress measurement, a further test after pre-shear and 1 min equilibration was conducted and compared to initial results to ensure that shear

history did not adversely affect results. This yield stress development procedure was repeated for several samples, with results average by normalising the yield stresses to the value obtained after 1 min equilibration.

2.2.7 Cell settling

Cell settling behaviour in bio-ink formulations and DMEM was assessed by pipetting 100 µL of a C2C12 cell suspension into a 96-well plate and monitoring the base of the well over time. For low cell concentrations ($\leq 1x10^6$ cells/mL), the rate of cell settling could be quantified by imaging the well base over time and counting the number of cells using Image J software (§2.1.3). The percentage of settling at each time point was calculated by comparing the number of settled cells (determined by dividing the average number of cells counted in at least 3 microscope images by the fraction of the well area captured in that image) to the total number of cells in the 100 µL aliquot. For higher cell concentrations ($\geq 2x10^6$ cells/mL), the number of cells on the well base could not be counted accurately due to overcrowding. Consequently, microscope images of the well base over time were captured to provide a qualitative assessment of cell settling behaviour.

2.2.8 Cell response to bio-inks

The response of both C2C12 and PC12 cells to exposure to the bio-ink with and without surfactants, and to the various surfactants in DMEM, was primarily investigated by measuring cell viability following exposure. Cells were suspended in 100 µL to 1 mL solutions at concentrations relevant to cell printing applications (2-$6x10^6$ cells/mL) in 1.5 mL Eppendorf tubes at RT. At various time points, an aliquot of ~ 5000 cells (e.g. 2.5 µL for a cell concentration of $2x10^6$ cells/mL) was removed and added to 100 µL of pre-warmed CPM in 96-well plates and incubated under culture conditions. For solutions where cell settling occurred, cells were re-suspended intermittently throughout the exposure period, and thoroughly mixed prior to the removal of an aliquot. Cell viability was assessed after either 2 hr or 24 hr in culture as described previously (§2.1.5). The proliferation and differentiation of cells exposed to the bio-ink was investigated during inkjet printing experiments described later in this chapter (§2.4.5).

2.3 Microvalve Printing

2.3.1 Printer design

Microvalve printing in this thesis was carried out using a commercially available Deerac Equator™ GX1 liquid handling system from Labcyte (Figure 2.10A). This system is designed to quickly and accurately transfer small reagent volumes using a 3-axis robotic arm which controls the movement of a dispensing head over a deposition platform. The dispensing head houses a tip (Figure 2.10B) connected to a pressure (deposition) or vacuum (aspiration) source. The tip itself contains a magnetic boss that rests against a 160 µm internal diameter capillary, and movement of the boss is controlled by sensing and actuating coils to open and seal the capillary thereby acting as a microvalve. The droplet deposition mechanism is based on Magnetic Feedback-Controlled (MFC) technology (Figure 2.10C), where the applied pressure and opening time of the microvalve is controlled to adjust the dispensed droplet volume. Control of the system was facilitated through Spot Station™ software (Labcyte, v. 4.4.0). Useful specifications for the system are outlined in Table 2.3. This technology is analogous to other forms of pneumatic microvalve printing discussed in the introduction to this thesis (§1.3.4), however because the system is not designed for use in printing tasks, there are some limitations to the control over deposition that will be highlighted throughout this chapter. Nonetheless, this system provided a simple tool with which to examine the use of the bio-ink in the microvalve printing of living cells.

Table 2.3: Specifications for the Deerac Equator™ GX1 liquid handling system

Equator™ specifications	
Needle diameter	160 µm
Dispense volume	10 nL* - 50 µL (± 5%)
X/Y positioning resolution	5 - 10 µm
Max. aspirate volume	1 mL
Min. aspirate volume	3 µL
Tip lifetime	~ 10^6 cycles
Deposition speed	> 100 s^{-1} (100 nL droplets into 1536-well plate)

*nominal minimum volume of the system is 50 nL. This was circumvented using a software patch provided by the manufacturer at request.

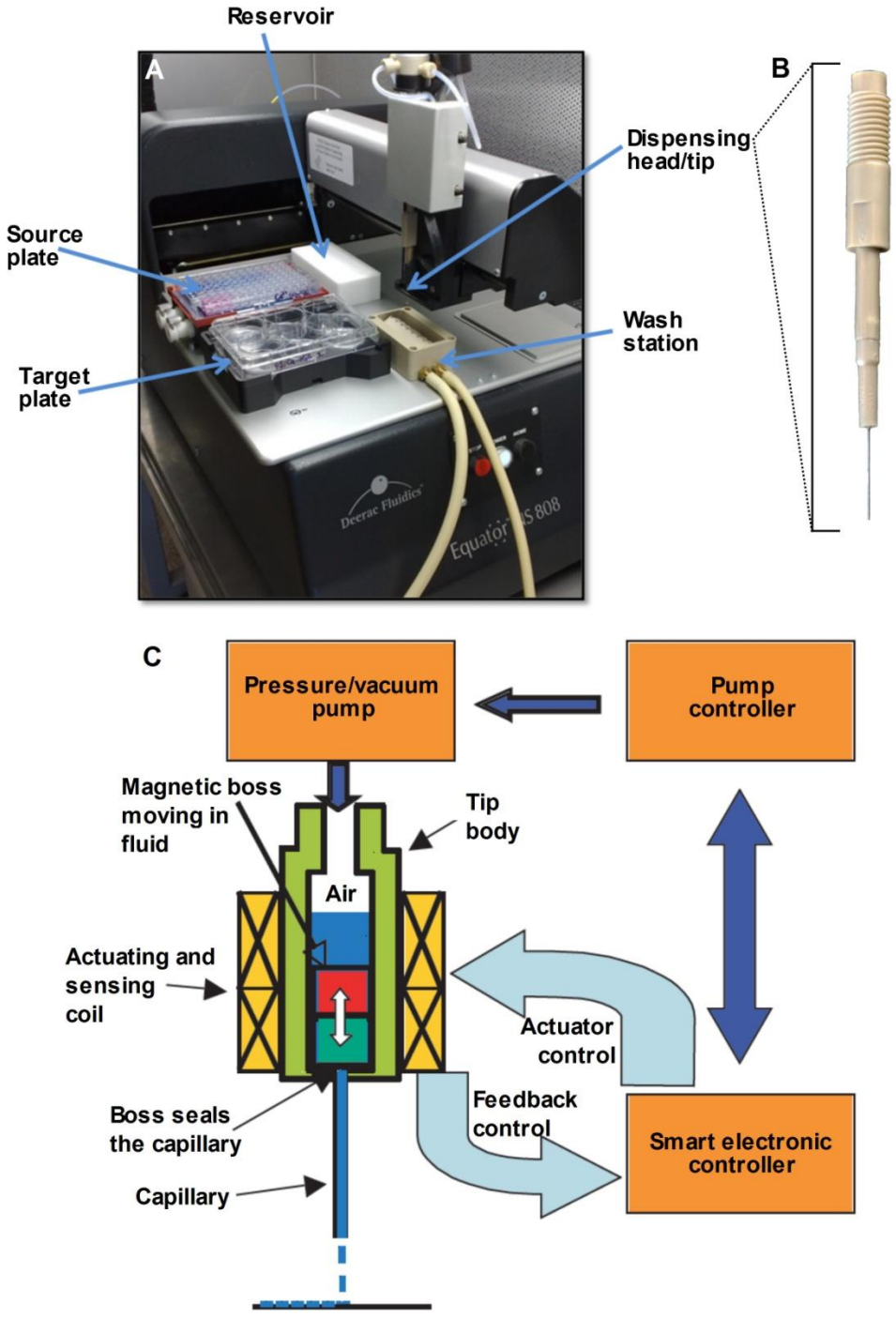

Figure 2.10: The Deerac Equator™ deposition system. **(A)** Photograph of the system, indicating location of the source plate and reservoir from which solutions are aspirated, the target plate deposition area, the wash station and dispensing head. **(B)** The dispensing head and tip. **(C)** Schematic representation of the Magnetic Feedback-Controlled (MFC) deposition technology.

2.3.2 General printing approaches

In an effort to maintain sterility during printing experiments, the Deerac system was placed in a bio-safety cabinet (BSC), sprayed liberally with 70% (v/v) ethanol and irradiated with UV light for 20 min prior to and at the completion of each experiment. Internal tubing and the printing tip were not sterilised regularly, but rather flushed with sterile water. The printer incorporated two separate washing mechanisms: a FastWash™ system, where wash reagent from a pressurised container is purged through the tubing and tip; and an active wash system, where a peristaltic pump delivers wash reagent from an external reservoir to the wash station (Figure 2.10A). Both wash reagent reservoirs were sterilised using 70% (v/v) ethanol, dried and filled with sterile water. Both wash procedures were implemented regularly through printing experiments. In all cell printing experiments, pen/strep was used to control potential contamination.

Printing solutions were aspirated either from the wells of a 96-well plate in the 'source plate' area or from a Teflon reservoir (Figure 2.10A). Deposition substrates, as described in the following sections, were placed in the 'target plate' area. The accompanying Spot Station™ software requires selection of a 'liquid class', which is used to calculate aspirate/dispense pressures and valve opening times. Unless stated otherwise, all printing experiments were conducted using the preset liquid class for water.

2.3.3 Deposition modes

As previously outlined, the Equator™ system is designed for liquid transfer between well plates, and as such the control over deposition and the design of printed patterns is limited. This section outlines three different deposition modes that provided the ability to facilitate the deposition of droplets in desired patterns. All three of these approaches employed Plate Designer (Labcyte, v. 3.1.0.0) software that accompanied the Equator™ system (Figure 2.11). This software was either used to define the position of well regions, which were implemented in 'spotting' deposition (§2.3.3.1), or to define a pixel map which was used in on-the fly (OTF) and platemap dispensing (§2.3.3.2 and §2.3.3.3, respectively). Pixel maps were custom 'well plates' where each 'well' was considered a pixel of an image; the size and distance between 'wells' therefore defined the resolution or droplet spacing of the printed image.

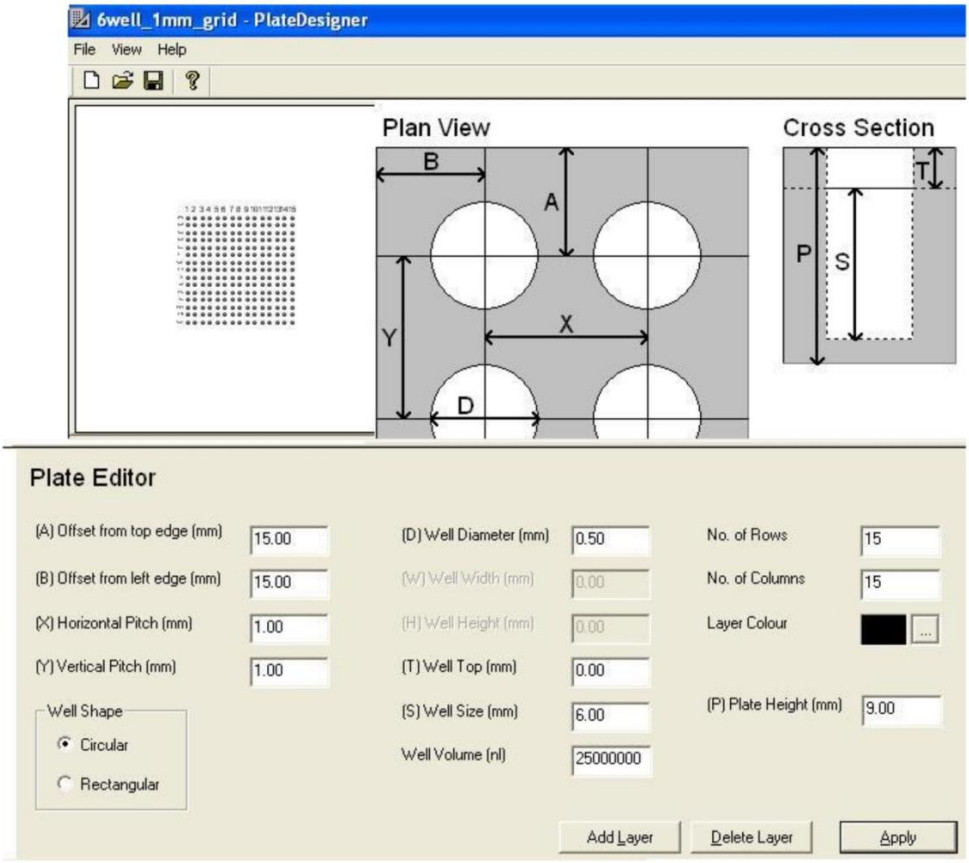

Figure 2.11: Screenshot of the Plate Designer software, which allows the user to define the dimensions of a custom well plate. This screen shot shows the generation of a pixel map, a 15x15 grid with a pixel (or 'well') spacing of 1 mm.

2.3.3.1 Spotting

In spotting mode deposition, the user is able to create a grid *within* a single well region, and manually select the grid points at which droplets should be deposited. This principle is illustrated in Figure 2.12, and allows the creation of simple patterns with defined droplet spacing. Definition of complex patterns via this approach, however, would be limited and tedious. This deposition mode was implemented in DRIP fabrication (§2.3.6) and in analysis of cell output and cell responses (§2.3.4 and §2.3.5, respectively)

2.3.3.2 On-the-fly (OTF) dispensing

In OTF dispensing, the Equator™ tip moves quickly along a row of wells and dispenses a defined volume into each well. OTF dispensing was combined with the creation of custom pixel maps, so that lines of closely-spaced droplets could be deposited at high speed. This method was implemented to fabricate continuous lines in DRIP fabrication (§2.3.6).

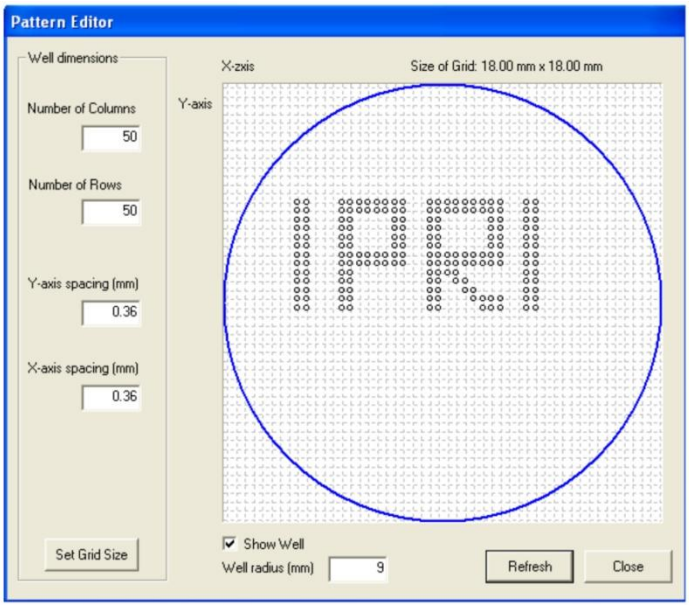

Figure 2.12: Screen shot of the spotting dispense function in Spot Station™ software. A 50x50 grid has been created, with an x/y spacing of 360 µm, to cover the area of a circular well region with a radius of 9 mm. Grid points have been selected manually to command deposition of droplets in a pattern spelling 'IPRI'.

2.3.3.3 Platemap dispensing

Platemap dispensing allows the volume to be deposited into each well of a plate to be defined using a spreadsheet .csv file. We envisaged that, in combination with the design of custom pixel maps, this method could be implemented to deposit droplets in patterns by setting the deposition volume for each pixel, or 'well', in the pixel map to either zero or the desired droplet volume (e.g. 50 nL) to create an image. Manually entering each volume into a spreadsheet, however, would be impractical. We therefore sought a means to convert a standard bitmap image into a spreadsheet .csv file where each pixel of the image was converted to a meaningful deposition volume that could facilitate recreation of the image by platemap dispensing.

Design of a software tool to enable this conversion was carried out by Dr. Jeffrey Keisler and A/Prof. Roger Blake from the University of Massachusetts (Boston). Their group had already developed software for spreadsheet-based Geographical Information System (GIS) models, and at our request this tool was slightly modified for our purposes. The principle of the image processing is demonstrated in Figure 2.13. A standard bitmap image is loaded into the custom software spreadsheet which extracts the red colour value (0-256) for each pixel and displays that value in spreadsheet cells. These values are converted to deposition volumes using standard

Excel filter functions, to create a .csv file which is imported into a Deerac™ platemap dispense task. It should be noted that the distortion of the spiral image seen in Figure 2.13B and C is an artefact of the cell dimension settings in the Excel spreadsheet. This approach was used to print various patterns of cell suspensions as detailed in Chapter 4 (§4.4).

2.3.4 Cell output

The cell output was investigated by depositing droplets onto glass slides using spotting mode deposition (§2.3.3.1) of separated droplets of varying volume. Droplets were imaged by bright-field microscopy, and both droplet diameters and the number of cells per droplet were determined using Image J or Image Pro software (§2.1.3).

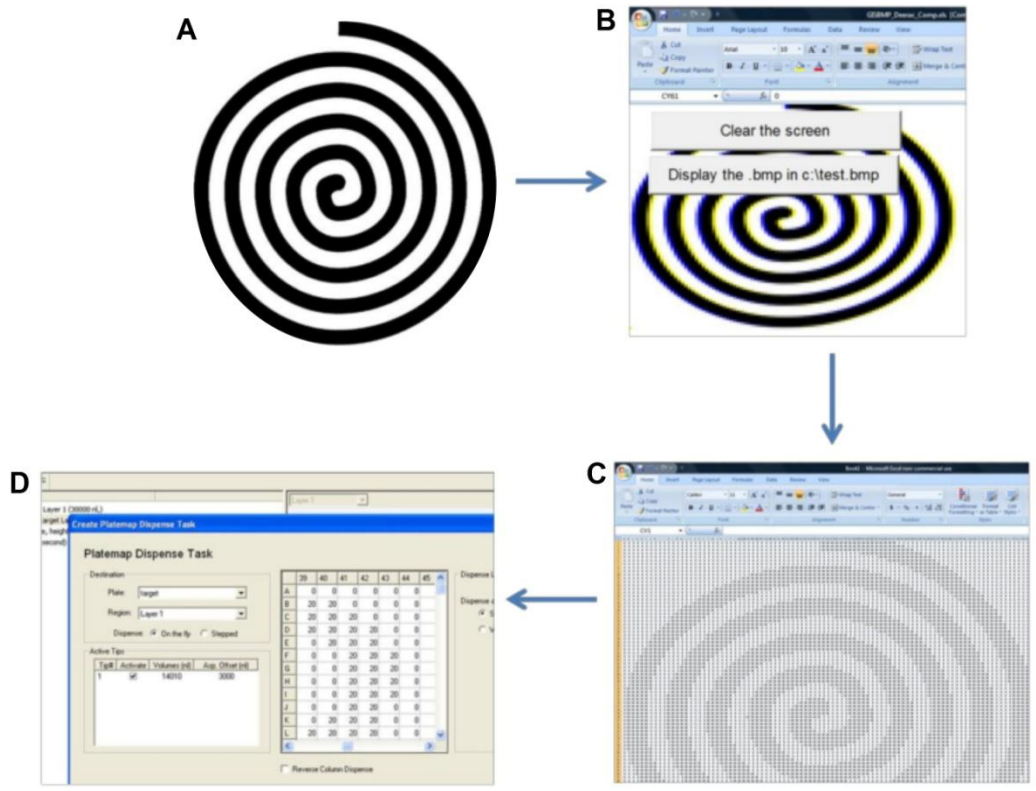

Figure 2.13: Sequence for processing a standard bitmap image to render it printable using platemap dispensing. **(A)** 100x100 pixel bitmap image of a spiral. **(B)** Custom software converts the bitmap image to a 100x100 cell Excel spreadsheet by extracting the red colour value (0-256) for each pixel. **(C)** Excel filtering is used to convert the cells containing a red colour value below a certain threshold (black pixels) to a user-defined value representing a deposition volume (e.g. 20). **(D)** Spreadsheet .csv file is imported into a platemap dispense task in the Spot Station™ software.

For analysis of the cell/drop distribution, suspensions of C2C12 cells in bio-ink at a concentration of either $2x10^5$ or $1x10^5$ cells/mL were aspirated and an array of 50 nL droplets were deposited on glass slides. The number of cells in at least 250 droplets for each cell concentration were counted as described previously (§2.1.3) to give a large sample size for statistical analysis of the distribution.

Cell output over time was investigated by aspirating 100 µL of a C2C12 cell suspension at $5x10^5$ cells/mL in either the bio-ink or DMEM alone, and depositing arrays of 50 nL droplets at several time points over the course of 1 hr. At each time point (0, 5, 10, 15, 20, 30, 60 min), an array of 120 droplets was deposited onto glass slides using spotting mode deposition. The time period between dispensing tasks was automated using a timed pause function in the Spot Station™ software.

2.3.5 Cell response

In order to characterise the phenotypic response of cells to the microvalve printing process, droplets were deposited directly into 100 µL of CPM within 96-well plates. For assessment of viability, C2C12 cells were suspended in bio-ink at either $1x10^6$, $2x10^6$ or $4x10^6$ cells/mL. Spotting mode dispensing, with an arbitrary pattern, was used to deposit into each well the number of 50 nL drops required to reach ~ 5000 cells/well for the three cell concentrations; this was 100, 50, or 25 droplets, respectively. The total deposited volume (5, 2.5 or 1 µL) corresponding to each condition was also manually pipetted into separate wells to act as controls. Three wells were seeded per condition, and cell viability was assessed after 2 hr in culture as previously described (§1.1.5).

For analysis of cell proliferation and differentiation, the above process was repeated using C2C12 cells in the bio-ink at $2x10^6$ cells/mL. For differentiation experiments, the only adjustment was that ~ $1x10^4$ cells were required in each well, and so the number of deposited 50 nL droplets was doubled (to 100 droplets), along with the pipetted control volume (5 µL). Proliferation was measured over 48 hr in culture as described previously (§2.1.6). Differentiation was induced by a change to CDM after 48 hr in culture, and cells were fixed for immunostaining (§2.1.4.3) after a further 5 days in culture.

2.3.6 Application: DRIP fabrication

Bioplotting is one approach to extrusion-based biofabrication where the dispensing tip is immersed within a liquid medium during deposition *(109)*. We have modified the general bioplotting technique to develop a new biofabrication approach that will here-in be referred to as DRIP fabrication; this acronym stands for Drop-on-demand Reactive In-solution Plotting. The basic premise of this approach is represented in Figure 2.14. The tip of a microvalve deposition tool (eg. Deerac Equator GX1) is immersed into a biopolymer solution (eg. gellan gum) where it deposits an ink containing a cross-linking species for the biopolymer (eg. Ca^{2+} ions).

In initial experiments with the DRIP fabrication approach, GG gum solutions (0.1 - 1.5% (w/v)) in Milli-Q water were added to standard 6-well plates (~ 10 mL/well) and place on the target plate region. Solutions of $CaCl_2$ (5 - 500 mM) were placed in 96-well plates at the source plate region. $CaCl_2$ solutions were aspirated and droplets were dispensed into the GG solutions using spotting mode deposition (§2.3.3.1). In order to immerse the tip within the GG solution, the height of the deposition plate was adjusted iteratively in the software until the tip position was close to the middle of the solution height in the well. Gelled regions were difficult to visualise due to the lack of contrast with the surrounding solution, but imaging was achieved using a macroscope (Leica) with a variable angle light source below the samples that could be adjusted to highlight the edges of the gelled regions. This approach was employed to study the optimal concentrations for DRIP building block fabrication, and the dimensions of the deposited features were measured using Image J software (§2.1.3).

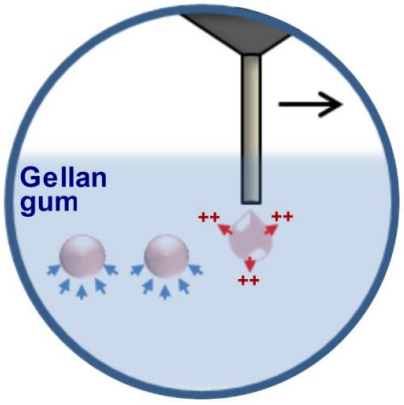

Figure 2.14: Schematic representation of the DRIP fabrication approach. Droplets of media containing cations are deposited within a gellan gum solution. Cation diffusion from dispensed droplets (red arrows) induces gelation of the surrounding solution, forming hydrogel regions that are stabilised by buoyant forces (blue arrows).

To investigate the joining of individual DRIP building blocks to create larger hydrogel structures, 20 mM $CaCl_2$ solution containing 100 µM methylene blue was deposited into 0.5% (w/v) GG solutions in 6-well plates via spotting mode deposition as before. The methylene blue was added to aid visualisation of the deposition. A spotting mode grid with a spacing of 0.72 mm was defined within each well, and patterns were created manually. The volume deposited for each spot in these patterns was varied from 100 - 500 nL until individual DRIP building blocks joined to form a continuous hydrogel structure. Excess, un-crosslinked GG solution was removed from wells after deposition by aspiration using a pipette, and structures were imaged by brightfield microscopy.

A different approach to DRIP fabrication was to utilise OTF-mode dispensing (§2.3.3.2) with the tip in close proximity to the substrate Figure 2.15. In these expriments, a thin layer of GG solution (~ 300 µL) was pipetted into 4-well chamber slides (Becton Dickinson) that had been modified by grinding (Dremel rotary tool) the well walls to reduce their height; this ensured that the dispensing head would not collide with the wells. Again, the custom well height specified in Plate Designer software was adjusted iteratively until the tip was just above the well base (~ 0.5 mm). A range of GG and $CaCl_2$ concentrations as outlined previously were investigated in this approach. Droplet volume (20 - 50 nL) and spacing (100 - 400 µm) were varied in attempts to form continuous hydrogel lines. Some control over the speed of tip movement during deposition was provided through Spot Station™ software, by defining a percentage of the maximum OTF speed and acceleration (‘ramp’). Both these parameters were varied (OTF speed 50-85%, OTF ramp 45-75%) to achieve deposition without clogging at the tip.

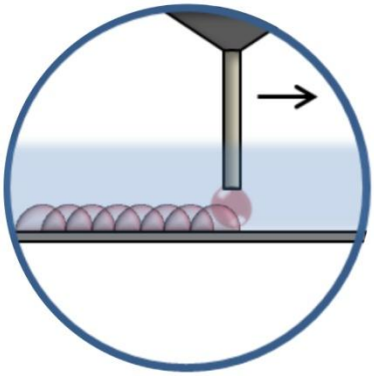

Figure 2.15: Schematic representation illustrating DRIP fabrication in OTF-mode deposition with the tip in close proximity to the substrate.

Cells were incorporated into the DRIP fabrication process using the OTF method. C2C12 cells were suspended in DMEM containing 20 mM $CaCl_2$ at concentrations ranging from $2x10^5$ - $5x10^6$ cells/mL, and hydrogel lines were formed as previously to encapsulate the cells. After printing, the surrounding thin GG layer could be crosslinked by pipetting excess CPM down the sides of the well walls. This stabilised the printed lines and allowed the whole construct to be transferred to separate plates for culture. Cells in DRIP fabricated constructs were imaged by both bright field and fluorescence microscopy, after calcein staining (§2.1.4.1). This technique was also replicated with cells suspended in bio-ink at $2x10^6$ cells/mL.

2.4 Inkjet printing

2.4.1 Printer design

Inkjet cell printing in this thesis was carried out with piezoelectric print heads. These heads are the industry standard for high-end printing applications, and have potential advantages over thermal print heads as discussed in the introduction to this thesis (§1.3.6). We utilised commercially available Xaar-126 piezoelectric print heads (Figure 2.16), which are characterised by large nozzle diameters and droplet volumes (Table 2.4). The relatively large number of nozzles (126 nozzles) in these print heads is also advantageous for higher throughput printing. The inlet and outlet ports (Figure 2.16) allowed simple filling and flushing of heads. The dimensions of the nozzles and nominal droplet volume for these heads are comparable to the HP26 thermal inkjet print heads used in the majority of cell printing work to date (§1.3.5).

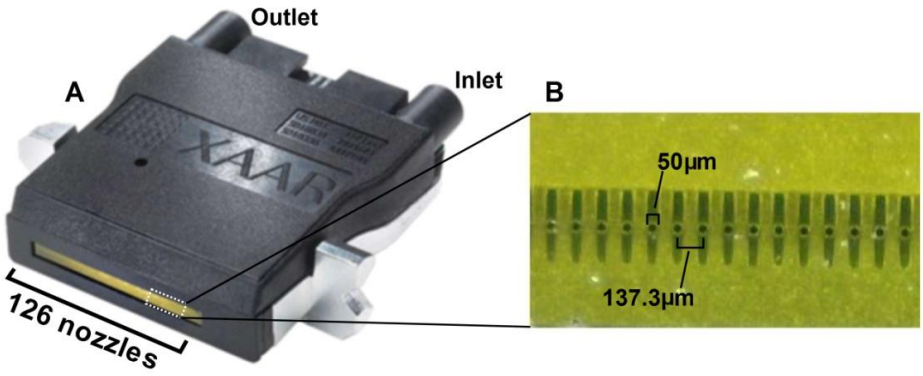

Figure 2.16: (A) Xaar-126 print head. **(B)** Magnified image of a section of the nozzle plate.

Table 2.4: Specifications of Xaar-126 print head.

Attribute	Value	Unit
Active nozzles	126	-
Nozzle diameter	50	µm
Print swathe width	17.2	mm
Nozzle pitch	137.3	µm
Drop velocity (nominal)	6	m/s
Drop volume (nominal)	80	pL
Firing frequency (typical)	5.2	kHz
Dimensions (WxDxH)	45x13x43	mm

Early experimentation was problematic, and it was identified that an in-line filter consisting of a stainless steel mesh with a nominal rating of only 2 µm in the Xaar-126 print heads was restricting the passage of cells through the printer. The internal filter was removed by cutting into the side casing (Figure 2.17A) and removing the mesh (Figure 2.17B). The resulting hole was sealed with a 3D custom-printed plug to restore the integrity of the casing (Figure 2.17A). Sealing was achieved using UV-curing adhesive. Internal filters were also removed from HP26 cartridges in previous cell printing work *(218)*.

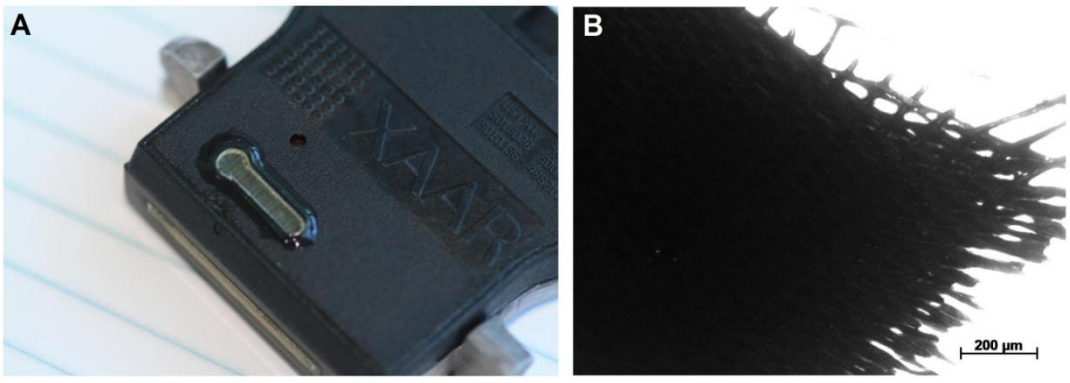

Figure 2.17: (A) Photograph of modified Xaar-126 print head, showing where the side casing was cut open to remove the internal filter and subsequently sealed with a 3D-printed plug and UV curing glue. **(B)** Microscope image of a section of the internal mesh filter removed from the Xaar-126 print head. Scale bar represents 200 µm.

The printer housing was designed as a simple system that could be utilised to test printing methods and ink formulations. The print heads remained stationary in a custom mount, positioning them above a modified Reliance RCMS17 Cool Motion stage coupled to a Reliance Cool Muscle servo motor system. This uni-directional stage moved underneath the print heads, and so the width of printed patterns was limited to the swathe width (17.2 mm) of the print heads. The distance between the substrate and print heads was maintained at 1-2 mm, and adjusted with stainless steel washers as required. Motion of the stage was controlled by Cool Works Lite software (Myostat). Communication with the print heads was facilitated through Xaar XUSB electronics and accompanying software. Stage position and movement was relayed to the print electronics through an optical strip (1 µm pattern) read by a Renishaw RGH22 read-head. An EFD Ultimus regulator (Nordson EFD) was attached to the laboratory N_2 source and controlled the pressures applied to print heads. All fluid connections were made with teflon (Tygon®) tubing and connectors. A diagram of the system is provided in Figure 2.18.

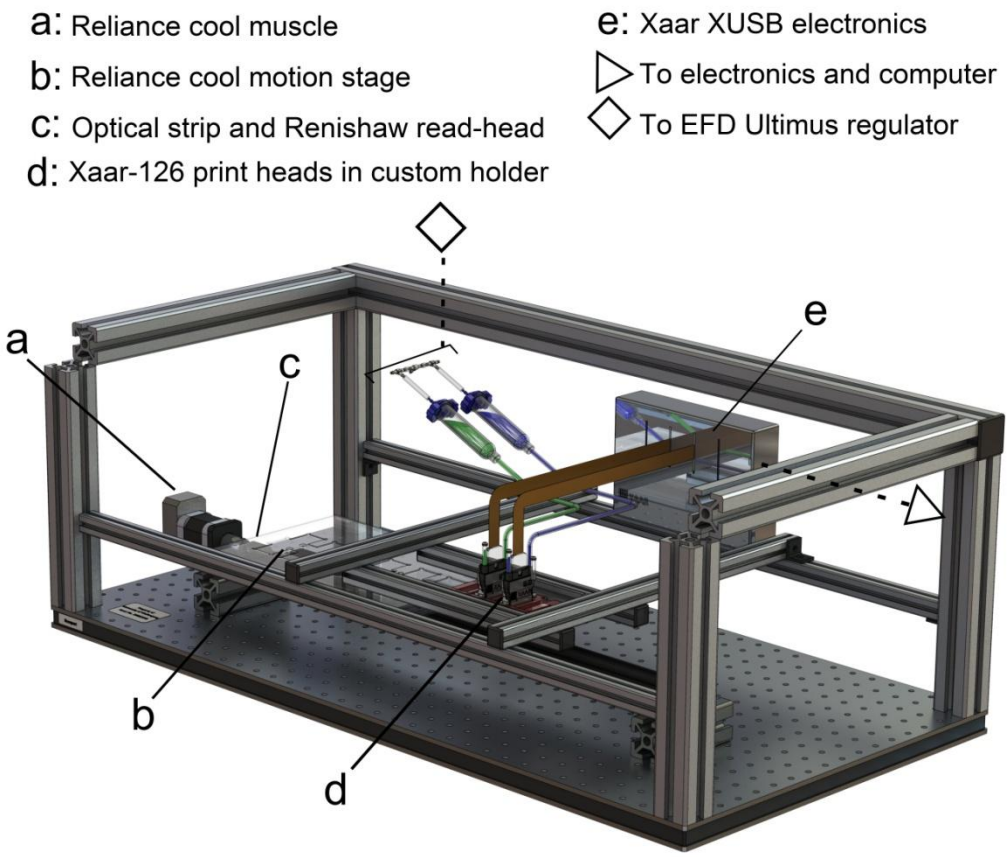

Figure 2.18: Schematic of the custom-built inkjet printing system to house Xaar-126 print heads. The system was designed to fit into a standard biological safety cabinet.

2.4.2 General printing approaches

The printer was housed in a BSC, and exposed surfaces were sterilised regularly with 70% (v/v) ethanol and UV light. The print head internals were not sterilised, in order not to risk damage to electronics. At the completion of each printing experiment, print heads were flushed exhaustively with sterile Milli-Q water via a small pump to ensure all residual bio-ink and cells were removed. Print heads were then dried using a high-pressure stream of N_2 gas, and stored in a plastic cover. All printed cells were subsequently cultured in media containing pen/strep (§2.1.1) to control any potential contamination.

Printing solutions were supplied to print heads by one of two approaches. In initial experiments, syringes (EFD) were filled with printing solution and connected to the regulator and the inlet port of print heads. A small length of tubing was connected to the outlet port of print heads and clamped, and application of a small vacuum pressure prevented fluid from passing through the print head nozzles. This is the approach illustrated in Figure 2.18 and Figure 2.19A. In final cell printing experiments with the bio-ink, both the inlet and outlet ports of the print head were connected to a single tubing line, as shown in Figure 2.19B. Cell suspensions in bio-ink were loaded into a custom reservoir (Figure 2.19C) and aspirated into the print head through the nozzle plate by manual suction applied through a syringe connected to the single tubing line. This approach allowed smaller volumes to be effectively loaded into the print head. This line was then clamped and connected to the regulator, which subsequently held the ink in the print head by application of vacuum as previously. The required vacuum pressure was determined iteratively in each experiment by small adjustments to find the minimum pressure at which no flow out of the nozzles was observed (usually 1-8 inches of H_2O, depending on ink volume).

Prior to printing, a small amount of ink solution was purged through the nozzle plate by application of a small back-pressure (1-2 kPa) through the EFD regulator. The nozzle plate was then wiped clean. This purge and clean process was repeated often throughout each printing experiment to prevent ink drying and salt crystallisation at the nozzle plate. When print heads were idle, they were set to ‘spit’ a small volume of ink from each nozzle at 10 s intervals. This also aided the prevention of drying,

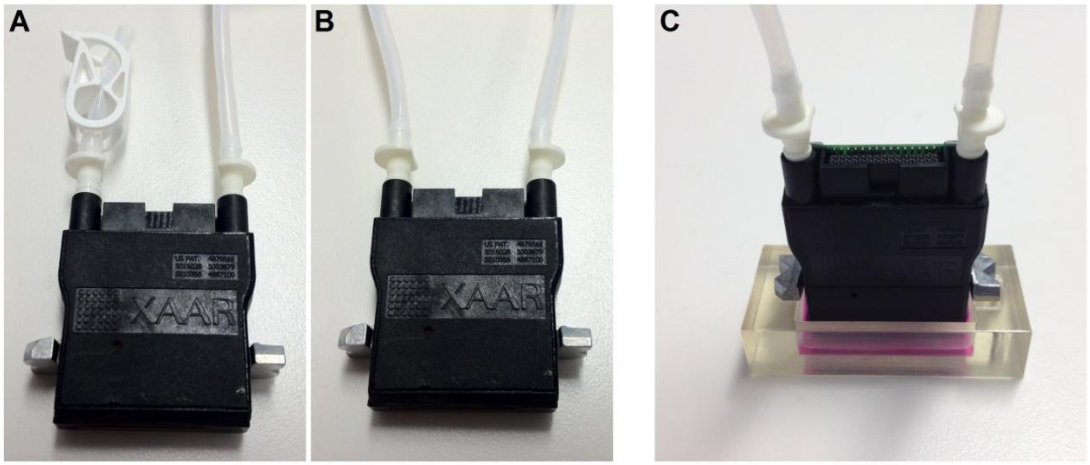

Figure 2.19: Different methods of ink supply to Xaar-126 print heads. **(A)** Single inlet (right) from syringe reservoir with clamped outlet (left). **(B)** Dual inlet, used for aspiration of ink through nozzle plate from custom reservoir as shown in (C).

and allowed a useful check mechanism; spitting patterns on glass slides were inspected regularly, as a uniform straight line of ink was indicative that every nozzle was firing correctly. During actual cell deposition, the BSC fan was usually switched off to minimise drying during printing.

The robotic stage was fitted with a stainless steel platform that was designed to house a single standard glass slide (Figure 2.20). The print area was therefore limited to 17.2 x 75 mm. The relative position (on the optical encoding strip) of each end of the glass slide region was measured for each print head mounting position, and input into the Xaar XUSB software to define the print area for each print head.

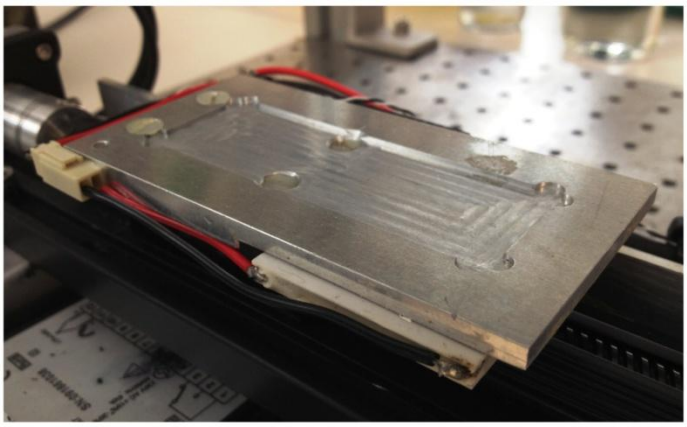

Figure 2.20: Custom stainless steel stage designed to hold a standard glass slide, mounted on the Reliance Cool Muscle.

Patterns were designed in Microsoft Paint, saved as a standard bitmap image and loaded into Xaar XUSB software. The paint canvas was set to 126 pixels wide and 1560 pixels long. The 126 pixels in the *x* direction represented the 126 nozzles of the Xaar-126 print head (Figure 2.21), while the 1560 pixels in the *y* direction represented the length of the print area; a black pixel indicated a deposited droplet. The *x* pixel spacing was controlled by the nozzle pitch (137.3 µm), while the *y* pixel spacing was set by software control to match this value (188 dpi, or 135 µm spacing). In this way, the speed of the stage (and therefore glass slide) movement under the print head did not affect the *y* spacing of deposited droplets. The stage speed was set to be relatively slow for cell printing experiments (5 mm/s). In all cases, unless stated otherwise, printing experiments were conducted using the Xaar proprietary 'standard' waveform for actuation of the piezoelectric nozzles.

2.4.3 Live cell printing

In order to print viable cells by inkjet printing, they were printed into a hydrated environment. Due to the very small droplet size, cell patterns printed onto glass slides would dry out very quickly, killing the cells. For analysis of cell responses to inkjet printing (§2.4.5), it was sufficient to print cells directly into CPM as was the case for microvalve printing (§2.3.5). However, standard culture plates would not fit

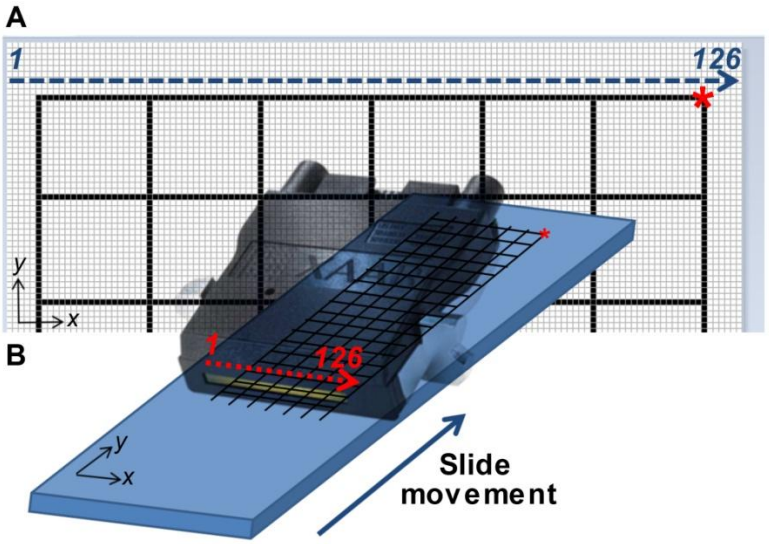

Figure 2.21: Schematic representation of pattern design for inkjet printing. Patterns were drawn using Microsoft Paint, with the canvas size set to be 126 pixels wide (A). Each pixel represented a nozzle of the Xaar-126 print heads (B). The glass slide substrate moved under the stationary print head and patterns were deposited as illustrated. The red asterisks' indicate corresponding points of the designed and printed patterns.

in the 1-2 mm gap between the substrate and print heads. We therefore fabricated customised thin polydimethylsiloxane (PDMS) wells that could be attached to glass slides providing a reservoir for media that would fit underneath the print heads. PDMS components (Sylgard® 184 silicone elastomer kit, Dow Corning) were mixed thoroughly and cast into a thin (0.5-2 mm) layer in a Petri dish to set at RT overnight. The PDMS was then cut to shape using a 3D-printed template (Figure 2.22A) to create 8 individual wells (8 x 11 mm). The PDMS mask was cleaned thoroughly with Pyroneg detergent (Sigma), rinsed, dried and plasma-bonded (Harrick PDC-002 Expanded Plasma Cleaner**,** 900 mTorr air, 29.6W for 3 min) to a clean glass slide before sterilisation with 70% (v/v) ethanol and UV light. The wells could then be filled with ~ 100 µL CPM without leakage (Figure 2.22B).

The above approach was sufficient for analysis of printed cell responses, but it did not allow retention of a specific pattern of printed cells. For viable cell patterning, cells were printed onto hydrated collagen 'bio-paper' in an approach similar to that employed previously by several workers *(137, 172, 197, 219)*. Collagen I (rat tail, 5 mg/mL, Invitrogen) was sonicated gently for 5 min on ice prior to use to reverse any gelation that had occurred during storage. It was then combined with ice-cold 5x concentrated DMEM to a final concentration of 4 mg/mL and neutralised with 0.1 M NaOH. A small volume (~ 50 µL) of the cold collagen solution was pipetted into~ 0.5 mm thick PDMS wells on glass slides and polymerised for ~ 2 hr at 37°C. In initial experiments, cells were printed directly onto these collagen hydrogels following polymerisation, and wells were subsequently filled with CPM shortly after

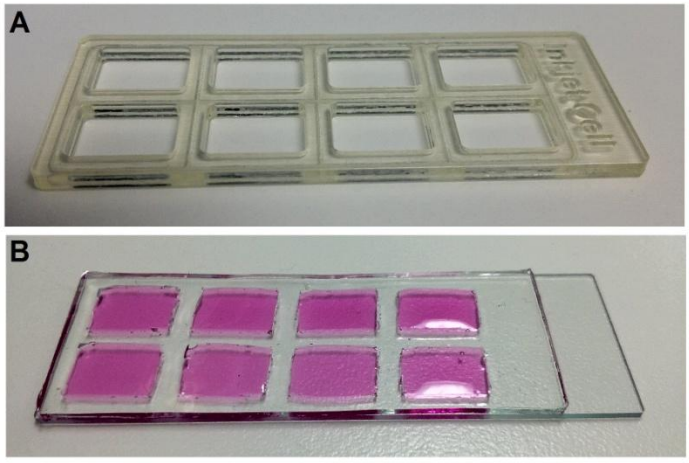

Figure 2.22: (A) 3D-printed template of well design used to cut out replicate wells from PDMS. **(B)** PDMS wells plasma-bonded to a glass slide and filled with 100 µL CPM.

printing. Slight modifications to this approach were required, however, in order to obtain a uniform pattern of well-adhered, viable, patterned cells. In final experiments, collagen solutions were prepared as previously described and ~ 100 µL was pipetted into thin (~ 0.5 mm) PDMS wells to completely fill each well, thereby forming a flat collagen hydrogel surface once polymerised (Figure 2.23A). Slightly thicker (~ 1 mm) PDMS wells were then placed on top of the existing wells to create a media reservoir, and the collagen hydrogels were soaked in CPM for ~ 1-2 hr (Figure 2.23B). Excess media and the upper wells were then removed and cells were printed onto the hydrated collagen layers (Figure 2.23C). Constructs were incubated under culture conditions for ~ 1 hr to allow time for cells to attach to the collagen, before the re-attachment of upper wells and addition of excess CPM (Figure 2.23D). Visualisation of printed cell patterns was achieved by live/dead staining as previously described (§2.1.4.1). Printing onto collagen hydrogels as described here was also employed in the deposition of multiple-cell type patterned constructs (§2.4.7).

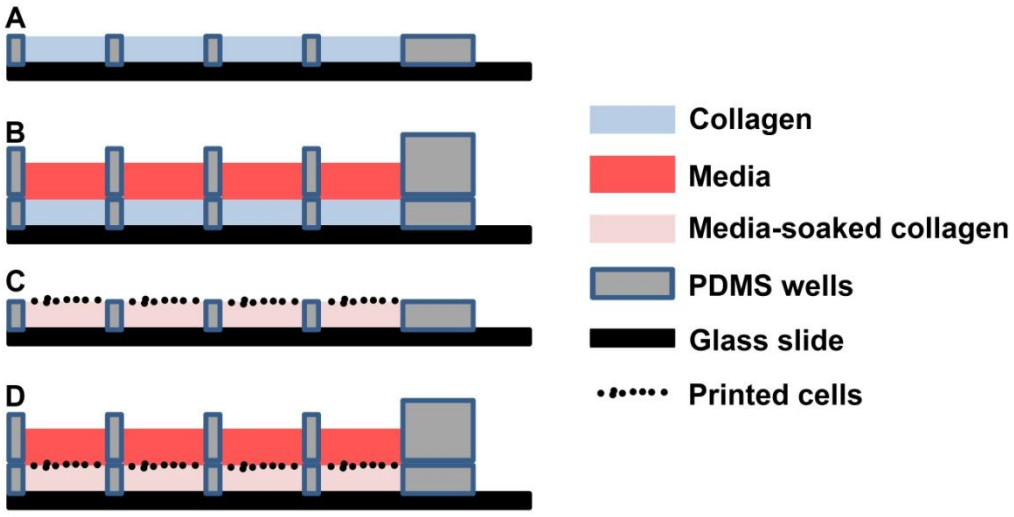

Figure 2.23: Cross-sectional schematic of flat collagen bio-paper formation in PDMS wells used in live cell patterning experiments. **(A)** Thin PDMS wells adhered to glass slide and completely filled with collagen gel to create a flat surface. **(B)** Thicker replicate PDMS wells attached to existing wells and collagen soaked in CPM for 1-2 hr. **(C)** Upper PDMS removed and cells printed onto the collagen surface. Cells were allowed to attach for 1 hr. **(D)** Upper PDMS wells re-attached and filled with CPM.

2.4.4 Cell output

Analysis of cell output was conducted by depositing C2C12 cells onto glass slides and allowing the printed patterns to dry. Individual droplets and patterns were imaged and measured using the software tools previously described (§2.1.3). In some cases, counting the number of cells in printed droplets was difficult due to salt crystallisation on drying that complicated the imaged droplets. This problem was solved by placing printed slides into a sealed Petri dish containing a small amount of water prior to imaging, which would quickly (< 1 min) re-hydrate the printed ink and aid visualisation.

To assess printing reproducibility and distribution, we printed cells onto glass slides in patterns that allowed statistical analysis of the deposition. In order to determine whether cell deposition was even across the print head, continuous squares comprising 10x10 droplets were printed in six lateral positions across the width of the print head in a single pass (Figure 2.24A). To analyse the cell/drop distribution, three replicates of arrays containing 10x10 separated droplets were printed in three lateral positions across the width of the print head in a single pass (Figure 2.24B). Each array therefore contained 100 individual droplets, providing a large data set for statistical analysis.

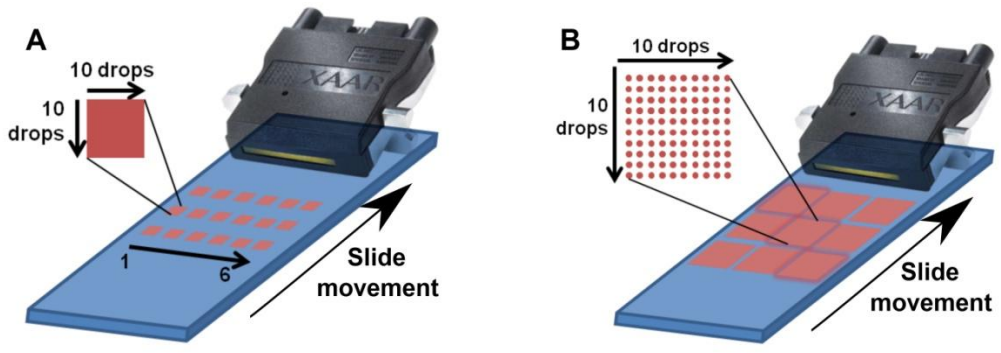

Figure 2.24: (A) Printed cell number across print head width was analysed by counting cells printed in squares of 10x10 droplets (utilising 10 nozzles each). Each sample contained 18 replicate squares as illustrated, printed in a single pass. **(B)** Cells per drop distribution was analysed by counting cells in individual drops printed in 10x10 arrays. Each sample contained 9 replicate arrays as illustrated, printed in a single pass.

Cell output over time was not investigated as it was for microvalve printing (§2.3.4), to avoid the risk of clogging the inkjet nozzles with aggregated and settled cells printed from DMEM alone. Instead, the density of cells printed from the bio-ink at initial and 1 hr time points was compared. This experiment doubled as an assessment of printed cell viability over time and is thus outlined in the following section (§2.4.5)

The volume of deposited droplets was determined using an absorbance-based assay utilising the phenol red (from DMEM) in the bio-ink. Varying volumes (1-10 µL) of a suspension of C2C12 cells at $5x10^5$ cells/mL in the bio-ink were pipetted onto small strips (~ 6x20 mm) of a glass cover-slip and allowed to dry. The dried ink was then washed into the wells of a 96-well plate using 100 µL of Milli-Q water. The absorbance at 560 nm (λ_{max} for phenol red) was measured on a plate reader (SpectraMax 190, Molecular Devices) for three samples at each volume to construct a calibration curve of absorbance as a function of deposited volume. The same cell suspension in the bio-ink was then inkjet printed onto the glass strips with varying layers (1-40) of a 30x30 droplet pattern and allowed to dry. The dried ink was rinsed into 96-well plates and absorbance measured as previously for three replicate samples. Using the calibration curve, this allowed the average droplet volume to be calculated.

2.4.5 Cell response

The phenotypic response of cells to the inkjet printing process was investigated for both C2C12 and PC12 cells lines. For these experiments, cells were printed directly into 100 µL of CPM in the custom PDMS wells described previously (§2.4.3), and immediately transferred to 96-well plates at the conclusion of printing for further culture and analysis.

For characterisation of printed cell viability, cells were suspended in bio-ink at 2-$6x10^6$ cells/mL and rectangular patterns containing 1250 drops each (25x50 drops) were printed into PDMS wells. The number of layers printed into each well was varied (3-8 passes) in order to deposit ~ 5000 cells per well. A corresponding volume of non-printed control cells in bio-ink was pipetted into PDMS wells, and subsequently transferred to 96-well plates in the same way as printed cells in order to

ensure consistent conditions. Viability was assessed by live/dead staining after 2 hr or 24 hr in culture as described previously (§2.1.5).

To study the viability and output of cells over an extended printing time, C2C12 cells were printed as described above and then left in the idle print head for approximately 1 hr before repeating the procedure. This also gave an indication of cell output at these two time points; by counting cells for viability analysis, the printed cell density at each time point was also obtained. Comparison of the cell density was used to give an indication of any cell settling in the print head over the 1 hr period between printing cycles.

The putative protective effect of the P188 surfactant on cells during the printing process was investigated in stand-alone experiments where the viability of C2C12 cells printed from the complete bio-ink formulation was compared to cells printed from a bio-ink without the added P188 component. Control cells that had been exposed to each bio-ink formulation were seeded directly after printing of each condition was completed, to account for any change in viability due to the time difference between printing cells with and without P188. In these experiments, an additional control condition was also introduced where cells were not printed, but rather purged from the print head via application of pressure. This was to give an indication whether any differences in viability of cells without P188 resulted from the inkjet firing process or from passage through the print head.

C2C12 and PC12 cells to be monitored for proliferation and differentiation were printed in the same manner as that described for viability experiments, except that for differentiation experiments the number of printed layers was doubled to attain ~ $1x10^4$ cells per well. These experiments also allowed analysis of the proliferation and differentiation of cells exposed to the bio-ink in comparison with cells exposed to DMEM alone. Therefore, in addition to a set of wells containing non-printed cells that had been exposed to the bio-ink, an additional set of control wells was included with non-printed cells that had been exposed to DMEM alone. Proliferation was quantified by the MTS assay as previously outlined (§2.1.6). Differentiation of C2C12 cells was induced by the gradual change of media conditions described in §2.1.1, which was instigated after 24 hr in culture in CPM, and cells were fixed after 4 days in the final CDM conditions. For PC12 cells, media was changed to CDM

after 24 hr and cells were fixed after a further 5 days in culture. Staining of differentiated C2C12 and PC12 cells was conducted by immunostaining (§2.1.4.3) or phalloidin staining (§2.1.4.4), respectively.

2.4.6 Application 1: Single cell mass spectrometry

In order to demonstrate the utility of inkjet printed cell microarrays in single cell analysis, a collaborative project was undertaken with Shane Ellis at the University of Wollongong. Printed cell arrays on glass slides were analysed for their lipid content by mass spectrometry (MS) using a novel ambient surface profiling tool termed liquid extraction surface analysis (LESA). These experiments were conducted using C2C12, PC12 and L929 cell lines, which were printed from surfactant-containing bio-ink at concentrations from 2-5x10^6 cells/mL.

Cells were printed onto standard glass slides that had been marked (on the reverse side to cell deposition) with a 4x11 array of circular regions ~3 mm in diameter. Cell patterns consisting of either a single droplet, or squares containing 9 droplets (3x3 square) or 100 droplets (10x10 square), were printed so that they were located within these marked regions (Figure 2.25A). Printed cell patterns dried quickly, and were then stored under N_2 in sealed Petri dishes until analysed by LESA-MS. Arrays were imaged by bright-field microscopy and the number of cells in each printed pattern was counted manually (for few cells) or using Image J software (for large cell numbers) (§2.1.3).

All mass spectrometry experiments were conducted by Shane Ellis at the University of Wollongong. A detailed description of the methods is outlined in the published manuscript *(308)*, and is summarised here. LESA was performed using a TriVersa NanoMate® (Advion Biosciences, Inc) system, and analysis was through a coupled QTRAP® 5500 mass spectrometer (AB Sciex). Analytes were extracted from printed cell regions by depositing 1.5 - 2 µL of a solvent mixture onto the substrate for 7 s (Figure 2.25B) before aspirating the entire volume back into the conducting tip. The solvent mixture contained 4:2:1 (v/v) of isopropanol, methanol and chloroform, respectively, with 20 mM added ammonium acetate. The sample was sprayed into the mass spectrometer source using a voltage of 1.3 kV applied to the tip and a backing gas pressure of 0.6 psi.

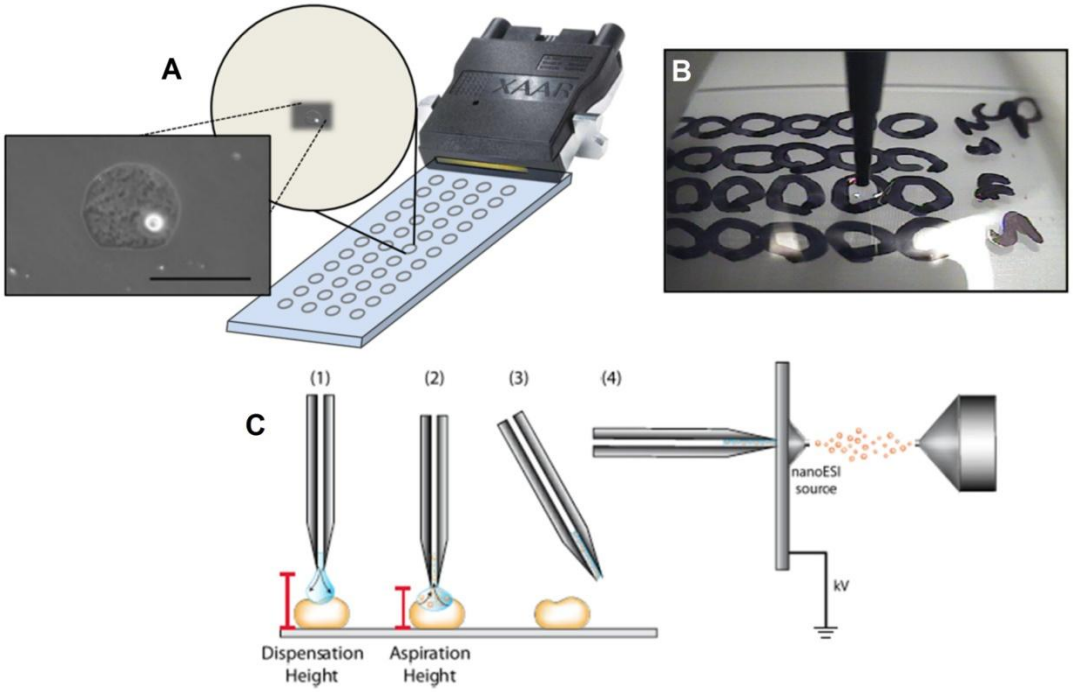

Figure 2.25: Printed cellular arrays for analysis by LESA-MS**. (A)** Cell patterns containing either 1 or 100 droplets were printed onto glass slides marked (on the reverse side to cell deposition) with circular regions (~ 2 mm diameter). **(B)** Image showing LESA probe depositing solvent on a printed cell spot. **(C)** Schematic of the LESA-MS process.

A range of lipids were detected by MS using precursor ion scans as indicated in Table 2.5. All spectra were acquired using a scan rate of 200 Da.s^{-1} and 100 or 200 scans were summed for analysis of 10-200 cell spots or 1-5 cell spots, respectively.

Table 2.5: Precursor ion scan and collision energy used for MS analysis of different lipid classes.

Lipid class	Precursor ion (m/z)	Collision energy (a.u.)
Phosphatidyl cholines (PC) and sphingomyelins (SM)	184.1	40
Ceramides	264.3	35
Cholesterol esters	369.4	25

2.4.7 Application 2: Multiple cell-type patterning

Patterns containing two different cell types (C2C12 and PC12) were printed simultaneously from two different Xaar-126 print heads onto collagen hydrogel substrates within PDMS wells (§2.4.3). Cells were stained prior to printing with green or red CellTracker™ fluorescent dyes (§2.1.4.2) to aid visualisation and distinguish between the two cell types (Figure 2.26).

Alignment of the two print heads was achieved by printing alignment patterns (Figure 2.27) onto glass slides and manually adjusting the print head positions until the patterns deposited from each head overlapped. This alignment process was very tedious and lacked accuracy. A system to overcome this challenge has been described previously *(190)*, where in situ microscopy of printed droplets accompanied with image analysis software guided software-driven offsets in print head positions. A similar system would be a useful addition to the printer used in this work.

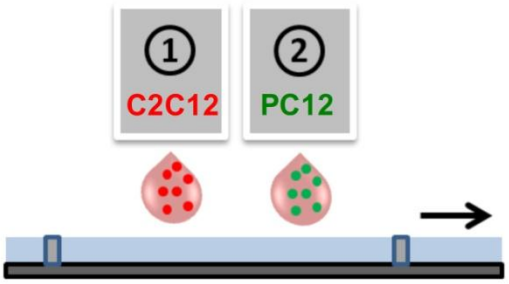

Figure 2.26: Schematic representation of multiple cell-type patterning, through simultaneous deposition of C2C12 and PC12 cells from two different Xaar-126 print heads onto collagen hydrogel substrates in custom-made PDMS wells.

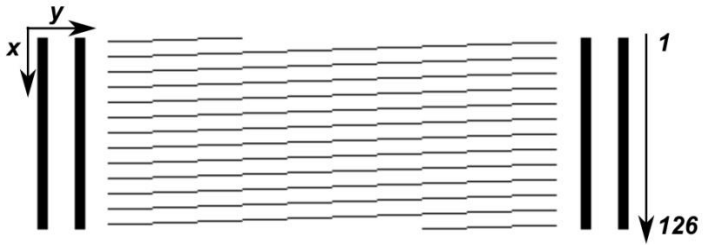

Figure 2.27: Pattern used to aid alignment of print heads in multiple head printing experiments.

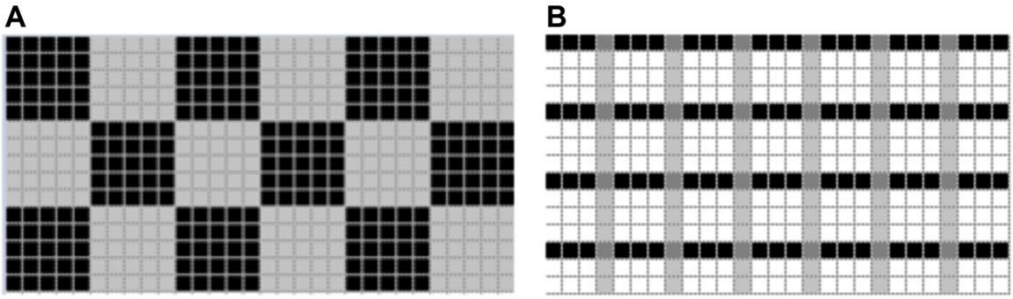

Figure 2.28: Representative patterns designed for dual cell printing experiments. Black and grey patterns, representing two different cell types, were created in separate Microsoft Paint files and sent to respective print heads. **(A)** Checkerboard pattern consisting of 25 droplets per square. **(B)** Lattice pattern with a line width of 1 droplet.

The cell patterns printed onto collagen in these experiments were either: checkerboard patterns, with 1, 4, 9 or 25 droplets per square; or lattice patterns, where horizontal and vertical lines were printed using different cell types, with line widths of 1 or 2 droplets (Figure 2.28). Both cell types were suspended in bio-ink at $6x10^6$ cells/mL and 10 layers of each pattern were printed for each sample.

The printed co-cultures of C2C12 and PC12 cells were subsequently maintained in the specific CPM media for C2C12 cells. After 24 hrs, the media was changed to the CDM for PC12 cells; this contained similar serum content to the CDM for C2C12 cells and the added NGF was not expected to influence C2C12 differentiation. Cells were fixed after 8 days under differentiation conditions and immunostained as described previously in this chapter (§2.1.4.3).

2.4.8 Application 3: Reactive printing

As outlined in the introduction to this thesis, one of the most common approaches to inkjet cell printing has been the reactive printing approaches. This is where cells are effectively encapsulated within hydrogels through the printing process by an ionic reaction between two components, usually alginate and Ca^{2+} ions. We endeavoured to demonstrate a similar approach with our GG systems.

Initial experiments were conducted with C2C12 cells suspended at $1x10^6$ cells/mL in CPM containing 20 mM added Ca^{2+}. Two separate reactive printing approaches were taken, as illustrated in Figure 2.29. Firstly, a thin layer of 0.5% (w/v) GG solution was smeared on 13 mm diameter glass cover-slips, and various patterns of the

C2C12 cell suspension were printed on top of this layer, crosslinking the GG on contact with the cations present in the media (Figure 2.29A). In a second approach, two print heads were used to simultaneously deposit GG solutions and cell suspensions (Figure 2.29B). In these initial experiments, 0.5% (w/v) GG was modified by brief sonication (Branson Digital probe sonifier, 3 min pulsed sonication, 0.5 sec on/off) with the addition of 15% (w/v) glycerol and 0.2% (v/v) Tween-20 to aid printability. Immediately following printing, constructs were transferred to 12-well plates containing CPM for further culture. Cells were stained with calcein (§2.1.4.1) after 5 days in culture.

The dual-head reactive printing approach shown here was also achieved by printing un-modified 0.5% (w/v) GG solution and C2C12 cells at $2x10^6$ cells/mL in a 0.05% (w/v) GG microgel suspension in DMEM, with 0.01% (v/v) Triton X-100 added to both solutions to aid printing. In all dual-head approaches, complementary patterns were designed using Microsoft Paint and loaded simultaneously into Xaar-XUSB software to direct printing from each head.

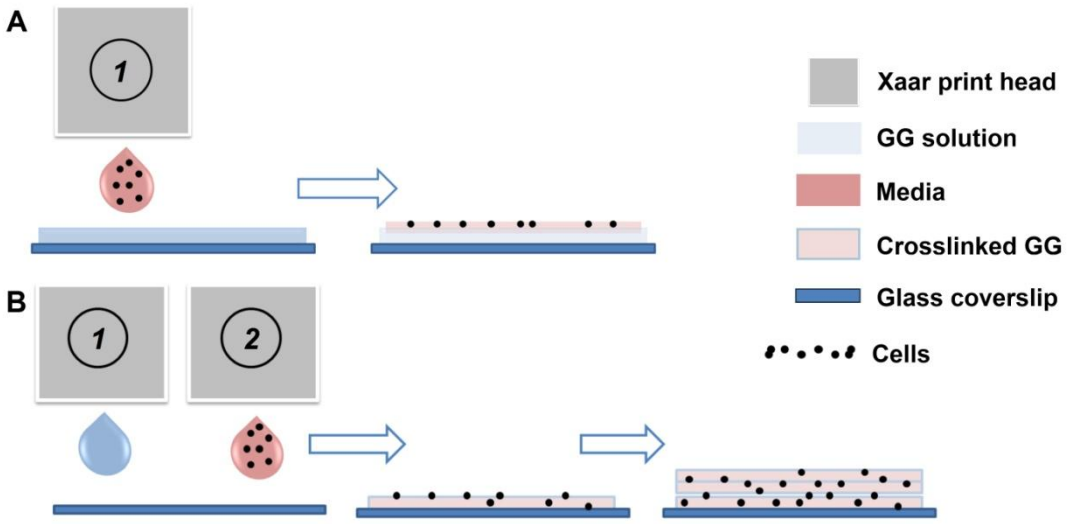

Figure 2.29: (A) Schematic representation of the single-head reactive printing approach, where a cell suspension is printed onto a thin layer of GG solution. **(B)** Schematic representation of the dual-head reactive printing approach, where GG solution and cell suspension are printed simultaneously from two separate heads in a layer-by-layer approach.

2.5 Modification of Gellan Gum

2.5.1 Surface seeding on hydrogels

The response of C2C12 cells seeded onto hydrogel surfaces was used to provide an initial indication of cell-material interactions. Hydrogels were formed using either a 'pre-gelled' approach or a 'media-gelled' approach. In the pre-gelled approach, GG solutions (0.1-1% (w/v)) were combined while hot (~ 60°C) with a source of cations, which was either $CaCl_2$ solution (5-50 mM), DMEM, or a combination of both. Aliquots of the hot mixture were then pipetted into culture plates and allowed to cool to RT to crosslink the hydrogel. In the media-gelled approach, GG solutions (0.1-1% (w/v)) at RT were pipetted into 96-well plates and gelled by the slow addition of DMEM (with or without added $CaCl_2$ at 5-50 mM). In both cases hydrogels were equilibrated in two changes of CPM over a 1 hr period before cells were added in CPM at 5000 cells/well. Unless stated otherwise, media in surface seeding experiments was changed every second day. Cell responses were qualitatively assessed by bright-field microscopy, or fluorescence microscopy of calcein-stained cells (§2.1.4.1).

2.5.2 Cell encapsulation in hydrogels

Encapsulation of C2C12 cells in hydrogels was initially investigated using three different methods (Figure 2.30). All of these approaches utilised ionic crosslinking of GG solutions at RT; methods involving thermal gelation processes were avoided due to the risk of heat-induced cell injury. Again, hydrogels were formed by combining a range of GG concentrations (0.1-1% (w/v)) and DMEM with or without added $CaCl_2$ (5-50 mM) through injection of one component into the other. Method A, where cells were suspended in DMEM and injected into GG solutions, was initially studied as it is analogous to the DRIP fabrication process introduced previously in this chapter (§2.3.6). Methods B and C were then implemented in an effort to achieve a more homogeneous encapsulation of cells. In a typical encapsulation process for all methods, 75 µL each of the GG and DMEM components were combined in a 96-well plate, followed by post-gelation addition of a further 75 µL of CPM containing pen/strep at 3x the usual working concentration. The density of encapsulated C2C12 cells was varied between $5x10^4$ – $5x10^6$ cells/mL.

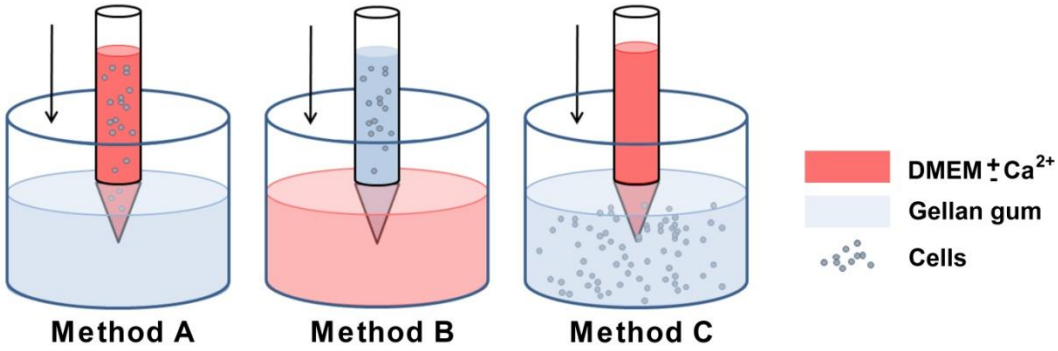

Figure 2.30: Schematic representation of methods for encapsulation of cells in GG hydrogels.

In final cell encapsulation experiments, Method C was employed with slight variations. Sucrose was used to protect cells from any potential osmotic injury resulting from exposure to the hypotonic GG solution before addition of DMEM. A GG solution at twice the desired final concentration was combined with an equal volume of a 20% (w/v) sucrose solution. This working solution, containing GG at the desired concentration and 10% (w/v) sucrose, was then used to re-suspend C2C12 cells at $2x10^6$ cells/mL and pipetted into 96-well plates. CPM containing 5 mM added $CaCl_2$ was then slowly added down the side of each well to crosslink the GG-cell suspensions. Media was changed for fresh CPM without additional $CaCl_2$ twice over a period of 1 hr, and cells were maintained and monitored over time in culture as before.

2.5.3 Protein-modification of gellan gum hydrogels

To encapsulate cells in GG/collagen composite hydrogels, a combination of the techniques previously outlined for the individual preparation of GG and collagen hydrogels was implemented to create hydrogels with a range of compositions. Collagen solutions were prepared as described in §2.4.3 (collagen concentration 4 mg/mL) and a small aliquot (< 10% of final volume) of a concentrated C2C12 cell suspension in CPM was added and mixed thoroughly. GG solution (0.5% w/v) was then mixed quickly with the collagen-cell suspension and the entire mixture pipetted into culture plates. The gel compositions are listed in Table 2.6, and in each case the final C2C12 cell concentration was $2x10^6$ cells/mL. Fresh CPM (100 µL) was gently pipetted into wells to crosslink the GG component (except for collagen only gels), and constructs were subsequently incubated at 37 °C for 1 hr to allow the collagen to polymerise. This process is represented schematically in Figure 2.31. Cells were cultured in CPM, then calcein stained and imaged after 5 days in culture.

Table 2.6: Volume fraction of 0.5% (w/v) GG and 4 mg/mL collagen included in different composite hydrogel compositions.

Gel composition	Vol. Fraction (%) of 0.5% w/v GG	Vol. Fraction (%) 4 mg/mL collagen
100G	100	0
75G:25C	75	25
50G:50C	50	50
100C	0	100

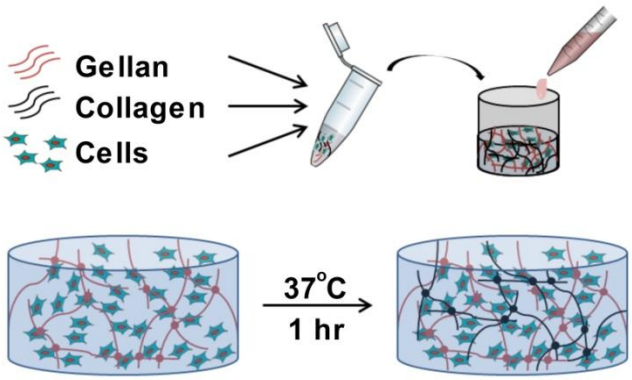

Figure 2.31: Schematic representation of the formation of cell-encapsulating composite hydrogels from gellan gum and collagen.

2.5.4 Peptide modification of gellan gum

In the following section, all work with radioactive materials was conducted at the Australian Nuclear Science and Technology Organisation (ANSTO) under the guidance of Dr. Ivan Greguric and Dr. Eskender Mume.

2.5.4.1 Peptides

All peptides used in this thesis were purchased from Auspep. Initial work was conducted with the peptide GRGDS. In subsequent work, a longer glycine tail was required, as well as a tyrosine residue for radio-iodination of the peptide, and so the peptide GGGGRGDSY (G_4RGDSY) was custom-synthesised. A corresponding peptide with the aspartic acid residue replaced by glutamic acid, GGGGRGESY (G_4RGESY), was also purchased to act as a control for the RGD-containing peptide. Peptides were reconstituted in Milli-Q water at 1 mg/mL and stored in aliquots at -20°C.

2.5.4.2 Peptide radiolabelling

For quantitative analysis of peptide binding to GG, the peptide G_4RGDSY was radio-labelled through radio-iodination of the tyrosine residue using the well-established chloramine-T method *(309)*. Iodine-125 carrier-free radionuclide was purchased from Perkin-Elmer ($Na^{125}I$, $t_{1/2}$=59.4 days, NEZ033H010MC). Chemicals and solvents were obtained from Sigma unless stated otherwise. Firstly, 50µL of a 1 mg/mL solution of G_4RGDSY in Milli-Q water was diluted with 180 µL of 0.1 M sodium phosphate buffer (pH 6.0). A 50 µL aliquot of diluted $Na^{125}I$ (1 µL of stock solution in 49 µL of 1 mM NaOH) was then added, followed by 10 µL of chloramine-T dissolved at 1 mg/mL in buffer. After 5 min, the reaction was quenched by the addition of 10 µL of sodium metabisulfite (Merck) at 2.5 mg/mL in buffer. The reaction mixture (300 µL total) was loaded onto an Oasis HLB SPE cartridge (Waters) that had been pre-equilibrated by eluting 5 mL methanol, 5 mL water and 10 mL 0.1% (v/v) TFA in water (solvent A). The cartridge was then washed with 20 mL of solvent A to remove unbound iodine-125. Two fractions were eluted, the first with 4 mL of a 1:1 mixture of solvent A with 0.1% (v/v) TFA in acetonitrile (solvent B), and the second with 4 mL of solvent B. The two fractions were pooled, dried in a rotary evaporator and re-dissolved in Milli-Q water (350 µL). For cold-labelling with non-radioactive iodine, the above procedure was repeated using NaI dissolved in Milli-Q water and added at a 1:1 molar ratio to the peptide.

2.5.4.3 Specific activity determination

Specific activity is defined as the amount of radioactivity (gamma emission), or the decay rate per unit mass of a particular radionuclide. Gamma emissions were analysed using a Perkin Elmer 2480 WIZARD^2 gamma counter. The radioactivity of ^{125}I-G_4RGDSY was determined by counting the emissions from a 2 µL aliquot and converting to disintegrations per minute, and thus activity, using the specified efficiency of the gamma counter [counting efficiency = CPM/DPM x 100% = 78% (for iodine-125), CPM = counts/min, DPM = disintegrations/min = 2.22 µCi]. The concentration and purity of the labelled peptide was determined by HPLC (high-performance liquid chromatography) analysis using a Shimadzu HPLC-DAD system equipped with an Eclipse XDB-C18 column (Agilent, 250x4.6 mm) with a 5 µm particle size. Compounds were eluted using 30% (v/v) acetonitrile and water at a

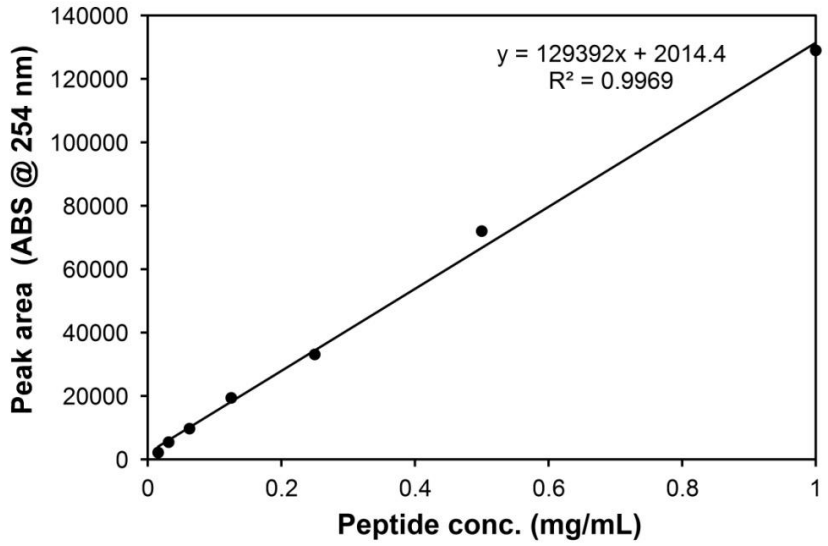

Figure 2.32: Peak area (λ = 254 nm) in HPLC chromatogram as a function of concentration of un-labelled G_4RGDSY peptide.

flow rate of 1 mL/min, isocratic, over 15 min. Peptide concentration was calculated using a calibration curve constructed from HPLC chromatograms of G_4RGDSY solutions of known concentration, plotting integrated peak area (λ = 254 nm) as a function of peptide concentration (Figure 2.32).

2.5.4.4 Gellan gum purification

Commercial samples of Gelzan™ CM were purified to remove divalent cation contaminants using a method based on that published by Doner and co-workers *(310, 311)*. Gelzan™ CM (0.5 g) was dissolved in Milli-Q water (50 mL) at 1% (w/v) as described previously (§2.2.1) and maintained at approximately 60 °C. A 1.25 g sample of Dowex 50W-X8 cation exchange resin (Fluka, H^+ form, 50-100 mesh), pre-rinsed in 1 M HCl and Milli-Q water, was then added and the hot mixture was stirred for 30 min (pH reduced to ~ 2 during this time) to convert GG to the free acid form (gellanoic acid). The resin was allowed to settle and the supernatant was decanted into a pre-heated beaker. The resin was rinsed twice with a small volume of 60 °C water and added to the supernatant. While maintaining the solution at ~ 60 °C, 4 M NaOH was added dropwise, until the pH stabilised at ~ 7.5, to convert the gellanoic acid to the sodium salt (sodium gellanate, NaGG). After stirring for an additional 5 min, 100 mL of 2-propanol was added with continued stirring to precipitate a white fibrous product. This product was recovered via vacuum filtration,

rinsed liberally with 2-propanol and dried under vacuum overnight. The product was chopped into a fine powder using a scalpel and stored under cool, dry conditions until required.

Ionic content of samples of Gelzan™ CM and the purified NaGG product was investigated by flame atomic absorption spectroscopy (AAS). These experiments were kindly performed by Damian Kirchmajer from the University of Wollongong. Briefly, samples were analysed using a Spectra AA 220FS (Varian) spectrometer equipped with sodium (589.6 nm), potassium (769.9 nm), calcium (422.7 nm) and magnesium (285.2 nm) hollow cathode light sources. The oxidant/fuel mixture consisted of air and acetylene. Samples were digested in hot concentrated sulphuric acid, treated with hydrogen peroxide (30% v/v) and diluted to a final matrix containing 5% (v/v) sulphuric acid and 2 mg/mL caesium chloride as an ionisation suppressant. Calibration standards were prepared using a certified multi-element standard solution (Inorganic Ventures). The limit of detection for each element (Table 2.7) was taken as twice the standard deviation of blank measurements.

Table 2.7: Limits of detection for sodium, potassium, calcium and magnesium.

Element	LOD (% w/w)
Sodium	0.02
Potassium	0.03
Calcium	0.06
Magnesium	0.03

2.5.4.5 Peptide conjugation

RGD-containing peptides must be covalently bound to biomaterials in order to encourage the development of strong cell adhesions *(312)*. The most common route to achieve this conjugation is using the ‘zero-length’ crosslinker 1-ethyl-3-(3-dimethylaminopropyl)carbodiimide (EDC), which mediates the formation of stable amide bonds between carboxyl and amine functionalities, often with *N*-hydroxysulfosuccinimide (sulfo-NHS) as a co-reactant to stabilise the reactive ester intermediate against the competing hydrolysis reaction (Figure 2.33).

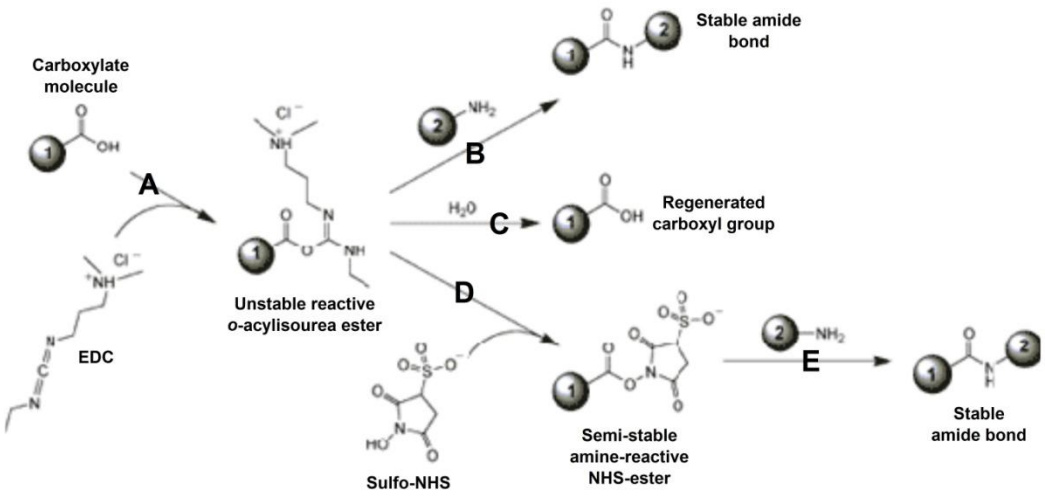

Figure 2.33: Schematic representation of EDC mediated conjugation between carboxyl and amine functionalities to form stable amide bonds. EDC reacts with carboxylic acids to produce an unstable reactive ester (A). This ester can then react with amine functionalities to form stable amine bonds (B), but competes with a concurrent hydrolysis reaction (C). Addition of sulfo-NHS can stabilise the intermediate (D) leading to a higher yield of the amide product (E).

To prevent activation of the carboxylic acid on the aspartate side chain, substrate carboxylic acids are typically activated with EDC/sulfo-NHS before addition of the RGD peptide, which is then conjugated through the *N*-terminus (Figure 2.34). When the reaction is carried out in water, protonation of the arginine side chain significantly reduces its nucleophilicity so that conjugation proceeds preferably through the terminal amine. The reaction is normally buffered by 2-(*N*-morpholino)ethanesulfonic acid (MES), as it does not contain carboxyl or amine groups and avoids the use of phosphates and acetates which readily form coordination complexes with metal ions.

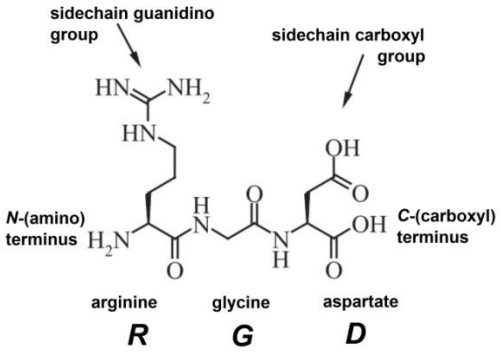

Figure 2.34: The RGD peptide sequence. Adapted from reference *(312)*.

One of the most common applications of this approach is the conjugation of RGD peptides to alginate, a polysaccharide similar in its chemical and physical characteristics to GG. Rowley and co-workers *(313)* were the first to characterise this conjugation, and their method has since been employed by several workers to conjugate a range of peptides to alginate *(314–318)*. We therefore used this well established method as a basis for our attempts to conjugate RGD peptides to GG. Throughout this section, concentrations of reactants (i.e. EDC, peptide) in conjugation experiments are referred to as a molar percentage of the carboxylic acid (COOH) groups on GG. For example, in a 1% (w/v) solution of GG, the concentration of carboxylic acids is 15 mM (GG repeat unit MW ~670 $gmol^{-1}$, 1 COOH/repeat unit); peptide added at 1% of COOH therefore refers to a peptide concentration of 0.15 mM.

Conjugation was performed with GG or NaGG dissolved at 0.1-1 % (w/v) in one of a range of buffers, all prepared at 50 mM in Milli-Q: MES buffer at pH 5 or pH 6.5, sodium phosphate buffer at pH 8, or sodium acetate buffer at pH 6.7. Control experiments were also performed un-buffered with GG dissolved in Milli-Q. A small volume of the GG solution, typically 100 µL, was equilibrated at the reaction temperature (21-60 °C) in an Eppendorf tube. EDC (Sigma) and sulfo-NHS (Proteochem) were weighed accurately and then dissolved in the volume of buffer required to give the desired final concentration (EDC at 5-20 % of COOH) through addition of a 5-10 µL aliquot to the GG or NaGG solution. Sulfo-NHS was always included at a 1:2 molar equivalent to EDC. EDC was handled carefully to prevent premature oxidation; the stock powder was stored desiccated at -20 °C, and reaction aliquots were removed under nitrogen and returned to -20 °C prior to dissolution and immediate addition to the reaction mixture. Activation of GG or NaGG with EDC and sulfo-NHS was allowed to proceed for 15-30 min before addition of the peptide. Aliquots of peptide in Milli-Q were added to the reaction mixture to give final peptide concentrations ranging from 0.15-15 % of COOH, and the conjugation reaction was left overnight. In experiments using radio-labelled peptide to enable quantification of the conjugation efficiency, radio-labelled G_4RGDSY was used to spike unlabelled peptide, with ~ 2 µCi activity added per reaction. Unless stated otherwise, conjugation reactions were performed in duplicate for each set of reaction conditions.

Following conjugation, it was necessary to remove unbound peptide, residual reactants and bi-products from the mixture. Initially, dialysis was conducted with the sample loaded into membrane tubing (SpectraPor, molecular weight cut-off MWCO ~1200 kDa) and dialysed against ~2 L Milli-Q water for 4 days. The purified product was either lyophilised, or precipitated with two equivalent volumes of 2-propanol (Sigma), recovered by vacuum filtration, rinsed with ethanol and allowed to air dry. The conjugated peptide content in products prepared in this way was assessed by elemental analysis (C, H, N content). This was performed at the microanalytical unit of the Research School of Chemistry, Australian National University (ACT, Australia).

Alternatively, for analysis of conjugation efficiency using radio-labelled peptides, faster separation methods were required. In all of the following approaches, the activity in all components of the system (i.e. sample, filtrates, eluates, dialysates, separation devices) was measured using a Perkin Elmer 2480 WIZARD^2 gamma counter as previously described (§2.5.4.2) and used to calculate the conjugation efficiency. The effectiveness of all separation approaches, and any non-specific peptide binding to GG or NaGG, was assessed using control samples with no added EDC or sulfo-NHS. All centrifugation steps were carried out using a Spectrafuge 24D bench-top centrifuge (Labnet International). Initially, centrifuge filtration devices (Amicon™, Merck Millipore; or VectaSpin™, Whatman) with a range of nominal molecular weight cut-offs (10-100 kDa) were assessed, but proved ineffective in separating the components, with labelled products becoming bound to the filter unit. Consequently, we employed Zeba spin desalting columns (0.5 mL, MWCO 40 kDa, ThermoScientific) that contain a size exclusion resin for removing small compounds (< 2 kDa), which become trapped in the resin, while allowing the passage of larger compounds (> 40 kDa). This was suitable for separating un-conjugated peptide (~1 kDa) and smaller reaction species from the peptide-conjugated GG (~ 500 kDa). These columns were used according to the manufacturer's specifications, with a slight modification in that the devices were heated (~ 50 °C) prior to sample loading to prevent the possibility of GG gelation within the device. Samples conjugated using the optimised reaction conditions were also purified by dialysis against Milli-Q water over 5 days using Slide-a-Lyzer MINI dialysis devices (0.1 mL, MWCO 10 kDa, ThermoScientific).

2.5.4.6 Cell response

To prepare peptide-conjugated products for experiments assessing cellular responses, un-labelled G_4RGDSY and G_4RGESY peptides were utilised, and conjugation proceeded as described previously with the following conditions: NaGG at 1% (w/v) in 50 mM MES buffer (pH 6.5), EDC added at 10% of COOH (therefore sulfo-NHS added at 5% of COOH), peptide added at 0.1% or 1% of COOH, reaction proceeded overnight at 37 °C. Conjugations were performed under aseptic conditions to maintain sterility. Purification of the product was achieved by dialysis against sterile Milli-Q water over 4 days using Slide-a-Lyzer MINI dialysis devices (0.5 mL, MWCO 20 kDa, ThermoScientific). The dialysate was changed under aseptic conditions every day.

The phenotypic cellular response to peptide-conjugated NaGG was assessed with C2C12 cells seeded on the surface of, and encapsulated within, 0.15% (w/v) hydrogels. For surface seeding experiments, hydrogels were formed using the media-gelled approach (§2.5.1) with CPM containing 20 mM added $CaCl_2$. Cells were encapsulated in hydrogels using the sucrose method previously outlined (§2.5.2). Cell morphology was assessed daily by bright-field microscopy, and by calcein staining after 2 or 4 days in culture for surface seeded or encapsulated cells, respectively. For surface-seeded cells, media was changed to CDM after 2 days in culture to induce differentiation. Cells were imaged daily as before, and after 5 days under differentiation conditions were fixed and immunostained for desmin as previously outlined (§2.1.4.3).

2.6 Statistical analysis

This section outlines the general statistical treatment applied to data throughout this thesis. If the analysis of a particular data set required variation from the methods described here, it is indicated clearly along with the presentation of that data.

2.6.1 Statements of error

Error bars in graphical presentations of data represent the standard error (SE) of the mean value, calculated according to Equation 2.1,

$$SE = \frac{\sigma}{\sqrt{n}}$$ **Equation 2.1**

where σ is the sample standard deviation and n is the size of the sample set. Where data values are quoted directly, the standard deviation is given following the mean value (mean ± standard deviation). For normalised data, error values are propagated according to standard statistical practice.

2.6.2 Statistical significance

2.6.2.1 Student's t-test

Application of an unpaired Student's *t*-test was used in instances where direct comparison of two distinct data sets was warranted. The test was conducted using freely available online statistical software (www.graphpad.com). The probability (P) of satisfying the null hypothesis is represented using asterisks; $P < 0.05$ (*), $P < 0.01$ (**), or $P < 0.001$ (***).

2.6.2.2 Analysis of variance

Where comparison of the means of three or more unmatched groups was required, one-way analysis of variance (ANOVA) was applied. The ANOVA test was conducted using freely available online statistical software (http://www.danielsoper.com/statcalc3). When one-way ANOVA indicated a statistically significant variation across groups, it is stated along with the corresponding significance level.

2.6.3 Principle component analysis

Principle component analysis (PCA) is a form of multivariate data analysis commonly employed to identify statistical differences that are difficult to determine directly *(319)*. PCA was applied to the LESA-MS spectral data obtained from printed C2C12, PC12 and L929 cells (§2.4.6) to highlight differences in the respective lipid profiles of each cell. PCA was performed using MarkerView software (AB Sciex). The scan data (MCA mode) of 5 microarray spots for each cell type was imported into the software and the 50 most abundant peaks were chosen. Of these 50 peaks, several were below *m/*z 700 and these were deselected to reduce the effect of sample oxidation on the statistical analysis. Data was then centroided and normalized to total peak area. PCA analysis was then performed using pareto scaling and no weighting.

3 BIO-INK FORMULATION

This chapter outlines the development of bio-ink formulations for drop-on-demand cell printing. For both microvalve (Chapter 4) and inkjet (Chapter 5) printing, prevention of cell settling and aggregation is important. For this purpose we investigated the structure and rheology of GG microgel suspensions and their effect on cell settling and printability. For inkjet printing (Chapter 5), surface tension reduction is also important, and so suitable surfactants were also explored. The response of cells to bio-ink formulations was monitored throughout development.

3.1 Gellan gum microgel bio-ink

3.1.1 Microgel formation and rheology *in-situ*

Previous work by our group *(281)* and others *(255)* has demonstrated that GG hydrogels can be formed through gelation induced by the cations present in standard cell culture media (CCM). The formation of microgel suspensions (fluid gels) had not, however, been previously demonstrated in CCM. Therefore, we first investigated the formation of GG microgel suspensions in CCM. For initial experiments, formation was carried out in situ in a rheometer; this allowed control over the applied shear and cooling rate, and simultaneous measurement of rheological properties during microgel formation. A GG solution (1% w/v) in Milli-Q water was combined with CCM at ~60°C to create a range of final GG concentrations. These solutions were then cooled at 1°C/min using the rheometer Peltier plate control with simultaneous application of shear stress at 500 s^{-1} by a cone and plate geometry (§2.2.6.2). Figure 3.1 shows the apparent viscosity of these solutions during this shear-cooling process. For GG concentrations ≥ 0.05% (w/v) there was a sharp increase in viscosity at ~44°C, and this transition temperature was independent of GG concentration. This increase indicated the gelation point of GG, which results in microgel formation under these shear conditions. The transition temperature agrees well with that observed previously for in-situ rheological GG microgel formation *(289, 296)*. The sharp transition also reflects the well known 'snap-set' gelation properties of GG. At GG concentrations ≤ 0.01% (w/v) no viscosity increase was observed, indicating that these concentrations were too low for the formation of GG microgels, in agreement with previous results *(296)*.

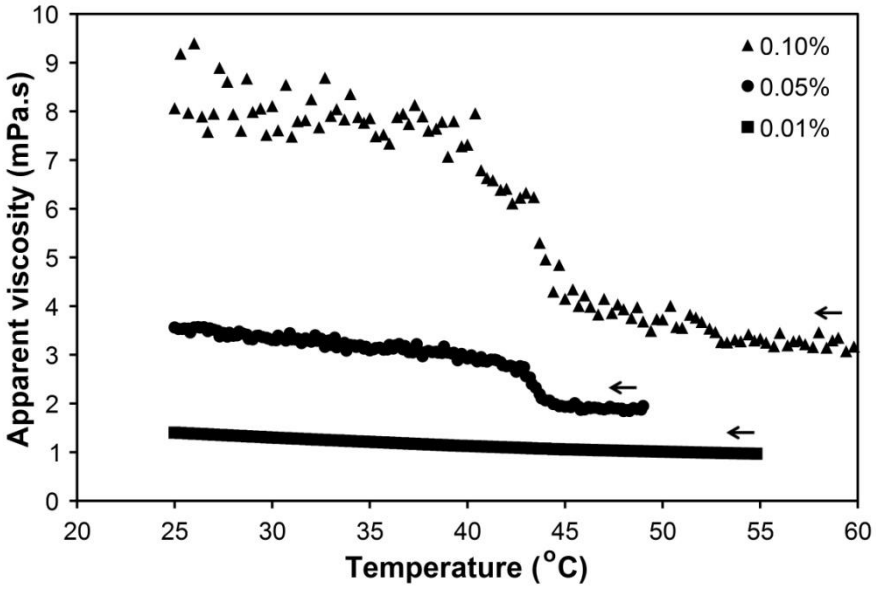

Figure 3.1: Temperature sweeps showing viscosity as a function of temperature for gellan gum in cell culture medium on cooling (arrows indicate sweep direction). Gellan gum concentrations were 0.01% (squares), 0.05% (circles) or 0.10% (w/v) (triangles). Samples were cooled at 1°C/min with a constant applied shear of 500 s^{-1}.

Directly after formation, the rheology of these microgel suspensions was investigated by measuring the apparent viscosity as a function of shear rate (Figure 3.2). Microgel suspensions with GG concentrations ≥ 0.05% (w/v) exhibited well defined shear-thinning behaviour (a decrease in viscosity with increasing shear rate). This was not observed with a GG concentration of 0.01% (w/v), emphasising that microgels did not form at this concentration. A 0.05% (w/v) solution of GG in Milli-Q water also showed low viscosity and Newtonian behaviour (viscosity independent of shear rate) as reported previously *(307)*, which highlights the pre-requisite of microgel formation in ionic media for the appearance of the non-Newtonian response.

3.1.2 Cell settling in microgel suspensions

Prior to further characterisation of GG microgel formation, structure and rheological properties, we carried out a preliminary investigation to explore their ability to prevent cell settling. C2C12 cells were suspended in 100 µL of CCM or a 0.05% (w/v) GG microgel suspension in DMEM at $1x10^6$ cells/mL and allowed to settle in the wells of a 96-well plate (§2.2.7). Analyses of cell number on the base of these wells by optical microscopy provided a comparison of the settling behaviour in the

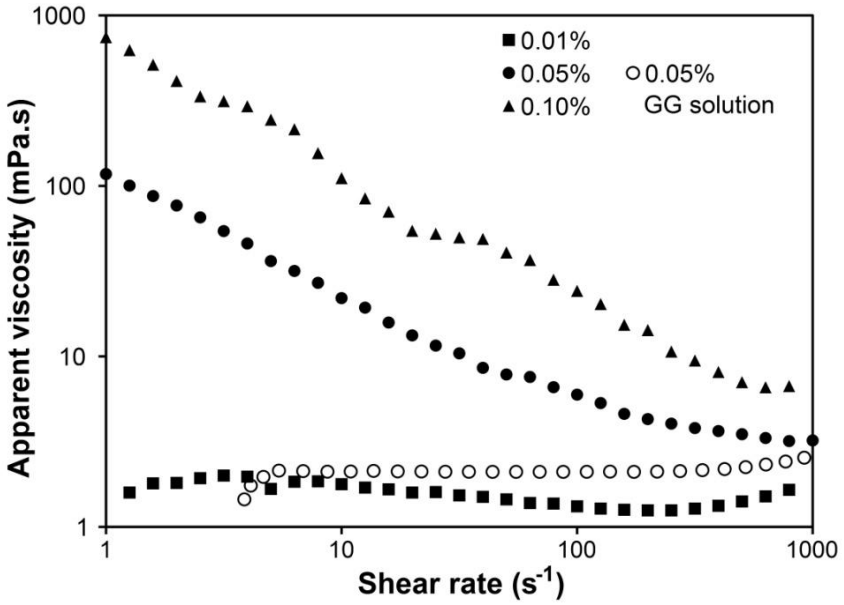

Figure 3.2: Flow curves for gellan gum microgels in cell culture medium formed in situ in a rheometer. Gellan gum concentrations were 0.01% (filled squares), 0.05% (filled circles) or 0.10% (w/v) (filled triangles). The flow curve is also provided for a 0.05% (w/v) solution of gellan gum in Milli-Q water (open circles). Measurements were conducted at 25°C.

two solutions (Figure 3.3). In CCM alone, cells completely settled to the base of the well within ~15 min. Conversely, no settling was observed in the microgel suspension, and there was no sign of cell aggregation over this period, as evidenced by representative micrographs in Figure 3.3. Quantitative data is provided for up to 45 min, but we observed no further settling over a period of 2 days. Cells settled completely after ~15 min when suspended in a 0.05% (w/v) solution of GG in Milli-Q water (data not shown), demonstrating that the prevention of settling was dependent on microgel formation.

This initial set of results confirmed that GG microgels could be formed in CCM, the microgel suspensions exhibited non-Newtonian flow properties, and that they could prevent the settling and aggregation of suspended cells. We then proceeded to further characterise the formation, structure, rheology and cell suspending capabilities of these systems to assess their suitability as components of a bio-ink formulation.

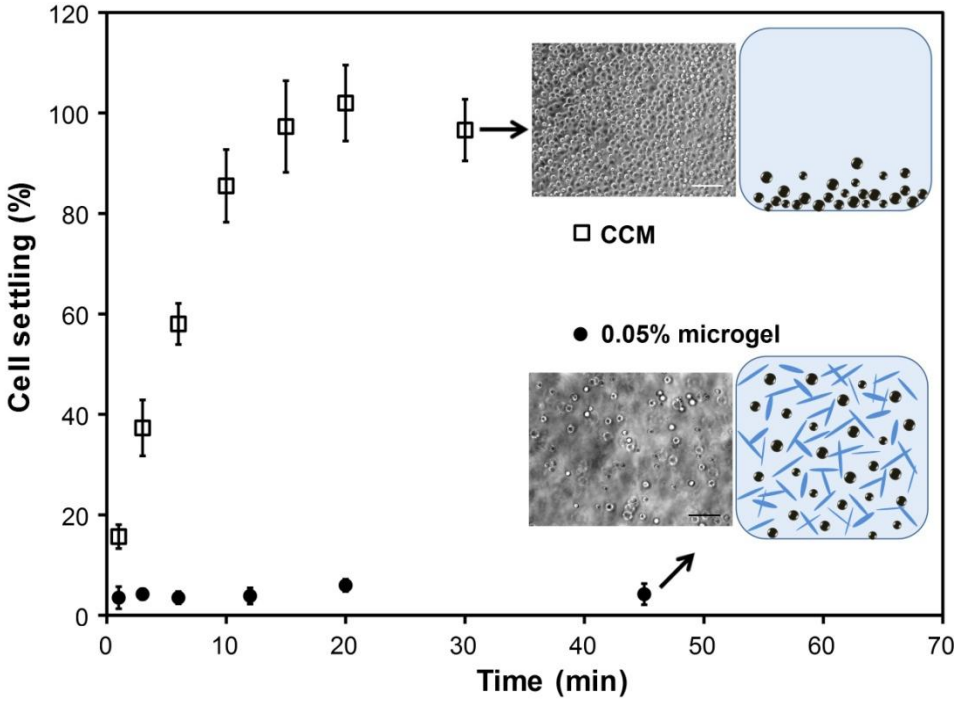

Figure 3.3: Cell settling (percentage of cells on the base of a 96 well plate) as a function of time for C2C12 cells suspended at $1x10^6$ cells/mL in CCM (open squares) or a 0.05% (w/v) GG microgel suspension in CCM (filled circles). Samples were analysed in triplicate, and error bars represent one standard deviation from the mean. Insets show the base of well plates 60 min after seeding cells (scale bars represent 100 µm) and cartoons depicting the ability of the microgel suspension to keep cells in suspension.

3.1.3 Bio-ink production and structure

It was impractical to use the rheometer with a cone and plate geometry for the application of shear required for microgel formation, and this approach was not scalable to the production of useful quantities of bio-ink. We therefore required a method capable of applying shear to relatively large solution volumes. Furthermore, it has been shown that the size of microgel particles is dependent on the applied shear rate *(294)*; larger particles are produced with lower shear. Their application in inkjet printing, where these microgels need to pass through relatively small (50 µm) nozzles, therefore necessitated high shear in order to minimise particle size.

Several different methods of applying high shear to suspensions during cooling were assessed for their impact on microgel structure and particle size. In these experiments, GG microgels were formed in DMEM without serum. For each technique, GG and DMEM solutions were combined at ~80°C in a water bath and cooling was achieved simply by exposure to ambient conditions until they had reached RT (~10 min). This slow cooling was intended to avoid the formation of temperature gradients which can potentially result in non-uniform gelation *(299)*.

Applying shear using either an overhead laboratory homogeniser or magnetic stirrer produced significant amounts of trapped air pockets and bulk gelled regions, so these approaches were not pursued further. Two methods that provided visually homogenous solutions were the use of a large volume (~30 mL) cup and vane-rotor assembly within the rheometer, and the use of a standard laboratory vortex mixer.

We then sought a means to visualise the microgel network structure produced via these two methods. Imaging of microgel particles is a challenge due to their lack of contrast with the surrounding solutions and the complexity of the network. It has been achieved previously by confocal scanning laser microscopy (CSLM) of fluorescently labelled GG *(289, 297)*. We stained the microgel particles with the common cell nuclear stain DAPI, and imaged by fluorescence microscopy. We realised that DAPI stained GG well after observing high fluorescence backgrounds when attempting to stain cells encapsulated in GG hydrogels (Chapter 6). Rheology of DAPI-stained microgel suspensions did not show any clear differences from that of un-stained microgels, suggesting that the staining did not alter microgel structure.

Representative DAPI-stained images of microgel suspensions formed using the two methods reveal significantly different structures (Figure 3.4). The rheometer method produced large particles (Figure 3.4A) that were reminiscent of GG *(289)* and agar *(294)* microgel particles produced under low shear. Although the nominal shear rate of this method was 750 s^{-1}, the shear was likely to be applied unevenly throughout the solution. Vortex mixing produced a homogenous network of relatively small microgel particles (Figure 3.4B). Although the high density of the microgel network made accurate characterisation of particle size difficult, they appeared to be irregular and elongated in shape with dimensions on the scale of 5-50 µm as previously reported for GG microgels formed under high shear *(298, 299)*. This non-spherical shape is important in the development of viscoelastic properties of the microgel suspensions even at low polymer concentration *(299)*. Importantly, the particle dimensions were such that they should be able to pass unimpeded through the nozzles of microvalve and inkjet printers. Note that higher magnification images of microgel particles, which aid visualisation, are provided in Figure 3.22.

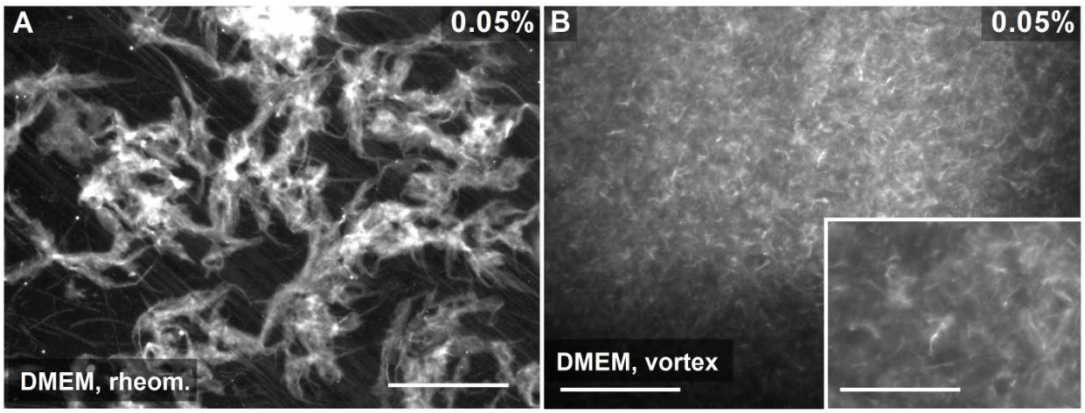

Figure 3.4: Fluorescence microscope images of microgel particles (stained with DAPI) formed with 0.05% (w/v) GG in DMEM by application of shear during cooling, either by a constant shear of 750 s^{-1} applied through a cup and vane geometry in situ in a rheometer (A), or by vortex mixing (B). Scale bars represent 200 µm or 100 µm (inset).

The work of Norton and co-workers *(294)* suggested that the size of microgel particles decreases with increasing polymer concentration. This is because, at a given shear rate, higher local shear forces due to the increased viscosity limits the equilibrium size of developing microgel particles. However, we found that increasing GG concentration from 0.05 to 0.25% w/v increased the microgel particle size (Figure 3.5). Since vortex mixing applies a constant shear stress, rather than constant shear rate, it is likely that the shear rate actually decreased for the more viscous 0.25% w/v solution, thus negating the aforementioned affect and producing larger particles. We found that the 0.25% w/v GG microgel suspension could not pass through the 50 µm nozzles of our inkjet print heads.

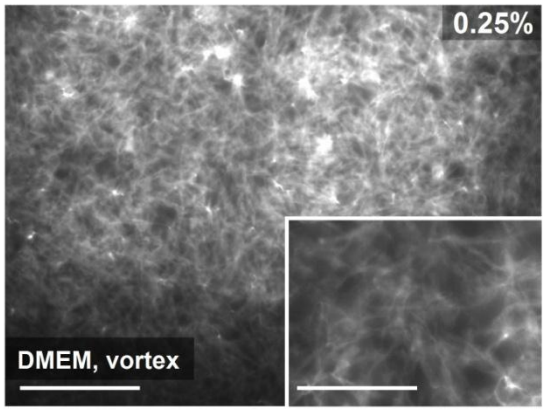

Figure 3.5: Fluorescence microscope images of microgel particles (stained with DAPI) formed with 0.25% (w/v) GG in DMEM by application of shear by vortex mixing during cooling. Scale bars represent 200 µm or 100 µm (inset).

A GG concentration of 0.05% (w/v) was therefore selected for the bio-ink, as it satisfied the requirements of microgel formation with a small particle size, to enable passage through the print head, and a low polymer content, which is advantageous in our previously stated bio-ink design philosophy (§1.4.1). Further characterisation in this chapter is performed on this formulation only produced using vortex mixing.

3.1.4 Bio-ink rheology

We endeavoured to characterise the viscoplastic behaviour of the bio-ink more thoroughly to assess its suitability to satisfy the demands of both cell suspending ability and printability. Specifically, we were interested in the rheological behaviour at both extremes of shear rate. The low shear behaviour, including both the yield stress required to initiate flow and the subsequent viscosity, is relevant to the stabilisation of cell suspensions. The viscosity at high shear is an important determinant of the printability of the ink, especially in inkjet printing applications. We measured these properties using continuous ramps of shear stress from rest and also stepped ramps of shear rate over the range of 1-1000 s^{-1} using a 40 mm sandblasted parallel plate geometry. As outlined previously (§2.2.6.3), the shear stress ramps were preferred for analysis of yield behaviour as they provide a direct measurement of the static yield stress (the stress required to initiate flow). In comparison, the stepped ramps of shear rate measure yield stress by extrapolation of flow behaviour back to zero shear and therefore provide an approximation of dynamic yield stress (stress at which flow stops). Conversely, for analysis of the flow behaviour at high shear rates, stepped ramps of shear rate were preferred as they provided the most accurate high-shear data with silicone viscosity standards (§2.2.6.3). Figure 3.6 shows both the shear stress and viscosity as a function of shear rate for both stress and strain ramps plotted between 0-100 s^{-1}. This highlights that the bio-ink displays both of the visco-plastic characteristics expected for a typical microgel suspension: a yield stress, evidenced by the non-zero shear stress at zero shear rate; and shear-thinning, evidenced by the significant increase in viscosity at low shear rate.

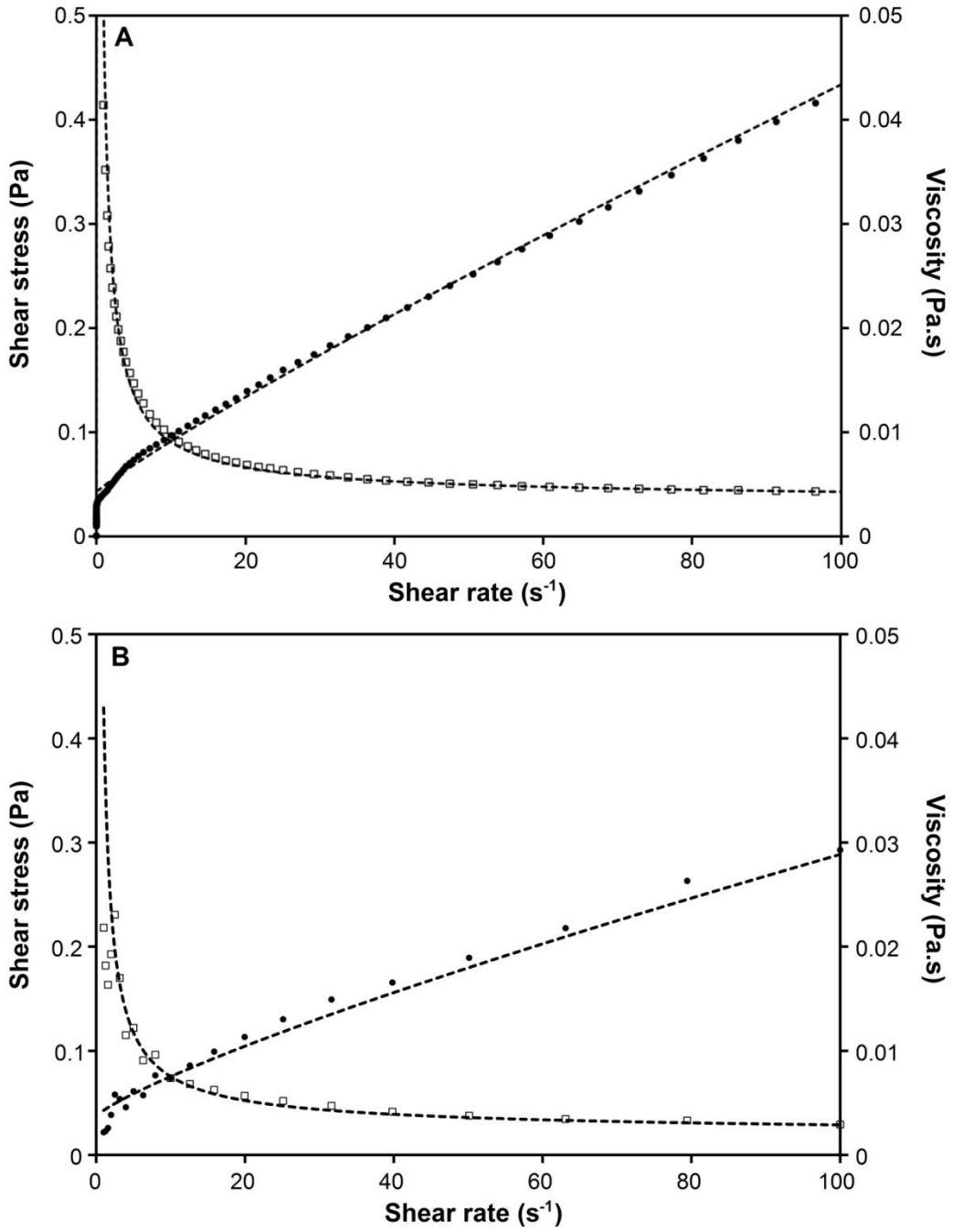

Figure 3.6: Apparent shear stress (filled circles) and viscosity (empty squares) as a function of shear rate for bio-ink measured using a continuous ramp of shear stress (A) or a stepped ramp of shear rate (B). Dotted lines indicated Herschel-Bulkley modelling of results, with fitting parameters given in Table 3.1.

These results were fitted (dotted lines in Figure 3.6) to the Herschel-Bulkley equation (Equation 3.1), which provides a good model for systems that exhibit both a finite yield stress and subsequent non-Newtonian flow. The equation defines the shear stress (σ) as a function of shear rate (γ) with the constants being the yield stress (σ_o), the consistency (m), and the rate index (n) which reflects the degree of pseudoplastic

(shear-thinning, n<1) or dilatent (shear-thickening, n>1) flow. The fitting parameters for both stress and rate ramps for the bio-ink are given in Table 3.1, showing generally good agreement between the parameters using both methods.

$$\sigma = \sigma_o + m\gamma^n \qquad \textbf{Equation 3.1}$$

Table 3.1: Fitting parameters for Herschel-Bulkley modelling of stress ramp and rate ramp results for bio-ink (average ± standard deviation, n=3).

Parameter	Stress ramp	Rate ramp
Yield stress, σ_o (mPa)	43 ± 4	43 ± 10
Consistency, m (mPa.s)	6.8 ± 1.3	6.2 ± 2.1
Rate index, n	0.90 ± 0.01	0.82 ± 0.05

3.1.4.1 Low-shear behaviour and cell settling

The modelled yield stress value (~43 mPa) was comparable to previous literature values for 0.05% (w/v) GG microgels formed in 200 mM NaCl solution *(298)*. Magnification of a typical stress ramp result in the very low shear region (Figure 3.7) clearly illustrates this yield stress before the initiation of flow in the bio-ink, in contrast to DMEM alone which exhibits instantaneous flow on the application of stress.

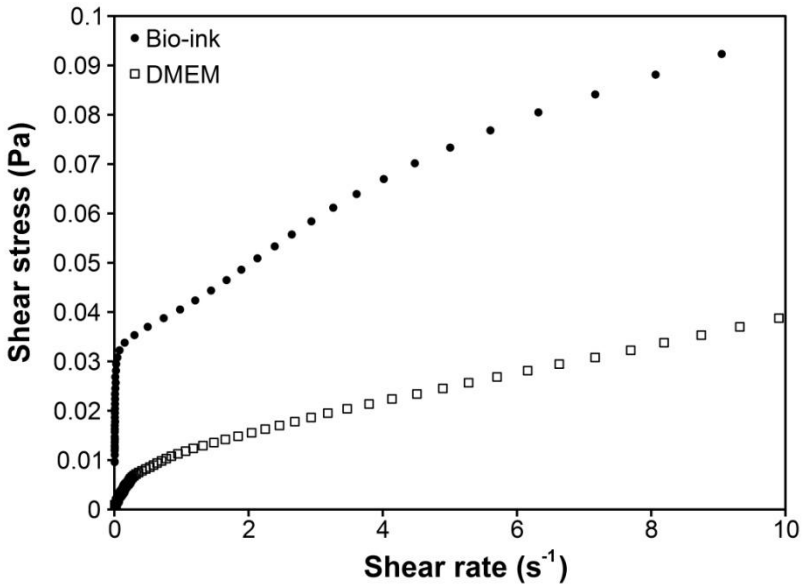

Figure 3.7: Yield behaviour of bio-ink (filled circles), DMEM (open squares) measured by continuous shear stress ramps from rest.

The magnitude of this yield stress has important implications for the stability of a cell suspension. Settling of spherical particles (eg. cells) in a non-Newtonian fluid (eg. bio-ink) can be described by the modified Stoke's law. Importantly, particles are prevented from settling if the following condition is met,

$$\frac{8\Delta\rho g D}{3} \leq \sigma_o \ ,$$

where $\Delta\rho$ is the density difference between particle and the medium, g is gravitational acceleration, D is the diameter of the particle and σ_o is the yield stress of the medium. For C2C12 cells suspended in the bio-ink, the left hand side of the above condition equates to ~ 5 mPa (ρ_{ink} = 0.998 g/cm^3, ρ_{cell} = 1.051 g/cm^3 *(218)*, D_{cell} = 15 µm). The yield stress of ~ 43 mPa imparted to the bio-ink by the microgel structure is therefore theoretically sufficient to maintain a stable cell suspension. Additionally, the yield stress is low enough so as not to hinder the passage of the bio-ink through the printing apparatus. For example, the capillary pressure that drives re-filling of an inkjet printing chamber is ~ 1000 Pa *(320)*. The yield stress measurements presented in Figure 3.6A and Figure 3.7 were taken after the bio-ink had been allowed to equilibrate at rest for 1 min after the cessation of pre-shear at 500 s^{-1}. This shows that a yield stress capable of suspending cells appears relatively quickly after the cessation of shear. This is not surprising given the low GG concentration; previous studies of GG microgels have shown that a lower GG concentration leads to faster structural recovery, because a less complex network needs to be redeveloped after the cessation of shear *(289)*. The development of the yield stress over time is explored further later in this chapter (§3.3.4.1), following addition of surfactants to the bio-ink. If the bio-ink does yield, or in the period immediately after the shear induced breakdown of the microgel structure before the yield stress has redeveloped, the high viscosity of the bio-ink in the low shear region will significantly hinder cell settling. The velocity of a settling cell (v) can also be described by Stoke's law,

$$v = \frac{\Delta p g D^2}{18\eta} \ ,$$

where η is the viscosity of the medium *(218)*. The viscosity of the bio-ink measured in dynamic flow at the shear rates associated with cell settling (1 s^{-1}) is ~ 50 mPa.s. This results in a cell settling velocity of only ~ 8 µm/min, which is about 50 times

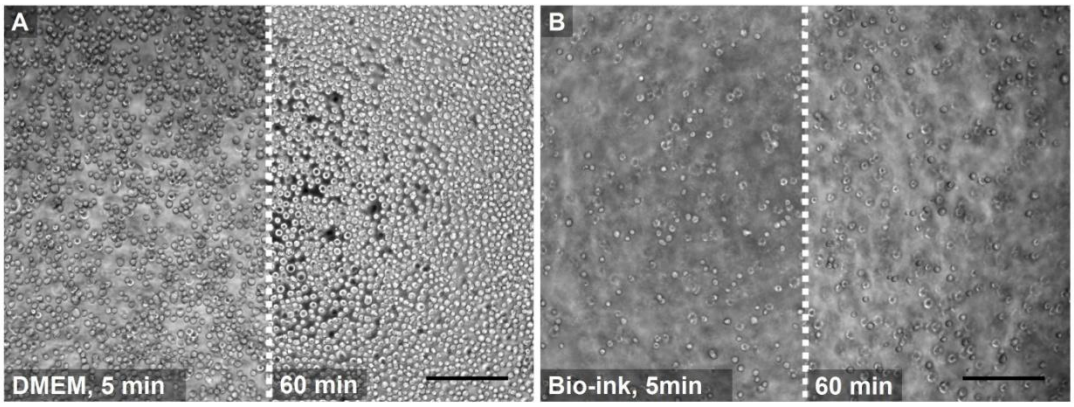

Figure 3.8: C2C12 cells settled on the base of a 96-well plate after 5 or 60 min suspended in either DMEM (A) or bio-ink (B) at $5x10^6$ cells/mL. Scale bars represent 200 µm.

slower than the settling velocity in DMEM alone. Consequently, even if the yield stress did take 1 min to rise above the ~ 5 mPa threshold where settling is prevented, cells would only settle a distance less than their own diameter in this time.

The cell suspending ability of the bio-ink was assessed experimentally with C2C12 cells included at a high concentration ($5x10^6$ cells/mL), which is relevant to application in cell printing. As previously, cells in 100 µL of bio-ink or DMEM were added to the wells of a 96-well plate and the well base imaged over time. Although quantification of settling was not possible due to the high cell density, the images in Figure 3.8 indicate significant settling between 5 and 60 min time points in DMEM, as expected, whereas no settling was observed for cells suspended in the bio-ink.

3.1.4.2 High-shear behaviour and printability

Analysis of the bio-ink viscosity pertaining specifically to printability was provided by stepped ramps of shear rate in the high-shear region (Figure 3.9). The shear rates associated with droplet ejection in drop-on-demand printing techniques are in the order of 10^4-10^5 s^{-1}. We were unable to analyse viscosity at these very high shear rates using our standard rheology equipment; rheological properties in this shear regime are often probed using instruments such as the piezo-axial vibrator (PAV) or torsion resonator (TR) rheometers *(321)* which were unavailable to us. Nonetheless, we were able to characterise viscosity accurately up to a shear rate of 10^3 s^{-1}, as validated using viscosity standards (§2.2.6.3). The viscosity of DMEM at these high shear rates showed a relatively Newtonian response with a viscosity of ~0.9 mPa.s.

The slight increase in viscosity observed with increasing shear is reported to be an artefact caused by Taylor instabilities, or turbulent flow *(307)*. For the bio-ink, the pseudo-plastic shear-thinning behaviour is also evidenced in this shear range. The viscosity of the bio-ink appears to approach a plateau at high shear, with a slightly higher viscosity than DMEM (~1.7 mPa.s at 10^3 s^{-1}). We can assume that only a very slight further reduction in viscosity would be observed at higher shear rates, which is consistent with previous findings that the infinite rate viscosity of microgel suspensions is slightly higher than the viscosity of the surrounding solution *(322)*. Importantly, this low viscosity at high shear rates should enable printing through standard drop-on-demand printing approaches.

This bio-ink, without surfactants, was utilised in microvalve printing experiments (Chapter 4). Any cytotoxic effect of the GG microgels on cells is explored later in this chapter (§3.3.2), alongside assessment of the surfactant-containing bio-ink. Further discussion on the printability of both bio-inks follows at the end of this chapter (§3.4).

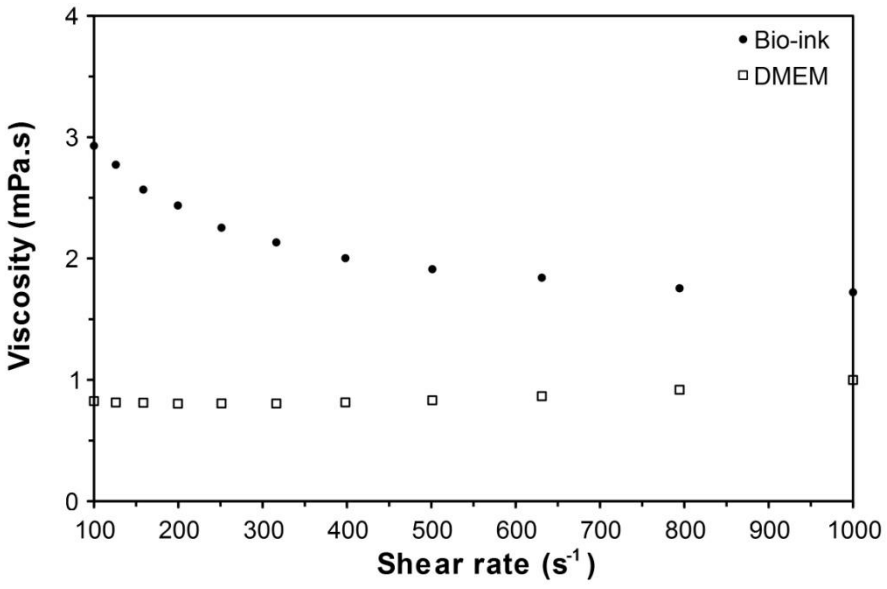

Figure 3.9: Viscosity at high shear rates for bio-ink (filled circles) or DMEM (open squares) measured by stepped ramps of shear rate.

3.2 Surfactants

To optimise the bio-ink for application in inkjet printing, it was necessary to reduce the surface tension. Our target surface tension was ~ 30 mN/m, which is within the optimal range specified for Xaar-126 piezoelectric inkjet print heads. In this section, we highlight the characterisation of several different surfactants in terms of their surface activity and any cytotoxic effect on suspended cells.

3.2.1 Triton X-100 and Tween 20

The first surfactants we investigated were Triton X-100 and Tween 20. These non-ionic surfactants are both commonly employed in routine cell biology work and were readily available in our laboratory. Initial investigations were carried out with these surfactants in cell culture media (DMEM + 10% (v/v) FCS), rather than in the bio-ink, so that their influence on fluid properties and cell responses could first be studied in the absence of other potentially complicating factors (i.e. the GG microgel suspension).

Throughout this chapter, 'surface tension' refers to the liquid-vapour interfacial surface tension as measured using the pendant drop method and the Young-Laplace transformation (§2.2.4). All surface tension measurements are expressed as the mean ± standard deviation ($n \geq 3$). The surface tension of Milli-Q water was tested periodically throughout all measurements to ensure that it remained within experimental error of the known value of 72 mN/m at 25°C. The surface tension of DMEM alone was measured at 72.1 ± 0.4 mN/m which, as expected, is comparable to that of water. DMEM + 10% (v/v) FCS had a lower surface tension of 59.9 ± 1.3 mN/m due to the mild surfactant nature of the added serum.

3.2.1.1 Surface tension

The surface tension of cell culture media as a function of added Triton X-100 or Tween 20 (0 - 0.1% (v/v) surfactant) is displayed in Figure 3.10. The curve for Triton X-100 is typical of micellar surfactants, with a sharp decrease in surface tension up to the critical micelle concentration (CMC), after which the surface tension remains relatively constant with further surfactant addition. We found the CMC to be ~0.2 mM, which is comparable to the CMC supplied by the manufacturer

(0.22-0.24 mM, Sigma). Triton X-100 reduced the surface tension to 31.0 ± 0.04 mN/m at a concentration of 0.1% (v/v); this is also very close to the literature value for the surfactant in water (30 mN/m at 25°C; Dow Chemicals). Addition of Tween 20 induced a more gradual reduction of surface tension. This differs from the literature value of ~0.05 mM for the CMC of the surfactant in water, and suggests interactions between Tween 20 and ionic content or serum in the cell culture media (interactions between Tween 20 and bovine serum albumin are well documented *(323)*). The surface tension of 41.0 ± 0.5 mN/m at 0.1% (v/v) was higher than the literature value (35 mN/m at 20°C, *(323)*), possibly due to these interactions. Nonetheless, it was envisaged that the surface tension reduction afforded by both these surfactants may provide significant improvements in printability, and so we proceeded to investigate the cytotoxicity of both surfactants against the C2C12 cell line.

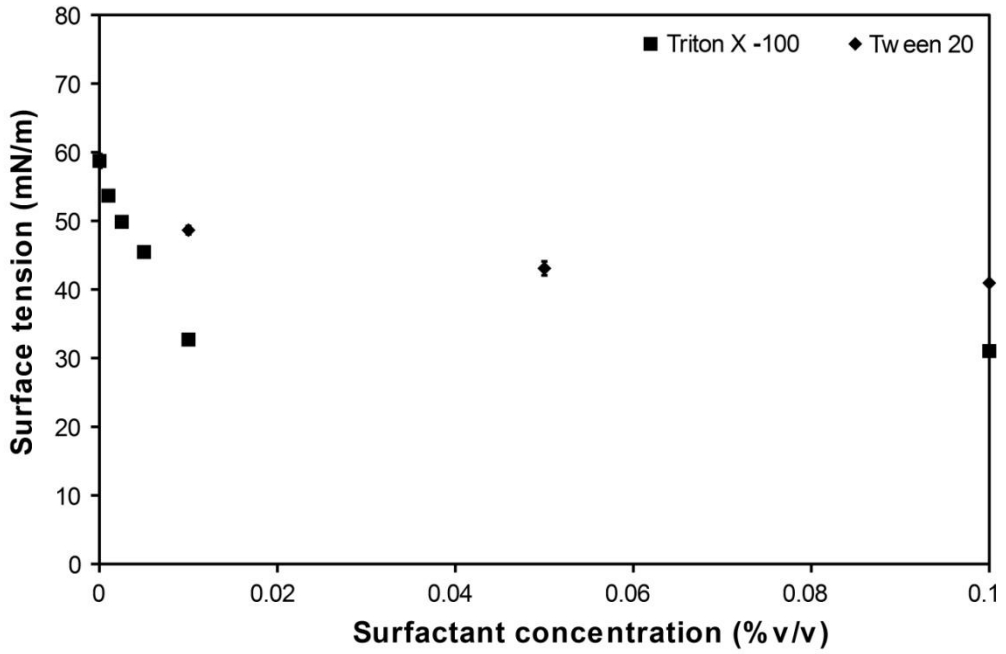

Figure 3.10: Surface tension as a function of surfactant concentration for Triton X-100 (squares) and Tween 20 (diamonds) in DMEM with 10% (v/v) FCS. Error bars represent the standard error of the mean (n≥5).

3.2.1.2 Cell response

C2C12 cells were suspended in cell culture media containing either 0.01% (v/v) Triton X-100 or 0.1% (v/v) Tween 20. These surfactant concentrations were chosen as in each case they represented the lowest concentrations at which the greatest surface tension reduction was achieved. The following results do not, therefore, constitute a direct comparison between the cytotoxicity of the two surfactants, but rather a measure of their ability to satisfy the commensurate requirements of low surface tension and high cell viability. The density of cells in suspension was $2x10^6$ cells/mL, which is comparable to that typically employed in cell printing. Furthermore, cells were exposed to these solutions for time periods appropriate for a typical printing experiment. After exposure, at room temperature, for 30, 60, 90 or 120 min, an aliquot (~ 5000 cells) of each suspension was transferred to a well of a 96-well plate containing 100 µL of cell culture media. This effectively diluted the surfactant 1:40, and is again comparable to the dilution that would take place during cell printing. After 24 hr in culture, cell viability was assessed by live/dead staining.

The results of this exposure experiment are shown in Figure 3.11A. C2C12 cells exposed to either surfactant for 30 min had a slightly lower viability than those exposed to CCM alone, although this was not statistically significant (by the Student's *t*-test). Exposure for longer time periods, however, led to significant cell death. After 60-90 min, the viability of cells exposed to either surfactant was significantly lower than that of controls. Further cell death occurred after 120 min exposure, and at this time point viability was also significantly lower for cells exposed to Tween 20 (0.1% v/v) in comparison with Triton X-100 (0.01% v/v). Representative live/dead stained images (Figure 3.11B-G) clearly demonstrate the progression of cell death for surfactant-exposed cells between 30 and 120 min exposure times. However, in addition to the relatively high viability, cells exposed to surfactants for 30 minutes (Figure 3.11D and F) did not display any clear morphological differences to control cells (Figure 3.11B). Thus, while these surfactants did not appear to be ideal due to their cytotoxicity after longer exposure times, we investigated further and characterised whether cells exposed for only 30 minutes would retain a functional phenotype.

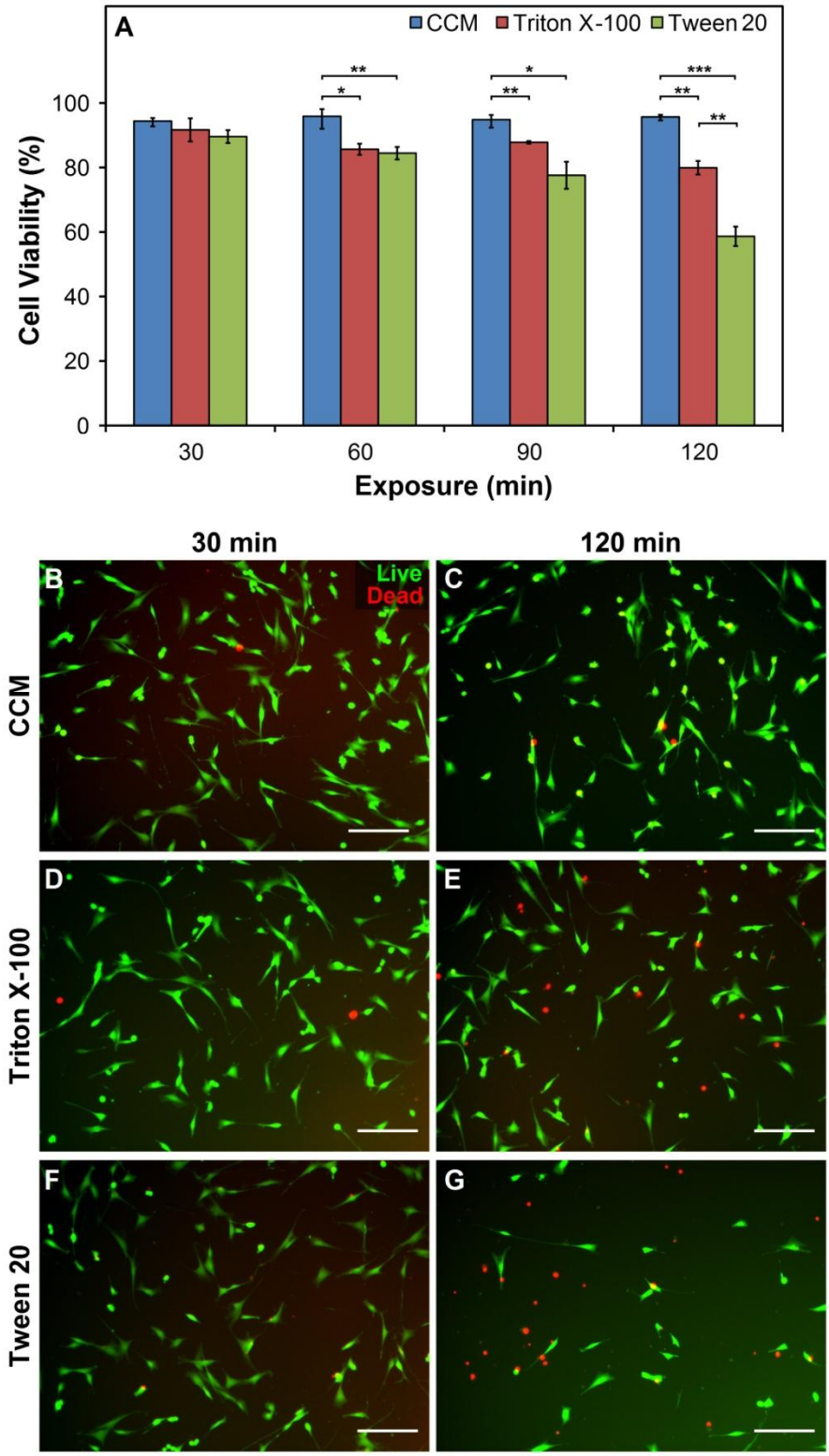

Figure 3.11: (A) Viability, assessed by live(green)/dead(red) staining after 24 hr in culture, of C2C12 cells exposed to DMEM with 10% (v/v) FCS containing no surfactant, 0.01% (v/v) Triton X-100, or 0.1% v/v Tween 20 for 30, 60, 90 or 120 min Error bars represent one standard error of the mean (n≥3). Statistical significance was analysed by a Student's t-test, with significance level as indicated; $P < 0.05$ (*), $P < 0.01$ (**), or $P < 0.001$ (***). **(B-G)** Representative images of live/dead stained cells exposed for either 30 or 120 min. Scale bars represent 200 µm.

The proliferation of cells exposed to surfactants for 30 minutes was assessed by the MTS metabolic assay (§2.1.6) over 48 hr in culture (Figure 3.12). MTS absorbance was normalised to the value obtained after 2 hr in culture to account for any differences in initial cell concentrations. At both 24 and 48 hr time points, the metabolic activity of cells exposed to both surfactants was significantly lower than that of controls. The increase in normalised absorbance between 24 hr and 48 hr was higher for cells exposed to Triton X-100 (~ 3 fold) and Tween 20 (~ 2.7 fold) compared to controls (~ 2 fold), which suggests that after time in culture surfactant-exposed cells may recover their proliferative capacity. After 48 hrs, cells exposed to 0.01% (v/v) Triton X-100 displayed greater proliferation than those exposed to 0.1% (v/v) Tween 20. Although these results suggested that C2C12 cells exposed to these surfactants for 30 min may be not be significantly damaged and recover their normal proliferative capacity over time in culture, the overall loss of metabolic activity and their apparent cytotoxicity after longer exposure times led us to pursue other surfactants.

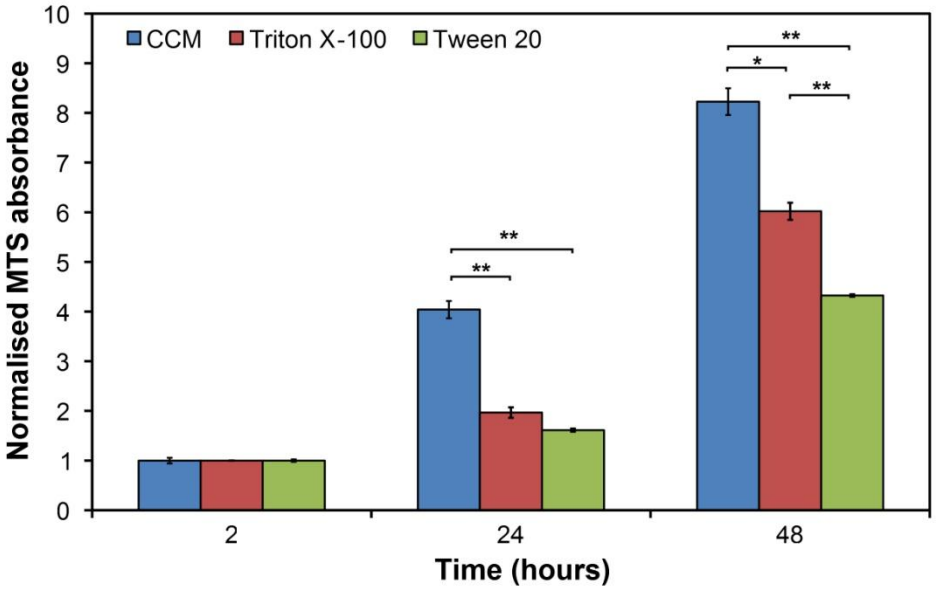

Figure 3.12: C2C12 proliferation, assessed by MTS metabolic assay over 48 hr in culture, for cells exposed to DMEM with 10% FCS containing no surfactant, 0.01% v/v Triton X-100, or 0.1% v/v Tween 20 for 30 minutes. Error bars represent one standard error of the mean (n≥3). Statistical significance was analysed by a Student's t-test, with significance level as indicated; $P < 0.05$ (*), $P < 0.01$ (**).

3.2.2 P188 and Novec FC4430

An extensive literature search was conducted in an attempt to identify surfactants which could provide an adequate reduction in surface tension without cytotoxic effects. This search led us to select two surfactants for further investigation. This section firstly outlines the properties of these two surfactants that warranted their selection before presenting results of surface tension and cell response experiments.

The first surfactant identified was Poloxamer 188 (P188). Poloxamers are a family of non-ionic triblock copolymers comprising a central hydrophobic poly(propylene oxide) (PPO) core flanked by two hydrophilic chains of poly(ethylene oxide) (PEO) (Figure 3.13). They are also known by the trade names Pluronic® and Lutrol®. The number nomenclature for Poloxamers defines their structure; the first two numbers (i.e. 188) multiplied by 100 give the molecular weight of the PPO core (i.e. 18x100 = 1,800 $gmol^{-1}$) while the last number (i.e. 188) multiplied by 10 gives the percentage of PEO content by mass (i.e. 8x10 = 80% w/w PEO).

It has been known for over 50 years that P188 can protect cells from fluid-mechanical damage in agitated and aerated cell cultures *(324)*, and it has been proposed that this protective effect could be due to either biological (enhanced membrane integrity) or physical (reduced shear forces and bubble break-up) factors *(324, 325)*. More recent work has elucidated mechanisms by which P188 was shown to insert into perforated cell membranes, restore membrane integrity, and then itself be excluded from the membrane once repair is completed *(326, 327)*. This makes it suitable to protect and repair cells exposed to high shear forces. P188 has been shown to enhance the viability of skeletal muscle *(328, 329)* and neuronal *(330)* cells

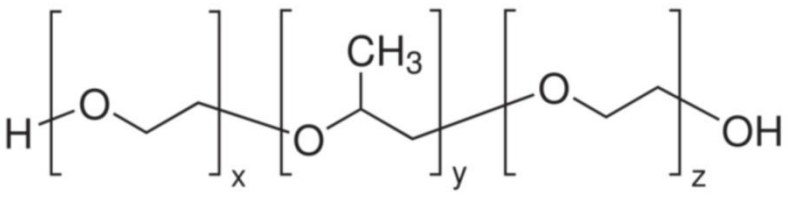

Figure 3.13: Structure of the Poloxamer family of non-ionic block copolymers, PEO-PPO-PEO. For Poloxamer 188, $y = 31$ and $x+z = 164$.

injured by mechanical forces, electropermeabilisation or high-dose irradiation. P188 is therefore of great interest in cell printing applications, not only for its surfactant properties and biocompatibility, but also its ability to protect cells from injury. Parsa and co-workers *(214)* used P188 as an additive to improve the droplet formation in inkjet cell printing, but while they showed that P188 did not decrease the viability or proliferation of cells in culture, they did not demonstrate a protective effect of P188 on printed cells.

The second surfactant selected was a non-ionic polymeric fluorinated surfactant (fluorosurfactant) sold under the trade name Novec™ FC4430 (3M™). The exact structure of this surfactant is proprietary, but we know from literature that it is a fluoroaliphatic ester *(331, 332)*. This surfactant was chosen on the basis of literature suggesting that fluorosurfactants possess both high surface activity and low cytotoxicity. The high surface activity is attributed to strong hydrophobic interactions and low van der Waals interactions as a result of the fluorinated chains *(333)*. There is a growing body of evidence that increasing the degree of surfactant fluorination decreases cytotoxicity in comparison with hydrocarbon analogues *(334)*, and this could be due to a number of factors including a decreased propensity for the removal of membrane proteins *(335)*. This combination of properties has been exploited previously in biological applications. For example, fluorosurfactant polymer-peptide complexes have been shown to support endothelial cell attachment and proliferation when used to promote endothelialization without inducing thrombosis in small-diameter vascular grafts *(336, 337)*. Fluorosurfactants have also been utilised to enhance the viability of cells encapsulated in micro-droplets for micro-fluidic drug screening applications *(338, 339)*. To our knowledge, however, fluorosurfactants have not previously been utilised in a cell printing application.

3.2.2.1 Surface tension in DMEM

In initial experiments with these surfactants, they were added to DMEM without serum. This was in order to avoid any potentially complicating interactions with serum proteins and to ensure that the results were more reflective of surfactant addition to the bio-ink which is based on serum-free DMEM. The surface tension of DMEM as a function of added P188 and Novec FC-4330 is displayed in Figure 3.14. Results are displayed for a concentration range of 0-0.1% (v/v) to highlight the

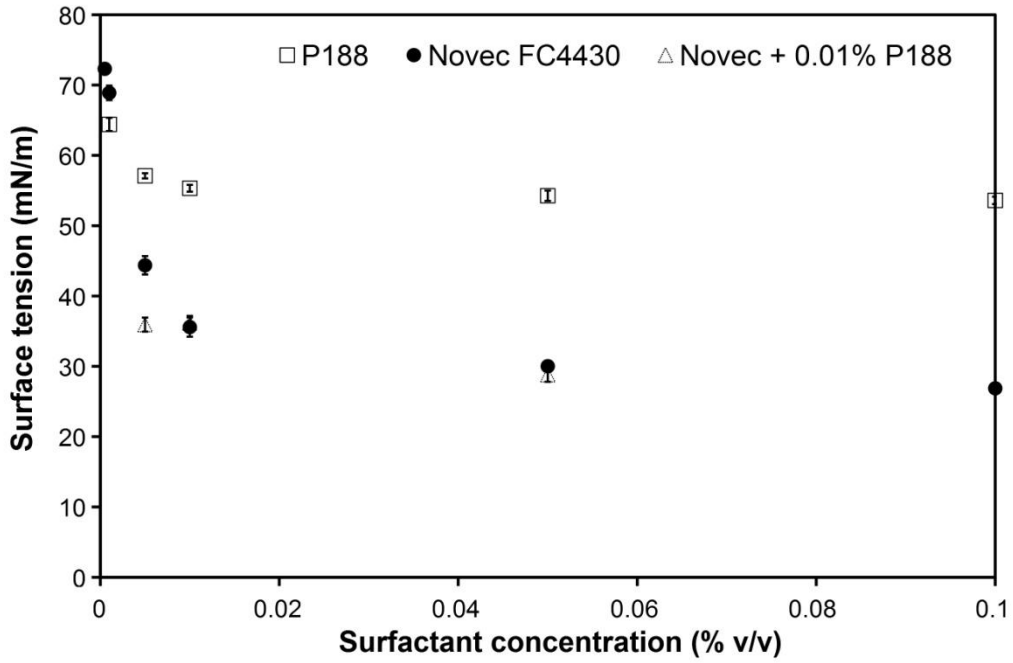

Figure 3.14: Surface tension as a function of surfactant concentration for P188 (open squares) and Novec FC4430 (closed circles) in DMEM. Open triangles indicate surface tension as a function of Novec FC4430 concentration with a fixed P188 concentration of 0.01% v/v. Where open triangles are not visible at a given concentration, they overlap with closed circles. Error bars represent one standard error of the mean (n≥5).

Triblock copolymer surfactants, unlike conventional surfactants, do not form micelles at a distinct CMC but rather aggregate over a broad concentration range. Depending on the method of measurement, the reported limiting aggregation concentration (LAC, the point at which the surfactant reaches saturation) can vary widely *(326)*. Our result is comparable to that obtained from previous measurements of surface activity at the air-water interface *(340)*. The surface tension at 0.1% (v/v) P188 (53.6 ± 0.5 mN/m) was slightly higher than that supplied by the manufacturer for a 0.1% (v/v) solution in water at 25°C (50 mN/m), which could be an effect of the ionic content of DMEM. Addition of Novec FC-4430 resulted in a more pronounced reduction in surface tension. The plateau behaviour was similar to that observed for P188; the surface tension reduced to 30.0 ± 0.4 mN/m at a concentration of ~ 0.05% (v/v) although it continued to decrease gradually to a value of 21.8 ± 0.6 mN/m at 1% (v/v). The lowest surface tension was close to that supplied by the manufacturer for the surfactant in distilled water (20 mN/m at 0.5% (v/v)), although they presented a clear lower plateau at a surfactant concentration of only ~ 100 ppm (~ 0.01%). As for P188, the observed differences could result from the ionic content of DMEM.

Importantly, the target surface tension for the bio-ink (30 mN/m) was reached by addition of the Novec FC-4430 fluorosurfactant at a concentration of 0.05% v/v. Although P188 did not exhibit adequate surface activity alone, it remained of interest as a cell-protective additive to the bio-ink formulation. We therefore also investigated the surface tension when both surfactants were added to DMEM together. Novec FC-4430 was added at a range of concentrations to DMEM containing a fixed concentration of 0.01% (v/v) P188 (Figure 3.14). At a Novec FC-4430 concentration of 0.005% (v/v), the surface tension was lower than for either surfactant alone; this apparent synergistic effect could be due to the ability of surfactants to co-exist at the liquid-air interface *(323)*. At higher concentrations of Novec FC-4430, the surface tension matched closely with this surfactant alone, indicating that it replaced the less surface active P188 at the surface *(323)*. This suggested that blends of the two surfactants could be utilised without compromising the surface tension reduction afforded by Novec FC-4430.

3.2.2.2 Cell response in DMEM

The effect of these surfactants on cells was initially investigated by exposing C2C12 cells to DMEM containing individual or combined surfactants at a range of concentrations for either 1 or 2 hr, then assessing cell viability after 2 hr (initial) and 1 day in culture using live/dead cell staining. For simplicity, only data for 0.05% (v/v) Novec FC-4430 or 0.1% (v/v) P188, or a blend of the two surfactants at these concentrations, is shown (Figure 3.15A). Exposure to 0.01% (v/v) Triton X-100 was used to enable comparison to be made to the results obtained previously for this surfactant. Initially, the viability of cells in a single well only per condition was measured in order to give a preliminary indication of any surfactant cytotoxicity in DMEM prior to investigations of cell responses to these surfactants when included in the bio-ink. In good agreement with the results presented previously in this section, cell viability decreased after exposure to Triton X-100 and was lower after 2 hr exposure (~ 78%) in comparison with 1 hr exposure (~ 86%) to this surfactant. The viability continued to decrease over 24 hr in culture. Conversely, exposure to P188 and Novec FC-4430, or a combination of these surfactants, for 1 or 2 hr did not result in any reduction in cell viability when measured after 2 hr or 1 day in culture. The surface tensions of the solutions used in these exposure studies were measured separately, and they agreed well with those obtained previously (Figure 3.14). This

confirmed that cells were exposed to solutions with a low surface tension and in the case of Novec FC-4430, and Novec/P188 combined, this was the target surface tension for the bio-ink. Representative live/dead stained images of cells exposed for 2 hr, after 1 day in culture (Figure 3.15B-E) revealed no clear morphological differences between cells exposed to surfactants when compared to those exposed to DMEM alone.

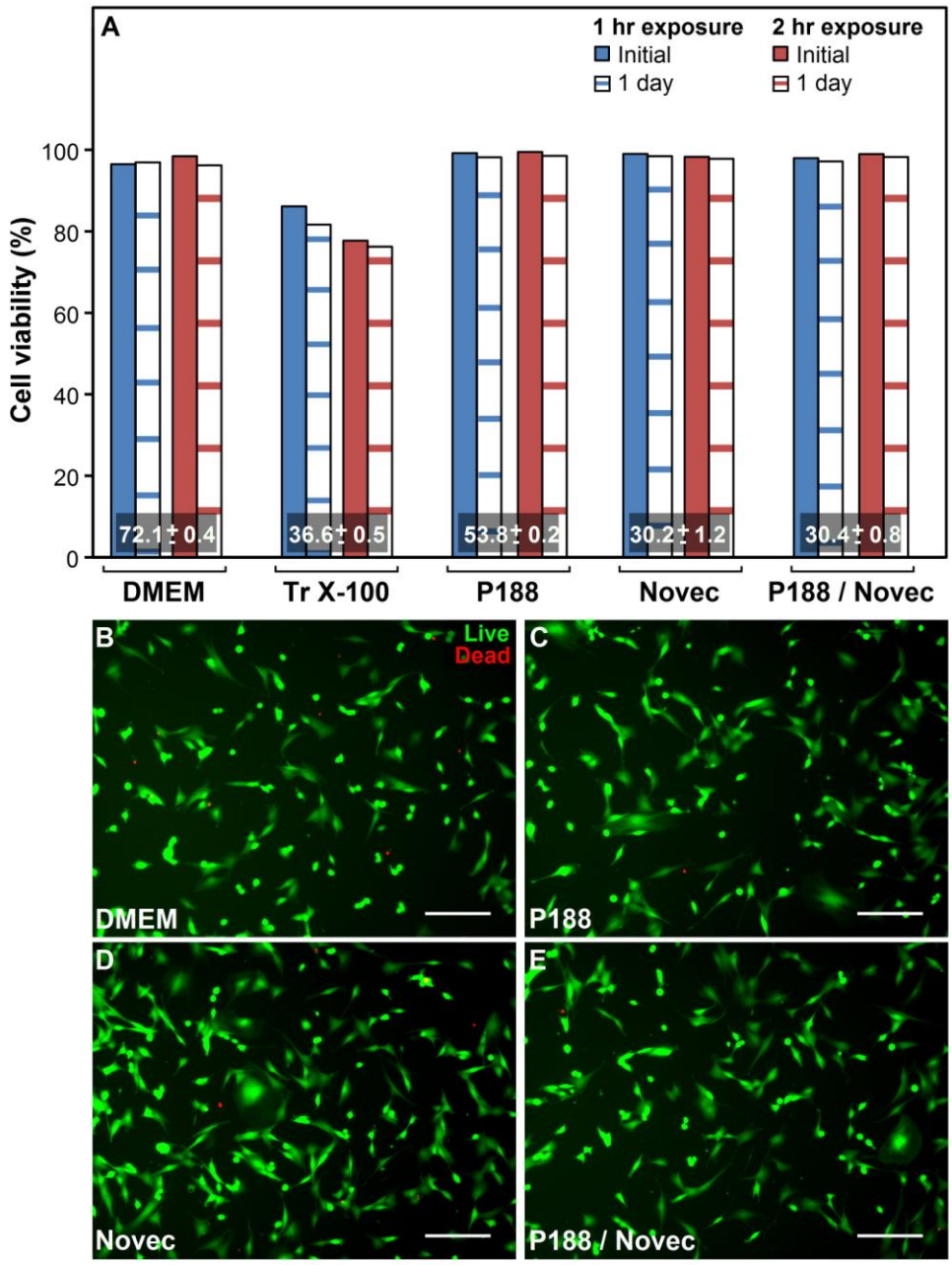

Figure 3.15: (A) Viability, assessed by live/dead staining after 2 hr (Initial) or 1 day in culture, of C2C12 cells exposed for either 1 or 2 hr to DMEM alone, or containing surfactants as indicated. Surfactant concentrations were 0.01% (v/v) Triton X-100, 0.1% (v/v) P188 and 0.05% (v/v) Novec FC4430. Numbers at base of each data set indicate the surface tension of actual solutions used in exposure experiments (mean ± standard deviation, n=3, units mN/m). **(B-E)** Representative live/dead stained images of cells after 1 day in culture, after exposure to DMEM alone or containing surfactants as indicated for 2 hr. Scale bars represent 200 µm.

3.3 Surfactant-containing bio-ink

3.3.1 Surface tension

The initial results suggested that our target surface tension could be achieved without cytotoxicity. We proceeded to measure the surface tensions and cell responses when these surfactants were included in the bio-ink formulation. Novec FC-4430 and P188 were added at a range of concentrations to 0.05% (w/v) GG microgel suspensions in DMEM. The surface tension results are displayed in Figure 3.16. The surface tension values with P188 added at 0-0.1% (v/v) matched very closely with the values for this surfactant in DMEM. In the case of Novec FC-4430, at concentrations below 0.05% (v/v) the measured surface tension values were slightly higher than for the equivalent surfactant concentrations in DMEM alone. This is suggestive of some interaction between the GG microgels and Novec FC-4430 at concentrations below the CMC. However, at concentrations ≥ 0.05% (v/v), the measured surface tensions matched very closely with the corresponding values in DMEM. We again investigated the surface tensions when both surfactants were included together. As before, the concentration of Novec FC-4430 was varied with a fixed P188 concentration, which in this case was 0.1% (w/v) (1 mg/mL). This concentration was chosen as it is at the lower end of the range of P188 concentrations reported previously in cell membrane sealing applications *(326)*. For all combinations studied here, the surface tension was equivalent to that for the most surface active component under the given condition, e.g. for < 0.01% (v/v) Novec FC-4430 the surface tension matched that for 0.1% (v/v) P188 alone, while for ≥ 0.01% (v/v) Novec FC-4430 the surface tension matches that for Novec FC-4430 alone.

The effect of cell addition on the surface tension was investigated by suspending fixed C2C12 cells in the surfactant-containing bio-ink at a concentration of $5x10^6$ cells/mL. The inclusion of cells resulted in a small increase in surface tension from 30.3 ± 0.6 mN/m to 31.2 ± 0.5 mN/m (n = 5), which could however have been caused by dilution of the surfactant-containing bio-ink with the small amount of residual DMEM associated with the cell pellet prior to re-suspension.

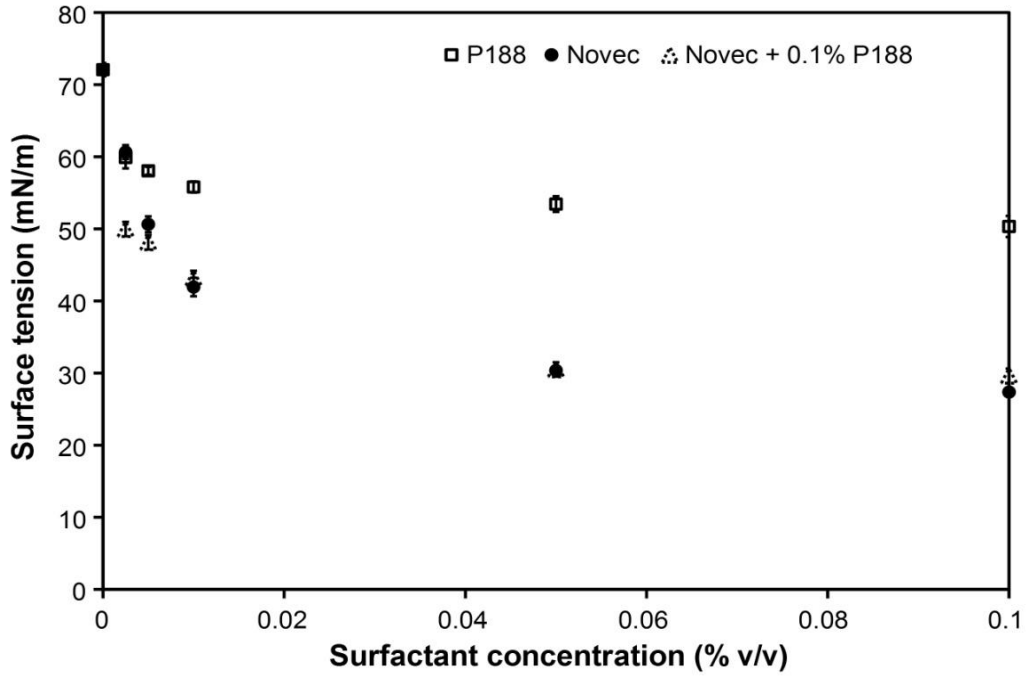

Figure 3.16: Surface tension as a function of surfactant concentration for P188 (open squares) and Novec FC4430 (closed circles) in bio-ink (0.05% (w/v) GG microgel suspension in DMEM). Open triangles indicate surface tension as a function of Novec FC4430 concentration with a fixed P188 concentration of 0.1% (v/v). Error bars represent one standard error of the mean (n≥5).

3.3.2 Cell response

Having confirmed that the bio-ink (0.05% w/v GG microgel suspension in DMEM) containing 0.05% v/v Novec FC-4430 and 0.1% v/v P188 had an appropriate surface tension (30.5 ± 0.2 mN/m) for inkjet printing, we then proceeded to probe cell responses to this complete surfactant-containing bio-ink formulation. Alongside these experiments the cell response to bio-ink without surfactants was also investigated to determine if the GG microgel suspension exhibited any cytotoxic effect in the absence of added surfactants. The response of both C2C12 and PC12 cells was investigated, as we intended to print both these cell types in inkjet printing experiments (Chapter 5). Cells were exposed to DMEM (control) and to bio-ink both with and without the above surfactants for 1 or 2 hr, and viability was assessed by live/dead staining after 2 hr in culture post-exposure. Bio-ink containing Triton X-100 was again used as a negative control, although in this case it was included at 0.05% (v/v) in order to match the concentration of Novec FC-4430 in the bio-ink formulation. Interestingly, exposure to bio-ink with Triton X-100 for even 1 hr resulted in significant cell death for both C2C12 and PC12 cells (Figure 3.17). It is

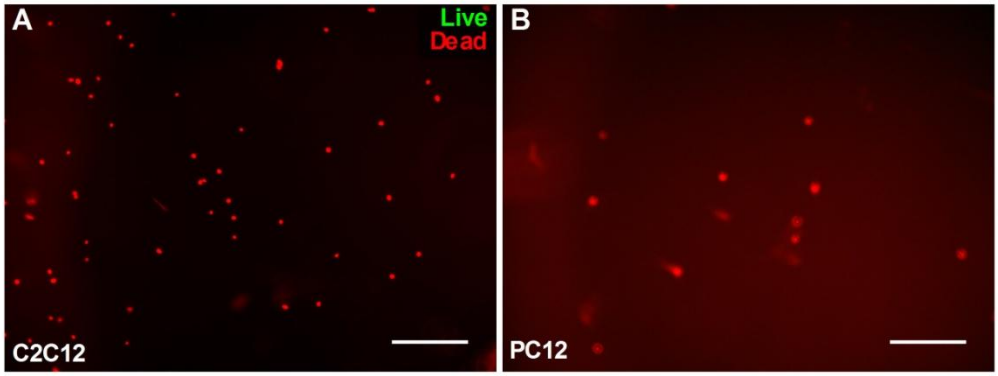

Figure 3.17: Representative images of live(green)/dead(red) stained C2C12 (A) and PC12 (B) cells exposed to bio-ink containing 0.05% (v/v) Triton X-100 for 1 hr and cultured for 2 hrs. Scale bars represent 200 µm.

not clear whether this accelerated cell death (in comparison with the results in §3.2.2.2) was a result of the higher Triton X-100 concentration or because the cells were suspended in the bio-ink and thus had greater exposure to the surfactant without settling. Nonetheless, this reinforces the need for non-cytotoxic surfactants.

The viability of C2C12 and PC12 cells exposed to the bio-ink formulations is presented in Figure 3.18. The cell viability was greater than 95% for all conditions, after both 1 hr and 2 hr exposure times. There was no statistically significant difference between the viability of C2C12 cells exposed to DMEM, or the bio-ink both with and without added surfactants. For PC12 cells, after 1 hr exposure, cells exposed to the surfactant-containing bio-ink had a significantly higher viability than controls, while after 2 hr exposure the viability was significantly higher than controls for cells exposed to both bio-ink formulations. Representative images of live/dead stained C2C12 cells (Figure 3.18B and C) exposed to DMEM (control) or the bio-ink with surfactants display no clear morphological differences. The morphology of PC12 cells also appeared unchanged in comparison with controls (Figure 3.18D and E), although the control cells had formed relatively large multi-cellular aggregates while this level of aggregation was not observed in the bio-ink.

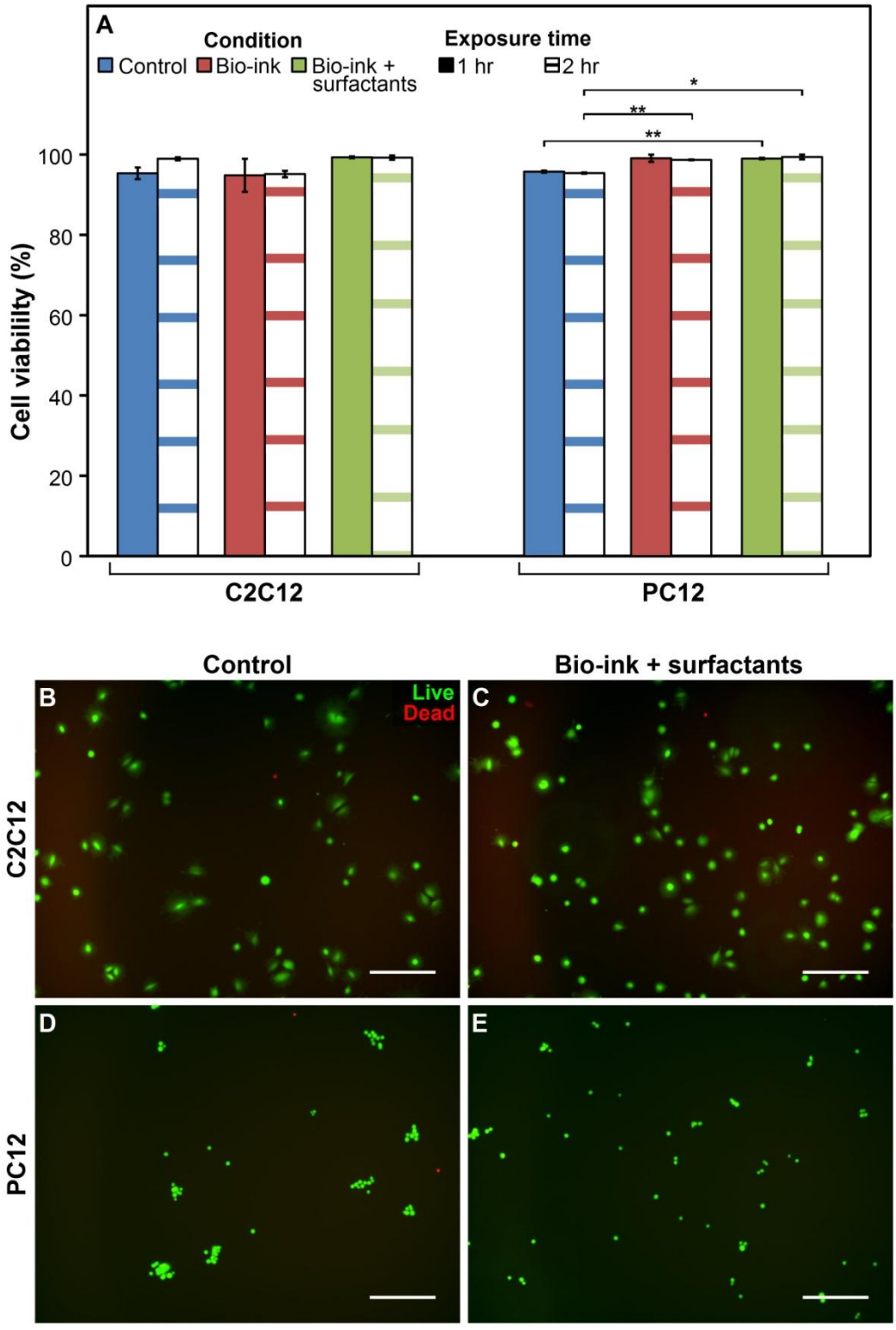

Figure 3.18: (A) Viability, assessed by live/dead staining after 2 hr in culture, for C2C12 (left) and PC12 (right) cells exposed to DMEM alone (blue), bio-ink without surfactants (red) or bio-ink containing 0.1% v/v P188 and 0.05% v/v Novec FC4430 surfactants (green) for 1 hr (solid) or 2 hr (striped). C2C12 cells were suspended at $6x10^6$ cells/mL while PC12 cells were suspended at $2x10^6$ cells/mL. Error bars represent one standard error of the mean ($n \geq 3$). Statistical significance was analysed by a Student's t-test, with significance level as indicated; $P < 0.05$ (*), $P < 0.01$ (**). **(B-E)** Representative images of live(green)/dead(red) stained cells exposed for 2 hr, taken after 2 subsequent hrs in culture. Scale bars represent 200 µm.

These results suggest that both bio-ink formulations had no detrimental effect on the viability of C2C12 or PC12 cells after exposure for up to 2 hr. We did not test exposure times longer than this, as we expected typical cell printing experiments to take no longer than 2 hr. The slight enhancement of PC12 cell viability when suspended in both bio-inks in comparison with control cells is likely a result of the maintenance of a single cell suspension in the bio-inks as opposed to cells in DMEM which aggregated (Figure 3.18D) and settled, and thus had to be re-suspended intermittently. The potential protective effect of the added P188 surfactant on cells was investigated in inkjet cell printing experiments detailed in Chapter 5, in order to assess its effect under real shear conditions experienced during printing (§5.3.2).

Further characterisation of the phenotypic response of C2C12 and PC12 cells exposed to the bio-ink with P188 and Novec FC-4430 surfactants was conducted alongside inkjet cell printing experiments (Chapter 5). Throughout the duration of a typical printing experiment, which usually took 30-60 min, non-printed cells were exposed to the surfactant-containing bio-ink, or to DMEM alone as a control. Subsequently, the proliferation and differentiation of these two non-printed cell conditions, and that of printed cells, was assessed. These results are presented in this chapter, indicating the effect of the surfactant-containing bio-ink on cell responses. In Chapter 5, the proliferation and differentiation of printed cells against cells exposed to the surfactant-containing bio-ink are compared (§5.3.1). This indicates the affect of the printing process on cell responses. It should be noted that these results were, however, obtained in the same experiments.

Figure 3.19 shows the analysis of cell proliferation, by the MTS metabolic assay (§2.1.6) over 48 hr in culture for both C2C12 and PC12 cells exposed to bio-ink with P188 and Novec FC-4430 surfactants or DMEM alone (control) throughout the time taken for a typical inkjet cell printing experiment. As in previous experiments, MTS absorbance was normalised to the 2 hr time point to account for any differences in initial cell numbers. There was no statistically significant difference (Student's *t*-test) in the MTS absorbance of exposed cell populations at either the 24 or 48 hr time point for both cell types in comparison with controls.

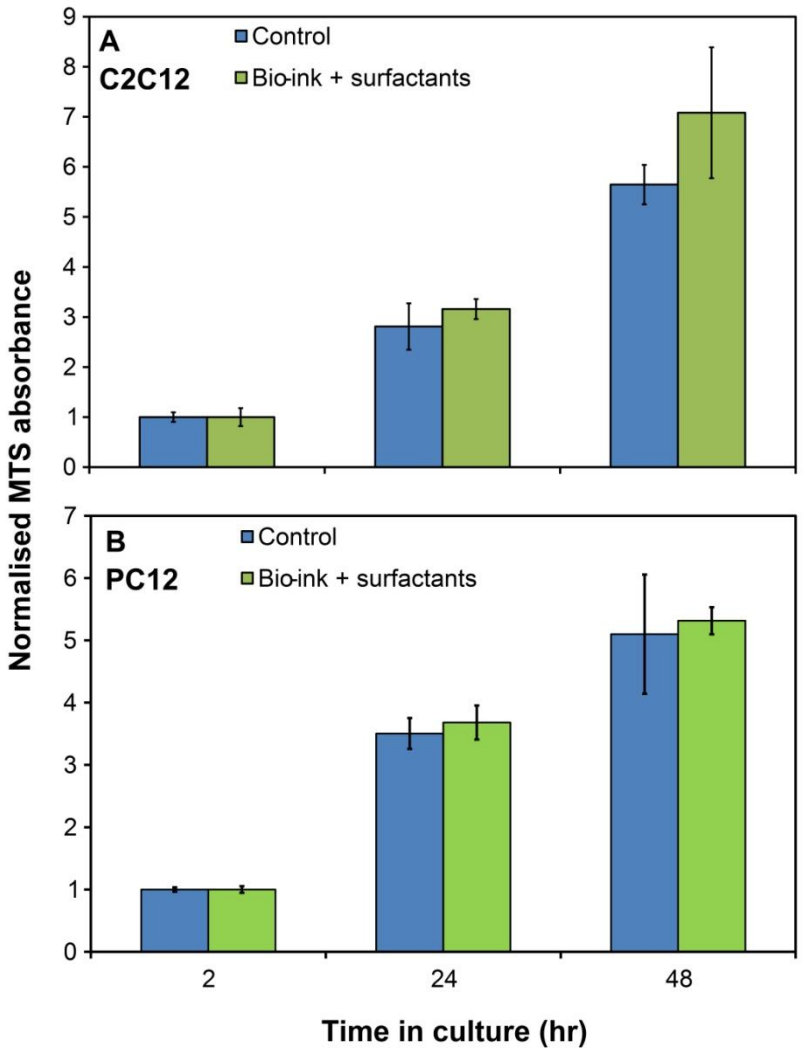

Figure 3.19: Proliferation, assessed by the MTS metabolic assay over 48 hr in culture, of C2C12 (A) and PC12 (B) cells exposed to the bio-ink with P188 and Novec FC-4430 surfactants during a typical cell printing experiment, in comparison with control cells exposed to DMEM alone. Error bars represent one standard error of the mean (n≥3).

Figure 3.20 shows fluorescence images of differentiated C2C12 and PC12 cells that had been exposed to either the bio-ink with surfactants or DMEM alone (control) for the duration of a typical inkjet cell printing experiment. C2C12 cells were subsequently cultured under differentiation conditions for 6 days before fixing and immunostaining against desmin (§2.1.4.3). PC12 cells were cultured under differentiation conditions for 5 days before fixing and staining F-actin filaments with phalloidin (§2.1.4.4).

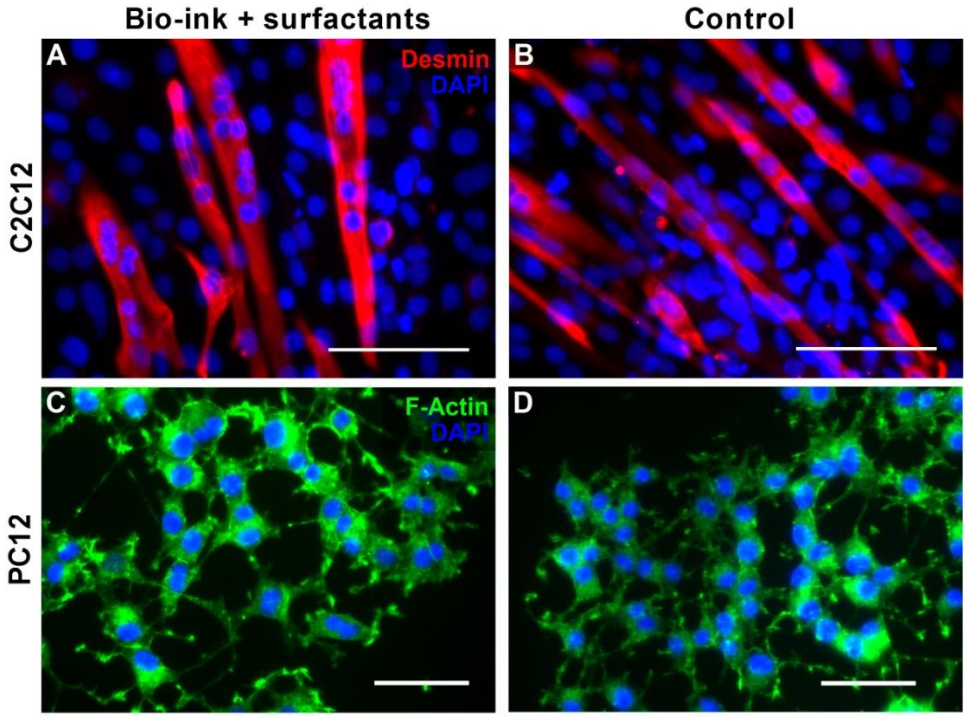

Figure 3.20: Fluorescence microscope images of C2C12 (A, B) or PC12 (C, D) cells exposed to bio-ink with P188 and Novec FC-4430 surfactants (A, C) or DMEM alone (B, D) for the duration of a typical cell printing experiment. Cells were subsequently cultured under differentiation conditions for 6 days (C2C12) or 5 days (PC12). C2C12 cells were immunostained against the protein desmin (red), and F-actin filaments in PC12 cells were stained with phalloidin (green). For both cell types, nuclei were counterstained with DAPI (blue). Scale bars represent 100 µm (A, B) or 50 µm (C, D).

C2C12 cells exposed to both solutions differentiated to form multinucleated myofibres expressing the skeletal muscle protein desmin. There were no obvious differences in the density or morphology of fibres in the two cell populations. Similarly, staining of F-actin filaments in differentiated PC12 cells revealed no clear morphological differences between the cell populations, with a similar density and length of neurites, and extent of neurite branching. These results suggest that exposure to the bio-ink formulation did not adversely affect the capacity of either C2C12 or PC12 cells to differentiate.

These results provide a good indication that exposure to the bio-ink formulation does not adversely affect the function of these cell lines. Similar results are presented in Chapter 4 (§4.3) and Chapter 5 (§5.3) to focus on the affects of microvalve and inkjet printing processes, respectively. However, it is acknowledged that other biological processes, including RNA synthesis and protein expression, could be impacted and that these are not analysed in this work. These additional analyses, as well as assessment of other cell types (primary cells, stem cells), are therefore suggested avenues for future work.

3.3.3 Structure

It was then important to determine whether addition of P188 and Novec FC-4430 surfactants to the bio-ink had a significant effect on the structure of the microgel network. Any increase in particle size as a result of surfactant addition could affect passage through printer nozzles and other changes to the network structure could result in altered rheology. We stained and imaged the bio-ink before and after addition of surfactants (0.05% (v/v) Novec FC-4430 and 0.1% (v/v) P188) with DAPI (§2.2.3). Furthermore, in order to confirm that the addition of DAPI did not alter the microgel network and therefore provide an inaccurate picture of its structure, we employed a second staining method using a black pigment ink (Derivan ink) (§2.2.3). The black pigment particles in the ink freely mixed through the bio-ink but were excluded from the microgel particles. This provided a negative-contrast image of the structure of the microgel particles. A comparison of the bio-ink structure stained using DAPI or the pigment ink before, and after, addition of surfactants is provided in Figure 3.21. The results suggest that surfactant addition had minimal effect on the GG microgel structure of the bio-ink. The samples stained with the pigment ink exhibited a very similar structure to those stained with DAPI, supporting the accuracy of the structure reflected by each method. Higher magnification images of both bio-inks, stained with the pigment ink, provide further evidence that the GG microgel particles were irregular and elongated with dimensions in the 5 - 50 µm range (Figure 3.22).

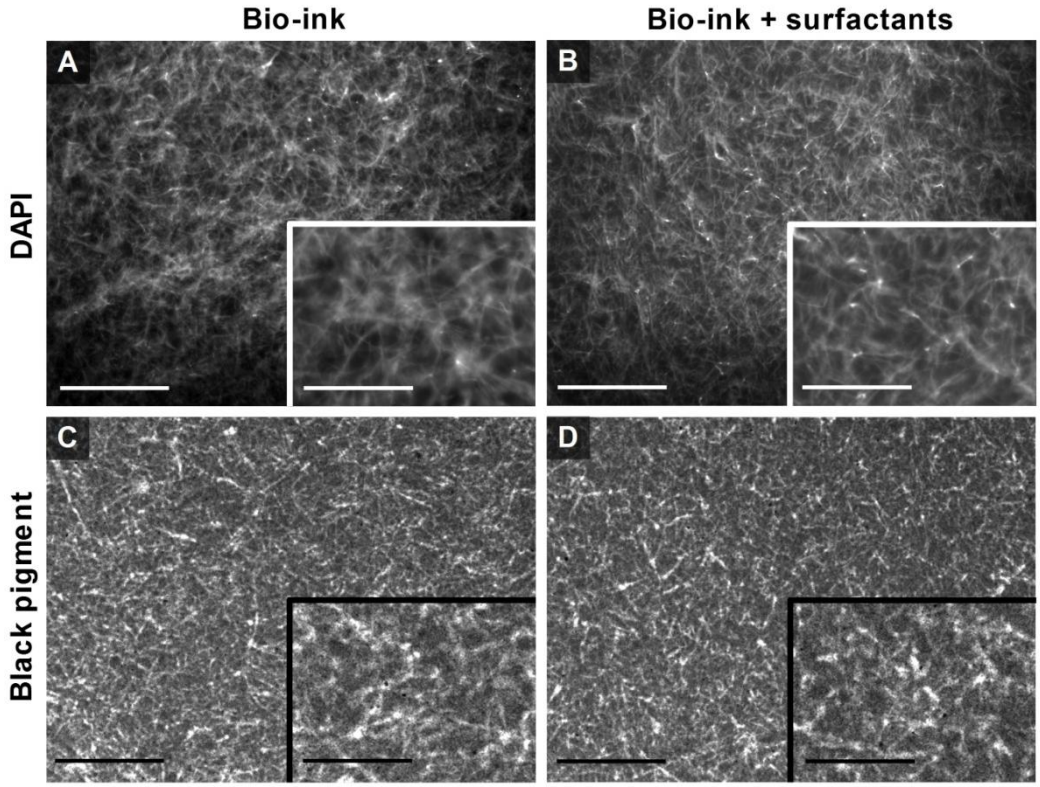

Figure 3.21: Structure of bio-ink without (A, C) or with (B, D) P188 and Novec FC-4430 surfactants stained with either DAPI (A, B) or black pigment ink (C, D). Scale bars represent 200 µm or 100 µm (insets).

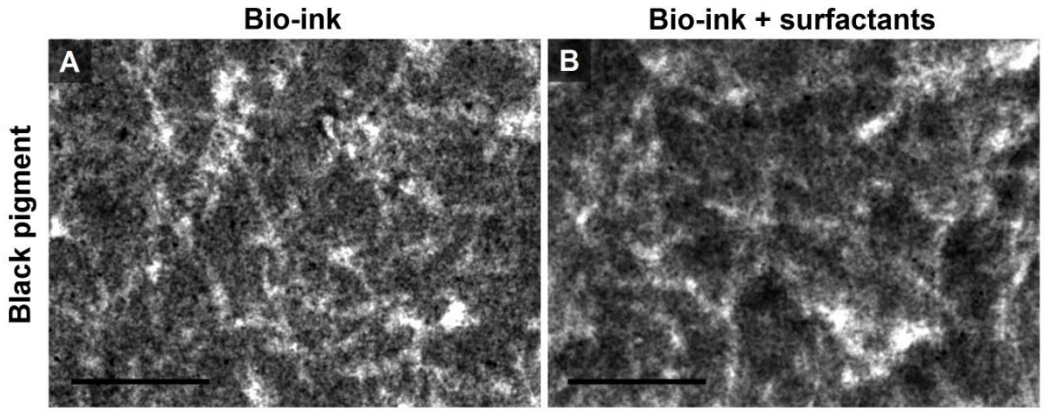

Figure 3.22: High magnification images of bio-ink structure without (A) and with (B) surfactants stained with pigment ink. Scale bars represent 50 µm.

3.3.4 Rheology

The effect of the surfactants on the rheology of the bio-ink was then assessed. The shear stress and viscosity as a function of shear rate from 0-100 s^{-1} (measured by a continuous ramp of shear stress from rest) is shown in Figure 3.23. The response was very similar to that observed for the bio-ink without surfactants (Figure 3.6), exhibiting yield followed by shear thinning behaviour. The results were also fit using the Herschel-Bulkley equation (Equation 3.1), giving the parameters listed in Table 3.2 in comparison with those previously obtained from shear stress ramps of the bio-ink without surfactants. The addition of the surfactants resulted in a small, but statistically insignificant (P=0.3), decrease in the modelled yield stress which is highlighted by a direct comparison of the yield behaviour for typical measurements of the bio-ink both with and without surfactants in Figure 3.24. This could be attributed to surfactant disruption of the inter-particle interactions that produce the yield stress, however the effect is minimal. The consistency term is larger for the bio-ink with surfactants, which is indicative of an increase in viscosity. The rate index term also suggests slightly more pronounced shear-thinning behaviour with surfactant addition. These differences are explored further in the following sections.

Table 3.2: Fitting parameters for Herschel-Bulkley modelling of stress ramp results for bio-ink with and without P188 and Novec FC-4430 surfactants (average ± standard deviation, $n \geq 3$).

Parameter	Bio-ink	Bio-ink + surfactants
Yield stress, σ_o (mPa)	43 ± 4	38 ± 6
Consistency, m (mPa.s)	6.8 ± 1.3	11.6 ± 2.4
Rate index, n	0.90 ± 0.01	0.84 ± 0.03

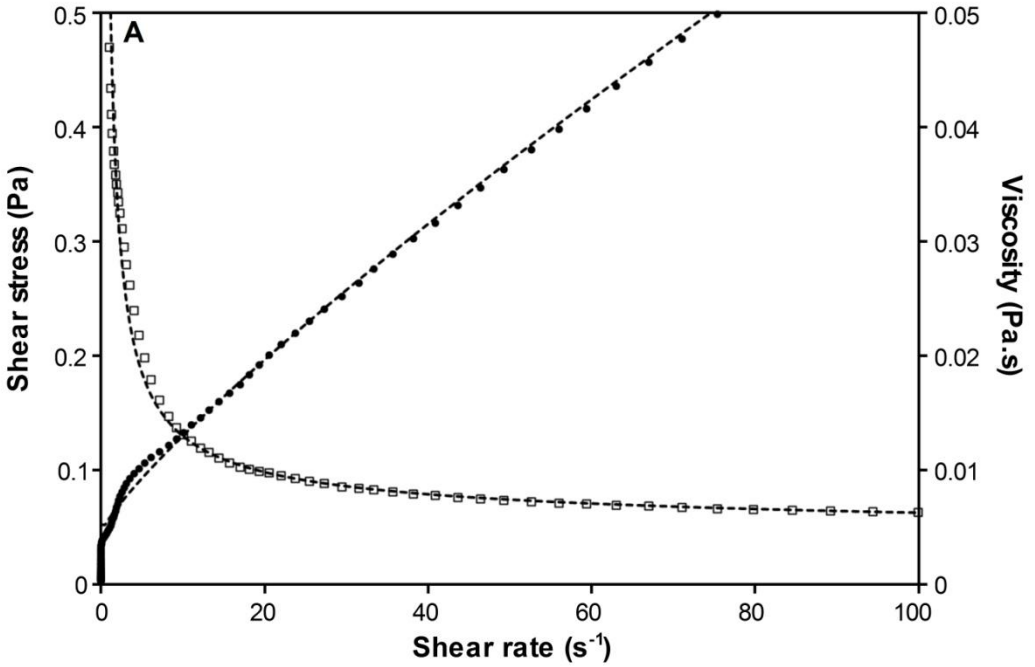

Figure 3.23: Apparent shear stress (filled circles) and viscosity (empty squares) as a function of shear rate for surfactant-containing bio-ink measured using a continuous ramp of shear stress. Dotted lines indicated Herschel-Bulkley modelling of results, with parameters given in Table 3.2

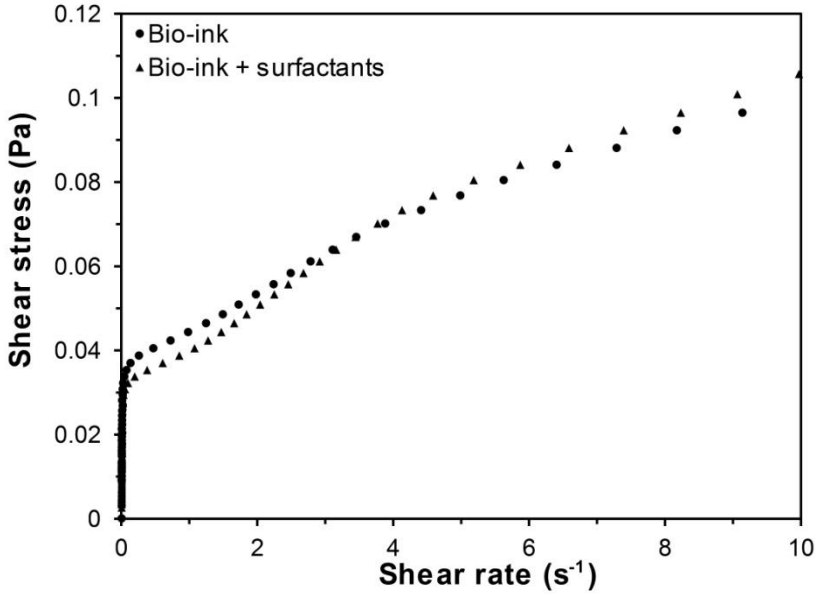

Figure 3.24: Typical yield behaviour of bio-ink (circles), and bio-ink containing surfactants (triangles) measured by continuous shear stress ramps from rest.

3.3.4.1 Structure development

The development of structure in the surfactant-containing bio-ink was then investigated to ensure that, over a time period appropriate for cell printing, the yield stress would not increase to a point where it hindered printability. Structure development was assessed by measuring the static yield stress as previously stated, varying equilibration time (time at rest) prior to measurement (§2.2.6.4). The results are expressed in Figure 3.25 as the average yield stress as a function of equilibration time, normalised to the yield stress value obtained after 1 min equilibration.

The results demonstrated that the development of the microgel network structure over time does not result in an increase in yield stress to values that would likely have detrimental effects on printability; the maximum yield stress measured after 2 hr equilibration was ~ 300 mPa, which is still well below the capillary force that drives the re-filling of inkjet nozzles (~ 1000 Pa). It is likely that the shear forces during this re-filling process would lead to a breakdown of any developed structure, and therefore the yield stress of the bio-ink formulation would be minimal at the firing event. We were unable to characterise shear-induced breakdown on timescales relevant to inkjet printing but found that a repeat measurement of the yield stress with a 1 min equilibration time, for the bio-ink that had been tested following

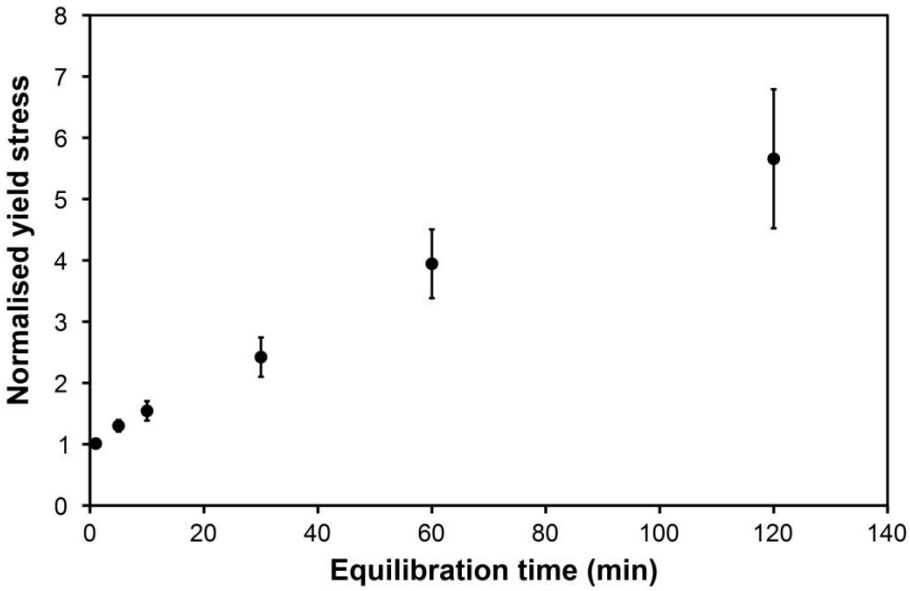

Figure 3.25: Yield stress development over time at rest (equilibration time) for surfactant-containing bio-ink. Yield stress is normalised to the value obtained after 1 min equilibration. Error bars represent one standard error of the mean (n≥3).

equilibration for 120 min, gave comparable results to initial values. This confirmed that the shear applied to the bio-ink during yield stress measurement was sufficient to cause shear-induced breakdown of the developed structure. This is also important for long-term storage of the bio-ink. The majority of the network structure develops over the first few hours *(296)*, and therefore a bio-ink solution that has been stored can be restored to its initial state by brief application of shear using, for example, vortex mixing.

3.3.4.2 Cell settling

Cell settling tests were performed, as described previously (§3.1.2), with C2C12 cells suspended at $5x10^6$ cells/mL to confirm that addition of surfactants did not affect the ability of the bio-ink to maintain a stable cell suspension. Qualitative assessment of settling behaviour in the surfactant-containing bio-ink and DMEM over time (Figure 3.26) confirmed the retention of cell suspending ability.

3.3.4.3 High shear behaviour and printability

The Herschel-Bulkley modelling of shear stress ramp results had suggested a slight increase in the viscosity and degree of shear-thinning on addition of P188 and Novec FC-4430 surfactants to the bio-ink. This was probed further by analysing the viscosity in the high shear region by stepped ramps of shear rate (Figure 3.27). The surfactants imparted a slightly higher viscosity to the bio-ink, which is likely to result from the extra mass of polymeric material contributed by the surfactants. At the maximum shear rate of 10^3 s^{-1}, the viscosity approached a plateau at ~ 2.2 mPa.s for the surfactant-containing bio-ink.

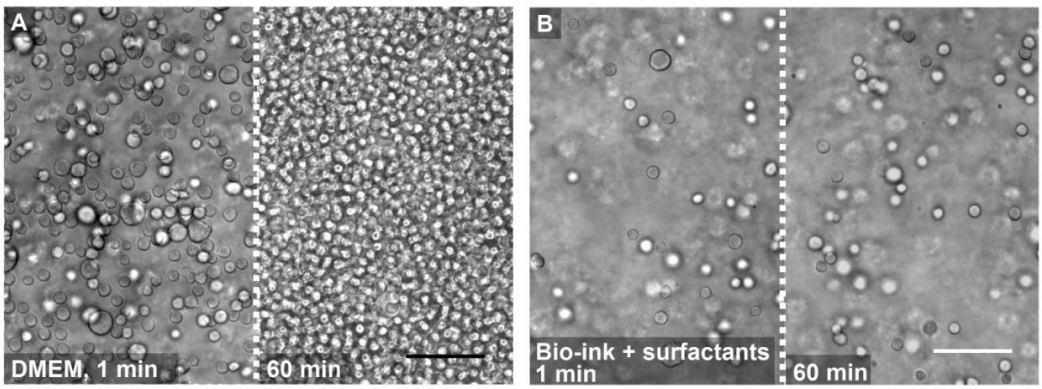

Figure 3.26: C2C12 cells settled on the base of a 96-well plate 1 min or 60 min after suspension in either DMEM (A) or surfactant-containing bio-ink (B) at $5x10^6$ cells/mL. Scale bars represent 100 µm.

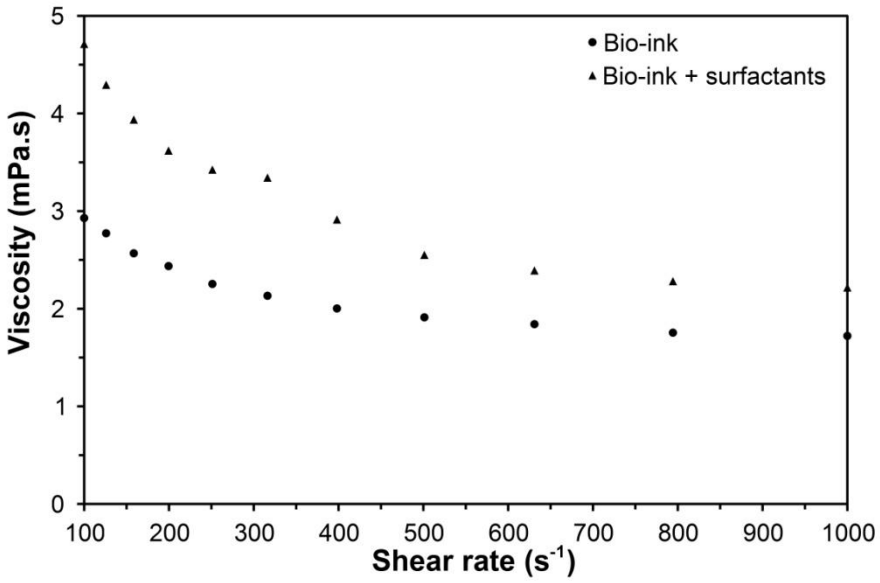

Figure 3.27: Viscosity at high shear rates for bio-ink (circles) and bio-ink with surfactants (triangles) measured by stepped ramps of shear rate. Data shown is representative of experiments which were repeated in triplicate.

3.4 Theoretical bio-ink printability

Having characterised the properties of the bio-ink formulations, we assessed the theoretical printability of the inks via inkjet and microvalve printing based on the Ohnesorge criteria outlined in the introduction to this thesis (§1.4). The relevant properties of the surfactant-containing bio-ink, as well as print head dependent parameters, are outlined in Table 3.3. The bio-ink properties included the viscosity (at 10^3 s^{-1}, as above) and the surface tension as measured in §3.3.1. Substituting these values into the equations outlined in §1.4 yields the values given in Table 3.4.

Table 3.3: Parameters for calculation of inkjet printability, derived from properties of the surfactant-containing bio-ink and the manufacturer's Xaar-126 print head properties.

Parameter	Value	Unit
Bio-ink properties		
Surface tension	30.3	mN/m
Viscosity (at ≥10^3 s^{-1})	2.2	mPa.s
Density	960	kg/m^3
Print head properties		
Nozzle radius	25	µm
Drop velocity	6	m/s

Table 3.4: Values obtained for the Reynolds number (*Re*, Equation 1.3), Weber number (*We*, Equation 1.2), Ohnesorge number (*Oh*, Equation 1.1), splashing constant (Equation 1.4) and Z number (reciprocal of *Oh*) using the parameters listed in Table 3.3.

Constant	Value
Reynolds number	65.5
Weber number	28.5
Ohnesorge number	0.082
Splashing constant	15.2
Z	***12.3***

In the introduction (§1.4) we discussed the criteria for an ideal 'printable fluid' for inkjet printing as obeying $1 < Z < 10$. The results presented in Table 3.4 indicate that the Z value for the bio-ink is just outside of this ideal range. The Z value of 12.3 places the bio-ink in the region where satellite droplet formation could occur. It should be noted that only a very slight increase in the high shear viscosity, to ~ 2.7 mPa.s, would achieve a value of $Z < 10$. In view of our aim to minimise the dry mass in the bio-ink formulation (§1.4.1) we did not pursue the addition of other additives to further increase the high-shear viscosity. Analysis of satellite droplet formation and its effect on cell patterning is explored further in Chapter 5 (§5.1). The additional conditions of a Weber number > 4 to overcome surface tension barriers to ejection, and a splashing constant < 50 to avoid droplet splashing on smooth flat surfaces (i.e. a glass slide) are both met.

Although the criteria outlined above give an indication of the printability of the bio-ink, they do not guarantee effective jetting, especially in this case due to the complexity of the bio-ink afforded by the presence of microgel particles, polymeric surfactants and cells. The printability of visco-elastic polymeric inks has been further defined using modelling *(341)*, rheological measurements at very high shear rates *(342)*, or by filament stretching to measure extensional flow properties *(321)*. These tools were not available to us, and the presence of relatively large particles (microgels, cells) would require a thorough treatment that was outside the scope of this work. Therefore, given that the surfactant-containing bio-ink met the general conditions required for inkjet printing (viscosity < 12 mPa.s, surface tension 28-33 mN/m) and was very close to satisfying the Ohnesorge criteria, we proceeded to experimental observation of printability by inkjet printing as reported in Chapter 5.

3.5 Conclusions

This chapter has outlined the development of novel bio-ink formulations for drop-on-demand cell printing applications. GG microgel suspensions could be formed in DMEM at low polymer concentration (0.05% (w/v)) by the application of shear during cooling (below 44 °C) using a standard vortex mixer. Staining of the microgel structure revealed elongated particles with dimensions in the order of 5-50 µm, which should be a suitable size to pass through printing nozzles. Rheological testing revealed a yield stress of ~43 mPa before flow and subsequent shear thinning behaviour resulting in a low viscosity of ~1.7 mPa.s at a shear rate of 10^3 s^{-1}. This microgel network was capable of maintaining a stable suspension of C2C12 cells, even at a high cell concentration ($5x10^6$ cells/mL). This bio-ink should prove advantageous in microvalve cell printing, and will be utilised for this purpose in Chapter 4.

In a second bio-ink formulation, surfactants were added to the GG microgel suspension in DMEM in order to achieve the low surface tension (~30 mN/m) required for inkjet printing. The common surfactants Triton X-100 and Tween 20 exhibited cytotoxicity. Potentially less cytotoxic alternatives, Novec FC-4430 and P188, were identified through a literature search. Addition of Novec FC-4430 to the bio-ink at 0.05% (v/v) produced a surface tension of 30.5 ± 0.2 mN/m which satisfied the target value, while P188 was included at 0.1% (v/v) for its potential cell-protecting qualities (explored in Chapter 5). Addition of these surfactants had no significant effect on the microgel structure or yield stress or its ability to suspend cells, and only resulted in a small increase in high-shear viscosity (to ~2.2 mPa.s at 10^3 s^{-1}). C2C12 cells exposed to the surfactant-containing bio-ink for up to 2 hr showed no immediate change in viability, while the viability of exposed PC12 cells was in fact slightly higher than controls. For both cells types, exposed cells proliferated and differentiated normally in subsequent culture. This bio-ink will be utilised for inkjet cell printing in Chapter 5.

3.6 Acknowledgments

Ross Clarke (CP Kelco) provided helpful advice on rheology measurements, and also suggested the use of a pigment ink to visualise gellan gum microgel networks.

4 MICROVALVE PRINTING

This chapter investigated the deposition of cells suspended in our bio-ink through microvalve printing, using the Deerac Equator™ GX1 liquid handling system (§2.3.1). Throughout this chapter, 'bio-ink' refers to a 0.05% (w/v) GG microgel suspension in surfactant-free DMEM.

4.1 Bio-ink and cell deposition

Droplets of water deposited on a glass slide by microvalve printing (Figure 4.1A) demonstrate that the Equator™ GX1 system (§2.3.1) was capable of reproducibly dispensing droplets of varying volume. This volume is simply selected in the Deerac™ software, and variations to the dispense pressure or valve opening time that allow this control are not able to be specifically adjusted by the user. This variation in dispensed volume is one key advantage of microvalve printing over, for example, inkjet printing, where each inkjet nozzle dispenses a fixed droplet volume. The deposition mechanism is also relatively simple in comparison to inkjet printing and the outlet dimensions are larger. Consequently, microvalve printing can deposit liquids with a much larger range of fluid properties. For example, the Deerac™ control software has preset 'liquid classes' for fluids with a wide range of viscosities, from water to 40% glycerol. We therefore expected the system to easily handle the deposition of surfactant-free bio-ink and cells.

Bio-ink and cell printing were initially investigated by depositing droplets on glass slides. Bio-ink droplets both with (Figure 4.1B) and without (Figure 4.1C) suspended C2C12 cells were deposited reproducibly, with no observed misfiring or formation of satellite droplets. Inclusion of C2C12 cells to the bio-ink at $5x10^5$ cells/mL increased the measured diameter of dried droplets on glass slides from 840±30 µm to 1030±40 µm (n=10, mean±standard deviation). It is not clear whether this represented a slight increase in drop volume or altered spreading/drying dynamics of droplets on the glass slide. The deviations associated with measured drop diameter are consistent with the variation in dispensed volume accuracy supplied by the manufacturer (± 5%). The system has a nominal minimum droplet volume of 50 nL, although by circumventing this software-based restriction with a patch supplied by the manufacturer we could dispense smaller droplets, and found that 30 nL bio-ink

droplets could be printed reproducibly even when C2C12 cells were included at relatively high concentrations ($2x10^6$ cells/mL) (Figure 4.1C). The average diameter of these droplets on glass slides was 800 ± 20 µm, which is comparable to dimensions reported in the current microvalve printing literature *(169, 171–174, 182)*. The droplet dimensions depend on the substrate, however, and the printed feature size can be much smaller in the absence of spreading on hydrophilic surfaces (§4.5). Nonetheless, if these droplets are considered the building blocks of cell-laden structures, then the poor achievable resolution is one potential limitation to microvalve printing of biomimetic structures. Passive diffusion limits in biological tissues are on the order of 100-200 µm *(343)*, so thick tissue constructs fabricated by microvalve printing could potentially suffer from inadequate nutrient and oxygen transport.

The Deerac™ system operates by aspirating solutions from assignable reservoirs prior to deposition; a feature that can be exploited to print either the same cells at different concentrations, or different cell types. This was demonstrated by printing an alternating array of 30 nL droplets containing C2C12 cells at two different concentrations (Figure 4.1E-F). The integrated tip-washing programs in the system ensure minimal cross-contamination between the two different ink reservoirs. This approach could be advantageous over that employed by Fedorovich and co-workers to print two different cell types using their microvalve system, where they were required to print one cell type before manually changing the tip prior to printing the second cell type *(111)*. An alternative system developed by Lee et al. *(171)* contains four microvalve needles, each individually addressable and fed by separate ink supplies, that is capable of depositing multiple cell types or biomaterials simultaneously.

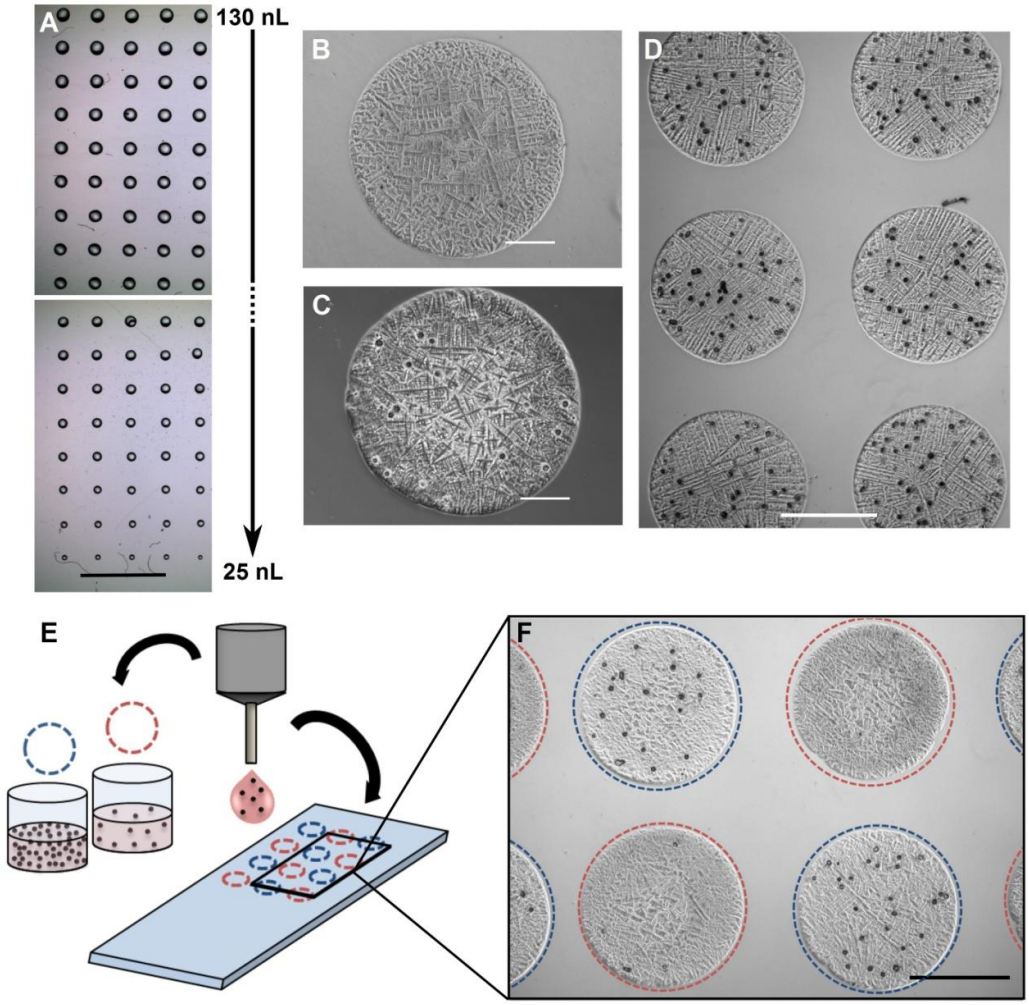

Figure 4.1: Droplets produced by microvalve deposition onto glass slides. **(A)** Water droplets of varying volume, decreasing by 5 nL increments from 130 nL (top row) to 25 nL (bottom row). **(B)** 50 nL bio-ink droplet without cells. **(C)** 50 nL bio-ink droplet with C2C12 cells (black dots) at $5x10^5$ cells/mL. **(D)** Array of 30 nL bio-ink droplets with C2C12 cells at $2x10^6$ cells/mL. Grid spacing 1 mm. **(E)** Schematic diagram of printing cells at varying concentrations by sequential aspiration and deposition from different reservoirs. **(F)** 30 nL bio-ink droplets deposited by method represent in E, where cell concentrations were $1x10^5$ cells/mL (red dotted circles) and $1x10^6$ cells/mL (blue dotted circles). Scale bars represent 5 mm (A), 200 µm (B, C) and 500 µm (D, F)

4.2 Cell output

We demonstrated previously in this thesis (§3.1.4.1) that cell settling and aggregation was avoided when C2C12 cells were suspended in our bio-ink. To demonstrate the benefits of this stability to microvalve printing, we compared the cell output for printed droplets of bio-ink or DMEM containing C2C12 cells over a printing period of 1 hour. In each case a fixed volume (100 µL) of the cell suspension was aspirated into the tip and an array of 50 nL droplets was deposited onto a glass slide (120 droplets per slide) at several time-points, followed by counting the number of cells per drop. In line with our expectations, cells suspended in pure DMEM settled within

the nozzle reservoir over the 1 hr period, resulting in variations in cell output (Figure 4.2A). The number of cells per drop increased initially, so that after ~15 min the printed cell density was almost double the initial value. This is indicative of cell settling within the nozzle. This was then followed by a reduction in the number of printed cells, which is attributed to the deposition of now cell-depleted media. In contrast, cell output for printed cell-laden bio-ink drops was consistent over the 1 hr period. One-way ANOVA of the bio-ink data indicated no significant variation ($F=0.96$) in the average cell number. This behaviour is highlighted by images of drops printed after 0, 15 or 60 minutes which clearly reveal significant fluctuations in cell output from DMEM suspensions in comparison to consistent cell numbers in bio-ink drops (Figure 4.2B).

A similar cell output profile to the one observed for C2C12 cells in DMEM was reported by Pepper and co-workers *(218)* for the deposition of D1 murine stem cells in culture media by inkjet printing. In this case, the initial increase in cell output was attributed to settling while the subsequent decrease was attributed to cell aggregation that prevented ejection from the relatively small inkjet nozzles. In our work, however, cell aggregation in DMEM is unlikely to have affected output due to the relatively low cell concentration, large nozzle diameter, and absence of any observed cell aggregates in dispensed droplets (Figure 4.2). Rather, we attribute the reduction in cell output to the deposition of media depleted of cells solely as a result of settling within the print reservoir; the majority of aspirated cells had been deposited in the initial printed samples.

The adverse affects of cell settling on microvalve deposition have been reported previously. Lee and co-workers *(171)* found that the number of cells in microvalve printed droplets was 3-4 times the value expected from theoretical calculations based on prepared cell concentrations in their culture media ink, and attributed this to cell settling. They also reported that cell concentrations greater than $3x10^6$ cells/mL caused clogging due to aggregation of cells within the dispenser that hindered printing. Consequently, this group resorted to lower cell concentrations and employed agitation or vibration of the reservoir in an attempt to limit settling and aggregation *(171, 172)*. Demirci's group *(169, 174)* took a different approach by printing cells from high-viscosity collagen hydrogel precursor solutions. While this

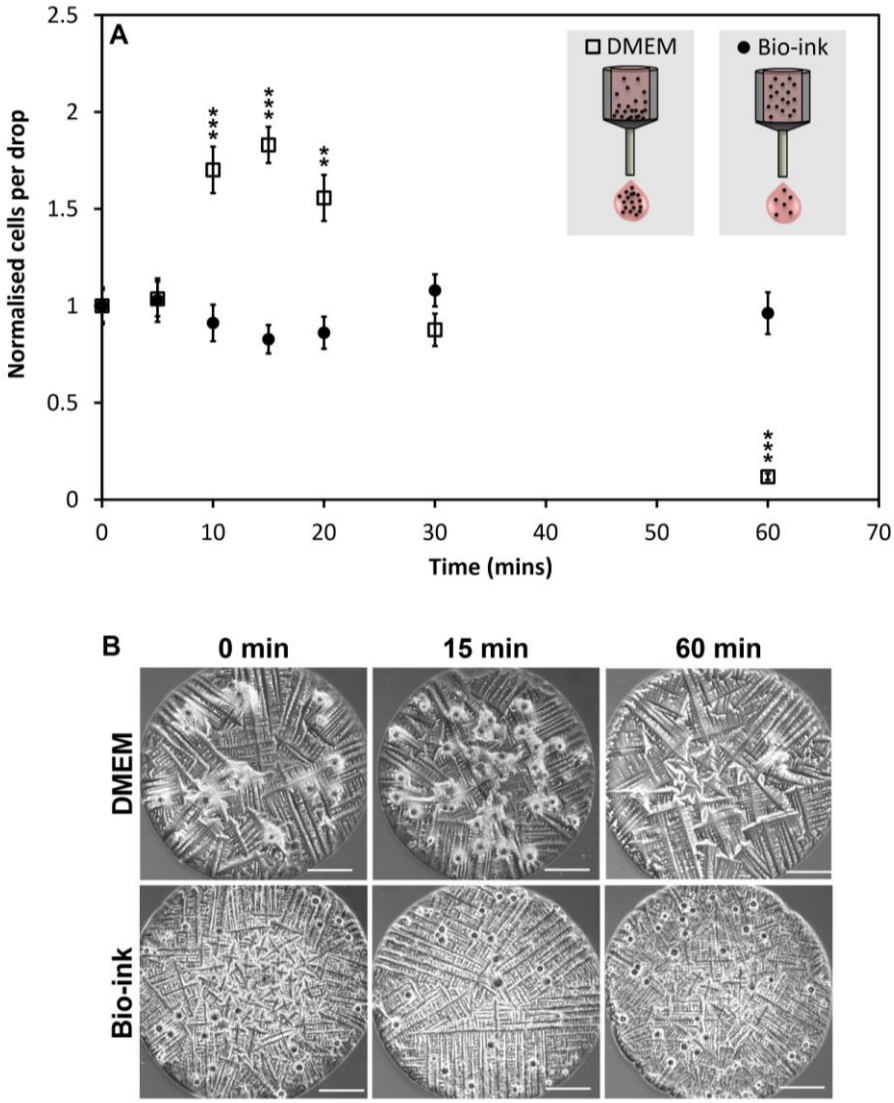

Figure 4.2: Cell output over time for microvalve deposition with and without the bio-ink. **(A)** Average number of cells per drop over time, for cells suspended in DMEM (open squares) or bio-ink (closed circles) at $5x10^5$ cells/mL. Values were normalised to the average number of cells per drop for deposition immediately after loading of cell suspensions. Error bars represent one standard error of the mean ($n \geq 3$). Statistical significance compared to the initial cell output was analysed by a Student's t-test, with significance level as indicated; $P < 0.01$ (**), or $P < 0.001$ (***). Inset – cartoon depicting the effect of settling, or lack thereof, on droplet output in each case. **(B)** Images of typical droplets at 0, 15 or 60 minutes for deposition of cells (black dots) suspended in DMEM or bio-ink. Scale bars represent 200 µm.

seemed to effectively avoid cell settling, the nature of their ink necessitated cooling of the printing nozzle to 5°C to avoid premature collagen gelation. This resulted in some decrease in cell viability. Our bio-ink alleviated cell settling problems and does not affect the viability of printed cells, as demonstrated in the following section (§4.3).

Having established that the bio-ink enabled deposition of droplets with reproducible average cell density over time, we sought to investigate the distribution of cell number within these droplets. This distribution is relevant to the fabrication of cell-based microarrays where the number of cells contained in individual droplets is important, not just the density across a population of droplets. We printed droplet arrays onto glass slides with bio-ink containing C2C12 cells at two different concentrations and, for each concentration, counted the number of cells in at least 250 droplets. In each case, the experimental cells/drop distribution could be fitted to a Poisson distribution (Figure 4.3), using *(215)*:

$$P(n,\lambda) = \frac{\lambda^n e^{-\lambda}}{n!}, \qquad \textbf{Equation 4.1}$$

where P is the probability of dispensing a given number (n) of cells in a given aliquot of liquid, and λ is the average number of cells in the aliquot volume calculated by taking the overall average of cells/drop across all printed droplets.

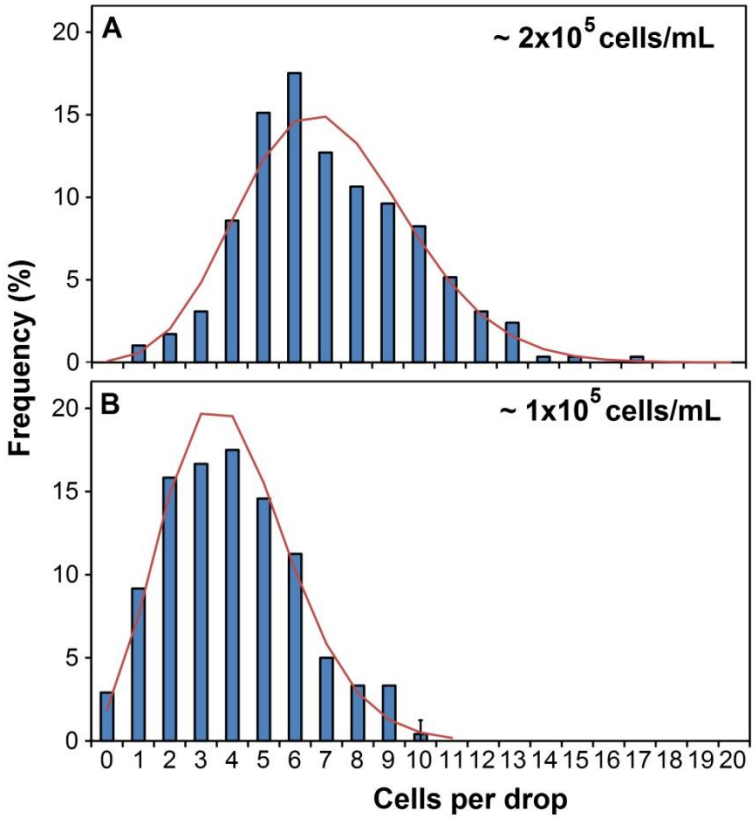

Figure 4.3: Frequency distribution (bars) of the number of cells within printed 50 nL droplets for C2C12 cells suspended in the bio-ink at $2x10^5$ cells/mL (A) or $1x10^5$ cells/mL (B) and microvalve printed onto glass slides. At least 250 cell-laden droplets were counted for each cell concentration. The red traces represent a Poisson distribution, calculated using the total average of cells/drop for all dispensed droplets at each concentration.

This distribution is a result of the random distribution of cells within the bio-ink; similar results have been found by numerous workers using microvalve printing *(176)*, inkjet printing *(215)* and other cell deposition techniques *(155, 344)*, as well as in work manipulating single cells using micro-fluidics *(338, 339)*. Unless some force acts to induce a more ordered suspension of cells, this random distribution is a fundamental feature of droplet-based cell deposition. The significance of this, particularly for controlled deposition of single cells, is discussed further in §5.4.

4.3 Printed cell response

The phenotypic response (morphology, viability, proliferation, differentiation) of cells to the microvalve printing process was investigated to determine whether exposure to the bio-ink in a practical setting, or forces experienced during printing, had adverse effects on cells.

In initial cell printing experiments, printer tubing and the deposition tip were flushed with 70% (v/v) ethanol prior to printing in an attempt to maintain sterility. However, with this approach death of printed cells was observed, likely as a result of contact with residual ethanol. In subsequent experiments, the printer was simply flushed with sterile Milli-Q water prior to use. Penicillin/streptomycin was included in further culture of printed cells, and no contamination was observed throughout the following experiments.

The phenotypic response of cells to microvalve printing was investigated by suspending C2C12 cells in bio-ink, which were then directly deposited into cell culture media in 96-well plates and assessed for viability, proliferation and differentiation alongside non-printed controls. Cell viability was assessed by live/dead staining after 2 hours in culture for cells printed at three different concentrations (Figure 4.4A). The range of cell concentrations was investigated due to previous evidence that cell viability can vary when printed at different concentrations through syringe-based deposition techniques *(174)*. To keep the number of cells in each well consistent, a greater number of individual drops were deposited for lower cell concentrations. In each case, the cell viability was > 95% and one-way ANOVA showed no significant variation ($F=3.02$) in viability across the three printed samples and the control. Fluorescence microscope images of

calcein-stained cells revealed no clear morphological differences between printed and control cells (Figure 4.4B, C). The high viability of printed cells in this work is in agreement with previous reports on microvalve cell printing. In similar conditions to those reported here, using a culture media ink and a microvalve printer with a 150 µm needle, Lee and co-workers have printed several cell types including human epidermal keratinocytes *(171)*, human dermal fibroblasts *(171, 173)* and embryonic rat astrocytes and neurons *(172)* and in each case reported a high viability of printed cells with no statistically significant difference compared to controls. Demirci's group reported a slightly lower viability of printed primary bladder smooth muscle cells in comparison with cell viability in control cultures *(169, 174)*, but this could have resulted from ink preparation rather than the printing process, especially considering that their collagen inks were maintained at 5°C prior to deposition.

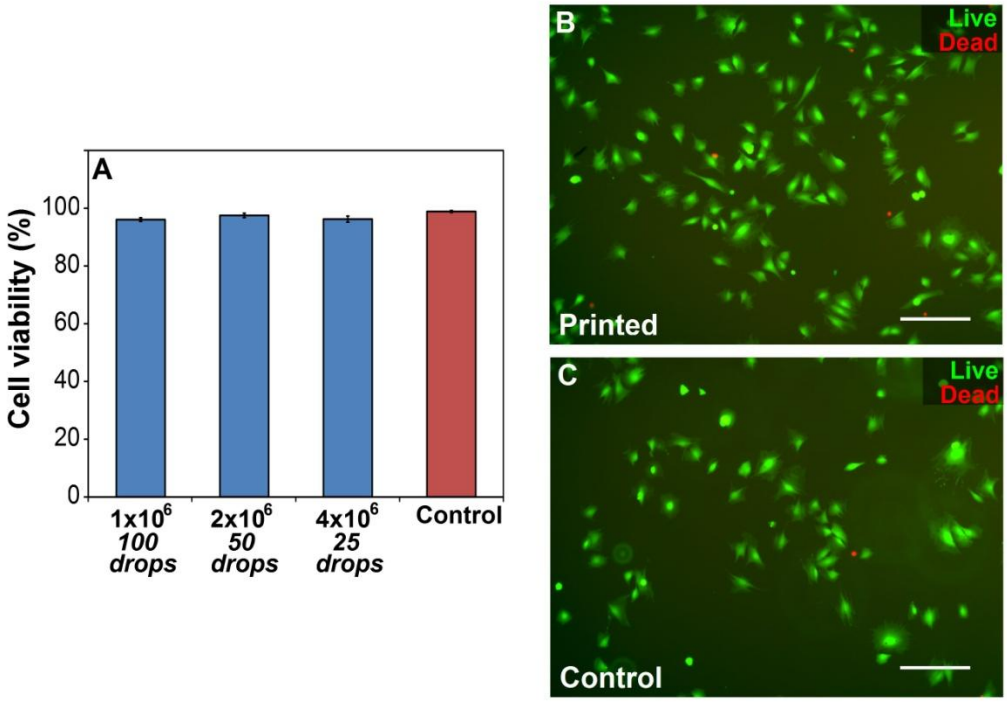

Figure 4.4: Viability and morphology of microvalve printed C2C12 cells. **(A)** Viability, assessed after 2 hr in culture by live/dead staining, of C2C12 cells printed from the bio-ink in comparison with a non-printed control. Cells were suspended at three different concentrations ($1x10^6$, $2x10^6$, $4x10^6$ cells/mL) resulting in a different number of required printed 50nL drops to obtain ~5000 cells in each well. Error bars represent one standard error of the mean (n≥3). **(B,C)** Morphology of printed C2C12 cells, calcein stained after 2 hr in culture, in comparison with non-printed controls. Scale bars represent 200 µm.

In order to assess the effect of cell printing on subsequent cell metabolism, the proliferation of cells printed at $2x10^6$ cells/mL was quantified using the MTS metabolic assay (§2.1.6). Figure 4.5 shows that printed cells proliferated at a rate comparable to non-printed controls over 48 hrs in culture and, interestingly, there was a reproducible and statistically significant enhancement in printed cell metabolism compared with that of controls measured at the 24 hr time point. This trend was observed for three separate repeats of this experiment and, in some cases, the number of cells was also significantly enhanced after 48 hrs in culture. Since the MTS assay requires analysis of a different population of cells for each time point, it could be possible that the difference was a result of variations in the number of deposited cells. However, we have shown that cell deposition using the bio-ink is consistent (§4.2), and furthermore the deposition sequence (order of printing etc.) was altered in different experiments, reducing the likelihood of systematic errors in printed cell numbers.

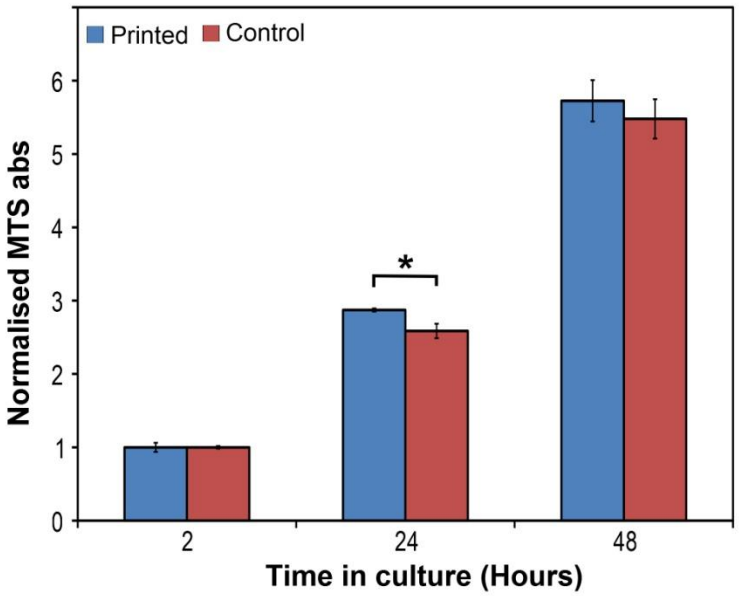

Figure 4.5: Proliferation over 48 hr, assessed by using the MTS assay, of C2C12 cells suspended in bio-ink at $2x10^6$ cells/mL and microvalve printed in comparison with non-printed controls. Absorbance was normalised to the 2 hr time point to account for any differences in cell concentration in printing solutions. Error bars represent one standard error of the mean ($n \geq 3$). Statistical significance was analysed by a Student's t-test, with significance level as indicated; $P < 0.05$ (*).

Our proliferation results add further evidence to the literature that suggests microvalve printing has no adverse affects on cell viability and proliferation rate *(171, 174)*. It is particularly interesting that printed C2C12 growth was reproducibly enhanced compared to controls over 24 hrs. It is possible that this hyperproliferation could be a result of stresses experienced by the cells during printing. There is substantial evidence that various applied stresses can stimulate hyperproliferation in cells including osteoblasts *(345)*, chondrocytes *(346)* and keratinocytes *(347)*. This effect does appear to be cell-type dependent; for example, applied shear stress can inhibit the proliferation of vascular endothelial cells *(348)*. It is well known though that mechanical stretch (i.e. applied stress) can stimulate enhanced proliferation in skeletal muscle cells *(349)*. In most of these reports, the nature of the stress differs from that experienced by cells in our printing system, in that it is applied over considerably longer time-scales. However, a recent study has shown that stimulation of C2C12 cells with local stress waves created by just 10 pulses of a femtosecond laser resulted in hyperproliferation over the ensuing 24 hr period in comparison with controls *(350)*. Interestingly, the effect was reversed for PC12 cells. We cannot conclude definitively that the enhanced proliferation measured in our work resulted from the applied stress of printing. In any case, our results clearly suggest that the proliferation of C2C12 cells was not attenuated by the printing process.

Printed cells also retained the ability to differentiate, as evidenced by immunostaining of cells that were printed and subsequently cultured under differentiation conditions for 5 days. Staining of the skeletal muscle protein desmin revealed long multi-nucleated myofibres (Figure 4.6A), with no clear differences from differentiated non-printed control cells (Figure 4.6B). These results support previous microvalve cell printing reports that have demonstrated the ability of printed cells to exhibit a normal differentiated phenotype. For example, printed neural cells developed extensive neurite networks *(172)* and printed smooth muscle cells expressed actin and connexin-43 *(169)*.

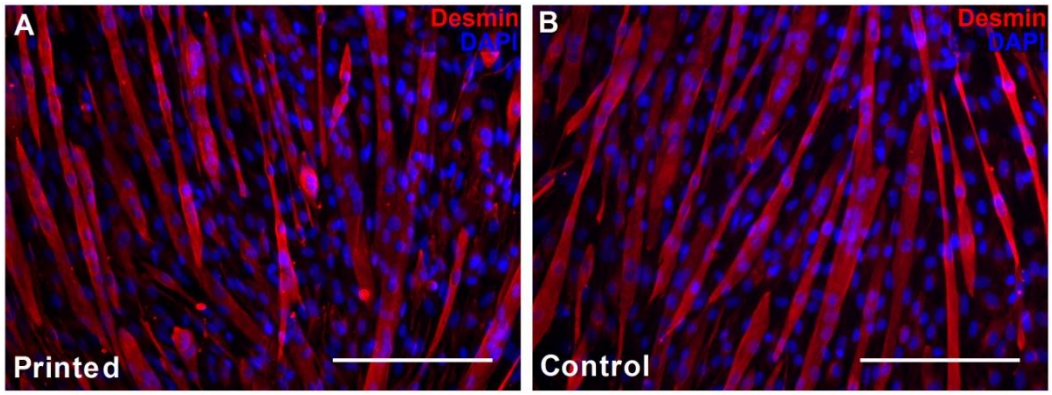

Figure 4.6: Fluorescence microscope images of printed C2C12 cells, after 5 days of culture under differentiation conditions (A), compared to non-printed controls (B). Cells were immunostained against desmin and nuclei were stained with DAPI. Scale bars represent 200 µm.

4.4 2D image printing

Drop-on-demand techniques, such as microvalve printing, have application in the fabrication of droplet-based arrays. For the fabrication of tissues and other cell constructs, droplets must be combined to form larger-scale patterns. The deposition of complex user-defined patterns using the Deerac™ control software is limited. The two modes which enable patterning of droplets are the spotting (§2.3.3.1) and platemap dispense (§2.3.3.3) functions. In spotting mode, a grid can be defined within a well region and droplet deposition at points of this grid can be toggled on/off. This is useful for the deposition of simple patterns, but is limited and tedious. Alternately, the platemap dispense function allows the user to define a volume to be dispensed into each well in a given plate, and these values can be imported from a spreadsheet .csv file. Using the Deerac™ plate designer software (§2.3.3), a 'plate' can be created where each 'well' represents a pixel of an image and a platemap dispense task can then be used to deposit a droplet of specified volume into these 'wells' to create an image. One can envisage that simple bitmap images, or even gray-scale or colour images, could be deposited using this approach. However, to alleviate the need to manually enter volumes for each pixel of an image, we needed a method to easily convert an image into meaningful deposition volumes in a .csv file that could be imported into a Deerac™ platemap dispense task.

The design of a software tool to process images was outlined in the experimental chapter (§2.3.3.3). Using this image processing tool and the platemap dispense function, we deposited various C2C12 cell patterns onto glass slides (Figure 4.7). C2C12 cells were suspended in bio-ink at $1x10^6$ cells/mL and 50 nL droplets deposited in 50x100 pixel spiral or lattice patterns using a droplet (pixel) spacing of 500 µm. The individual droplets coalesced to form continuous patterns that accurately reflected the original images (Figure 4.7A and B). Higher magnification images (Figure 4.7C and D) showed that cells were homogeneously distributed throughout these patterns.

This demonstrated that the image processing tool could be utilised to print more complex patterns that would not otherwise be readily achieved using the Deerac™ Equator GX1 system. It also showed that the bio-ink could be used to print relatively large-scale patterns with uniform cell density throughout. Importantly, the principle of joining individual 'building blocks' to create a continuous structure was demonstrated. We did not investigate printing gray-scale (different droplet volumes) or colour (different cell types or concentrations) images, however the software and system should be amenable to this approach.

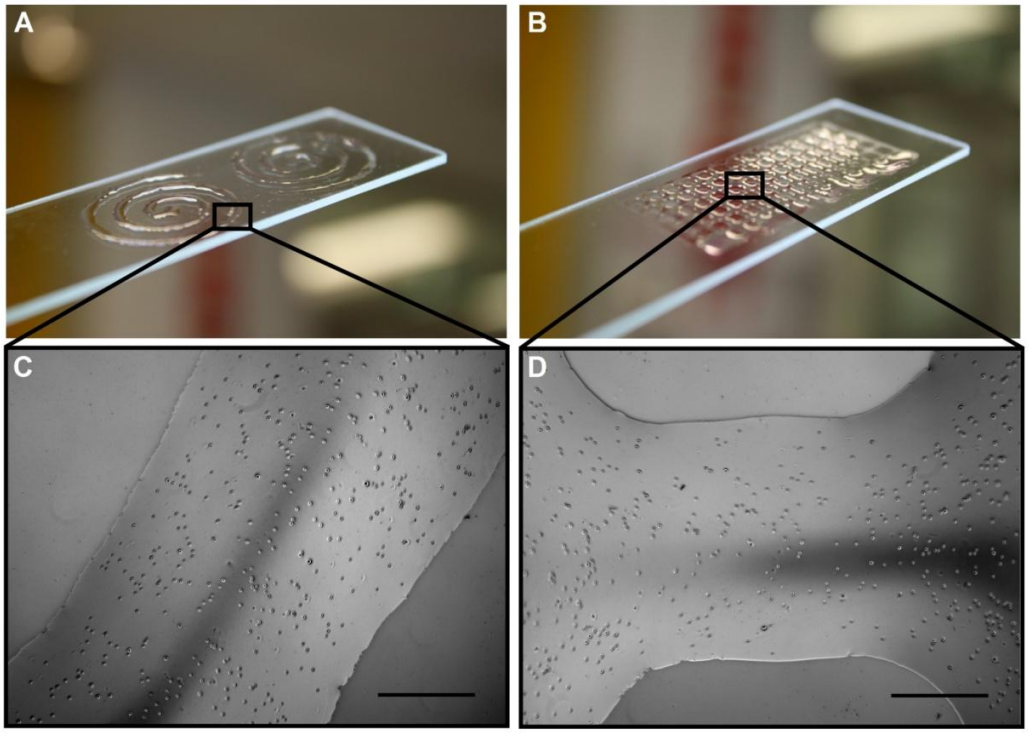

Figure 4.7: Image reproduction by deposition of C2C12 cells, suspended at $1x10^6$ cells/mL in bio-ink, onto standard glass slides. **(A,B)** Bitmap images of spirals (A) or a lattice (B) were transformed to a plate-map and printed using a single layer of 50 nL droplets with a spacing of 500 µm. **(C,D)** Sections of the printed patterns imaged by optical microscopy, showing a uniform cell distribution. Scale bars 500 µm.

4.5 Application: *D*rop-on-demand *R*eactive *I*n-solution *P*lotting (DRIP) fabrication

This chapter has thus far demonstrated the reproducible deposition of living cells by microvalve printing into microarrays and 2D patterns, with high cell viability. In this section, this capability is applied to the fabrication of cell-encapsulating hydrogel constructs through a novel reactive printing approach. As outlined in the experimental section (§2.3.6), Drop-on-demand Reactive In-solution Plotting (DRIP) fabrication is based on the bioplotting principle. The concept of bioplotting, where the dispensing tip is submerged in a liquid plotting medium, was introduced by Landers and co-workers in 2002 *(109)*. The advantage of this approach is that the surrounding solution can act as a supporting medium for the printed structure. The following paragraphs highlight the differences between DRIP fabrication and other bioplotting approaches to provide context to the development of the technique, presented thereafter.

While traditional bioplotting is based upon extrusion printing, DRIP fabrication involves droplet-based deposition. The tip of a microvalve deposition tool (eg. Deerac Equator GX1) is immersed into a biopolymer solution (eg. gellan gum) where it deposits an ink containing a cross-linking species for the biopolymer (eg. Ca^{2+} ions) (Figure 4.8A). The cross-linker diffuses from the printed droplet and reacts with the surrounding biopolymer to form defined hydrogel regions (Figure 4.8B). Since the density of these gelled regions is similar to the surrounding solution, the droplets maintain their spatial location in three dimensions. These small gelled regions can then be considered the 'building blocks' for the fabrication of 3D hydrogel structures.

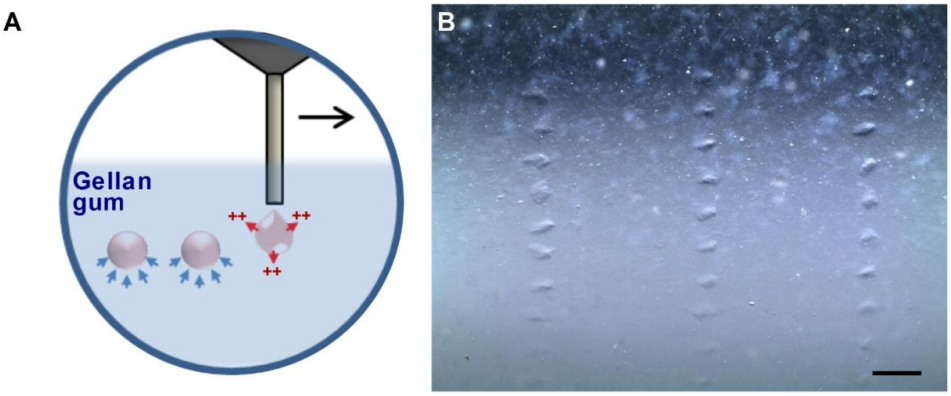

Figure 4.8: (A) Schematic representation of the DRIP fabrication approach. **(B)** Distinct hydrogel regions formed by deposition of 50 nL drops of 20 mM Ca^{2+} into 0.5% (w/v) GG. Scale bar represents 1 mm.

The majority of reports presenting the implementation of bioplotting have used thermal gelation principles, in which a heated material is printed into a cooler viscous plotting medium where it subsequently solidifies *(109, 110, 351)*. Thermal processes, however, can be detrimental to cell viability and premature solidification within the printing apparatus is a concern. Reactive approaches are an attractive alternative. For example, Maher and co-workers extruded alginate solutions into a bath containing Ca^{2+} which crosslinked the alginate, forming printed hydrogel structures *(351)*. Fedorovich and co-workers used a similar approach in their work *(111)*, although it is unclear whether they submerged the dispensing tip or extruded onto a thin layer of Ca^{2+} solution. To our knowledge, there are no reported examples comparable to the DRIP fabrication approach where this reactive combination is reversed and the crosslinking solution is deposited within a solution of the polymer. There are two key advantages to this approach. Firstly, the plotting medium is naturally viscous and should prevent the movement of deposited droplets, alleviating the need to add thickeners like glycerol to the plotting medium *(351)*. Secondly, In DRIP fabrication, diffusion of Ca^{2+} out of deposited droplets should aid in fusion with successive droplets. For example, in a previously reported inkjet printing approach where Ca^{2+} was deposited onto the surface of alginate solutions, the author noted no delamination of successively printed layers, likely due to the diffusion-mediated bonding *(202)*. Conversely, when depositing alginate filaments into Ca^{2+} solution, Fedorovich and co-workers reported poor adhesion of successive layers *(111)*.

4.5.1 Development of DRIP fabrication

The principle of DRIP fabrication was first investigated by depositing droplets of $CaCl_2$ solution into GG solutions in 6-well plates using spotting mode deposition (§2.3.3.1). The gelled regions, or DRIP building blocks, shown in Figure 4.8B were formed by dispensing droplets of 20 mM $CaCl_2$ solution into a 0.5% (w/v) GG solution at room temperature. This combination of Ca^{2+} and GG allowed distinct hydrogel regions to form, and their location in the surrounding solution was maintained. These building blocks had an average diameter of 330 ± 20 µm (n=10). We found that at higher Ca^{2+} (≥ 100 mM) and GG (≥ 1% w/v) concentrations, gelation tended to occur too quickly and the dispensing tip became clogged with

hydrogel material. High Ca^{2+} concentrations also lead to excessive diffusion of the cross-linker away from the point of deposition. This is demonstrated in Figure 4.9, which highlights a general increase in the size of the gelled region when increasing the concentration of Ca^{2+} droplets deposited on the surface of a 0.5% (w/v) GG solution. Similar observations have been made previously for inkjet printed droplets of Ca^{2+} deposited onto alginate solutions *(189)*. Conversely, we observed that when lower Ca^{2+} ($\leq$ 10 mM) or GG ($\leq$ 0.1% w/v) concentrations were used, the gelled regions did not form adequately. Furthermore, GG solutions were not very viscous at concentrations below 0.5% (w/v) and were therefore not as effective at maintaining the integrity of printed structures, so that deposited hydrogel regions tended to move significantly due to fluid flow induced by tip motion through the solution.

It was then investigated whether these individual DRIP building blocks could be joined together to form larger, continuous hydrogel structures (Figure 4.10). To aid visualisation in these experiments, methylene blue dye was included in the printed $CaCl_2$ solution and larger (100-500 nL) droplets were printed. Droplets were deposited with a grid spacing of 0.72 mm whilst the drop volume was varied to study building block fusion.

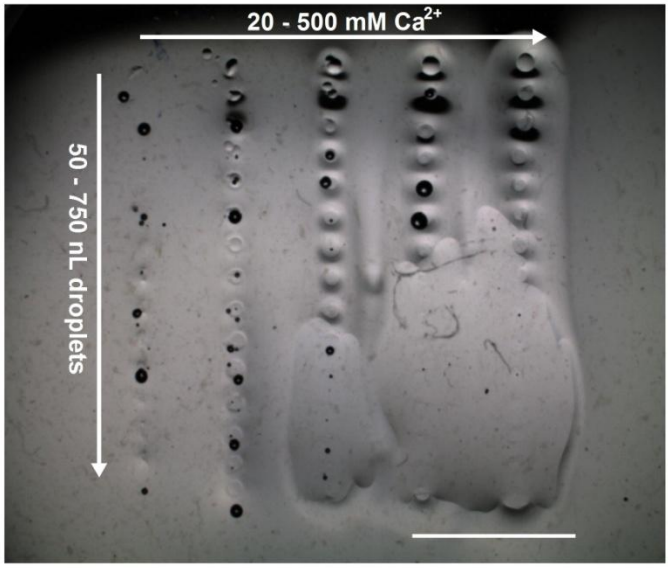

Figure 4.9: Droplets of $CaCl_2$ solution deposited on the surface of a 0.5% (w/v) GG solution. Ca^{2+} concentration was 20, 50, 100, 200 or 500 mM (left to right) and dispensed droplet volumes varied from 50 – 750 nL increasing in 50 nL increments (top to bottom). Scale bar represents 5 mm.

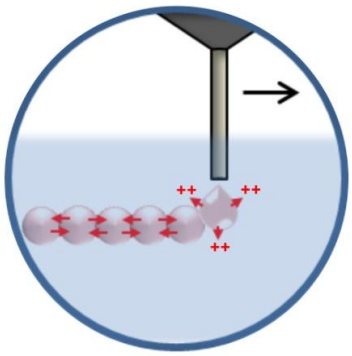

Figure 4.10: Schematic representing the coalescence of DRIP building blocks with adjacent droplets due to Ca^{2+} diffusion.

Deposition of 100 nL droplets in a 15x15 square array led to the formation of distinct individual gelled building blocks (Figure 4.11A), as seen previously. The z-plane (i.e. vertical deposition height) for these droplets was set at around half the height of the GG solution in the 6-well plate, and the dispensed 100 nL drops remained suspended within this plane. The building blocks did not appear to join together, however, and this hydrogel 'sheet' could not be removed intact from the surrounding solution. The droplet volume was subsequently increased to 250 or 500 nL in an effort to encourage building block coalescence. We observed that, as the droplet volume increased, the vertical distance between the dispensing tip and the final location of gelled regions increased and became more variable. We were unable to extensively characterise this variation, but it presents a challenge for the accurate deposition of 3D structures. The Deerac Equator GX1 only provides control over dispensed volume, not fine control over the applied pressure and valve opening times during dispensing. A system which allows this control could be useful for further investigating and minimising this variation. With a droplet volume of 250 nL, the hydrogel sheet could be removed from the surrounding solution but was very weak and broke apart easily. With a 500 nL droplet volume, the building blocks initially appeared disconnected (Figure 4.11B), but after a short time (< 1 min) they appeared to coalesce by diffusion of Ca^{2+} out of the printed droplets, as visualised by diffusion of methylene blue (Figure 4.11C and inset). The resulting hydrogel sheet had sufficient mechanical integrity to allow easy handling and removal from the surrounding solution (Figure 4.11D). Using these parameters, we also printed other free-standing hydrogel structures (Figure 4.11E and F).

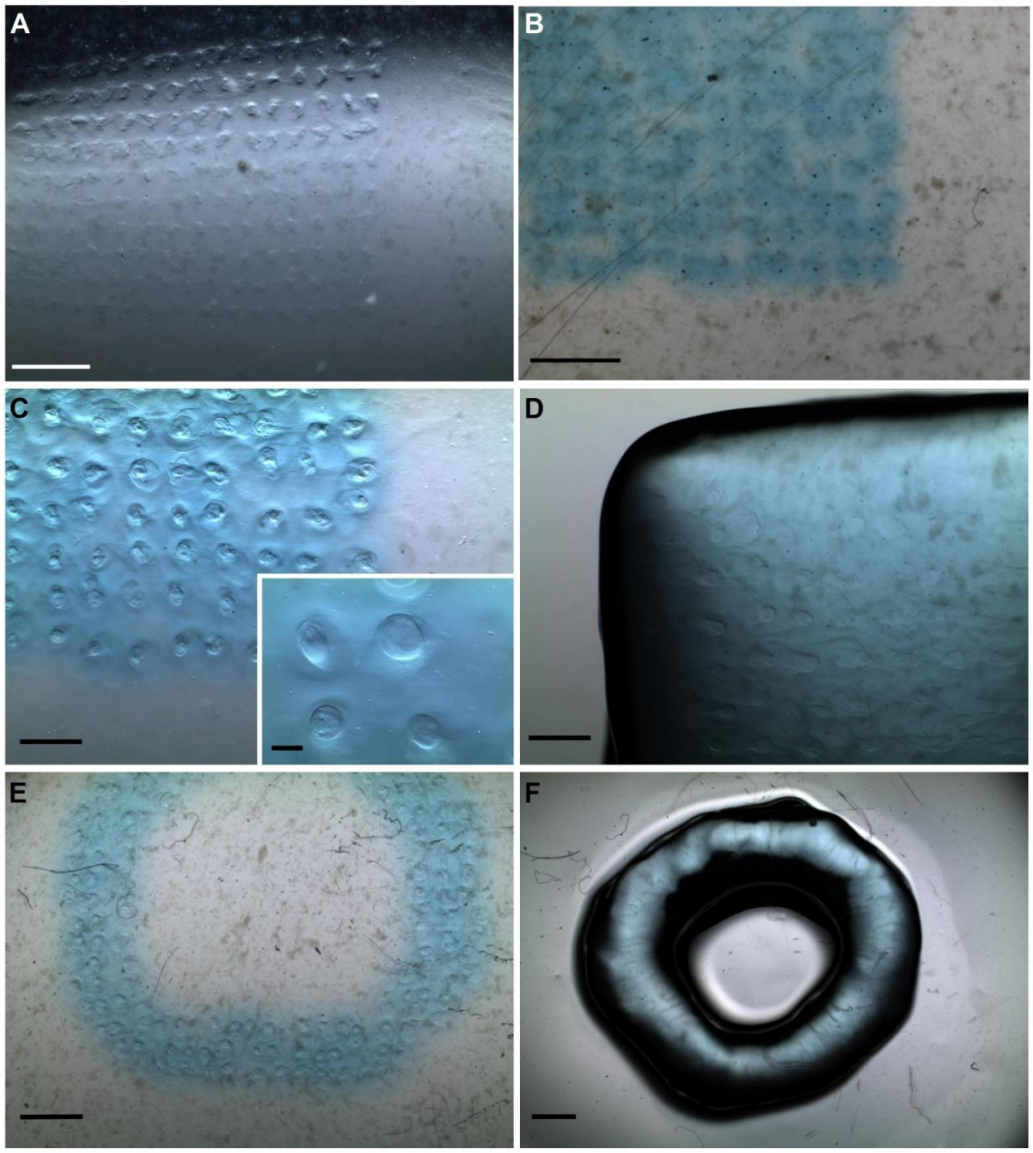

Figure 4.11: Deposition of 20 mM $CaCl_2$ solution containing 100 µM methylene blue into 0.5% (w/v) GG solution. **(A)** Square pattern created by depositing 100 nL drops. Scale bar 1 mm. **(B)** Square pattern created by depositing 500 nL. Image taken immediately after printing. Scale bar 1mm. **(C,D)** Square pattern created by depositing 500 nL drops. Images taken ~1-2 min after printing, before (C) and after (D) removal of surrounding GG solution. Scale bars 1 mm, inset 200 µm. **(E,F)** Circular pattern created by depositing 500 nL drops. Images taken ~1-2 min after printing, before (E) and after (F) removal of surrounding GG solution. Scale bars 2 mm.

The results demonstrate a key principle of DRIP fabrication; that individual building blocks can be joined together to form continuous hydrogel structures. Although the relatively large drop volume and z-axis variability in drop placement imparted pseudo three-dimensionality to these printed structures, we have only demonstrated deposition of droplets in one vertical plane. This is a result of limitations in the Deerac Spot-station control software, where changing the z-axis position of the dispensing tip required alteration of the nominal height of the customised well plate

and consequently it was not possible to quickly print a layer of droplets at a different height. Thus while the particular printing system used in this work may not be suitable for constructing 3D hydrogels in a layer-by-layer approach, the general approach is certainly amenable to this; considering that individual DRIP building blocks coalesce in the x-y plane it follows logically that inter-layer fusion in the z-dimension would also be possible.

4.5.2 DRIP fabrication of cell-laden hydrogels

Focus was then turned to improving the resolution of simple DRIP hydrogel structures with a view to including living cells in the fabrication process. In a slight modification of the DRIP technique, 20 mM $CaCl_2$ droplets were dispensed into 0.5% (w/v) GG solutions as previously, but with the dispensing tip in close proximity to the substrate (Figure 4.12A). We had observed that using this approach allowed the deposition of smaller volume droplets, likely due to forces that encouraged tip-droplet detachment. The tip height was optimised by iteratively adjusting the height of the custom well plate to ensure that the tip did not contact the substrate and that droplet deposition was unimpeded. In these experiments, we used OTF-mode deposition (§2.3.3.2) with a droplet spacing of 200 µm. Figure 4.12B shows that distinct hydrogel lines could be formed by the coalescence of DRIP building blocks with volumes of 30, 25 and 20 nL using this deposition mode. The width of these features was measured to be 218±27, 149±22 and 112±13 µm, respectively. Importantly, this demonstrates that the dimensions of printed hydrogel features from DRIP fabrication can be reduced to dimensions which should allow for adequate nutrient and oxygen transport to encapsulated cells.

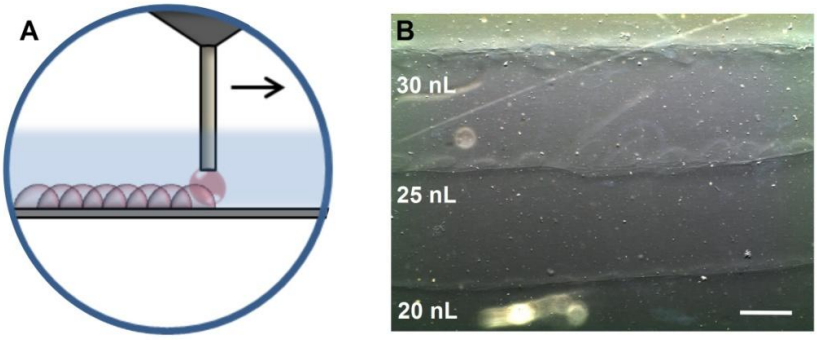

Figure 4.12: (A) Schematic representation of OTF-mode deposition with the tip in close proximity to the substrate. **(B)** Deposition as illustrated with 30, 25 or 20 nL droplets of 20 mM $CaCl_2$ deposited into 0.5% (w/v) GG with a droplet spacing of 200 µm. Scale bar represents 500 µm.

C2C12 cells were then included in the DRIP fabrication process in an attempt to fabricate cell-laden hydrogel structures (Figure 4.13A). C2C12 cells were suspended in DMEM containing 20 mM added $CaCl_2$ and deposited into 0.5% w/v GG solutions using OTF-mode deposition, with a droplet volume of 30 nL and droplet spacing of 200 µm. This approach enabled the coalescence of cell-laden DRIP building blocks to form a continuous hydrogel line that encapsulated the C2C12 cells (Figure 4.13B). After 9 days in culture, however, encapsulated C2C12 cells remained rounded and a number of cells did not stain positively with calcein, indicating that cell death had occurred (Figure 4.13C). This behaviour had also been seen for cells encapsulated in bulk GG hydrogels, during work reported in Chapter 6 (§6.1.1). We also observed that, in one experiment, cells leaked from a DRIP fabricated hydrogel line following transfer of the structure between well plates (3 days post-printing) and subsequently adhered and proliferated on the TCPS substrate (Figure 4.13D). This suggested that, while the printed cells retained the potential to exhibit normal phenotypic behaviour, the GG hydrogel did not provide a permissive matrix for cell attachment and growth. These results highlighted the need for modification of GG hydrogels to encourage the normal function of encapsulated C2C12 cells (see Chapter 6).

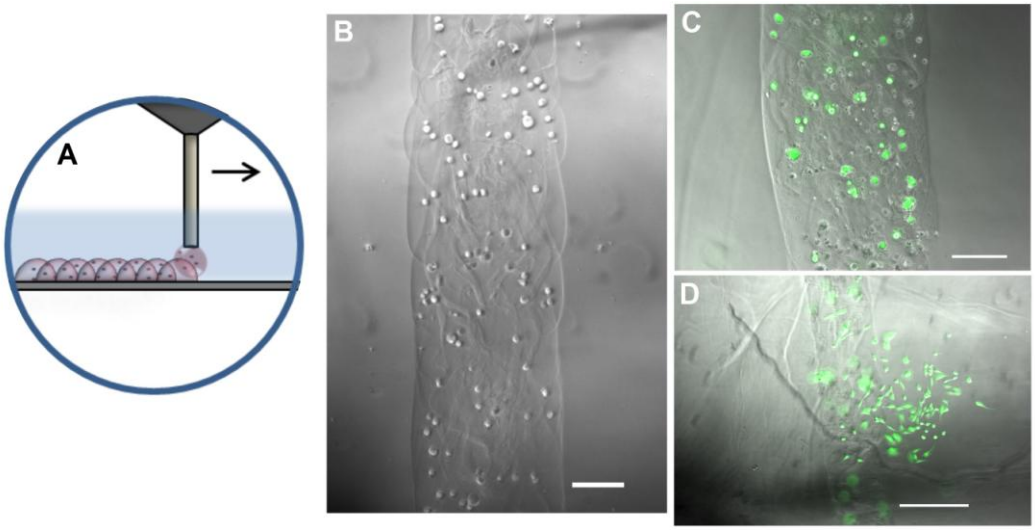

Figure 4.13: (A) Schematic representation of DRIP fabrication by OTF-mode dispensing of cell-laden droplets **(B)** Hydrogel structures formed by deposition (30 nL droplets, 200 µm droplet spacing) of a suspension of C2C12 cells at $5x10^5$ cells/mL in DMEM + 20 mM $CaCl_2$ into 0.5% (w/v) GG solution. Scale bar represents 200 µm. **(C)** Calcein-stained C2C12 cells encapsulated in a DRIP fabricated GG hydrogel structure after 9 days in culture. Scale bar represents 200 µm. **(D)** C2C12 cells leaked from a DRIP fabricated hydrogel line and proliferated on the base of TCPS culture well. The printed structure was transferred to a fresh well 3 days after fabrication, and cells were calcein-stained and imaged after a further 6 days in culture. Scale bar represents 500 µm.

Further work on the DRIP fabrication process was not pursued in this thesis for two main reasons. Firstly, the lack of interaction between encapsulated cells and the GG hydrogel matrix instead encouraged further materials development. This was explored through GG modification (Chapter 6). Secondly, the microvalve system was limited in its ability to print in three-dimensions which hindered further exploration of the fabrication of complex structures, as previously discussed. Nonetheless, this brief section has introduced the novel concept of DRIP fabrication and demonstrated the fundamental principle that continuous hydrogel matrices can be printed through the coalescence of individual DRIP 'building blocks'. It is envisaged that future work could implement this approach, armed with a more advanced microvalve printing system and the modified GG materials presented in Chapter 6, in order to fabricate functional cell-laden matrices.

4.6 Conclusions

The combination of microvalve printing with the surfactant-free bio-ink formulation developed in Chapter 3 provided excellent control over cell deposition. The Deerac Equator GX1 system, despite not being specifically designed as a printing tool, proved to be suitable for cell printing. This was aided by software modifications that enhanced the printing capabilities by allowing deposition of smaller droplets and provided a versatile method of depositing 2D patterns. Cells could be reproducibly deposited from droplets of varying volume (down to 30 nL). The number of cells per drop followed a Poisson distribution, indicating that cells within the bio-ink were randomly distributed. Importantly, printing with the bio-ink gave consistent cell output over a 1 hr period, in contrast to cells suspended in DMEM alone where output varied significantly. The printing process caused no significant reduction in cell viability for C2C12 cells suspended in the bio-ink at a range of concentrations (1-4x10^6 cells/mL). The proliferation and differentiation of printed cells was comparable to controls, although there was some evidence that the proliferation rate of printed cells was enhanced over 24 hr in culture. We have yet to confirm a mechanistic explanation of this effect.

DRIP fabrication was found to be a novel reactive printing technique enabling the

fabrication of cell-laden hydrogel constructs. The DRIP principle was effectively demonstrated through the formation of distinct hydrogel building blocks that were stabilised within a viscous GG plotting solution. These building blocks could be combined to form 3D hydrogel constructs, although shortcomings in the printing software limited control over the fabrication process. C2C12 cells encapsulated within GG hydrogels through DRIP fabrication maintained a rounded phenotype in subsequent culture, suggesting the need for modification of GG hydrogels to enhance cellular interactions, which is explored in Chapter 6.

4.7 Acknowledgements

Jeffrey Keisler and Roger Blake (University of Massachusetts, Boston) developed the software to convert bitmap images to .csv files for platemap dispensing to print 2D images.

5 INKJET CELL PRINTING

This chapter investigated the deposition of cells suspended in our bio-ink through inkjet printing, using Xaar-126 piezoelectric inkjet print heads housed in a custom printer (§2.4.1). Throughout this chapter, 'bio-ink' refers to a 0.05% (w/v) GG microgel suspension in DMEM containing 0.1% (v/v) P188 and 0.05% (v/v) Novec FC-4430.

5.1 Droplet and cell deposition

Cells (C2C12, PC12 and L929) were initially printed onto glass slides to provide a preliminary assessment of the deposition. Representative images of single printed droplets are displayed in Figure 5.1A-D. Droplets that contained cells (Figure 5.1B) had a similar size and shape to droplets without cells (Figure 5.1A), demonstrating that cells could be ejected cleanly through the nozzles of the print head. In some cases, however, printed droplets were accompanied by an associated satellite droplet (Figure 5.1C). Satellite droplets occurred even when printing without cells, but their frequency tended to increase with the concentration of cells in the bio-ink. These droplets only rarely contained a cell (Figure 5.1D) however, and thus even in printed patterns that exhibited several associated satellite droplets cells were normally contained within the desired pattern region (Figure 5.1E).

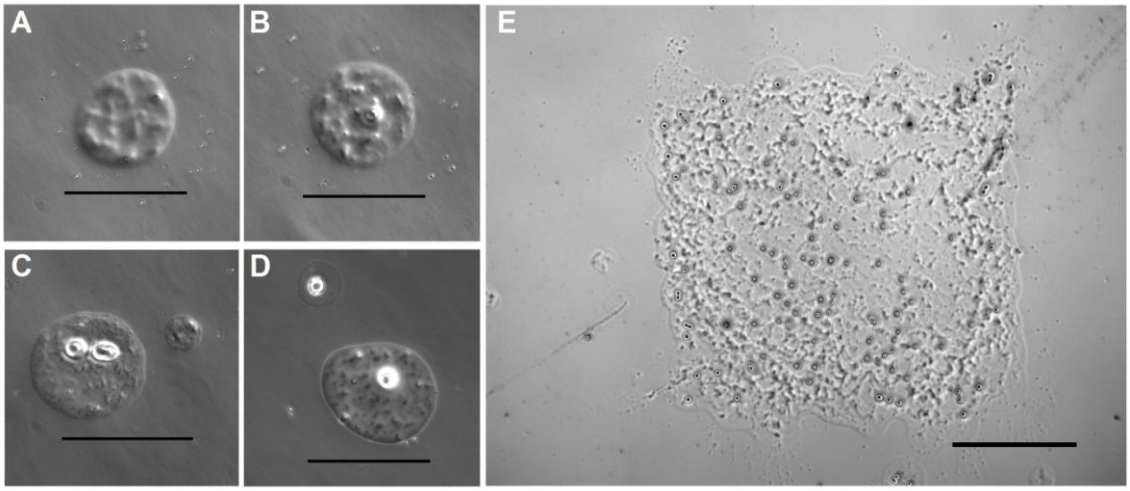

Figure 5.1: Printed cell droplets and patterns on glass slides. **(A-C)** Single droplets printed from bio-ink containing PC12 cells at $6x10^6$ cells/mL, showing droplets containing no cells (A), one cell (B), or multiple cells with an associated satellite droplet (C). Scale bars represent 200 µm. **(D)** A single droplet printed from bio-ink containing L929 cells at $6x10^6$ cells/mL, where the associated satellite droplet contains a cell. Scale bar represents 200 µm. **(E)** Printed square, 10x10 droplets, printed from bio-ink containing C2C12 cells at $6x10^6$ cells/mL. Scale bar represents 500 µm.

In the absence of a camera system that would allow direct visualisation of the dynamics of droplet formation during printing, images of printed patterns on glass provided an insight into the process. The presence of some satellite droplets was expected due to the fluid properties of the bio-ink, as discussed in Chapter 3 (§3.4). That the satellite droplet frequency increased with a higher cell concentration in the bio-ink suggests that the cells added even further complications to the dynamics of droplet formation. Exploring these complexities further was outside the scope of this thesis; nonetheless, printing performance with the bio-ink formulation was adequate in this case, as evidenced by the achieved pattern fidelity.

The manufacturer-specified nominal drop volume for the Xaar-126 heads used in this work was 80 pL. Considering the modifications made to the print head, and the use of a non-standard ink formulation, we employed a method (§2.4.4) to determine the actual volume of bio-ink droplets ejected using a standard printing waveform. The absorbance of light at 560 nm by phenol red present in the DMEM component of the bio-ink was measured as a function of known volumes of ink to produce a calibration curve (Figure 5.2A). Samples were then printed with an increasing number of layers in a square pattern containing 900 droplets, and the absorbance measured after washing the printed material into a well plate (Figure 5.2B). This allowed the absorbance per droplet to be calculated and converted, using the calibration curve, to a printed droplet volume of 262 ± 9 pL. The large droplet volume compared to the nominal droplet volume is likely a result of the ink fluid properties, the removal of the filter, and/or the presence of cells. Reis and co-workers showed that the volume of droplets ejected from piezoelectric inkjet printers increases with the Z number (reciprocal of the Ohnesorge number) of the ink *(352)*. We showed in Chapter 3 (§3.4) that our bio-ink has a Z number slightly higher than the optimal range for inkjet printing. The measured droplet volume was used to give an indication of expected printed cell numbers in further experiments.

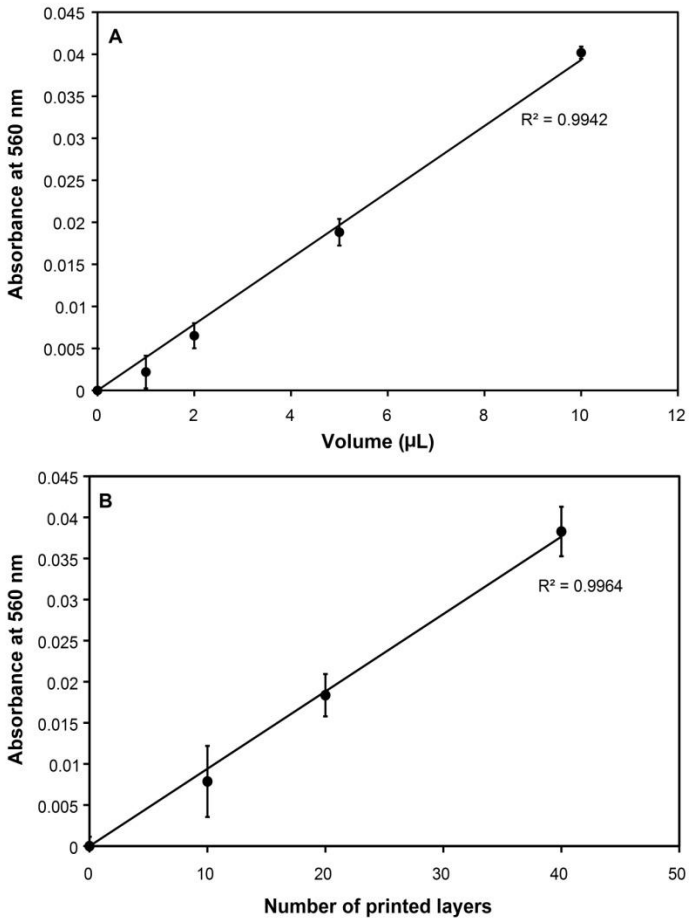

Figure 5.2: Determination of printed drop volume, using bio-ink containing 0.01% (v/v) Triton X100 as the surfactant component and fixed C2C12 cells suspended at $5x10^5$ cells/mL. **(A)** Calibration curve showing absorbance of phenol red in bio-ink as a function of pipetted volume. **(B)** Absorbance of phenol red as a function of the number of printed layers of bio-ink, for a square pattern containing 900 drops per layer. Error bars represent one standard error of the mean (n≥3).

An attractive feature of inkjet printing for cell deposition is its capacity for high resolution deposition. The average diameter of droplets in this work (Figure 5.1), once on the substrate, was 172 ± 11 µm. This does not necessarily equate to the minimum feature size achievable, as the diameter is dependent on droplet volume as well as the properties of the fluid and substrate that control droplet spreading. Deposition onto a different substrate (for example, one where instantaneous gelation takes place), or altering the printing waveform to achieve droplet volumes closer to the nominal volume of 80 pL, could enable smaller features to be printed. Importantly, this demonstrates that inkjet printing provides the capability to deposit structures smaller than the diffusion limit of oxygen in tissues (~200 µm), which is a key advantage of inkjet printing over microvalve printing (§4.1).

5.2 Printing reproducibility and distribution

Droplet deposition, as presented in the previous section, is dependent on the fluid properties of the ink (i.e. viscosity and surface tension). The reproducibility and distribution of cell output across the width of the multiple-nozzle print heads used in this work is dependent on factors including ink flow through the print head and cell settling (or the lack thereof). One important step required to allow cell printing with the Xaar-126 print heads was the removal of an internal filter, as described in the experimental section (§2.4.1), which has also been necessary in previous work using thermal inkjet print heads *(218)*. The method of ink supply was also optimised to achieve an even distribution of cell deposition from all nozzles. When a single ink inlet was used (Figure 2.21A), cell output decreased from nozzles that were further from the ink supply (Figure 5.3A). This was rectified by using a paired inlet approach (Figure 2.21B), which gave more even cell output across all nozzles (Figure 5.3B). Regular priming (application of pressure to force a small amount of ink through the nozzles) was also found to aid in achieving reproducible cell output over successive printed samples (Figure 5.3). It should be noted that these initial optimisation experiments were carried out with fixed C2C12 cells suspended at $5x10^5$ cells/mL in a bio-ink containing 0.01% (v/v) Triton X-100 as a surfactant.

The reproducibility and distribution of cell output was also investigated by printing live C2C12 cells from bio-ink containing the Novec FC-4430 and P188 surfactants onto glass slides in patterns that allowed statistical analysis of the deposition. In order to confirm even cell deposition across the width of the print head, squares containing 10x10 droplets were printed in six lateral positions in a single pass (Figure 5.4A). Three samples were printed successively, and the number of cells in replicate squares and replicate samples were combined to give an average for each position (Figure 5.4B). A one-way ANOVA test of the average printed cell numbers for the six positions indicated no statistically significant difference, showing that cell deposition was evenly distributed across the width of the print head.

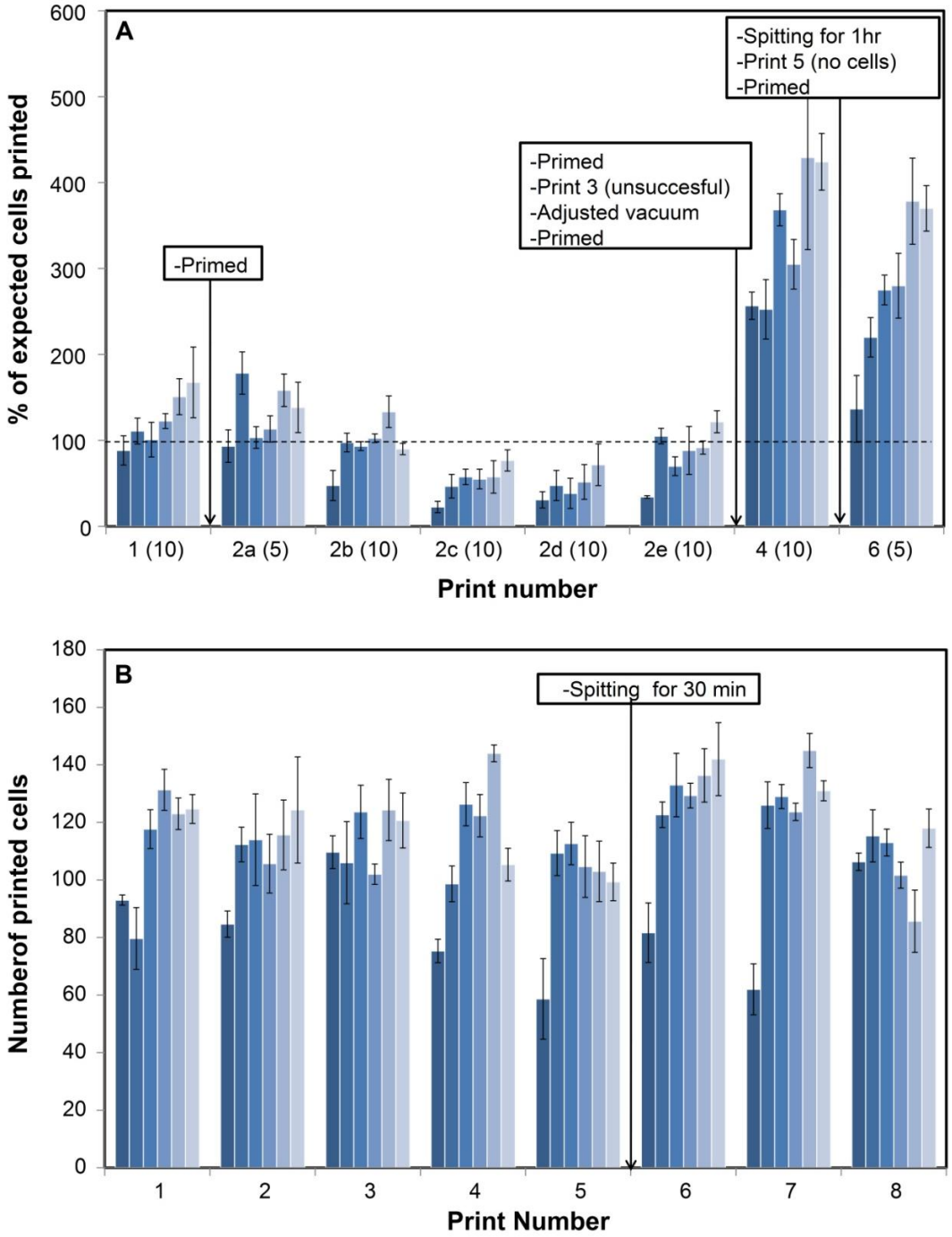

Figure 5.3: Distribution and reproducibility of cell output (fixed C2C12 cells) from a Xaar-126 print head. Cells were suspended at $5x10^5$ cells/mL in bio-ink with 0.01% (v/v) Triton X-100 as surfactant. The six columns in each group represent deposition from six groups of 10 adjacent nozzles across the width of the print head. Sequential print numbers refer to sequentially printed samples, and boxes refer to any significant actions between prints. **(A)** Deposition without regular priming, using a single ink inlet. Columns on the right of each group represent nozzles closer to the ink inlet. Brackets following the print number indicate the number of printed layers in each sample. To account for different number of layers, cell output is presented as a percentage of expected cell output based on theoretical calculations. **(B)** Deposition with regular priming in between each sequential printed sample (each sample was 10 layers), using a paired ink inlet. Note that the first column in each group shows low cell numbers due to some nozzles being blocked in this part of the print head. Error bars represent one standard error of the mean ($n \geq 3$).

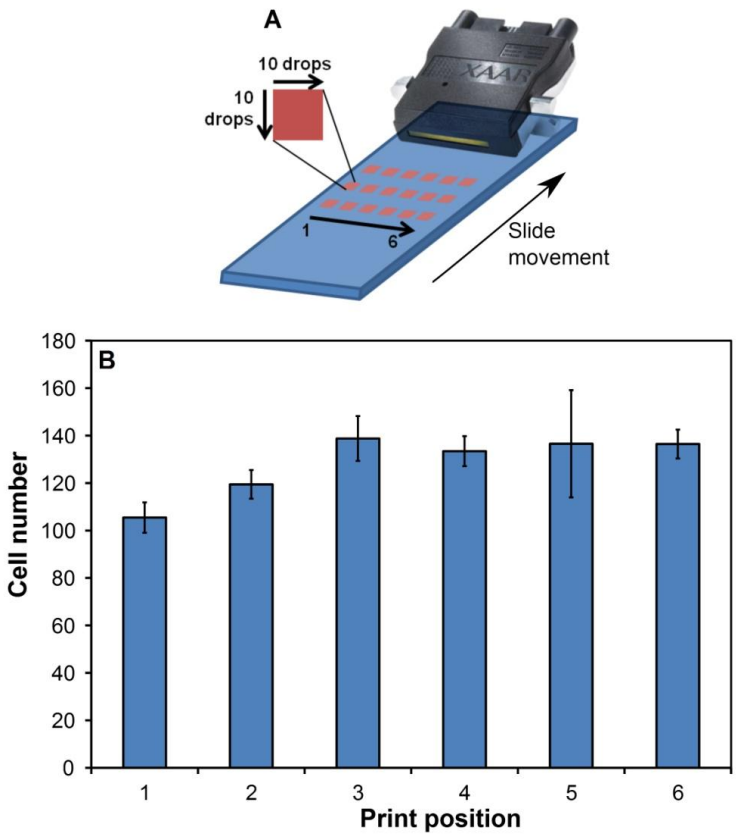

Figure 5.4: (A) Printed cell number across print head width, analysed by counting cells printed in continuous squares of 10x10 droplets (each utilising 10 adjacent nozzles). Each sample contained 18 replicate squares as illustrated, printed in a single pass. **(B)** Average cell number in the six squares positioned across the print head width, in a typical experiment where C2C12 cells were printed from a suspension at $6x10^6$ cells/mL in surfactant-containing bio-ink. For each position, three vertical replicates in three sequentially printed samples were averaged (n=9). Error bars represent one standard error of the mean.

As discussed in Chapter 4, the distribution of the number of cells in each deposited droplet is important for the fabrication of cell-based microarrays. For inkjet printing, this was assessed by depositing arrays containing 10x10 separated single droplets in three lateral positions across the width of the print head (Figure 5.5A). As was the case for microvalve printing (§4.2), a frequency histogram of the number of cells per printed droplet closely represented a Poisson distribution (Figure 5.5B). The practical implications of this distribution are discussed later in this Chapter in the context of using printed cell microarrays in a mass-spectrometric analysis application (§5.4).

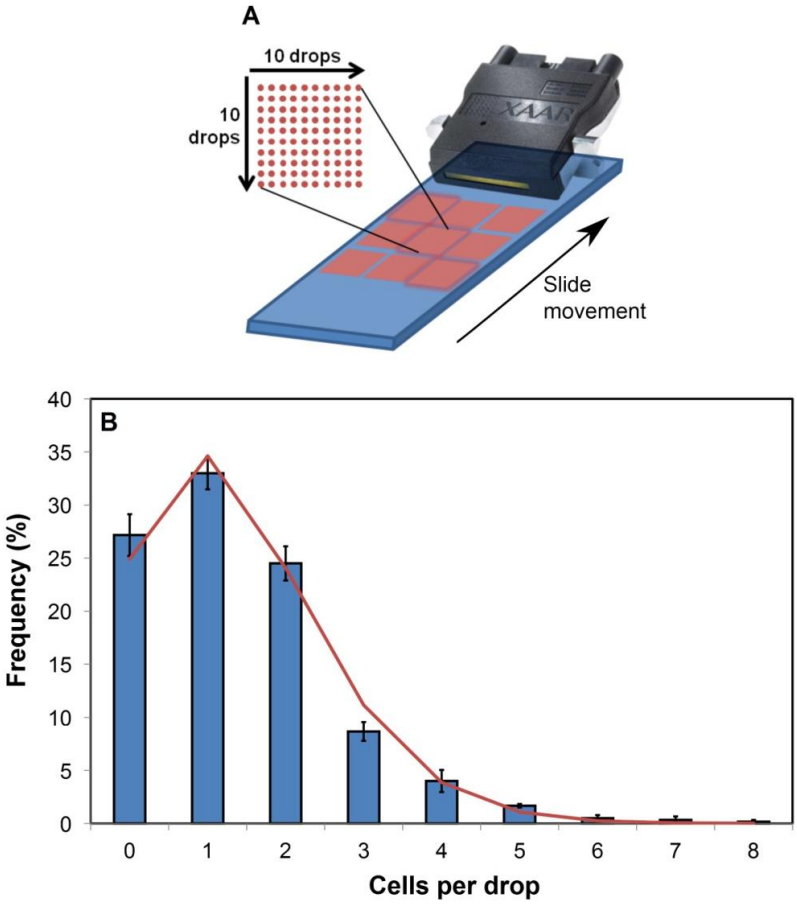

Figure 5.5: (A) Cells per droplet distribution was analysed by counting cells in individual drops printed in 10x10 digital arrays. Each sample contained 9 replicate arrays as illustrated, printed in a single pass. **(B)** Frequency distribution (columns) of the number of cells within individual printed droplets, in a typical experiment where C2C12 cells were printed from a suspension at $6x10^6$ cells/mL in surfactant-containing bio-ink. These values were obtained by averaging the distributions in 3 arrays across the print head width (highlighted arrays in (A)) for two samples printed sequentially. Error bars represent one standard error of the mean (n=6). Line graph represents a Poisson distribution, calculated using Equation 4.1 and the total average of cells per drop (λ) in the analysed arrays (λ = 1.4 in this case).

A single Xaar-126 print head was used for the majority of the cell printing work presented in this chapter. Extensive printing experiments were conducted over the space of ~1 year. Although printing performance was not quantitatively monitored over this period, general observation of jetting performance (i.e. pattern fidelity, satellite droplet formation) did not indicate any clear signs of deterioration. This is in contrast to reports outlining relatively short lifetimes before failure for thermal inkjet print heads when printing salt-based solutions, where evaporation led to crystallisation within the print head that adversely effected performance *(216)*.

5.3 Printed cell response

5.3.1 Phenotypic analysis

Previously in this thesis (§3.3.2), we demonstrated that exposure to the bio-ink for up to 2 hr caused no reduction in the viability of C2C12 or PC12 cells. Here, we investigated cellular responses to the printing process by printing cells directly into cell culture media and studying key phenotypic indicators: viability and morphology (by live/dead staining); proliferation by the MTS assay of metabolic activity; and differentiation by immunostaining.

Live/dead staining results from typical printing experiments presented in Figure 5.6A indicated that both C2C12 and PC12 cells could be printed with > 95% viability. While printed C2C12 viability was comparable to unprinted controls, printed PC12 cells showed a slightly lower viability which could be due to the tendency of these cells to persist as small cell aggregates that would be more restricted in their passage through the printer. This is highlighted by the images of printed and control PC12 cells in Figure 5.6B, where in both cases several multi-cell aggregates can be seen. Control PC12 cells contained larger aggregates, as naturally-occurring continued aggregation of these cells was not hindered by the bio-ink. Apart from this, there were no indications of morphological differences between printed and control cells for either cell line.

For analysis of printed cell proliferation and differentiation, the results presented in this chapter compare the response of printed cells to those exposed to the bio-ink for an equivalent time period (control). An MTS metabolic assay (§2.1.6) over 48 hrs in culture showed that printed C2C12 and PC12 cells proliferated at a rate comparable to controls (Figure 5.7). There was no statistically significant difference, determined by an unpaired Student's t-test, between printed and control cells at any time point. This result is in agreement with previous reports which show normal proliferative behaviour of cells printed using single-nozzle piezoelectric Microdrop *(214)* and Microjet *(212)* printers.

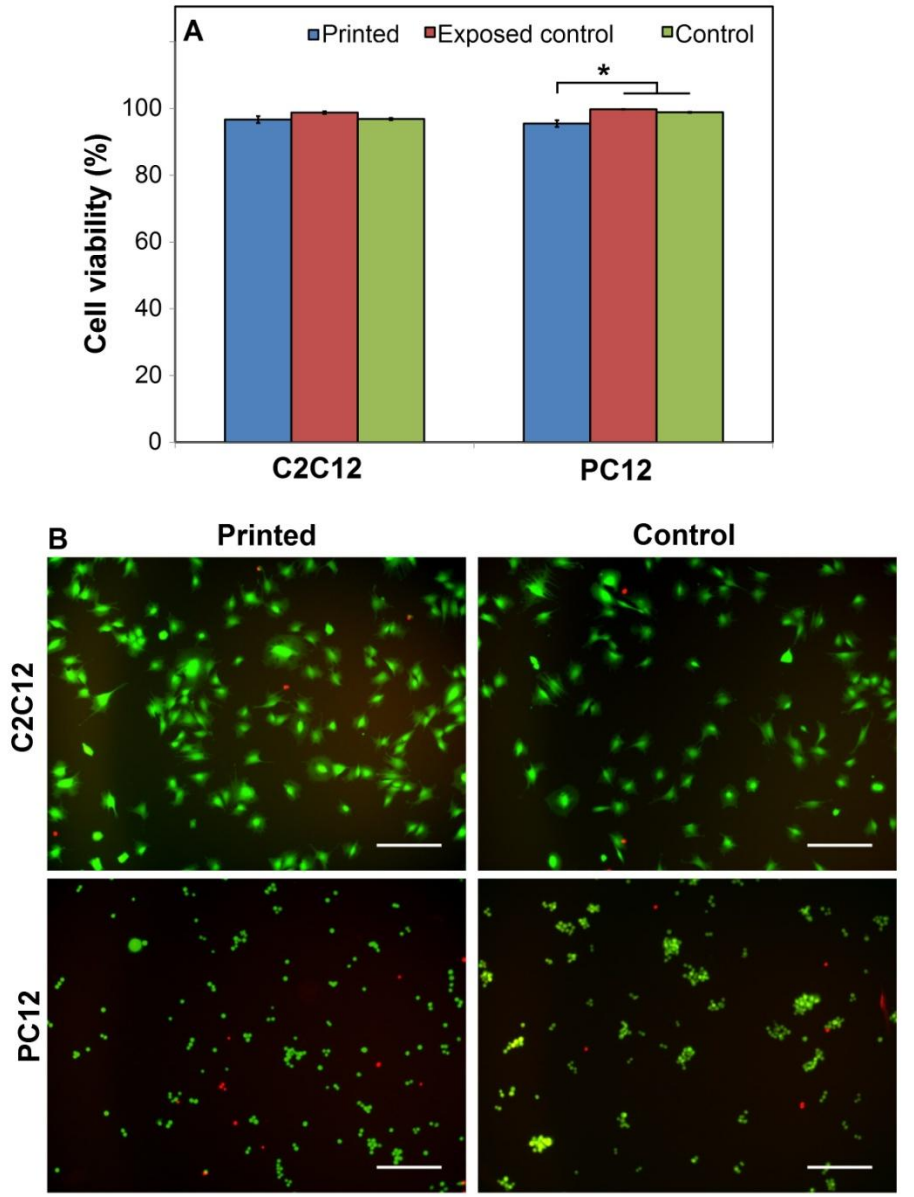

Figure 5.6: (A) Viability (assessed by live/dead staining after 2 hrs in culture) of C2C12 and PC12 cells from typical experiments where cells were suspended in the bio-ink and either pipetted (exposed control) or printed into cell culture medium. Control cells were suspended in DMEM for equivalent times to exposed and printed cells. Error bars represent one standard error of the mean ($n \geq 3$). Statistical significance was analysed by a Student's t-test, with significance level as indicated; $P < 0.05$ (*). **(B)** Representative live(green)/dead(red) staining of printed C2C12 and PC12 cells and non-printed controls. Cells were stained and imaged after 2 hrs in culture. Scale bars represent 200 µm.

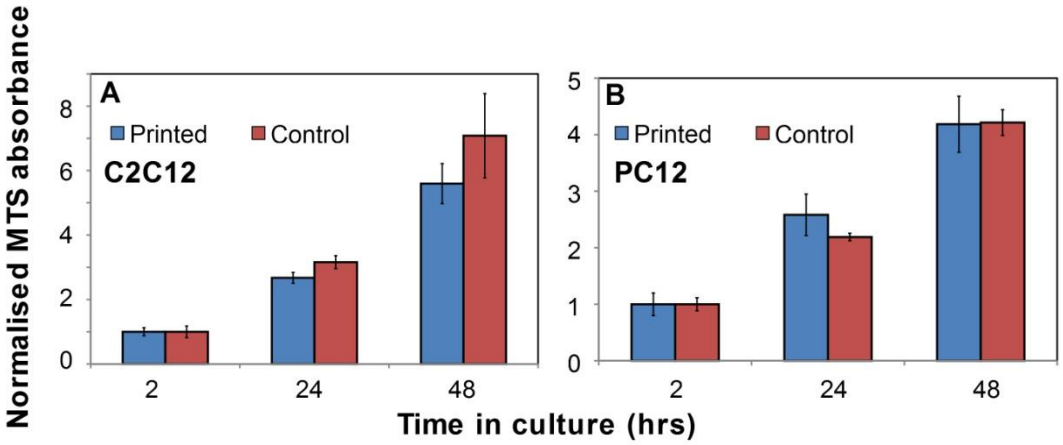

Figure 5.7: MTS metabolic assay indicating the proliferation of printed and control C2C12 (A) and PC12 (B) cells over 48 hrs in culture. Absorbance was normalised to the value obtained after 2 hr in culture. Error bars represent one standard error of the mean (n≥3).

The differentiation potential of these cell lines was then assessed. Printed C2C12 cells were subsequently differentiated on tissue culture polystyrene (TCPS) and stained for the muscle protein desmin (Figure 5.8A). Compared with control cells (Figure 5.8B), no apparent differences in desmin expression or multi-nucleation density were observed. Phalloidin staining of the F-actin filaments of printed PC12 cells differentiated on TCPS (Figure 5.8C) revealed wide-spread neurite extension and no apparent morphological differences to control cells (Figure 5.8D).

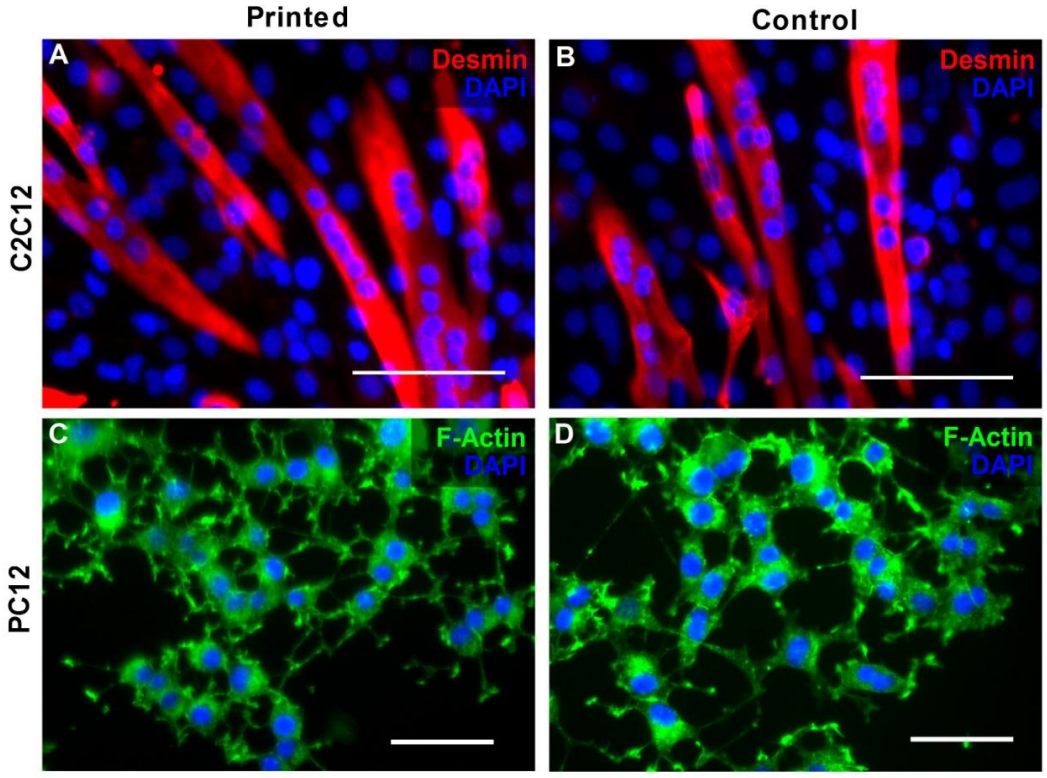

Figure 5.8: Differentiated C2C12 (A,B) and PC12 (C,D) cells on tissue culture polystyrene, comparing printed (A,C) and control (B,D) cells. Cells were stained for desmin (C2C12) or F-actin (PC12). Scale bars represent 100 µm (C2C12) or 50 µm (PC12).

5.3.2 Protective effect of P188

It was demonstrated in Chapter 3 of this thesis (§3.3.1) that the P188 surfactant did not contribute to the surface tension reduction in the complete surfactant-containing bio-ink formulation (i.e. the Novec FC-4430 surfactant dominates surface tension). The P188 surfactant was included for its ability to protect cells from shear-induced damage (§3.2.2). It was therefore important to investigate whether P188 significantly influenced printed cell viability in order to justify its inclusion in the bio-ink. In a previous report, hepatocytes printed from an ink containing 0.05% (v/v) P188 onto collagen using a single-nozzle Microdrop printer had a viability > 95% *(214)*, although it was not directly demonstrated whether the P188 influenced the viability. Figure 5.9A and B show live/dead stained images of printed cells which indicate that omitting P188 from the bio-ink resulted in greater cell death in printed cell populations after 2 hrs in culture. Conversely, the viability of purged cells (forced through the print head by application of positive pressure), with or without P188 (Figure 5.9C,D), was comparable to controls (Figure 5.9E,F). The purged cells were not subjected to actuation of the piezoelectric firing chamber, and were likely ejected from the print head at a lower velocity than printed cells. This implicates forces experienced by cells during droplet generation or impact as the cause for the cell death observed when printing without P188, and demonstrates that P188 provided some protection from these forces resulting in enhanced cell viability. Quantitative analysis of cell viability by live/dead staining confirmed that omission of P188 from the bio-ink led to a statistically significant (by Student's t-test, $P<0.05$) reduction in printed cell viability compared to cells printed from bio-ink containing P188, and non-printed controls (Figure 5.9G). The viability without P188 (88 ± 4%) is comparable to previous work where cells were printed from thermal inkjet heads (HP-26 cartridge) with a similar size (50 µm) and number of nozzles (50 nozzles per print head). Cell viability has been reported at ~ 90% for a range of different cell types printed using these heads, including Chinese Hamster Ovary (CHO) cells *(197, 199)*, human articular chondrocytes *(353)* and beta-TC6 cells *(207)*.

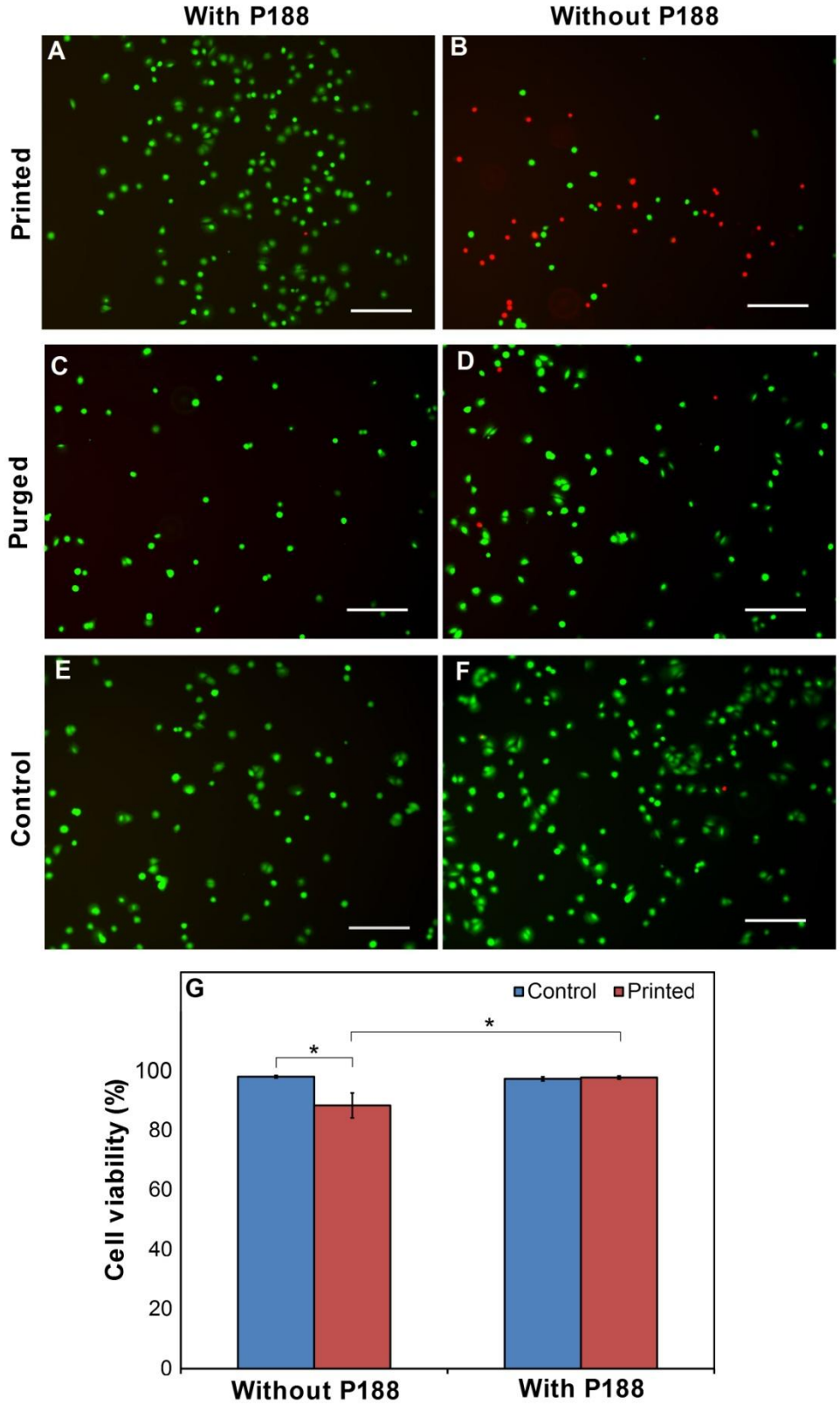

Figure 5.9: The protective effect of P188 surfactant on printed C2C12 cells. **(A-F)** C2C12 cells were suspended at $1x10^6$ cells/mL in a bio-ink with (A,C,E) or without (B,D,F) 0.1% (v/v) P188 and either printed (A,B) or purged (C,D) into cell culture medium, and compared to controls (E,F) that were exposed to bio-ink and pipetted into wells. Cells were cultured for 2 hrs before live/dead staining. Scale bars represent 200 µm. **(G)** Viability, assessed by live/dead staining after 2 hrs in culture, of C2C12 cells suspended at $6x10^6$ cells/mL in bio-ink and printed into cell culture medium. Viability is compared to control cells that were exposed to bio-ink but not printed. Error bars represent one standard error of the mean ($n \geq 3$). Statistical significance was analysed by a Student's t-test, with significance level as indicated; $P < 0.05$ (*).

5.3.3 Printing cells over an extended time period

One of the primary objectives of developing the bio-ink was to be able to print cells over longer time periods than previously possible. Cell settling experiments (§3.3.4.2) showed that the bio-ink maintained a single-cell suspension in culture plates, with no observed settling or aggregation. We endeavoured to show that this suspending ability was retained within the inkjet print head. To demonstrate this, we printed C2C12 cells immediately, and then 1 hour after loading into the print head. After this 1 hour gap in printing, cell viability (Figure 5.10A) and the printed cell density (average number of cells/drop) (Figure 5.10B) were not significantly different to initial values ($P>0.05$). Representative live/dead stained images of cells printed at these different time points (Figure 5.10C and D) show cells with similar density, morphology and viability.

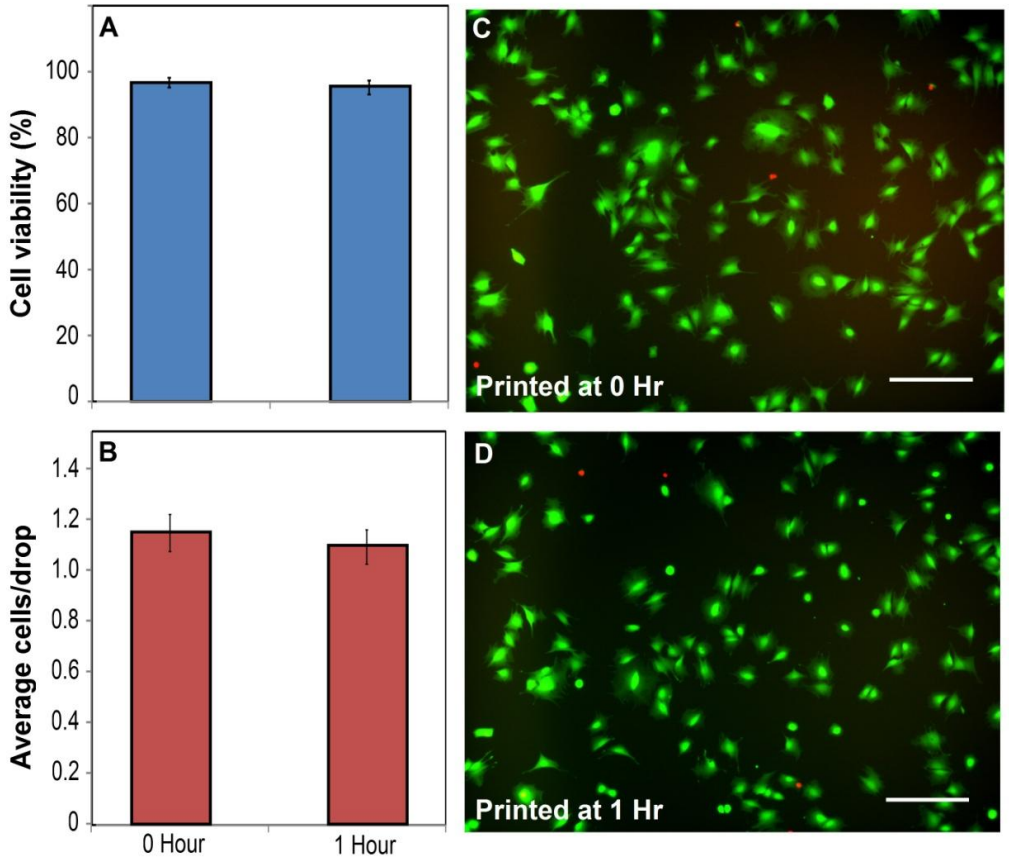

Figure 5.10: Comparison of C2C12 cell printing immediately, and 1 hr after loading the cells into the print head. **(A)** Cell viability (assessed by live/dead staining after 2 hours in culture) at both time points. **(B)** Average number of cells/drop at each time point. Error bars represent one standard error of the mean ($n\geq3$). **(C,D)** Live/dead stained cells after 2 hrs in culture, for cells printed immediately (C) and 1 hr (D) after loading into the print head. Scale bars represent 200 µm.

Work reported in this chapter has demonstrated the utility of the bio-ink in enabling controlled and reproducible deposition of viable cells through inkjet printing. The following sections outline three demonstrations of the use of this capability in the fabrication of cell micro-arrays, patterned co-cultures and cell-encapsulating hydrogels.

5.4 Application 1: Mass spectrometry of single printed cells

The work presented in this section was conducted in collaboration with Shane Ellis (PhD student, School of Chemistry, University of Wollongong), and has been published *(308)*. An outline of the contribution by each author is provided in the acknowledgments section at the end of this chapter.

Having demonstrated good control over cell patterning, even at the single-cell level, we endeavoured to show that printed cellular arrays could be utilised to subsequently detect and characterise cell-based analytes with single-cell resolution. The study of single cells is at the forefront of analytical chemistry; it provides insights into many important physiological processes that occur in individual cells, as well as the heterogeneity of cell populations, and could aid in the detection and diagnosis of disease. Recent reviews on single-cell analysis provide a good overview of the various techniques and applications in the field *(354, 355)*. Mass spectrometry (MS) is one powerful method that can provide an expanse of both qualitative and quantitative information about cellular components including proteins, peptides, glycoproteins, lipids and metabolites. Analysis on the single cell level has been facilitated by advances in the sensitivity and spatial resolution of MS techniques, which are also the subject of a recent review *(356)*. Most commonly these analyses have been implemented by sampling via extraction using a fine capillary *(357)*, or the ablation of single cells using a focussed laser *(358)* or ion beam *(359)*.

Liquid Extraction Surface Analysis (LESA) is a relatively new surface sampling technique where a liquid micro-junction is created between the substrate of interest and a conductive tip; extracted analytes are then injected into a nano-electrospray ionisation (nano-ESI) source coupled to a mass spectrometer (MS) *(360)*. LESA-MS has been applied to biological systems previously, for example in the study of the distribution of drugs and their metabolites in tissue sections *(361)*. We sought to

couple this technique with inkjet printing of cell microarrays to enable analysis of individual cells by LESA-MS. In this proof-of-principle study, we chose to detect and characterise the lipid profiles of these printed cells. Lipids are ideal targets for direct analysis of single cells owing to their high concentrations near the surface (i.e. in cell membranes). Once considered spectators to biological interactions, lipids are now recognised to possess key roles in biochemical processes and have been implicated in numerous disease states *(362, 363)*.

Three different cell lines (C2C12, PC12 and L929 cells) were suspended in the bio-ink and printed into micro-arrays on glass slides (Figure 5.11A). The number of cells contained in each array region (Figure 5.11B) was controlled by changing the number of deposited droplets (§2.4.6). The printed droplets dried quickly on the glass slide, which resulted in dehydration of the cells. Techniques have been described to avoid this dehydration (i.e. covering the printed droplets in a thin oil layer *(215)*, but for the purposes of this experiment, analysis on dehydrated cells was sufficient. The number of cells in each array region was determined post-printing by microscopic visualisation. While this step was time consuming, it was unavoidable due to the random distribution of cells within the bio-ink, and the resultant Poisson distribution of the number of cells in each printed droplet (§5.2). In fact, this distribution defines a fundamental limit on the 'dispensing efficiency' (percentage of droplets containing a single cell) of ~37% (for λ=1 in Equation 4.1). One approach that has attempted to address this problem was reported by Yusof and co-workers *(364)*, where a specially designed dispenser chip (called the single-cell manipulator, SCM) contained an optical particle detection mechanism and sorting algorithm. The chip dispensed to waste unless a single cell was detected close to the outlet nozzle, and although this technique was slow and showed relatively low printed cell viability, the dispensing efficiency reached a maximum of 87%. Printed arrays were subsequently analysed by LESA-MS (Figure 5.11C) as described in Chapter 2 (§2.4.6). Microscope images of the same array region before (Figure 5.11D) and after (Figure 5.11E) LESA sampling showed some remaining cell material, indicating that only a fraction of the cell content was analysed in this case.

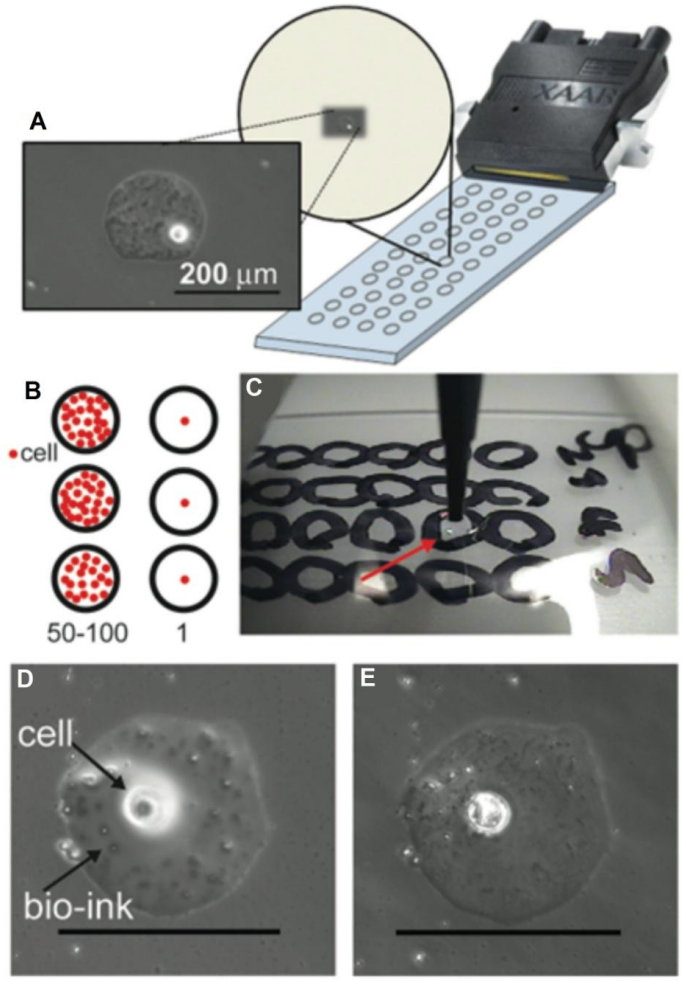

Figure 5.11: Printing cellular arrays for analysis by LESA-MS. **(A)** Schematic representing the deposition from a Xaar-126 print head of a single cell spot into a micro-array on a glass slide. **(B)** Either 100 droplets (50-100 cells) or a single droplet (average 1 cell) were deposited into array regions. **(C)** Image showing the LESA probe depositing solvent on a printed cell spot. **(D,E)** Comparison of droplet containing a single L929 cell before (D) and after (E) LESA analysis. Scale bars represent 200 µm.

Lipid profiling from printed cells was first demonstrated on array spots containing up to 100 cells (Figure 5.12A-C). A variety of lipid classes including cholesterol esters, triacylglycerides, ceramides, glycosphingolipids, phosphatidylcholines (PC) and sphingomyelins (SM) could be detected in printed cells. PC and SM lipids were the most abundant species and were thus the focus of further characterisation. PC and SM lipid profiles were also readily obtained from array spots containing single L929, C2C12 and PC12 cells (Figure 5.12D-F). In each case, the spectra from single cells showed the same PC and SM lipids with similar relative abundances observed for array spots containing up to 100 cells. As expected, the peak signal was lower when analysing single cells (Figure 5.12). These single cell spectra were reproducible for each cell type, and highlighted the excellent sensitivity of this technique.

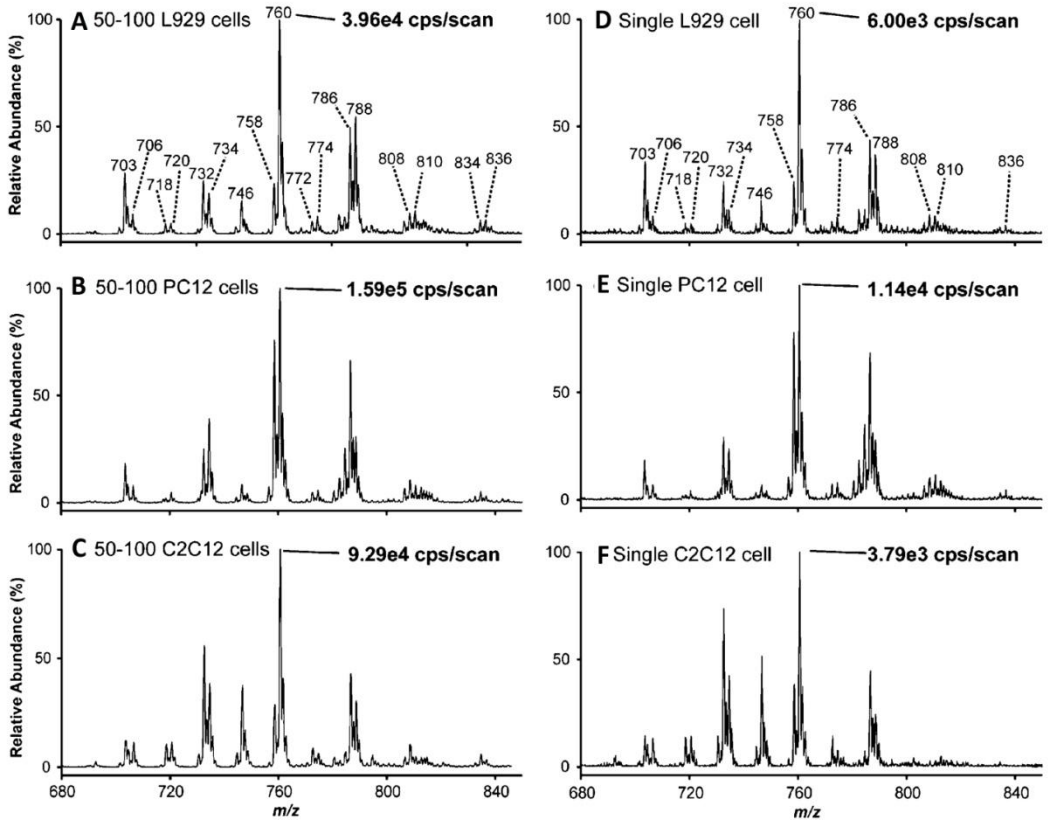

Figure 5.12: Precursor ion scans (PIS) on inkjet printed cells. **(A-C)** Typical m/z 184.1 PIS obtained from printed cell microarray spots (50−100 cells per spot) of L929 (A), PC12 (B), and C2C12 (C) cells. Spectra were produced from 100 summed PIS. **(D-F)** Typical m/z 184.1 PIS on printed cell microarray spots (1 cell per spot) of L929 (D), PC12 (E), and C2C12 (F) cells. Spectra were produced from 200 summed PIS. Values in the top right of each spectrum correspond to the average intensity in counts per second (cps) per scan of the base peak.

The PC and SM lipid profiles from each printed cell type provided a characteristic "fingerprint" that allowed differentiation of cell type by principal component analysis (PCA, §2.6.3). PCA plots produced using the spectral data from array spots containing up to 100 cells (Figure 5.13A), or single cells (Figure 5.13B) showed clear groupings based on cell type, indicating that each cell type's lipid profile was different and characteristic. Cell culture conditions are known to affect cellular lipid compositions *(365)*. While PC12 cells were cultured with a different serum composition to the other cell types, C2C12 and L929 cells were cultured under identical conditions and so the different lipid profiles observed for these cell types can be attributed to inherent differences in membrane composition. Non-printed L929 cells analysed by lipid extraction and direct infusion nano-ESI analysis also showed tight PCA grouping with printed L929 cells analysed by LESA-MS (Figure 5.13). This suggests that the printing and analysis process did not affect the lipid composition in cell membranes. This supports previous results presented in this

chapter which indicated no effect of printing on phenotypic cell response (§5.3). It also demonstrates that the components of the bio-ink formulation did not interfere with the detection of cell-based analytes. The fact that the spectral data from single cell spots of the same cell type (Figure 5.13B) were closely grouped suggests that there is little heterogeneity between individual cells for these cell lines. This could be a result of the preparation of cells under controlled culture conditions, or the fact that PC lipids perform primarily structural roles in the cell membrane and therefore are less subject to metabolic variation.

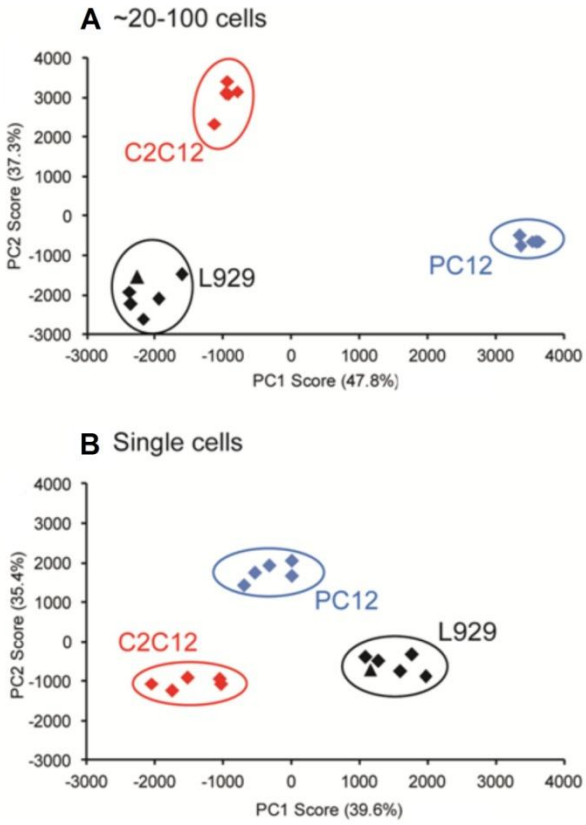

Figure 5.13: Principal component analysis (PCA) on inkjet printed cells. PCA score plots using PC/SM lipid profiles acquired from 5 microarray spots for each cell type (L929, C2C12, or PC12 cells) containing (A) up to 100 printed cells and (B) a single cell. Triangles indicate the data point obtained by direct infusion of lipid extract from non-printed L929 cells.

5.5 Application 2: Patterning multiple cell types

The fabrication of constructs containing multiple cell types is an important advance in the development of both engineered tissues and cell-based assay devices. To achieve functionality in engineered muscle tissues, for example, rapid integration with the host neuromuscular system is required. Several *in vitro* studies have shown that co-culturing muscle constructs with neural cells enhances muscle differentiation and force generation, and can lead to the formation of functional neuromuscular junctions *(366, 367)*. Spatial control over these cell-cell interactions could further illuminate the role of innervation in muscle development and enable the fabrication of tissue constructs with enhanced functionality. Additionally, spatially-defined arrays of neuromuscular and other co-cultures can be implemented as tissue test systems for drug discovery and the study of cell behaviour *(160, 190, 368)*. In this section, our work on the inkjet printing of multiple cell types to fabricate patterned co-cultures is presented.

For cells to remain alive after printing, they must be deposited into a hydrated environment. For experiments investigating the phenotypic response of printed cells, presented earlier (§5.3), we printed cells directly into cell culture medium. Printing and retaining a defined pattern of living cells, however, requires a different approach. To achieve this, we took the same approach used previously by others *(137, 197, 206, 219, 220)* and printed cells onto thin collagen hydrogels. These hydrogels provided a hydrated environment along with cell attachment cues, so that cell dehydration was prevented during the development of cell-substrate adhesions. We initially formed collagen hydrogels (4 mg/mL) in thin custom-made PDMS wells that were plasma-bonded to cleaned glass slides (§2.4.3). This resulted in uneven collagen surfaces due to the meniscus effect, and consequently dehydration in the centre of wells (where there was very little collagen) led to cell death (Figure 5.14A). This problem was solved by completely filling thin PDMS wells with collagen to achieve a flat hydrogel surface, and then attaching a replicate PDMS layer to act as a media reservoir (§2.4.3). We pre-equilibrated the collagen hydrogels in CPM for ~1 hr, removed all excess media prior to cell printing, and then allowed the printed cell patterns to attach to the collagen for ~1 hr in a humidified incubator prior to adding media on top of the patterns for continued culture. We found that this approach

facilitated good retention of printed patterns with no clear reduction of cell viability (Figure 5.14B). Some cells were found outside the pattern area (arrow in Figure 5.14B), although it was not clear if this was due to misfiring during printing or pattern disruption on media addition. Burg's group have thoroughly explored pattern fidelity in printed co-cultures *(220)*, and suggested several useful post-printing methods such as the application of media via a nebuliser or additional inkjet print head to avoid pattern disruption *(219)*.

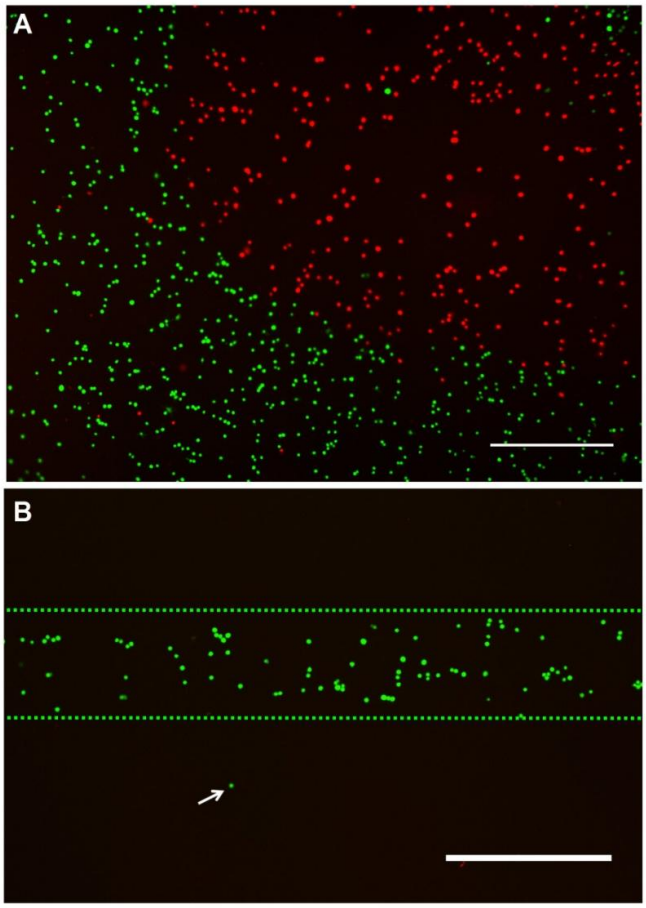

Figure 5.14: Printing a single cell type - C2C12 cells printed onto collagen hydrogel surfaces and live/dead stained after 2 hrs in culture. **(A)** Cells printed on an uneven hydrogel surface. Dehydration in the centre of well led to cell death (stained red). **(B)** Cells printed in a simple linear pattern on a flat hydrogel surface. Dotted lines indicate the outline of the printing pattern, and the white arrow highlights a cell outside the pattern region. Scale bars represent 500 µm.

Our custom printer housing was amenable to the inclusion of a second print head (§2.4.1) which allowed us to explore the simultaneous deposition of two different cell types onto collagen hydrogels to create patterned co-cultures (Figure 5.15A). C2C12 and PC12 cells were pre-stained with different CellTracker™ dyes (§2.1.4.2) prior to printing to allow identification of each cell type in the printed patterns. A relatively crude method was used to align the two print heads (§2.4.7), as more sophisticated methods such as those employed by Burg's group *(190)* were not available to us. Figure 5.15B,C show examples of printed patterns 1 hr after cell printing, following the addition of excess media. Again, several cells were misplaced, either during printing or on media addition, although general pattern fidelity was good. Printed patterns were subsequently cultured under differentiation conditions for 8 days to assess cell-substrate and cell-cell interactions. Cells were fixed and immunostained (§2.1.4.3), using two different antibodies to simultaneously stain desmin (C2C12) and β-III tubulin (PC12) (Figure 5.15D,E). The bio-ink did not impede cellular interactions with the collagen substrate and both neural (PC12) and skeletal muscle (C2C12) cells were unimpeded in their ability to express the respective neural (β-III tubulin) and skeletal muscle (desmin) markers and to differentiate normally, as evidenced by the extension of dense neural networks from PC12 cells into surrounding areas populated by skeletal muscle cells (Figure 5.15D,E)

The results exhibit the potential of the bio-ink to be utilised in printing multi-cellular structures and subsequent analysis of cell-cell and cell-substrate interactions. Multiple cell types have been patterned previously by inkjet printing *(190)*, however in this work cell types were printed sequentially. The process of loading both print heads with cells and aligning the print heads in our work took, on average, 30 minutes. During this time, cells would normally settle significantly within the print heads, but with the cells suspended in the bio-ink settling was avoided and cells could be printed at the desired density following completion of pre-printing procedures.

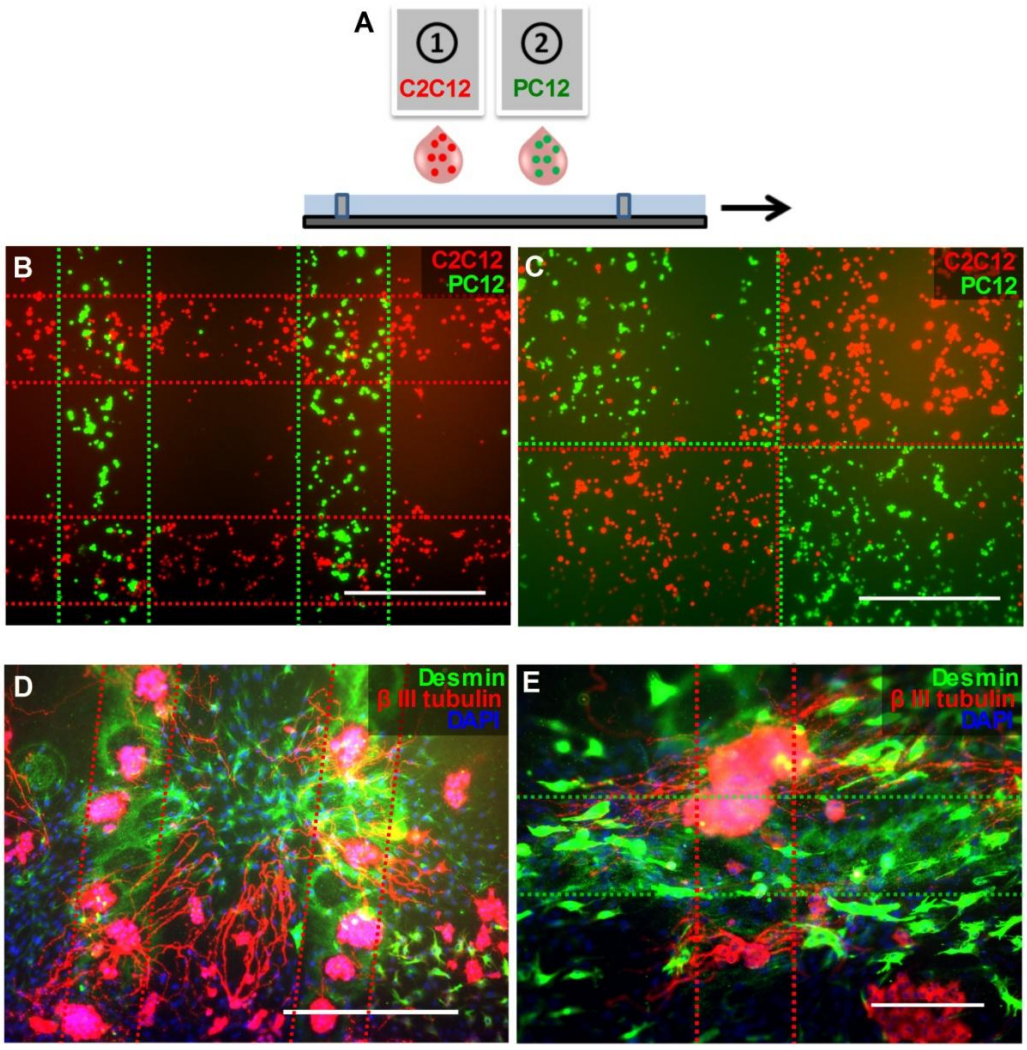

Figure 5.15: Patterns of two cell types printed simultaneously from two separate print heads onto collagen hydrogel substrates. **(A)** Schematic representation of multiple head printing. **(B,C)** C2C12 (red) and PC12 (green) cells pre-stained with CellTracker™ dyes and printed in various patterns. Images were taken 1 hr after printing, following the addition of culture media. **(D,E)** Printed cell patterns after 8 days under differentiation conditions. Cells were immunostained for desmin (C2C12, green) and β-III tubulin (PC12, red). Dotted lines represent the outline of the printing pattern. Scale bars represent 500 µm (B-D) and 200 µm (E).

5.6 Application 3: Reactive printing

A common approach to inkjet printing of living cells has been 'reactive printing', where cells are encapsulated in a hydrogel through a printing process in which the cell-containing ink is one component of a fast-gelling reactive system. These approaches, primarily using alginate/calcium and fibrin/thrombin systems, were described in the introduction to this thesis (§1.3.5). We explored similar reactive printing approaches using GG and our bio-ink.

In initial experiments, cells were printed from DMEM containing added $CaCl_2$ (20 mM) into a 0.5% (w/v) GG solution smeared on a glass slide (Figure 5.16A). The cell solution crosslinked GG at the points of droplet impact, and in this way a bulk hydrogel could be formed. This is analogous to work reported into the literature where cells in calcium-containing inks were printed into alginate solutions *(198, 205)*. In an extension of this approach, a modified GG solution and the cell suspension were printed from two separate print heads (Figure 5.16A) in overlapping patterns. Here, crosslinking occurred on combination of these solutions, and multiple layers of each component could be deposited to encapsulate cells in all-printed GG hydrogel structures (Figure 5.16B). This is, to the best of our knowledge, the first example of reactive bioprinting where cells and a hydrogel biomaterial have been printed from two separate inkjet print heads, and demonstrates the principle of separate cell and matrix deposition. It is also significant in that it achieves cell encapsulation while avoiding harsh temperature, pH or ionic conditions. After 5 days in culture, however, cells exhibited a rounded phenotype reflective of poorly attached cells. This was similar to the response of cells encapsulated in hydrogel structures through DRIP fabrication, presented in Chapter 4 (§4.5.2), and further confirmed the need for modification of GG to encourage cell attachment and growth (see Chapter 6).

Figure 5.17A displays preliminary results using the bio-ink in this reactive printing approach, illustrating that it was still possible to form cell encapsulating hydrogels. These hydrogels appeared weaker, however, than those in Figure 5.16B. This was likely due to a lack of added Ca^{2+} ions in the bio-ink. Notably, this work also showed that GG solutions could be printed effectively with surfactant as the only additive, without the need for the modification used to print the structures shown in Figure 5.16B. Although these experiments used Triton X-100, which was proven to be cytotoxic in Chapter 3, the non-cytotoxic fluorosurfactant Novec FC4430 would likely achieve comparable printability.

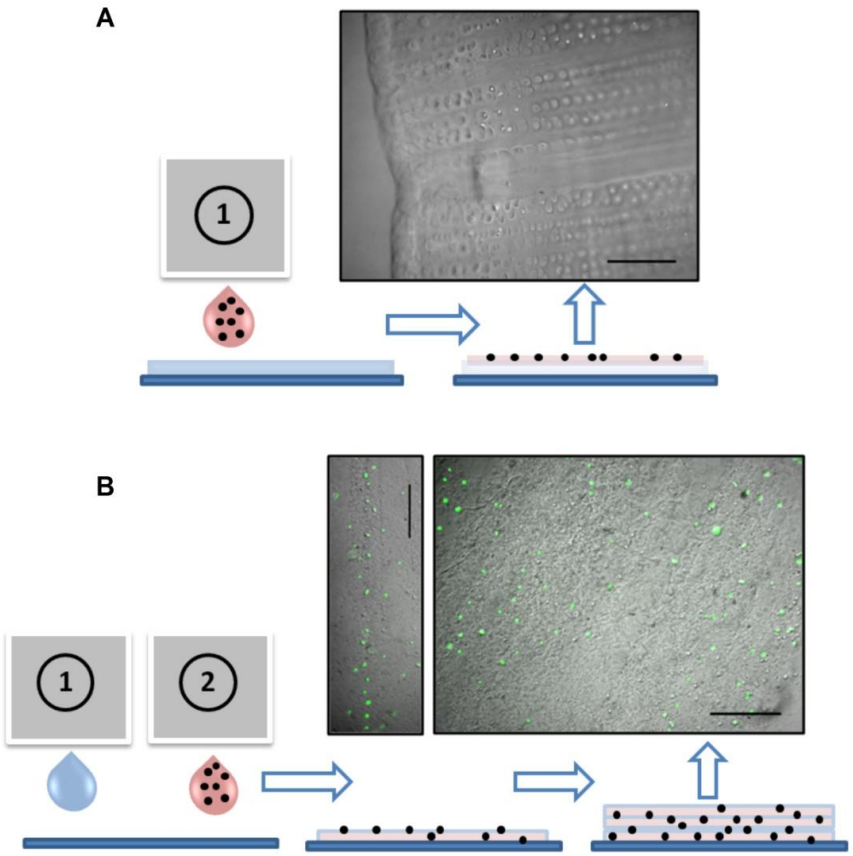

Figure 5.16: Reactive printing approaches. **(A)** Schematic representation of single-head approach. C2C12 cells were suspended in DMEM with 20mM $CaCl_2$ at $1x10^6$ cells/mL and printed into a thin layer of 0.5% (w/v) GG solution. Image shows hydrogel structure immediately after printing. Scale bar represents 500 µm. **(B)** Schematic representation of dual-head approach. Print heads contained: a 0.5% w/v GG solution that had been briefly sonicated and combined with 15% (w/v) glycerol and 0.2% (v/v) Tween-20; and a C2C12 cell suspension as above. Images display cells encapsulated in printed hydrogels, calcein stained after 5 days in culture. Scale bars represent 500 µm.

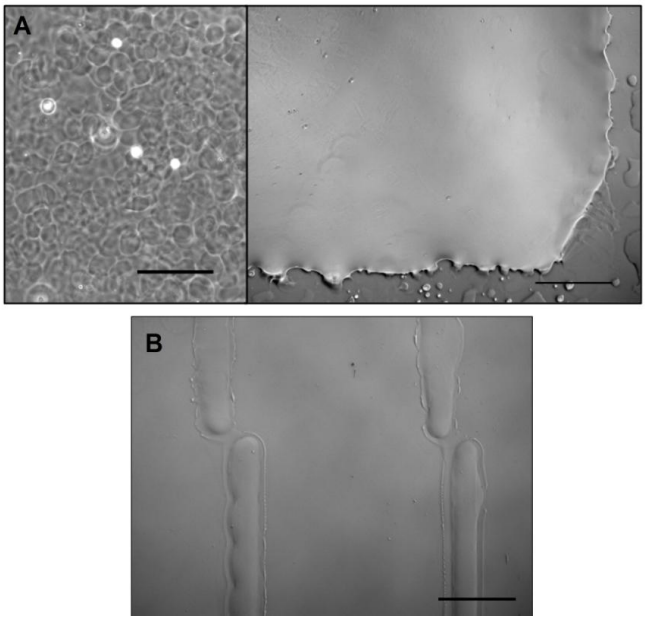

Figure 5.17: Reactive printing utilising the bio-ink. **(A)** Hydrogel (left – high magnification, right – low magnification) formed by dual-head reactive printing with bio-ink. Print heads contained: C2C12 at $2x10^6$ cells/mL in bio-ink with 0.01% (v/v) Triton X100 as surfactant; and a 0.5% w/v GG solution with 0.01% (v/v) Triton X100. Scale bars represent 200 µm (left) and 500 µm (right). **(B)** 32 layers of a printed pattern of 0.5% (w/v) GG solution with 0.01% (v/v) Triton X100. Scale bar represents 500 µm

5.7 Conclusions

The surfactant-containing bio-ink developed in Chapter 3 allowed effective cell deposition from multiple-nozzle Xaar-126 piezoelectric inkjet print heads. As expected from theoretical calculations there was some formation of satellite droplets, although these rarely contained a cell and so cell patterns could be printed with good fidelity. Measured droplet volume (~260 pL) was larger than the nominal drop volume for these print heads (80 pL), which was attributed to the bio-ink fluid properties or the presence of cells. Droplets produced spots with a diameter of ~170 µm after impact on a standard glass slide, which highlights the improved resolution of inkjet printing over microvalve printing (Chapter 4). As was the case for microvalve printing, the number of cells in each droplet followed a Poisson distribution. Cell output was evenly distributed across the width of the print head, and with regular priming output was reproducible over successive print cycles. The bio-ink effectively avoided cell settling and aggregation within the print head, as demonstrated by reproducible deposition of viable cells over a 1 hr period. One print head was used regularly over a ~ 1 year period with minimal, if any, deterioration, indicating that this was a robust approach to cell deposition.

The viability of printed C2C12 cells was comparable to controls while printed PC12 cells exhibited a slight reduction in viability, possibly due to their tendency to form clusters, although they remained >95% viable. Both printed cell types showed normal proliferation and differentiation in subsequent culture. These results highlight the efficacy of the bio-ink in simultaneously satisfying biological requirements (i.e. no cytotoxicity) as well as the multiple engineering requirements associated with deposition from multiple-nozzle piezoelectric inkjet print heads (i.e. viscosity, surface tension, no cell settling). It was also demonstrated quantitatively that P188 had a protective effect on C2C12 cells during the printing process; C2C12 cells printed from a bio-ink without P188 showed reduced viability (88 ± 4 %).

Three different applications of inkjet cell printing were then demonstrated to further highlight the utility of the bio-ink. Firstly, cells were printed into microarrays and subsequently analysed by LESA-MS, where PC and SM lipid profiles could be detected even from single cells. These profiles were characteristic of cell type

(C2C12, PC12, L929), and were similar to direct extracts from non-printed cells, which provides validation of the method. Secondly, the bio-ink enabled deposition of two cell types (C2C12 and PC12) simultaneously from two separate print heads onto collagen substrates. Highly viable cells were patterned with good fidelity, although these were not characterised quantitatively. Subsequent co-culture of these patterned constructs suggested that the bio-ink did not interfere with cell-substrate interactions, and that they could provide a useful system to study cell-cell interactions. Finally, in a preliminary demonstration of a reactive inkjet printing approach, C2C12 cells in bio-ink and GG solutions were printed from two different print heads to form cell-encapsulating hydrogels on combination. As was the case in Chapter 5, cells in printed GG hydrogel constructs maintained a rounded phenotype with no visible interaction with the surrounding gels. This provided further impetus for the GG modification strategies pursued in Chapter 6, as a means to improve the cell-substrate interactions.

5.8 Acknowledgements

The custom printer that housed the Xaar-126 print heads used in this work was developed and constructed by Dr. Don McCallum, Dr. Stephen Beirne and Binbin Zhang (University of Wollongong). Stephen modified the print heads by removing the internal filter. Stephen and Binbin provided advice in printer operation.

Shane Ellis (University of Wollongong) completed all the LESA-MS experiments and data analysis presented in this chapter (§5.4), and helped to prepare the figures. Todd Mitchell and Stephen Blanksby (University of Wollongong) also provided guidance for this collaborative project.

6 GELLAN GUM MODIFICATION

Work reported in previous chapters has shown that C2C12 cells encapsulated in GG hydrogels through reactive microvalve (Chapter 4) and inkjet (Chapter 5) printing processes did not interact with the surrounding matrix. In this chapter, the responses of cells seeded on the surface of, and encapsulated within, GG hydrogels were investigated further and strategies to encourage cell-hydrogel interactions were explored.

6.1 Gellan gum hydrogels

6.1.1 Surface-seeded and encapsulated cells

The response of C2C12 cells to GG hydrogels was first examined by seeding cells on pre-formed and equilibrated hydrogel surfaces (§2.5.1). The hydrogel composition was varied in terms of both GG concentration (0.1 - 1% w/v) and the amount of $CaCl_2$ (0 - 50 mM) added to the CCM used in gel formation. These concentrations were chosen as they encompassed the compositions we had previously found to provide optimal support for surface-seeded L929 fibroblast cells *(281)*. In this current work, however, C2C12 cells on the surface of all hydrogel compositions studied formed large multi-cellular aggregates, indicating that cell-cell adhesion was favoured over adhesion to the substrate. Representative images of cellular aggregates on both 0.5 and 0.1 % (w/v) GG hydrogels (formed using CCM with 5 mM added $CaCl_2$) over 10 days in culture are shown in Figure 6.1. The lack of cell-substrate interaction resulted in many cell aggregates being washed off the hydrogel surface with media changes over the culture period, particularly for cells on 0.5% (w/v) GG (Figure 6.1E). Cell aggregates on 0.1% (w/v) GG hydrogels were comparatively smaller and more numerous, and after 10 days a slightly flattened morphology was observed in some aggregates (Figure 6.1F). This may suggest increased interaction with the substrate. Our previous work also showed a more favourable cell response on hydrogels with lower GG concentration, and this correlated with the mechanical properties of the material *(281)*. Nonetheless, these results highlight that for both GG concentrations, the hydrogels did not provide a permissive growth substrate.

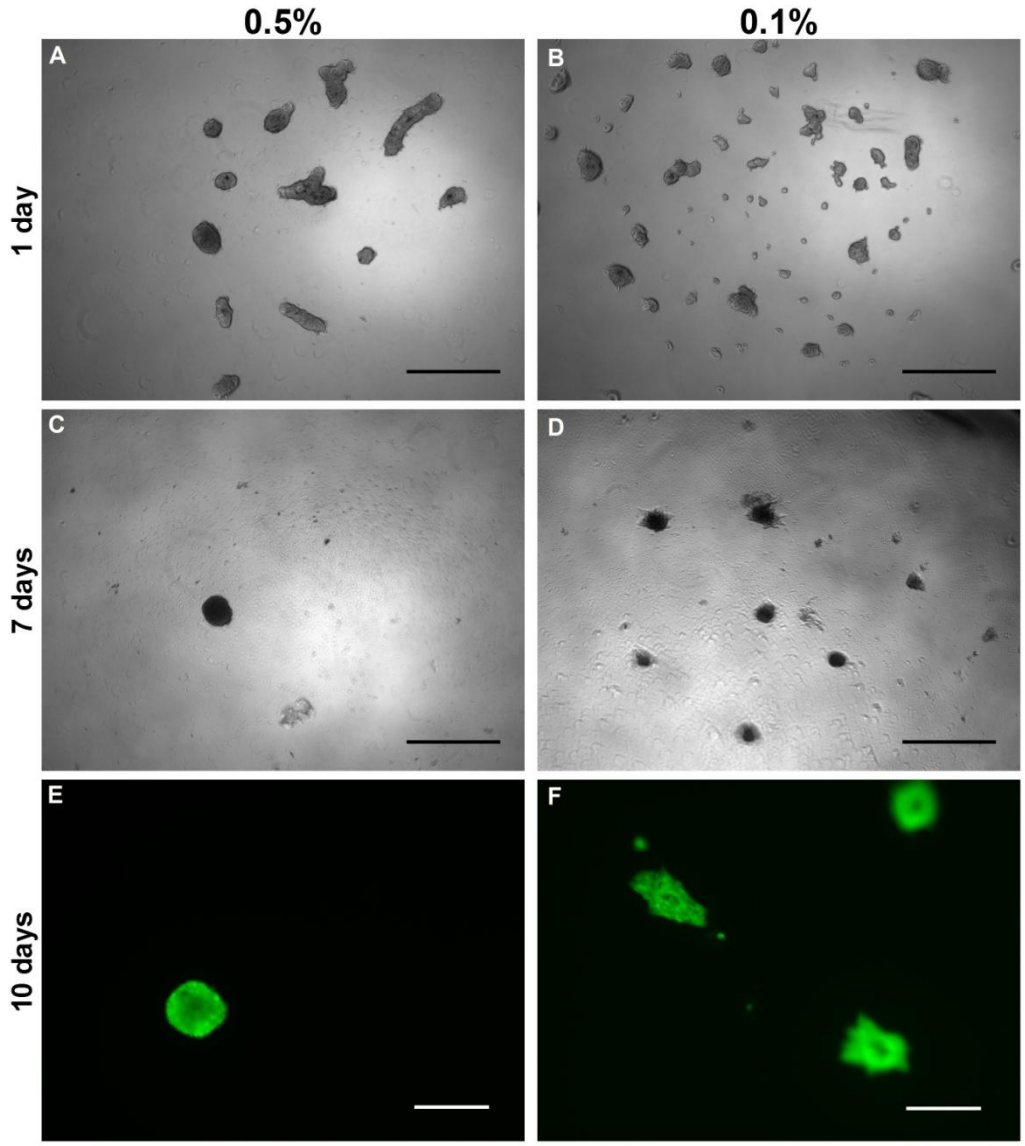

Figure 6.1: C2C12 cells seeded on the surface of 0.5% (w/v) (A, C, E) or 0.1% (w/v) (B, D, F) GG hydrogels formed using CCM with 5 mM added $CaCl_2$, over time in culture as indicated. Cells imaged by phase contrast microscopy (A-D) or fluorescence microscopy of calcein stained cells (E, F). Scale bars represent 500 µm (A-D) or 200 µm (E, F).

In addition to surface-seeding experiments, the response of C2C12 cells encapsulated in GG hydrogels was also investigated. These studies were designed to parallel the work presented in Chapters 4 and 5 where cells were printed into 3D hydrogel constructs. Consequently, we employed encapsulation techniques that utilised ionic crosslinking methods to mimic reactive printing approaches (§2.5.2). Initially, cell-laden CCM (with added $CaCl_2$) was injected into GG solutions. This process is effectively an analogue to DRIP fabrication (§4.5.2). This method did not facilitate uniform cell encapsulation, although it produced interesting cell responses which are

presented in the following section (§6.1.2). Subsequent methods that aimed to achieve more homogenous cell distributions included suspending cells in GG solutions in a culture well and adding CCM, or suspending cells in GG and injecting into CCM in a culture well. The same range of hydrogel compositions was investigated as for the surface-seeding experiments, and in addition a range of cell densities ($1x10^5$-$5x10^6$ cells/mL) was studied. In each case, C2C12 cells encapsulated within GG hydrogels of all compositions exhibited a rounded morphology typical of non-interactive cells over time in culture. This is highlighted by representative images of the cells encapsulated in both 0.5% and 0.1% (w/v) hydrogels present in Figure 6.2A and B. Furthermore, live/dead staining after 4 days in culture revealed significant death of cells encapsulated in both compositions (Figure 6.2C and D).

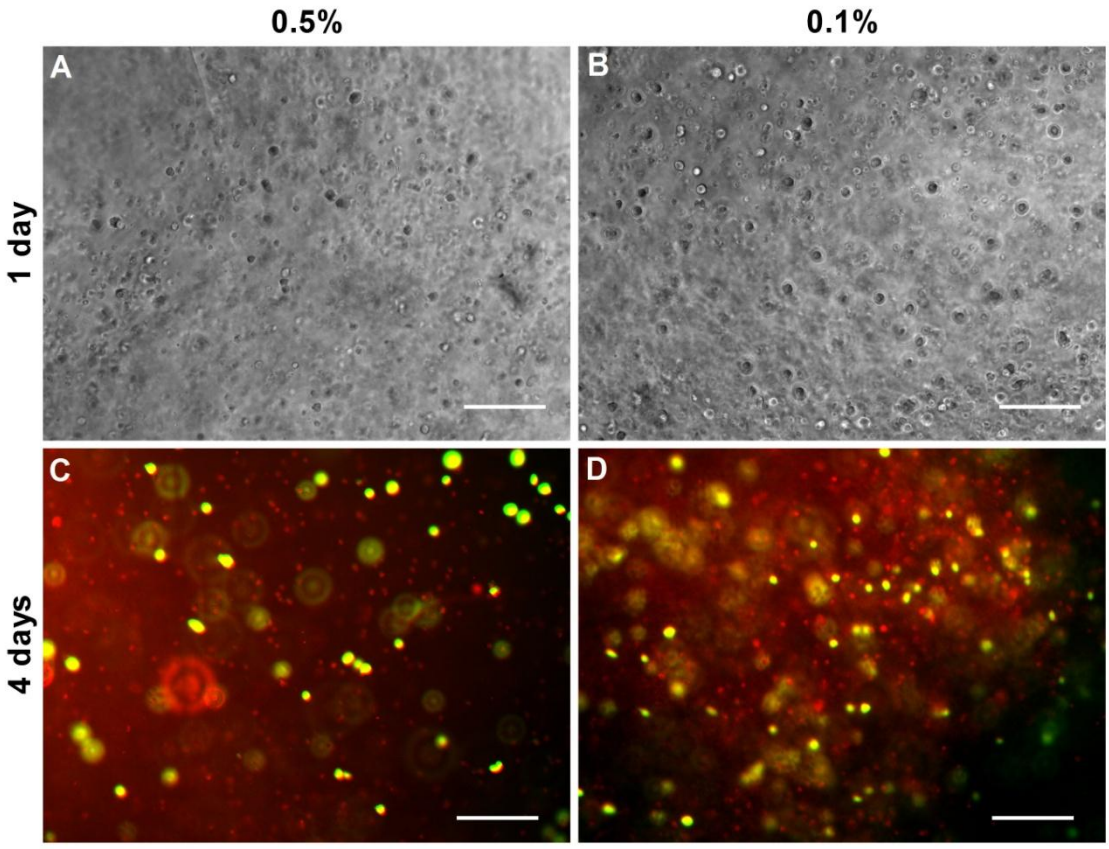

Figure 6.2: C2C12 cells encapsulated in 0.5% (w/v) (A, C) or 0.1% (w/v) (B, D) GG hydrogels after time in culture as indicated. Cells were imaged by phase contrast microscopy (A, B) or fluorescence microscopy of cells stained with calcein (green) and PI (red) (C, D), Scale bars represent 200 µm.

C2C12 cells are attachment-dependent, and therefore must be able to anchor to a suitable substrate in order to display normal behaviour. Cells that are not provided with such a substrate are said to suffer 'anoikis'. This term, meaning 'homelessness', is defined as apoptosis induced by inappropriate or inadequate cell-matrix interactions *(369)*. These results, particularly the substantial cell death observed for encapsulated cells, confirm that GG does not possess the necessary bio-functionality to offer a 'home' for these attachment-dependent cells. They also support our findings from the experiments presented in Chapters 4 and 5 where cells encapsulated in GG hydrogels through reactive printing approaches remained rounded and did not appear to interact with the surrounding matrix.

Previous reports have also shown that GG is not an interactive cell encapsulation matrix. Rat bone marrow cells remained viable in GG hydrogels for up to 10 days *(255)*, and encapsulated human chondrocytes (nasal *(256)* and articular *(258)*) survived for several weeks and produced their own ECM, however these cell types are not attachment-dependent. Conversely, attachment-dependent cells including fibroblasts photo-encapsulated in methacrylated GG hydrogels *(260)* and oligodendrocytes *(259)* maintained a non-responsive phenotype and showed reduced viability after a few days in culture. Similar results have been observed for cardiomyocytes encapsulated in chitosan hydrogels *(370)*, and for endothelial cells encapsulated in alginate *(314)*, where these matrices were not modified with cell-adhesion peptides. The results presented in this thesis are compatible with these published reports.

Encapsulated cells may also lose viability if the surrounding hydrogel network is too dense to allow cell motility, as well as oxygen and nutrient diffusion. For example, primary myoblasts did not proliferate within stiff, non-degrading peptide-modified alginate hydrogels, although they proliferated extensively on 2D substrates of the same material *(371)*. It was suggested that this difference was due to confinement of the cells within a non-malleable 3D matrix. Human umbilical vein endothelial cells (HUVECs) encapsulated in 2% (w/v) alginate hydrogels showed a rapid loss of viability even though the alginate was modified with RGD peptides *(372)*. Reducing the concentration of the peptide-modified alginate to 1% (w/v) allowed HUVEC survival, while the cells lost viability in un-modified alginate even at lower

concentrations *(314)*. Taken together, these results clearly highlight the interplay between cell viability and the effects of excessive polymer concentration. We have employed lower polymer concentrations than in these published reports. Combined with the fact that decreasing GG concentration in this work did not seem to enhance the viability of encapsulated cells, and that there was no apparent heterogeneity in the distribution of dead cells in relation to the distance from the hydrogel-media interface, this implies that the cell death was the result of anoikis rather than hypoxia or serum starvation.

Our results suggested that modification of the GG hydrogels was required to encourage the adhesion, growth and normal function of attachment-dependent cells. As with alginate, GG could potentially act as a 'blank slate' where the lack of non-specific interactions with cells provides an opportunity to engineer specific interactions into the material. Our attempts to achieve this by modification with ECM proteins and RGD peptides are presented in §6.2 and §6.4, respectively. However, the following section highlights an interesting phenomenon whereby surface topography was found to dramatically influence cell behaviour on GG hydrogels.

6.1.2 Curved surface topography affects cell response

During initial attempts to encapsulate cells in GG hydrogels, we employed a protocol where C2C12 cells suspended in cell culture media (with added Ca^{2+} ions) were injected into GG solutions in 96 or 24 well plates (§2.5.2, method A). We found that these cells exhibited an elongated morphology and proliferated rapidly to form networks that resembled concentric circles radiating from the centre of the wells (Figure 6.3A, B). The cells also stained positively for the skeletal muscle protein desmin (Figure 6.3C). Further investigation revealed that these cells were not encapsulated, but rather growing on the surface of concave GG hydrogels formed during the injection process (Figure 6.3D). This behaviour was repeatable, and was highly surprising given the lack of adhesion and proliferation of C2C12 cells on flat hydrogel surfaces of identical composition (Figure 6.1).

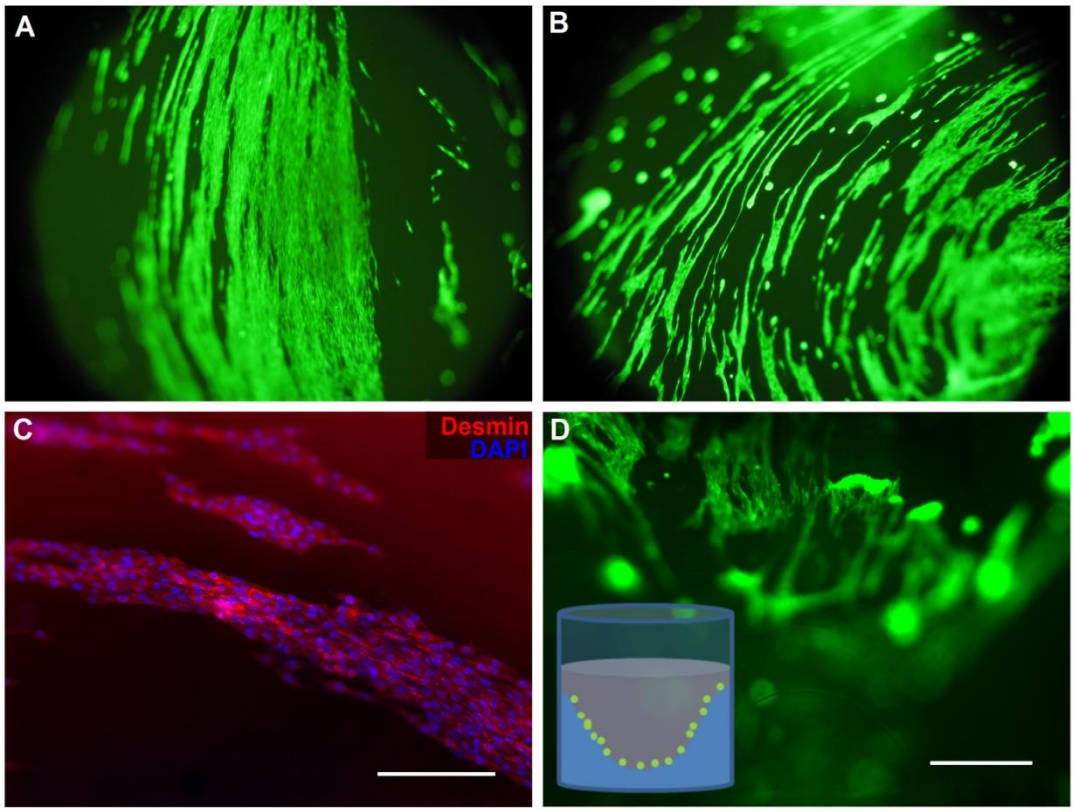

Figure 6.3: Fluorescence microscope images of C2C12 cells growing on the surface of curved GG hydrogel surfaces. **(A,B)** Calcein-stained (green) cells on 0.5% (w/v) hydrogels in 24-well plates after 7 days in culture. Images taken at 5x magnification. **(C)** Cells on 0.5% (w/v) hydrogels in 96-well plates fixed after 8 days in culture and immunostained against desmin (red). Nuclei stained with DAPI (blue). Scale bar 200 µm. **(D)** Side-on view of calcein-stained (green) cells on 1.0% (w/v) GG hydrogel in 96-well plate after 8 days in culture. Scale bar represents 500 µm. Inset - schematic representation of cell position on curved GG hydrogel surfaces.

In subsequent experiments, cell proliferation was monitored over time in culture by imaging cells at the centre and edge of concave hydrogels at several time points (Figure 6.4). We found that cells initially formed relatively large aggregates as seen previously on GG hydrogel surfaces, although the size of these aggregates decreased significantly towards the edge of the hydrogels (Figure 6.4A and B). After several days, however, extensive proliferation from aggregates was observed and cell growth again appeared to follow hydrogel contours (Figure 6.4C-F). The proliferation of cells out from an aggregate is highlighted in Figure 6.4G.

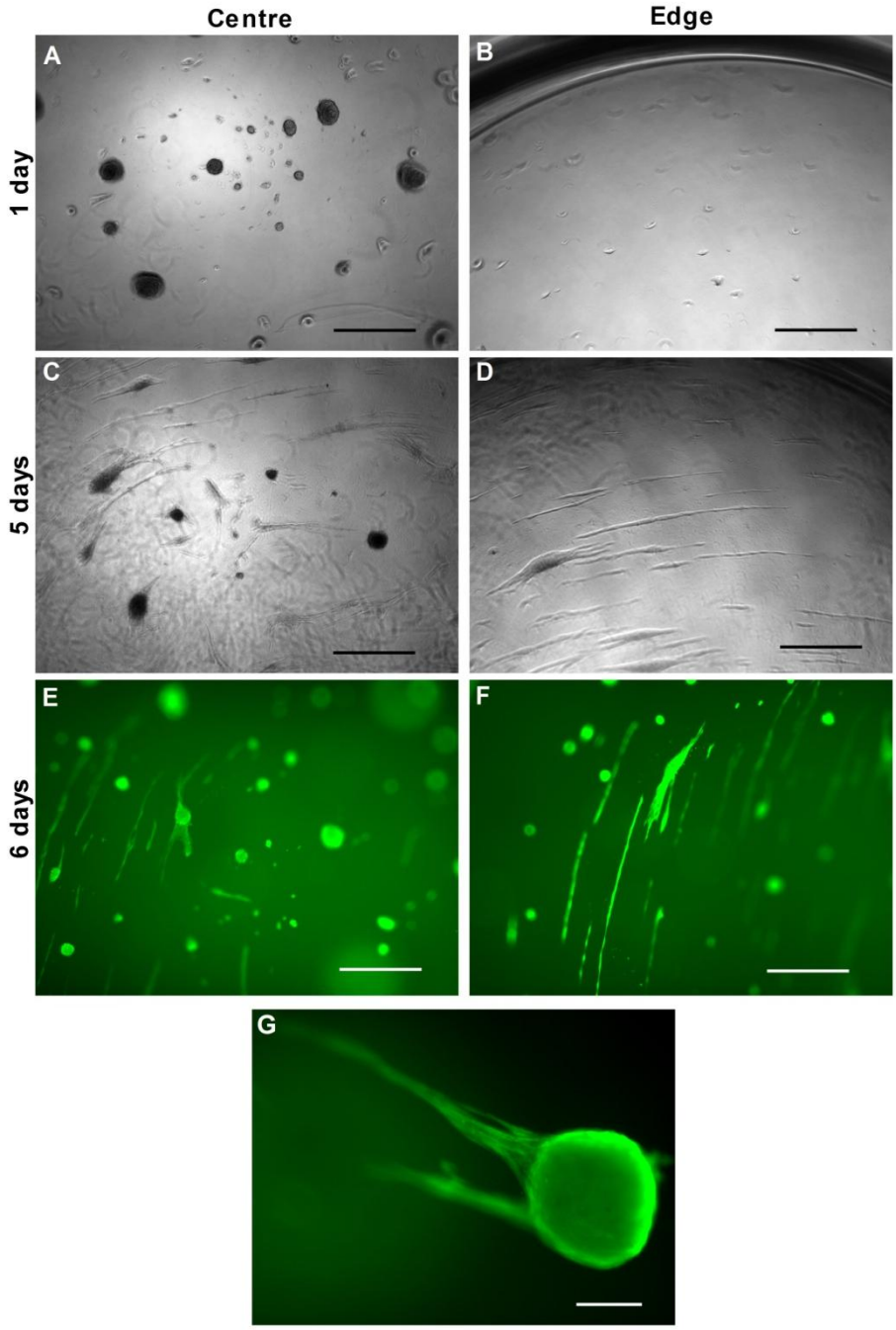

Figure 6.4: (A-F) Progression of C2C12 growth when seeded on the surface of curved 0.5% w/v GG hydrogel surfaces in 96 well plates. Images were taken using phase contrast microscopy (A-D) or fluorescence microscopy of calcein stained (green) cells (E-F), either in the centre (A,C,E) or edge (B,D,F) of hydrogels over time in culture as indicated. Scale bars represent 500 µm. **(G)** Higher magnification image of proliferating cell aggregate after 6 days in culture. Scale bar represents 100 µm.

It is well established that, in addition to biological and biochemical signals, cell behaviour is dictated by the physical nature of the microenvironment. For example, cells sense and respond to the stiffness of their substrate *(373, 374)* as well as to local force and geometry *(375)*. The latter has been manipulated to control cell responses using micro-scale *(376, 377)* and nano-scale *(378, 379)* topographical features. We have shown that the proliferation of L929 fibroblasts on the surface of GG hydrogels can be modulated by the inclusion of micro-scale ridges *(281)*. In the current work, it seemed that cell responses were modulated through substrate curvature on the millimetre scale. Although further work is required to definitively exclude other factors, this conclusion was supported by the difference in cell behaviour with high curvature at well edges, the patterned growth of cell networks and the fact that cells appeared to show greater proliferation on hydrogels formed in 24-well plates (Figure 6.3A and B) in comparison with those on hydrogels formed in 96-well plates (Figure 6.4).

Recent research suggests that cells have the ability to sense and respond to radii of curvature on a scale much larger than the diameter of the cell. This has been described as curvature-controlled tissue growth (CCTG), and has important implications in the understanding of morphogenesis. For example, studies on the growth of pre-osteoblastic cells seeded on hyaluronic acid (HA) substrates with large concave pores have revealed an enhanced proliferation rate in regions of greater substrate curvature *(380, 381)*. The mechanisms for this behaviour are still not clear, but alignment of cellular stress fibres with the curvature implied that mechanical stress and its effect on intercellular and intracellular processes was the guiding factor *(380)*. This is supported by a seminal study on the response of epithelial cells to patterned islands of fibronectin on flat substrates that found a distinct correlation between enhanced cell proliferation and regions of high mechanical force *(382)*. We therefore propose that culture of C2C12 cells on concave GG hydrogel surfaces resulted in localised mechanical forces that were sensed by the cells and translated to enhanced adhesion and proliferation that was not observed on flat surfaces. To our knowledge, this is the first reported example where substrate curvature has been shown to encourage cell growth on a material that would not normally be permissive to cell attachment and proliferation.

It would be of interest to investigate these findings further in the context of CCTG, particularly in systems where greater control over GG hydrogel curvature could be achieved. However, as this was not a focus of this thesis we did not pursue this further, but instead sought means by which GG hydrogels could be modified to encourage the growth of cells seeded on printed hydrogel surfaces or encapsulated within hydrogels.

6.2 Protein-modified gellan gum

In the design of biomaterials that can elicit specific interactions from cells, the inclusion of full length ECM proteins or recombinant protein fractions is one popular approach. ECM proteins (i.e. collagen, fibronectin, laminin, albumin) contain the biofunctionality required to elicit favourable cell responses; their drawback is that they are poorly characterised and often do not possess the physical and chemical properties required for application-based processing. Consequently, they are either chemically grafted, or simply mixed, with synthetic or natural polymers to create hybrid systems. For example, polysaccharides including alginate *(282, 383)*, chitosan *(384)* and hyaluronic acid *(385)* have all been combined with collagen or collagen/laminin to create composite hydrogels to encourage the attachment and growth of encapsulated cells. Fibronectin has been grafted with methacrylated poly-ethylene glycol (PEG) chains to create a photo-crosslinkable and biofunctional hybrid *(386, 387)*. Covalent grafting of gelatin (derived from collagen) onto GG microspheres has been shown to improve the attachment and proliferation of human dermal fibroblasts and fetal osteoblasts *(268)*. As outlined in the introduction to this thesis (§1.3.1), hybrid bio-inks containing some combination of alginate or chitosan with proteins including collagen, gelatin and fibrinogen have been utilised in extrusion printing *(100)*.

Here, we sought to facilitate the attachment of encapsulated C2C12 cells by combining GG with collagen. Collagen is the most abundant protein in the ECM and plays an important role in the development of cell-matrix interactions *(388)*. Combination of the two hydrogel materials was not trivial due to their different gelation mechanisms, and the procedure used is outlined in detail in the experimental section of this thesis (§2.5.3). Briefly, cold collagen and GG solutions were

combined with cells and pipetted into culture wells, followed by addition of cell culture media to crosslink the GG hydrogel and subsequent incubation at 37°C for 1 hr to allow collagen gelation, resulting in a cell-encapsulating hydrogel. C2C12 cells encapsulated in hydrogels containing different ratios of GG and collagen, after 5 days in culture, are shown in Figure 6.5. Cells in GG hydrogels without collagen maintained a rounded morphology as observed previously. With increasing collagen concentration, cells adopted an elongated morphology indicative of attached cells. The morphology of cells encapsulated in hydrogels containing a 1:1 ratio of GG and collagen appeared comparable to cells in collagen hydrogels alone. In collagen-only hydrogels a significant number of cells settled to the base of the culture wells during the slow gelation process, however with the addition of GG this was avoided.

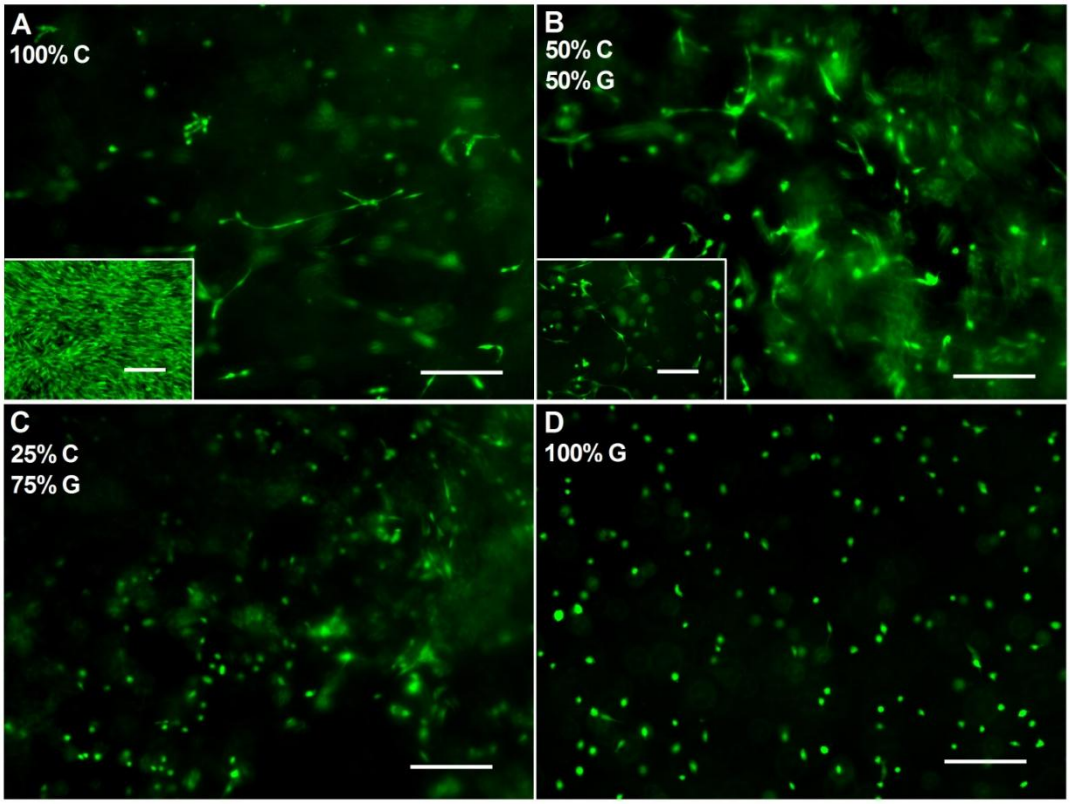

Figure 6.5: C2C12 cells encapsulated in hydrogels containing various proportions (% v/v) of 0.5% w/v gellan gum (abbreviated G) and 0.4% (w/v) collagen (abbreviated C) as indicated. Cells were imaged by calcein (green) staining and fluorescence microscopy after 5 days under proliferation conditions. Inset images in (A) and (B) show cells that had settled to the base of the well during gelation of the hydrogels. Scale bars represent 200 µm.

These results suggest that blending GG with collagen could take advantage of the inherent advantages of both materials. The GG provides a fast-gelling mechanism whereby addition of cell culture media crosslinks the GG network to effectively encapsulate cells before any significant cell settling is possible. Hydrogels containing GG were easily handled and transferred between culture wells, contrary to the soft and weak collagen hydrogels. Concomitantly, the presence of collagen imparts biofunctionality which led to greater evidence of cell attachment.

6.3 Proteins vs peptides

The use of ECM proteins like collagen, however, may not be the best approach to instilling biofunctionality in GG-based hydrogels. An alternative is the use of short peptide sequences that mimic ECM protein function. The tri-peptide sequence arginine-glycine-aspartic acid (RGD) has been identified as the cell attachment site in many adhesive ECM proteins and is pivotal in integrin-mediated cell binding *(389, 390)*. This peptide has been widely utilised to modify polymer biofunctionality *(312)*. The relative merits of ECM proteins in comparison with these peptides was the subject of a recent four-paper debate in the journal *Biomaterials* on the notion that "the use of short synthetic adhesion peptides, like RGD, is the best approach in the design of biomaterials that guide cell behaviour for regenerative medicine and tissue engineering". The debate was concluded with a 'judgment' from the editor *(391)* in favour of the above motion. This conclusion was reached largely due to the ability of RGD and similar peptides to impart biofunctionality to materials in a controlled, well defined manner. This is particularly important in bio-ink development, where the material must be well defined not just biologically, but where precise control over physical and chemical properties are required. For this reason, we chose to focus on the modification of GG with RGD peptides.

6.4 Peptide-modified gellan gum

As described in the experimental chapter (§2.5.4.4), we used the well established method developed by Rowley and co-workers for the conjugation of RGD peptides to alginate *(313)* as a basis for our attempts to conjugate RGD peptides to GG. This section outlines several iterations of adjustments to these techniques, the characterisation of peptide conjugation efficiency, and the resulting cell responses.

6.4.1 Peptide conjugation I

Initial peptide conjugation experiments were conducted with the peptide GRGDS. This sequence was readily available from commercial sources, and has shown good general affinity for integrins *(312)*. As outlined in the introduction to this thesis (§1.5), GG is similar to alginate although it differs significantly in its gelation behaviour. We found that this necessitated several changes to the conditions that Rowley and co-workers established to give optimal conjugation (~80% efficiency) of the GRGDY peptide to alginate.

The gelation of GG is not dependent on 'ionic bridging' between carboxylic acid groups by divalent cations, but rather on cation mediated aggregation of double-helices. Consequently, gelation can occur at much lower divalent cation concentrations than those required for alginate, or even in the presence of monovalent cations alone. As a result of this gelation behaviour, we found that dissolution of GG under Rowley's conditions (1% (w/v) in 0.1 M MES buffer solution, with or without the addition of NaCl), led to unwanted gelation that hindered the conjugation reaction. We therefore employed changes to prevent gelation. The polymer concentration was reduced to 0.5% (w/v), and the buffer concentration was reduced to 0.05 M. A potassium phosphate buffer system facilitated easily dissolution of GG under these conditions, possibly aided by chelating of Ca^{2+} ions present in GG by the phosphate.

Rowley performed conjugation reactions at 25°C. At this temperature GG chains adopt a double helix confirmation, which we postulated could shield carboxylic acid groups from activation and conjugation. The reaction temperature was therefore increased to 60°C to ensure that GG chains were in a random coil confirmation, where the availability of these groups for reaction may be enhanced. We also experienced difficulty in re-dissolving lyophilised GG products, so an alternative method was adopted where GG was precipitated with isopropanol, washed and air-dried. These changes in experimental conditions are summarised in Table 6.1. Peptide conjugation experiments were conducted using a range of EDC and peptide concentrations similar to those employed by Rowley and co-workers.

Table 6.1: Initial peptide conjugation conditions. Optimal conditions for conjugation of GRGDY to alginate *(313)* are compared to conditions initially employed to conjugate GRGDS to GG in this work. EDC and peptide concentrations are expressed as a molar percentage of carboxylic acid groups present in alginate or GG. In each case, sulfo-NHS was included at a molar ratio of 1:2 to EDC.

Parameter	Alginate conditions *(313)*	Gellan gum conditions
Buffer	0.1M MES with 0.3M NaCl, pH 6.5	0.05M potassium phosphate, pH 6
Polymer conc. (%w/v)	1.0	0.5
EDC conc. (% COOH)	10	5 - 15
Peptide conc. (% COOH)	0.005 - 5	0.15 - 15
Reaction temperature (°C)	25	60
Product recovery	Dialysis, lyophilisation	Dialysis, precipitation and drying

We investigated several different approaches to characterise the amount of peptide conjugated to GG using these conditions. These approaches included nuclear magnetic resonance (NMR) spectroscopy, Fourier-transform infra-red (FTIR) spectroscopy, capillary electrophoresis (CE) and elemental analysis. The first three methods proved unsuccessful, although our work on CE of GG developed into a separate project that is not included in this thesis but led to a publication *(392)*. Elemental analysis of peptide-conjugated GG products identified a measurable quantity of nitrogen, indicating the presence of peptide, in samples with the highest input peptide concentration (15% of COOH groups). The carbon:nitrogen ratio (~650:1) indicated that only ~ 3% of the input peptide remained in the product. We were unable to confirm whether this peptide was covalently attached to GG or non-specifically incorporated, but it had minimal effect on cell adhesion. C2C12 cells seeded on the surface of hydrogels formed using this product formed small clusters and only few cells exhibited a flattened morphology, even after 10 days in culture (Figure 6.6).

It was clear that optimisation of the peptide conjugation chemistry was required in order to increase the conjugation efficiency. As the optimisation process would require constant quantitative analysis of peptide conjugation, it was also necessary to employ a fast and sensitive method of peptide quantification. For this purpose, we endeavoured to use peptide radio-labelling, as was utilised in Rowley's seminal paper.

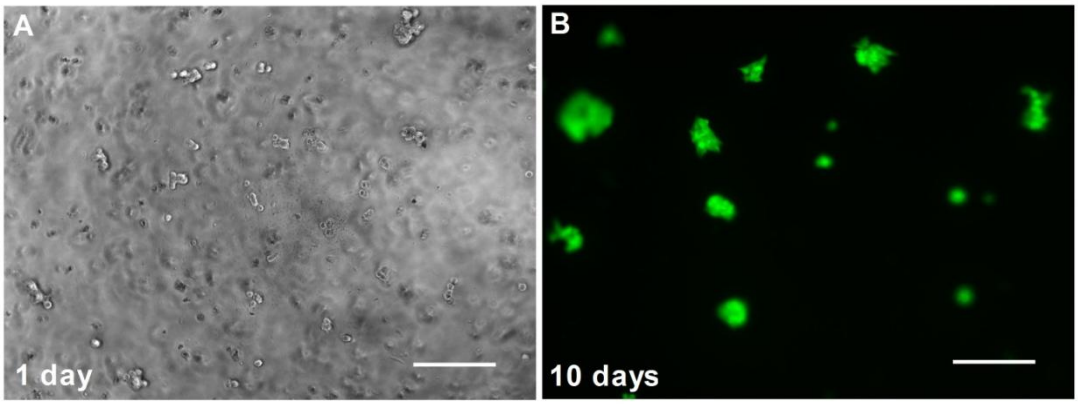

Figure 6.6: C2C12 cells seeded on the surface of 0.5% (w/v) GG hydrogels conjugated with GRGDS peptide. Cells were maintained under proliferation conditions for the time indicated, and imaged by phase contrast microscopy (A) or fluorescence microscopy of calcein (green) stained cells (B). Scale bars represent 200 µm.

6.4.2 Peptide sequence and radiolabelling

For these experiments, we chose to use an RGD-containing peptide with a longer glycine tail than the GRGDS peptide used in initial experiments. This was due to evidence from several studies indicating the need for a 'spacer' that separates the RGD sequence from the material to which it is conjugated, enhancing its availability to cell integrins *(312)*. The required length of this spacer, or the need for one at all, is largely dependent upon the structure of the host material. We were therefore guided by work characterising the effect of glycine tail length on the response of human fibroblast cells to RGD-modified alginate hydrogels *(317)*. In this report, Lee and co-workers showed that a minimum spacer length of four glycine units was required to facilitate the development of focal adhesions, cell proliferation and a reduction in cell stress markers. We therefore chose a four-glycine spacer for RGD conjugation to GG. Furthermore, to allow facile radiolabelling, a tyrosine (Y) residue was required for iodination. We therefore used a custom-synthesised peptide with the sequence GGGGRGDSY (G_4RGDSY).

This peptide was radiolabelled through iodination of the amino acid tyrosine using the well-established chloramine-T method *(309)*. $Na^{125}I$ was added to the peptide in the presence of chloramine-T, where iodine chloride undergoes electrophilic substitution with the activated aromatic ring of tyrosine. After quenching the reaction with the anti-oxidant sodium metabisulfite, the product was purified by solid-phase extraction and analysed by HPLC equipped with both UV and gamma detectors. The

chromatogram of cold-labelled peptide (i.e. labelled with non-radioactive NaI) (Figure 6.7B) exhibited a single peak slightly shifted to a shorter retention time (8.0 min) in comparison with the peptide alone (8.2 min) (Figure 6.7A). The radio-chromatogram of the hot-labelled peptide (i.e. labelled with radioactive $Na^{125}I$) (Figure 6.7C) showed a matching peak in the UV (8.0 min), coupled with a peak in the gamma detector. The slight delay in the appearance of this gamma detector peak is an artefact resulting from the distance between the two detectors. The specific activity of the labelled peptide was ~2 Ci/mmol, calculated using the calibration curve and method described in the experimental section (§2.5.4.2).

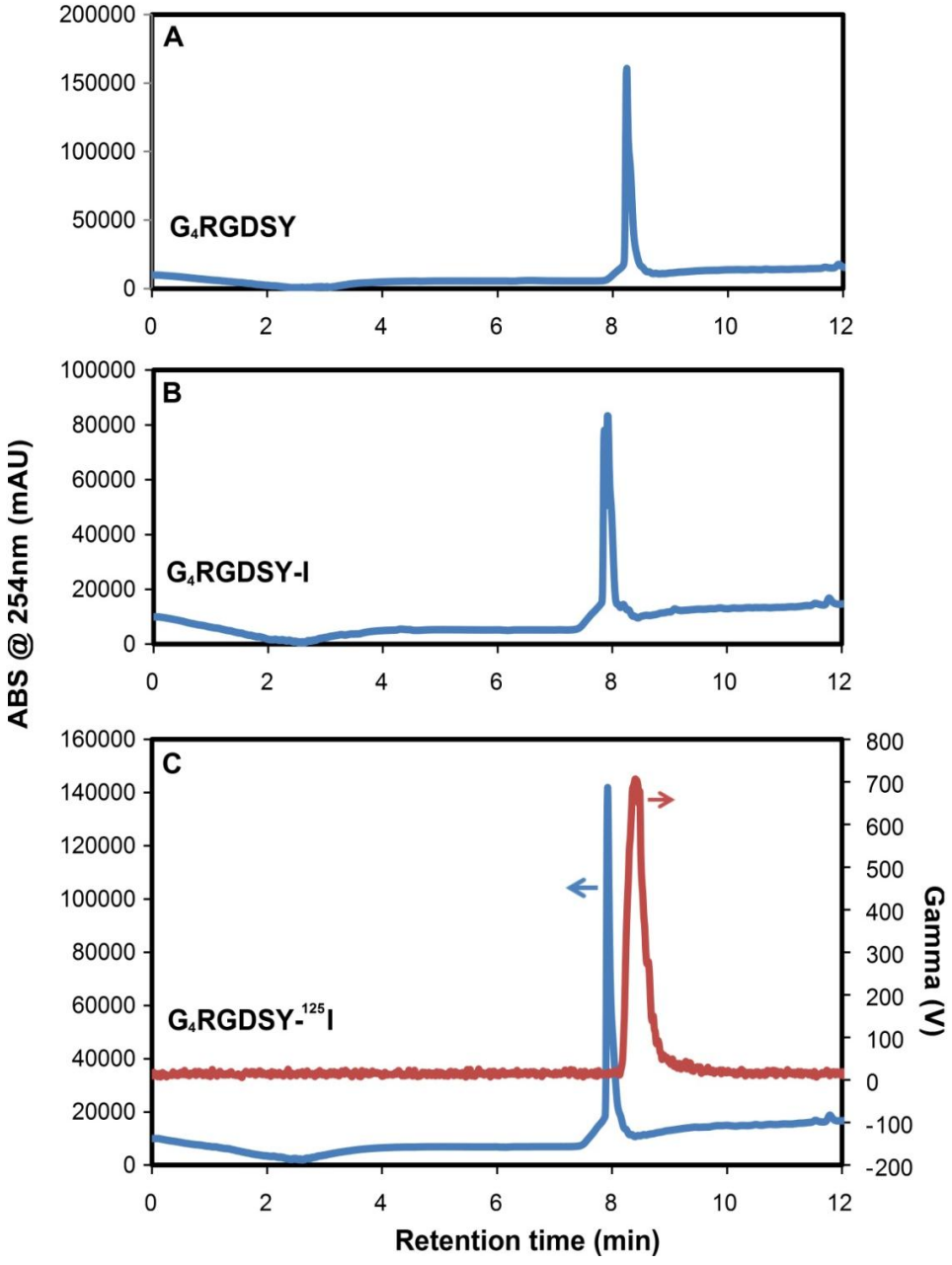

Figure 6.7: (A,B) HPLC chromatograms of unlabelled (A) and cold-labelled (B) peptide. **(C)** HPLC radio-chromatogram of hot-labelled peptide. Arrows indicate the relevant scale for each peak.

6.4.2.1 Peptide conjugation II

The use of radiolabelled peptide provided a facile and extremely sensitive method to monitor the efficiency of the conjugation reaction. Reactions were performed by spiking unlabelled peptide with hot-labelled peptide as a tracer molecule with ~2 µCi activity per reaction. Conjugation efficiency was defined as the percentage of activity (representing peptide) remaining in the GG sample after removal of unbound peptide, and could be measured very quickly using a gamma counter (§2.5.4.3). These reactions were conducted in 50 mM MES buffer at pH 6.5, which required reducing the GG concentration to 0.1% (w/v) to prevent gelation. Initial conjugation of radiolabelled peptide to GG, followed by removal of unbound peptide by dialysis, yielded a conjugation efficiency < 5%. We endeavoured to improve this efficiency by making several adjustments to the conjugation procedure. In order to facilitate this, a more rapid method to remove unbound peptide was required; dialysis took several days and feedback would be far too slow. Centrifuge filtration was attempted, using a range of different commercial products and molecular weight cut-offs (MWCO), however we found that labelled peptide tended to become trapped in these filters. Size exclusion chromatography, using spin desalting columns (§2.5.4.4), was therefore employed and proved to be a very efficient method to removed unbound peptide from GG (>99% peptide removed after 2 spin steps). Numerous adjustments to conjugation conditions (including temperature, peptide and EDC concentrations, reaction time and buffer), however, did not yield any significant improvements in conjugation efficiency, which remained < 5% and was not highly reproducible. We therefore we focussed our attention on investigating why the GG was perhaps hindering conjugation.

6.4.2.2 Gellan gum purification

Commercial samples of GG are predominantly in the potassium salt form, with lesser amounts of Na^+, Ca^{2+} and Mg^{2+} as the other major cations. Importantly, the presence of divalent cations can have significant implications on the properties of GG. As discussed previously (§1.5), the gelation of GG may proceed in the presence of monovalent cations alone, or at very low concentrations of divalent cations. Therefore, these divalent cation contaminants can hinder dissolution. For example, Milli-Q water must be heated to > 60°C to dissolve GG and at higher concentrations

gelation will occur on cooling to room temperature (~ 25°C), with no additional salts. Furthermore, these concentrations of divalent cations are sufficient to neutralize around one-third of the carboxyl groups in GG *(227, 310, 311)*. It therefore seemed likely that these contaminants could hinder the conjugation of the peptide to the carboxyl groups. Additionally, their removal could facilitate the dissolution of GG in the conjugation buffer at higher concentrations without unwanted gelation, which could enhance conjugation efficiency.

Commercial GG samples were therefore purified, following a published procedure *(310, 311)* to remove divalent cation contaminants and yield monovalent cation salts. The procedure involved conversion to the free-acid form using a cation exchange resin, followed by addition of NaOH to convert to the sodium salt form (sodium gellanate, NaGG) which was recovered by isopropanol precipitation and filtration. This process yielded a white, fibrous product at ~ 60% yield. The concentration of major monovalent (Na^+, K^+) and divalent (Ca^{2+}, Mg^{2+}) cations in both the as-supplied commercial GG and the purified NaGG was measured by atomic absorption spectroscopy (Table 6.2).

These results confirmed that the commercial GG contained significant divalent cation contaminants. The concentration of Ca^{2+} equates to ~ 20 mol% of carboxyl groups in GG, while the concentration of Mg^{2+} is ~ 3 mol%. These divalent cations, and the majority of K^+, were replaced with Na^+ in the purified NaGG samples, as expected. The concentration of Na^+ in NaGG was equivalent to ~72.5 mol% of carboxyl groups and concentrations of Ca^{2+} and Mg^{2+} were below the limit of detection (LOD) for each cation (LOD was 0.06% and 0.03% (w/w), respectively).

Table 6.2: Concentration of major cations present in as-supplied gellan gum (GG) and purified sodium gellanate (NaGG), measured by atomic absorption spectroscopy. LOD = limit of detection.

Element (%w/w)	Na^+	K^+	Ca^+	Mg^+
GG	0.6 ± 0.1	4.5 ± 0.2	1.2 ± 0.1	0.11 ± 0.01
NaGG	2.5 ± 0.1	1.0 ± 0.1	< LOD	< LOD

6.4.2.3 Peptide conjugation III

The NaGG product was easily dissolved in the conjugation buffer (50 mM MES, pH 6.5) at a concentration of 1% (w/v) at room temperature (~25 °C) without gelation occurring. Conjugation reactions were then performed with NaGG, varying conditions including peptide concentration, NaGG concentration, EDC/sulfo-NHS concentrations, temperature and reaction buffer (Figure 6.8). To expedite this optimisation process, unconjugated peptide was removed from these reactions by a single spin-desalting step. This separated only ~ 90% of peptide from controls without EDC (Figure 6.8C), but facilitated useful comparisons between conjugation conditions.

Importantly, conjugation using 0.1% (w/v) NaGG yielded an efficiency (~ 19%) that was significantly higher than controls (~ 10%), which had not previously been possible in reactions using 0.1% (w/v) GG. This is likely due to the removal of divalent cation contaminants that had previously prevented some carboxyl groups from activation *(311)*. Conjugation reactions were also possible at higher concentrations of NaGG due to its enhanced solubility in buffer solutions. Conjugations with 0.5 and 1.0% (w/v) NaGG yielded a further significant increase in efficiency (to ~ 37%) in comparison with reactions with 0.1% (w/v) NaGG (Figure 6.8A), which can be attributed to the increased concentration of carboxyl groups.

The G_4RGDSY peptide could be conjugated to 1.0% (w/v) NaGG over three orders of magnitude difference in input peptide concentration (0.02-2% COOH), with no statistically significant difference (by Student's t-test, $P>0.05$) in conjugation efficiency (Figure 6.8B). This range gives bound peptide concentrations similar to those used previously to encourage attachment of cells on the surface of, and encapsulated within, RGD-modified alginate hydrogels *(313, 314)*. The density of RGD peptides presented to cells has been shown to affect a range of cellular responses including attachment, spreading, proliferation and differentiation *(312, 393–395)*. These interactions are complex, however, and the optimal peptide density is dependent upon the nature of the polymer and peptide, the cell type and the desired cellular response *(312)*. Therefore, quantifying peptide conjugation over a wide range as demonstrated here shows that the peptide density could potentially be tailored to suit the intended application.

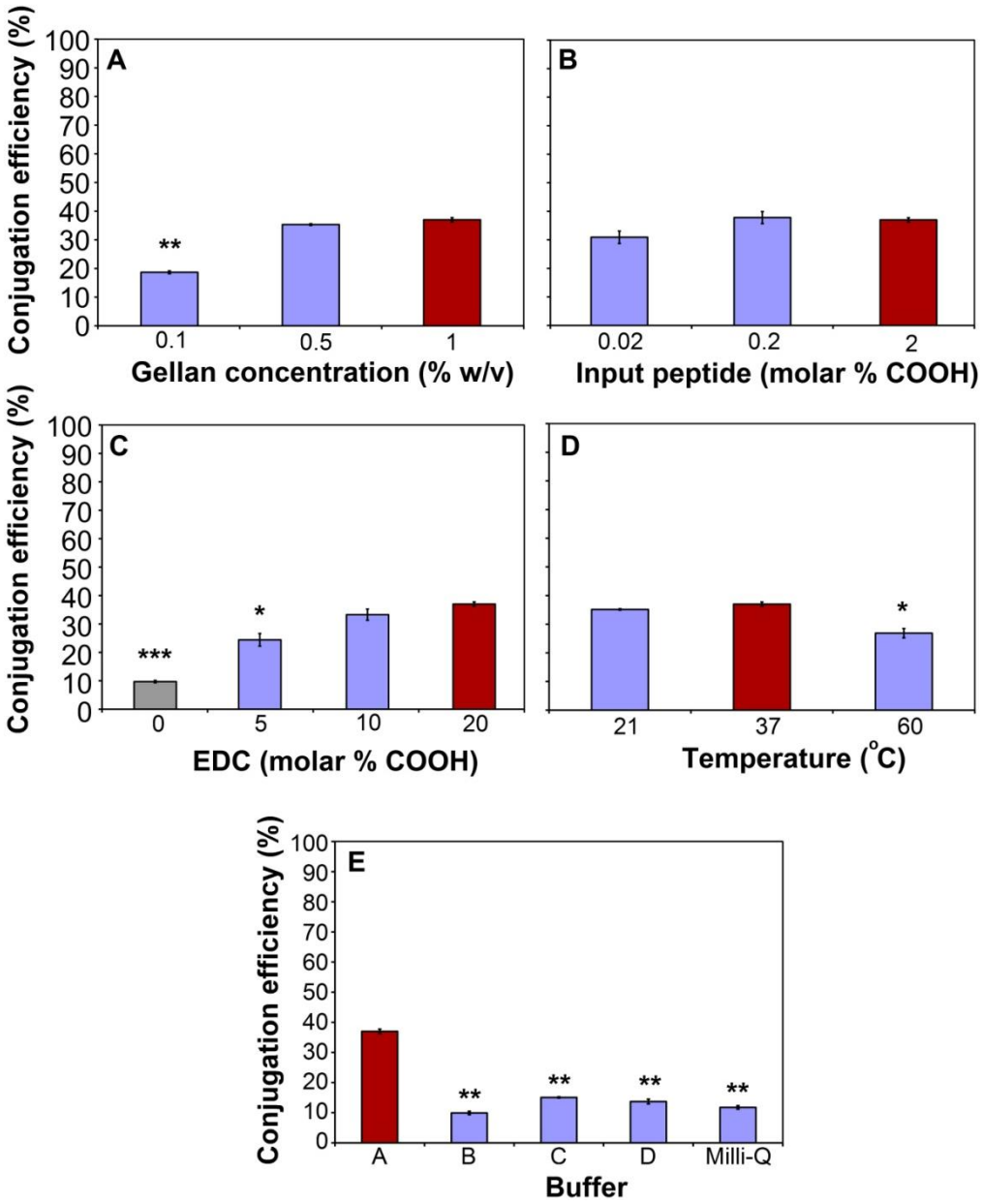

Figure 6.8: Peptide (G_4RGDSY) conjugation efficiency with varying concentrations of NaGG (A), input peptide (B) and EDC (C), varying temperature (D) and reaction buffer (E). Reaction buffers were all 50 mM, and were as follows: A – MES, pH 6.5; B – MES, pH 5; C – sodium phosphate, pH 8; D – sodium acetate, pH 6.7. In all cases, sulfo-NHS was included at a molar ratio of 1:2 with EDC. Red bars indicate the value of each parameter that was kept constant under conditions where other parameters were varied. Grey bar highlights process control with no added EDC. Error bars represent one standard error of the mean ($n \geq 2$). Statistical significance of each value compared to the condition represented by the red bar was analysed by a Student's t-test, with significance level as indicated; $P < 0.05$ (*), $P < 0.01$ (**), or $P < 0.001$ (***).

The concentration of EDC used in the reaction also significantly affected conjugation efficiency (Figure 6.8C). Obviously, with no added EDC no covalent attachment of the peptide is possible. Therefore, this sample represents a control for the presence of non-specifically bound peptide after one spin desalting step. The conjugation efficiency then increased with EDC concentration up to 20% of available COOH groups, although there was no significant difference between efficiencies at 10 and

20% EDC, by a Student's *t*-test. This result is similar to that found by Rowley et al. *(313)*, although in this case the efficiency reached a peak at an EDC concentration of 10% available COOH groups before decreasing slightly at 20% EDC and higher concentrations. This discrepancy could be a result of the different chemical structure of the two polysaccharides. Alginate has a carboxyl group on every saccharide unit, while GG has one carboxyl group per tetrasaccharide repeat unit. EDC concentration was not increased beyond 20% of available COOH groups due to the risk of internal rearrangement of the active ester which can then become stably incorporated into the product *(313, 396)*.

Conjugation appeared to be most efficient at 37°C, although there was no significant difference at 21°C, however efficiency was decreased at 60°C (Figure 6.8D). Generally, performing EDC coupling reactions at lower temperatures can increase yield *(312)*. In this case, however, it is likely that there is a trade-off between reaction kinetics and the availability of carboxyl groups for activation. Increasing the temperature of GG solutions encourages a conformational transition from double helix, where carboxyl groups could be shielded, to a random coil. The majority of chains are likely to be in the random coil conformation at 37°C, and so it is likely that a further increase to 60°C did not enhance the availability of carboxyl groups.

As discussed by Rowley et al. *(313)*, the pH of the reaction buffer should achieve a balance between the reactivity of the EDC and the terminal amine of the peptide. EDC is most reactive at pH ~4.5 while the pKa of the terminal amine (7.2-7.4) means optimal reactivity of the peptide is found at pH 8-9 *(312)*. We found good conjugation in MES buffer at pH 6.5, while efficiency was significantly reduced in all other buffer systems employed, and in Milli-Q water (Figure 6.8E). The poor conjugation efficiency in the sodium acetate buffer may be due to de-activation of EDC by nucleophilic attack from acetate ions at pH 6.7 *(397)*. Notably, conjugation in MES buffer at pH 5 yielded no significant increase over control values demonstrating that the reactivity of the peptide terminal amine was severely diminished at this lower pH. Similarly, conjugation in sodium phosphate buffer at pH 8 gave poor efficiency, likely as a result of reduced EDC reactivity. We also attempted a dual buffer approach where EDC/sulfo-NHS activation was carried out in MES buffer at pH 5 (to enhance EDC reactivity), followed by buffer exchange

with a spin desalting column to sodium phosphate buffer at pH 8 before addition of the peptide (to enhance peptide reactivity). Interestingly, the conjugation efficiency using this approach was poor at lower temperatures, and at 50°C was slightly lower than for conjugation in MES buffer at pH 6.5 (Figure 6.9). This could have resulted from a greater tendency for GG chains to adopt a double-helix conformation in this buffer.

For NaGG modified with G_4RGDSY under the optimal conditions (the conditions represented by the red bars in Figure 6.8), un-conjugated peptide was also removed by dialysis (20K MWCO) and compared to the results obtained above for separation by spin-desalting. Although a much slower technique and therefore not suitable for the optimisation process, we expected dialysis to be a more effective method to remove un-conjugated peptide prior to further use of the product. Indeed, for control samples without EDC, dialysed products showed a significantly lower retention of un-conjugated peptide than those separated by desalting (Figure 6.10). Even so, after 5 days of dialysis, ~3.5% peptide remained non-specifically bound to the NaGG control samples. This is in contrast to the findings of Rowley and co-workers who observed <1% peptide non-specifically bound to alginate after dialysis *(313)*. Separation by dialysis also yielded a small increase in measured conjugation efficiency compared to desalting, although this was statistically insignificant. The ratio of conjugated to non-specifically bound peptide increased from ~4 for desalting, to ~12.5 for dialysis, a significant improvement.

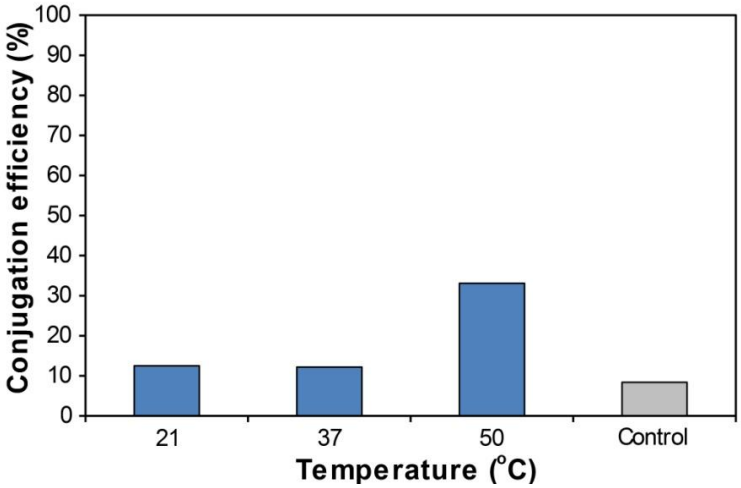

Figure 6.9: Efficiency of conjugation using the mixed buffer approach (MES pH 5, sodium phosphate pH 8) at varying temperatures, compared to control without EDC. All other reaction conditions were those represented by the red bars in Figure 6.8.

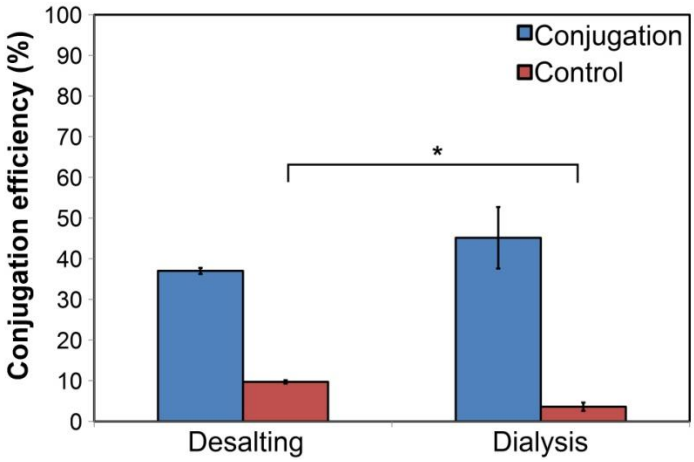

Figure 6.10: Comparison of measured conjugation efficiency for samples purified by desalting (one spin) or dialysis over 5 days. Conjugations employed optimal conditions, those represented by the red bars in Figure 6.8, and are compared to controls without EDC. Error bars represent one standard error of the mean (n≥3). Statistical significance was analysed by a Student's t-test, with significance level as indicated; $P < 0.05$ (*).

The highest efficiency for conjugation of G_4RGDSY to NaGG achieved in this work (~40%) was lower than that observed by Rowley and co-workers for conjugation of GRGDY to alginate (>80%). The reasons for this are not clear, but could be due to the use of a longer peptide sequence. This is supported by a subsequent report where Rowley and co-workers conjugated the peptide G_4RGDY to alginate with only 55-60% efficiency *(395)*.

6.4.2.4 Cell response to peptide-modified gellan gum

We then proceeded to investigate the response of cells to peptide-modified GG hydrogels. For these experiments, 1% (w/v) NaGG was modified by the conjugation of G_4RGDSY (without the ^{125}I-G_4RGDSY tracer) and purified by dialysis under aseptic conditions (§2.5.4.6). We investigated the responses of C2C12 cells seeded on the surface of, or encapsulated within, peptide-modified NaGG hydrogels prepared in CCM at 0.15% (w/v). Hydrogels formed from NaGG modified with G_4RGDSY are denoted NaGG-RGD(*n*%), where *n* is the concentration of peptide added during the conjugation as a percentage of available COOH groups.

A number of different control conditions were used in these experiments. In order to conclude that any changes to cell response were a result of specific integrin-mediated interactions with the RGD peptide, and not due to changes in the physical characteristics of the hydrogel, control samples were conjugated with the peptide G_4RGESY at 1% of available COOH groups, denoted NaGG-RGE(1%). The RGE

sequence differs chemically from the RGD sequence by only one $–CH_2$ group. This minor change has a significant effect on its integrin affinity, which is several orders of magnitude lower than RGD *(398)*. NaGG incubated with 1% G_4RGDSY without EDC, denoted NaGG-(RGD), acted as another control as it contained only the fraction of non-specifically bound peptide remaining after dialysis. Other controls included un-modified NaGG, and as-received commercial GG. In all cases we did not observe any significant difference between the response of cells to un-modified NaGG and commercial GG and so for simplicity, data for commercial GG is not shown.

Figure 6.11 shows cells seeded on the surface of peptide-modified hydrogels and controls after 24 hr in culture. As we have seen previously for GG hydrogels, cells on un-modified NaGG surfaces formed large aggregates typical of non-adherent C2C12s (Figure 6.11A). Cells formed similar aggregates on NaGG-RGE(1%) (Figure 6.11B), indicating that conjugation of this non integrin-targeting sequence did not modify cell attachment. On NaGG-(RGD), the hydrogel containing non-specifically bound peptide, cell aggregates were smaller but there was little evidence of cell spreading (Figure 6.11C). Conversely, cells on the surface of NaGG-RGD(1%) hydrogels, with conjugated peptide, exhibited a typically flattened and elongated morphology (Figure 6.11D), indicating the development of strong adhesions and implicating specific integrin-mediated interaction. Cell attachment was dependent on RGD density, as cells seeded on hydrogels with a lower concentration of RGD peptide, NaGG-RGD(0.1%), adopted a rounded morphology or formed small aggregates with few flattened and elongated cells (Figure 6.11E).

Cells proliferated rapidly on the surface of NaGG-RGD(1%) hydrogels (Figure 6.12A). After only 12 hours under differentiation conditions, cells had formed into large multi-cellular fibres and aggregates, and this contraction continued with further culture under these conditions (Figure 6.12B). C2C12 cells cultured on TCPS usually take several days to differentiate, although early differentiation has been observed for C2C12 cells on the surface of RGD-alginate hydrogels *(313)*. This was attributed to the compliant nature of the hydrogel substrate, and could be the reason for the fast cell response observed in this work. After 5 days incubation under differentiation conditions, fixed and immunostained samples showed some formation of

multinucleated myofibres, typical of differentiated skeletal muscle, although many cells were contained within large globular aggregates (Figure 6.12C).

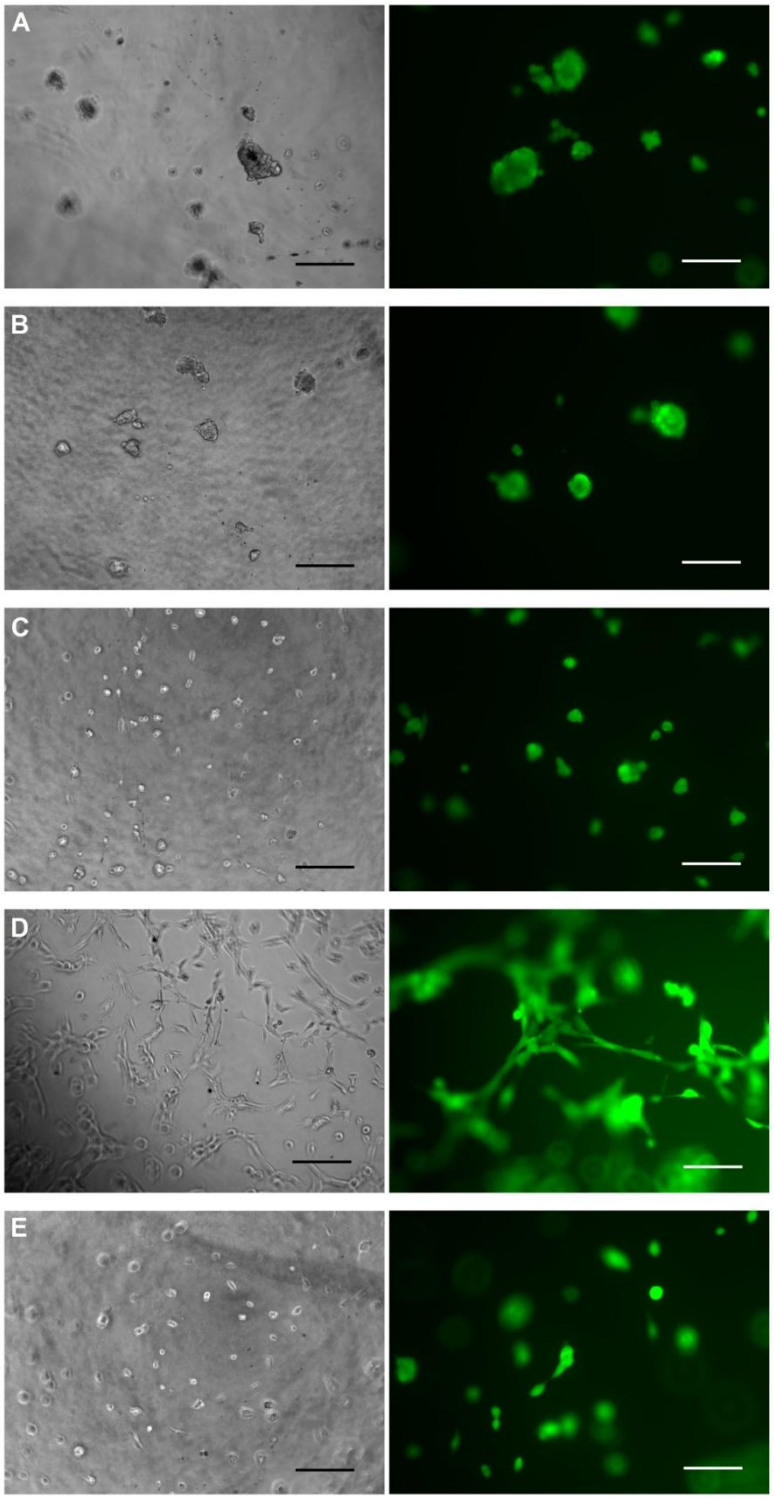

Figure 6.11: C2C12 cells seeded on the surface of un-modified or peptide-modified 0.15% w/v NaGG hydrogels: **(A)** un-modified NaGG, **(B)** NaGG-REG(1%), **(C)** NaGG-(RGD), **(D)** NaGG-RGD(1%), (**E)** NaGG-RGD(0.1%). All images show cells after 24 hr under proliferation conditions, either using phase contrast microscopy (left) or fluorescence imaging of calcein stained cells (right). Scale bars represent 200 µm (left) or 100 µm (right).

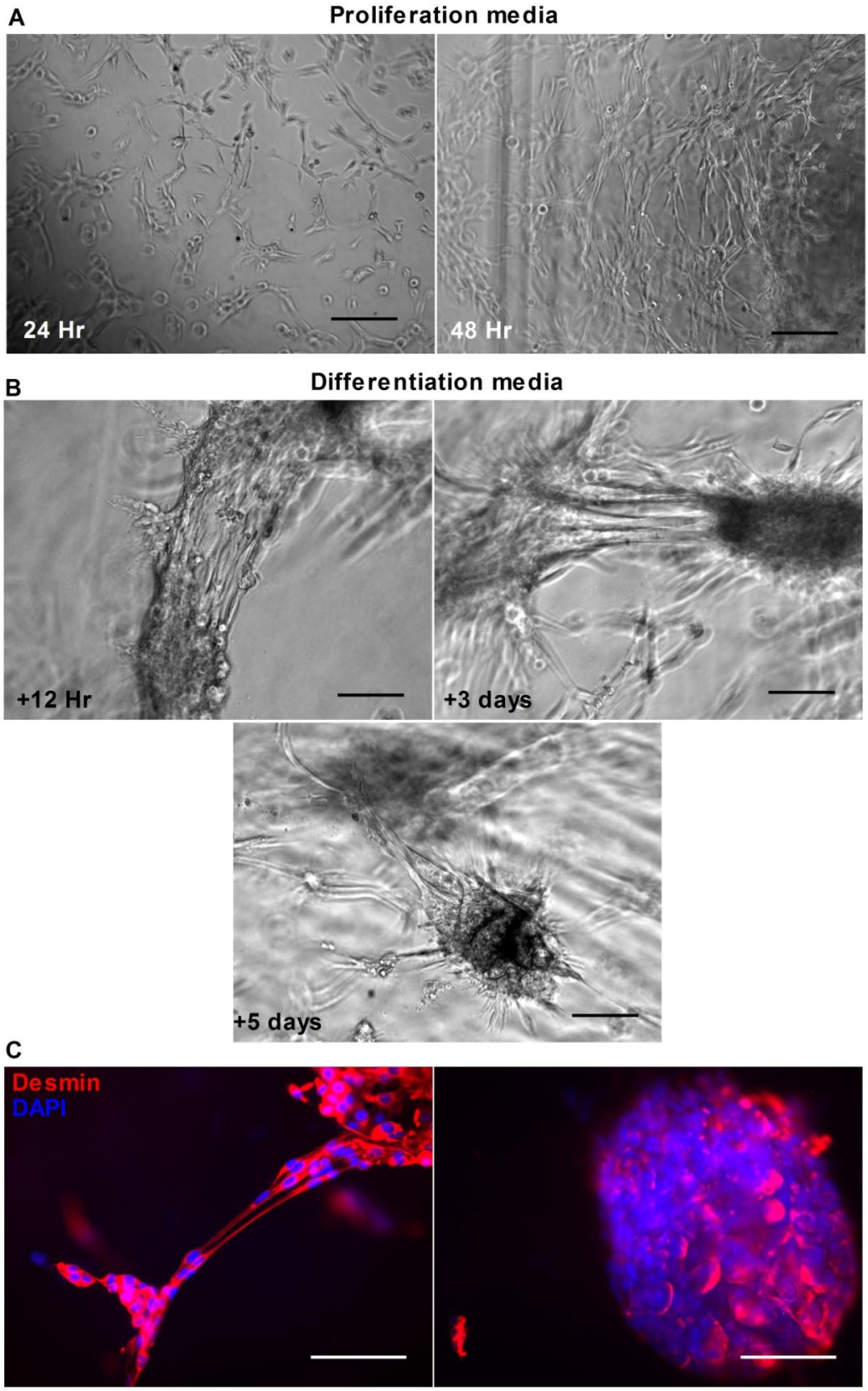

Figure 6.12: C2C12 proliferation and differentiation on the surface of 0.15% (w/v) NaGG-RGD(1%) hydrogels. **(A)** Cells under proliferation conditions after time in culture as indicated. Scale bars 200 µm. **(B)** Cells under differentiation conditions for time indicated (in addition to 48 hr under proliferation conditions). Scale bars represent 100 µm. **(C)** Cells fixed after 5 days under differentiation conditions, and immunostained against desmin (red). Nuclei stained with DAPI (blue). Scale bars represent 100 µm.

To investigate this system with relevance to 3D-printed constructs, we encapsulated cells in peptide-modified hydrogels using methods previously described (§2.5.2). C2C12 cells encapsulated in peptide-modified and control hydrogels (Figure 6.13) showed a similar range of responses to those seeded on corresponding hydrogel surfaces. Cells in NaGG retained a rounded morphology reflective of a lack of adhesive interactions (Figure 6.13A). After 4 days in culture, few cells stained with calcein indicating loss of cell viability as we observed previously for C2C12's encapsulated in GG hydrogels. A similar response was observed for cells encapsulated in NaGG-RGE(1%) (Figure 6.13B) and NaGG-(RGD) (Figure 6.13C) hydrogels, in agreement with surface-seeded results. NaGG-RGD(1%) hydrogels, however, supported the adhesion and proliferation of encapsulated C2C12 cells (Figure 6.13D). This effect was observed to a lesser extent for NaGG-RGD(0.1%) hydrogels (Figure 6.13E).

To further interpret these results, it is important to consider them in the context of the RGD peptide density presented to cells. The peptide concentration is ~9 µmol/L, based on a conjugation efficiency of ~40% and NaGG hydrogel concentration of 0.15% (w/v). Assuming that cells which remain on the hydrogel surface have access to the peptide in the top 5 nm of the hydrogel (the same assumption was made by Rowley *(395)* and others *(312)*), this gives a peptide density at the hydrogel surface of ~4.5 fmol/cm^2 for NaGG-RGD(1%) or ~0.45 fmol/cm^2 for NaGG-RGD(0.1%). Given these densities, cell responses in this work are consistent with previous findings *(394, 395)*. For example, in studies on the response of human foreskin fibroblasts seeded on glass substrates modified with varying densities of the peptide GRGDY, Massia et al. showed that a peptide density ≥1 fmol/cm^2 was required for integrin-mediated fibroblast spreading, although densities greater than 10 fmol/cm^2 were required for focal contact and stress fibre formation *(394)*. Furthermore, Rowley and co-workers have shown that for C2C12 cells seeded on alginate hydrogels modified with G_4RGDY, a peptide density at the surface of 10-100 fmol/cm^2 was required to support myoblast fusion; cells presented with a peptide density of 1 fmol/cm^2 tended to form aggregated clusters *(395)*. Taken together, these results indicate that although the peptide density presented to cells on NaGG-RGD(1%) hydrogels was sufficient to encourage adhesion, spreading and proliferation, it may have been too low to facilitate the development of good focal

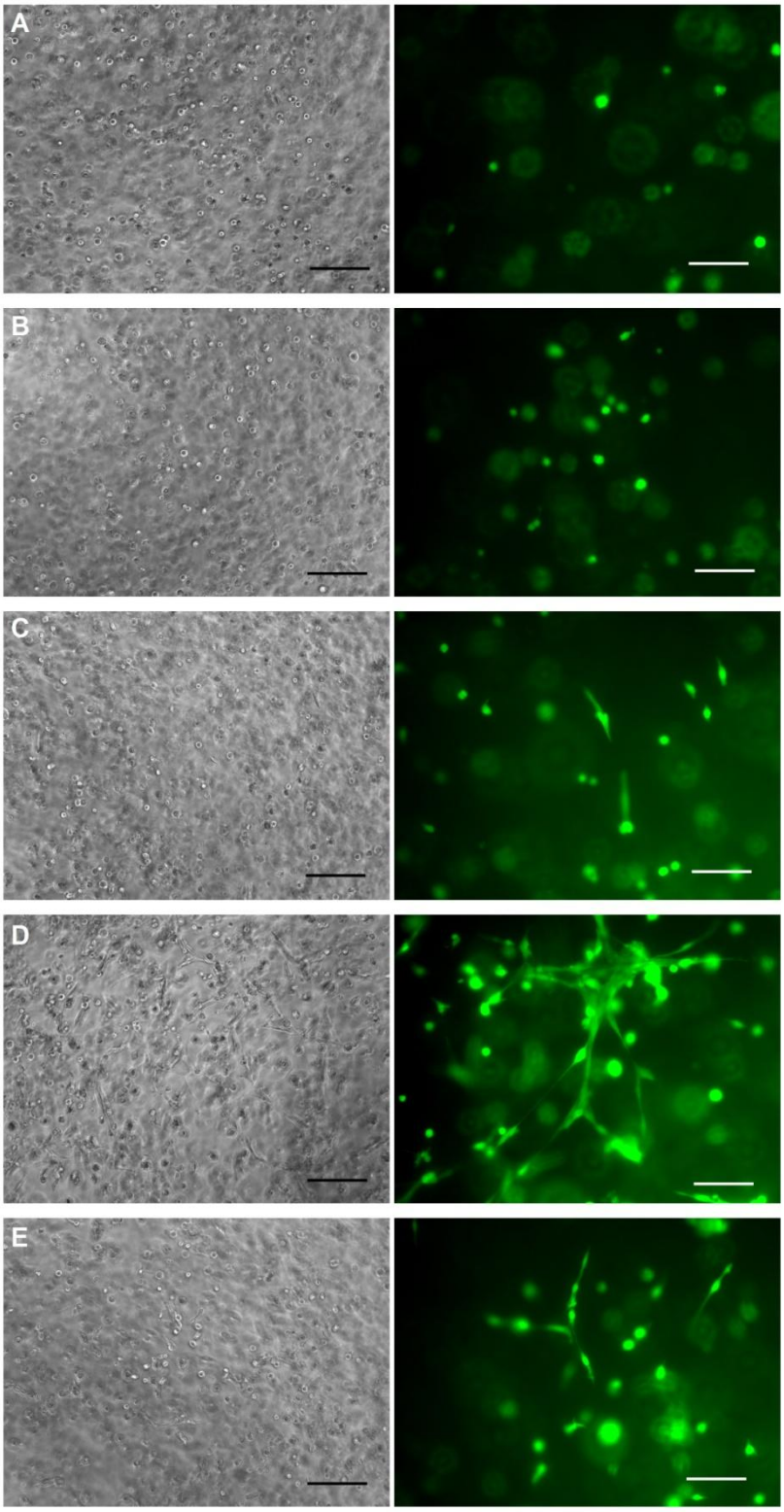

Figure 6.13: C2C12 cells encapsulated in un-modified or peptide-modified 0.15% (w/v) NaGG hydrogels: **(A)** un-modified NaGG, **(B)** NaGG-REG(1%), **(C)** NaGG-(RGD), **(D)** NaGG-RGD(1%), **(E)** NaGG-RGD(0.1%). Phase contrast images (left) show cells after 24 hr under proliferation conditions. Scale bars represent 200 µm. Fluorescence images (right) show calcein (green) stained cells after 4 days under proliferation conditions. Scale bars represent 100 µm.

contacts and subsequently support significant fusion into multinucleated myofibres.

The lack of myoblast fusion could also be associated with inappropriate mechanical cues. For example, it is known that C2C12 cells differentiate best on substrates with tissue-like stiffness *(399)*. Boontheekul and co-workers showed that the fusion of surface-seeded and encapsulated C2C12 cells into myofibres was dependent on the mechanical properties of their peptide-modified alginate hydrogels *(371)*. Furthermore, several workers have shown that C2C12 cells that exhibited adhesion and proliferation within hydrogels did not fuse into myofibres unless stimulated by mechanical stretch *(400, 401)*. GG hydrogels can be tuned to have a wide range of mechanical properties *(260)*, which could be exploited along with the application of mechanical stretch to optimise skeletal muscle differentiation on these materials.

6.5 Conclusions

The enhancement of GG bio-functionality presented here could have important application in the fabrication of cell-containing constructs. As expected from the response of encapsulated cells in previous chapters (Chapter 4 and Chapter 5), C2C12 cells exhibited minimal interaction with GG hydrogels for all tested compositions, forming non-adherent cell clusters on hydrogel surfaces or maintaining a rounded, single cell morphology when encapsulated. Furthermore, significant cell death was observed after 4 days in culture for encapsulated cells, which appeared to be due to inadequate cell-matrix interactions rather than a lack of nutrient or oxygen diffusion. C2C12 cells were found to attach and proliferate on curved GG hydrogel surfaces, although this does not translate to the fabrication of cell-encapsulating constructs.

The addition of collagen to GG hydrogels enhanced the interactions of encapsulated C2C12 cells with the matrix, appearing to effectively harness both the biofunctionality of collagen and the fast-gelling mechanism of GG. However, in order to translate more effectively to the cell printing work throughout this thesis, the conjugation of peptides was pursued as an alternative modification strategy. Initial experiments to conjugate the GRGDY peptide to GG using conditions previously optimised for peptide conjugation to alginate showed minimal peptide incorporation

by elemental analysis, and no effect on cell attachment. To expedite the optimisation and characterisation of conjugation to GG, the peptide G_4RGDSY was radiolabelled with ^{125}-iodine with a specific activity of 2 Ci/mmol. It was found that commercial GG hindered peptide conjugation, likely due to divalent cation contaminants that deactivated carboxylic acid groups to functionalisation. GG was consequently purified to give the sodium salt form, NaGG, in 60% yield. The peptide was successfully conjugated to NaGG over three orders of magnitude of input peptide concentration (0.02-2 mol% of carboxylic acid groups on NaGG), with optimised conditions achieving a conjugation efficiency of ~ 40%.

C2C12 cells seeded on the surface of, and encapsulated within, RGD-based peptide-modified NaGG hydrogels showed enhanced interaction with the matrix in comparison with controls. This improvement was attributed to cell integrin binding with the RGD domain, which was supported by a lack of cellular interaction with NaGG hydrogels modified with the G_4RGESY peptide. Cells proliferated on the surface of peptide-modified hydrogels, and there was some evidence of differentiation into myofibres, although the peptide density was likely too low in this work to facilitate significant fusion into multinucleated muscle fibres. These results demonstrate that RGD-peptide conjugation to NaGG is an effective means to influence cellular responses, and can significantly enhance the attachment, proliferation and differentiation of C2C12 cells.

6.6 Acknowledgements

Dr. Eskender Mume (ANSTO) assisted with some experiments including the purification of gellan gum, peptide radiolabelling and peptide conjugation. This work was also conducted under the guidance of Dr. Ivan Greguric (ANSTO).

Damian Kirchmajer (University of Wollongong) performed the analysis of ion content in commercial and purified samples of gellan gum.

7 GENERAL CONCLUSIONS AND RECOMMENDATIONS

The aim of this thesis was to explore new strategies towards the development of bio-inks for the fabrication of cell constructs through drop-on-demand printing techniques. The bio-inks were designed with the goal of simultaneously satisfying engineering and biological requirements to enable robust deposition of living cells. Specifically, certain criteria were defined for an ideal bio-ink to: prevent cell settling and aggregation; possess optimal fluid properties for drop-on-demand printing; contain little dry mass; have a physiological pH and ionic strength (i.e. based in culture media); and exhibit no cytotoxic effects. These criteria form part of an overarching view that drop-on-demand printing techniques enable precise deposition of cells without any particular polymer or hydrogel matrix, and therefore can be utilised to fabricate cell-only constructs (i.e. microarrays), or as part of a synergistic approach to fabricate 3D cell-laden constructs where a matrix is deposited by a separate means. This thesis also endeavoured to demonstrate the fabrication of such constructs through novel reactive printing approaches using gellan gum (GG), and to explore the modification of this material to encourage cellular interactions.

Two bio-inks were tailored for microvalve and inkjet printing, respectively. Both included a suspension of GG microgel particles (0.05% w/v) in cell culture media, while the inkjet formulation included the surfactants Novec FC-4430 (0.05% v/v) and Poloxamer 188 (P188, 0.1% v/v). These bio-inks were shown to successfully meet the criteria outlined above, with the two features of their design (i.e. the microgel suspension, and the combination of surfactants) critical in achieving this goal.

Firstly, the low-concentration GG microgel suspension provided rheological properties that prevented cell settling and aggregation while remaining amenable to drop-on-demand printing. Cells did not appear to be confined within the microgel suspension post-printing, as evidenced by the interaction of inkjet printed cells with collagen hydrogel substrates. This work therefore establishes that microgel suspensions offer an effective alternative to previous methods used to prevent cell settling, such as the use of high viscosity polymer solutions or high concentrations of density-balancing additives. While this thesis demonstrated utility in microvalve and inkjet printing, bio-inks may also provide stable cell suspensions for other

applications (i.e. microfluidics). With regards to inkjet printing, further characterisation of the extensional viscosity and droplet formation dynamics of the cell-laden bio-ink may allow tailoring of printing waveforms to minimise satellite droplet formation and further improve printing performance.

Secondly, the addition of surfactants to the bio-ink for inkjet printing demonstrated that careful surfactant selection can improve bio-ink properties without cytotoxicity. Importantly, the fluorosurfactant Novec FC4430 afforded an optimal surface tension for inkjet printing (~ 30 mN/m) at a low concentration (0.05% v/v) with no exhibited cytotoxicity. This finding encourages further use of fluorosurfactants in inkjet cell printing. While P188 has been included in bio-inks previously, the work in this thesis showed that its inclusion in the bio-ink (at 0.1% v/v) yielded a direct and quantitative enhancement of printed cell viability. This result adds to a growing body of evidence supporting the ability of P188 to protect or heal damaged cells, and warrants its inclusion in future bio-ink formulations. The work described here is the first extensive study on the use of surfactants in inkjet cell printing, and further work will be required to study any long-term effects of these surfactants on the function of a broader range of cell types.

The bio-ink facilitated robust cell deposition by microvalve and inkjet printing, as demonstrated by both reproducible cell output and the maintenance of normal behaviour in printed cell populations. Variation in cell output over time substantially reduces control over printed cell constructs and, although the problem has been highlighted in the literature, few solutions had previously been explored. The bio-ink enabled uniform printing over long printing periods, even from piezoelectric print heads that contain many nozzles. Piezoelectric inkjet is the current standard for high-end printing applications, and printing with many-nozzle heads could allow for higher throughput and the fabrication of larger cellular constructs. In agreement with literature, the number of cells within each printed droplet, from both techniques, followed a Poisson distribution. This presents a challenge in applications where a single cell, or defined number of cells, is desired in each droplet (i.e. in printed microarrays). Subsequent studies could investigate how to overcome this limitation without significantly effecting throughput.

The normal behaviour of printed cells reported here bolsters current evidence supporting the suitability of drop-on-demand printing for the deposition of viable, functional cells. There remains, however, relatively few reports on the viability of cells printed by piezoelectric inkjet heads (compared to thermal inkjet), and further studies should investigate the effect of printing waveform on cells printed from many-nozzle devices. The work in this thesis was carried out solely with tumour-derived cell lines of murine origin (C2C12, PC12, L929), and thus further work is also required to study the effect of bio-ink exposure and printing processes on other cell types (i.e. human primary and stem cells). It will be necessary to probe cell responses over the longer-term, and to study genotypic indicators to more thoroughly characterise printed cell function.

The preceding paragraphs have highlighted how the bio-inks developed in this work provided enhanced capability for robust deposition of living cells by microvalve and inkjet printing. This thesis also explored how to exploit this capability in the fabrication of useful cell-containing constructs. These included patterns of single or multiple cell types on 2D substrates, as well as cell-encapsulating hydrogels formed by reactive printing approaches.

Simple cell microarrays deposited on glass slides by inkjet printing were combined with LESA-MS to allow rapid profiling of cellular lipid composition with single-cell resolution. This approach could be used to study the role of lipids in cellular function and dysfunction. While we only sought to detect lipids in this work, it is not unreasonable to assume that other cellular components and metabolites could be detected. This technique could also be adapted to allow analysis of living cells; for example, by printing cellular arrays on hydrogels or other hydrated substrates. This could allow profiling of cellular components during dynamic processes, including controlled interactions with other cells, biomaterials or active compounds.

Live cell patterns containing two different cell types (C2C12 and PC12) were also printed on collagen hydrogel surfaces and retained in subsequent culture. The observed interaction of these cells suggests that simple printed 2D constructs such as these could help to shed light on the interplay between multiple cell types in an engineered structure, and pave the way for the fabrication of functional tissues. Further work in this area should examine functional arrangements of a range of cell

types and their response to alterations in cell-cell spatial organisation or various environmental challenges. It is envisaged that useful disease models could be fabricated and validated to provide screening platforms for drug candidates and other compounds.

Reactive printing approaches have been a well-implemented means to construct cell-encapsulating hydrogel structures through drop-on-demand printing. Both of the reactive printing approaches demonstrated in this thesis had an element of novelty. For microvalve printing, Drop-on-demand Reactive In-solution Plotting (DRIP) represents a new fabrication approach with potential advantages over existing techniques. In subsequent studies, it would be useful to implement a microvalve printing system that allows vertical axis movement during deposition and greater control over dispensing parameters in order to optimise the fabrication of 3D cell-laden hydrogels. For inkjet printing, the deposition of matrix (GG) and cells from separate print heads was demonstrated. While only simple several-layer constructs were fabricated, the inclusion of a vertical-axis stage in the printer hardware could allow more complex 3D constructs to be printed. This could be a particularly powerful approach if multiple print heads were used in combination to deliver additional support materials, cross-linkers or biomolecules.

The lack of C2C12 cell interaction within microvalve and inkjet printed GG hydrogel constructs encourages subsequent studies utilising the peptide-modified GG developed in this thesis, or other bio-functional materials, as the hydrogel component. While these approaches were mostly explored with calcium-containing solutions, initial studies were also conducted with cells suspended and printed in the bio-ink formulation. This is a preliminary validation that the bio-ink meets another of the stated design criteria in allowing the separation of cell and matrix delivery. Further work is required to more extensively characterise the fabricated hydrogel structures.

Finally, the modification of GG to enhance cellular interactions was presented. Radiolabelling of RGD-containing peptides provided a highly sensitive and rapid means to quantify peptide conjugation, enabling optimisation of the conjugation procedure using simple cross-linking chemistry. The purification of commercial GG samples required to achieve efficient conjugation was an important step, and

generally emphasises the need to be aware of the effects of divalent cation contaminants in commercial samples of GG. The response of C2C12 cells seeded on the surface of, and encapsulated within, modified hydrogels showed that specific binding with the RGD sequence resulted in enhanced cell attachment, proliferation and differentiation, although the peptide density was likely too low to facilitate the formation of focal adhesions and significant myofibre formation. An obvious extension of this work is the use peptide-modified GG in the previously outlined reactive printing approaches. The majority of reactive printing work to date has employed alginate as the hydrogel matrix, and so utilising cell-interactive materials like the peptide-modified GG developed here will be an important step towards the fabrication of functional constructs. Aside from application in reactive printing, peptide-modified GG could find use more generally as a cell culture matrix. Further work could also explore the regulation of cell responses by changing the concentration and nature of the peptide, including spacer arm length or arrangement, and there is scope to attach different peptide sequences to GG to target interactions with different cell types.

This work shows that smarter design of bio-ink materials can yield important advances in cell printing approaches, addressing some of the major challenges in the continuing evolution of drop-on-demand cell printing towards becoming a clinically relevant biofabrication tool. It is our hope that these results will encourage further work in the development of bio-inks, facilitating the application of cell printing to develop more complex and functional tissue constructs.

8 REFERENCES

1. R. Langer, J. P. Vacanti, Tissue engineering., *Science* **260**, 920–6 (1993).

2. T. S. Bentley, S. G. Hanson, *2011 U.S. organ and tissue transplant cost estimates and discussion*, Milliman (April 2011).

3. *OPTN/SRTR 2010 Annual Data Report*, Organ Procurement and Transplantation Network (OPTN) and Scientific Registry of Transplant Recipients (SRTR) (2011).

4. M. J. Lysaght, J. A. O'Loughlin, Demographic scope and economic magnitude of contemporary organ replacement therapies., *ASAIO journal* **46**, 515–21 (2000).

5. J. H. S. George, Engineering of fibrous scaffolds for use in regenerative medicine, thesis, Imperial College London (2009).

6. S. R. Khetani, S. N. Bhatia, Engineering tissues for in vitro applications., *Current opinion in biotechnology* **17**, 524–31 (2006).

7. D. W. Hutmacher, Biomaterials offer cancer research the third dimension., *Nature materials* **9**, 90–3 (2010).

8. E. Cukierman, R. Pankov, D. R. Stevens, K. M. Yamada, Taking cell-matrix adhesions to the third dimension., *Science* **294**, 1708–12 (2001).

9. S. Zhang, Beyond the Petri dish., *Nature biotechnology* **22**, 151–2 (2004).

10. F. Pampaloni, E. G. Reynaud, E. H. K. Stelzer, The third dimension bridges the gap between cell culture and live tissue., *Nature reviews. Molecular cell biology* **8**, 839–45 (2007).

11. F. Xu et al., Three-dimensional magnetic assembly of microscale hydrogels., *Advanced materials* **23**, 4254–60 (2011).

12. P. Honig, R. Lalonde, The economics of drug development: a grim reality and a role for clinical pharmacology., *Clinical pharmacology and therapeutics* **87**, 247–51 (2010).

13. K. I. Kaitin, Deconstructing the drug development process: the new face of innovation., *Clinical pharmacology and therapeutics* **87**, 356–61 (2010).

14. J. A. DiMasi, L. Feldman, A. Seckler, A. Wilson, Trends in risks associated with new drug development: success rates for investigational drugs., *Clinical pharmacology and therapeutics* **87**, 272–7 (2010).

15. S. J. Hollister, Scaffold engineering: a bridge to where?, *Biofabrication* **1**, 012001 (2009).

16. R. Langer, Tissue engineering., *Molecular therapy : the journal of the American Society of Gene Therapy* **1**, 12–5 (2000).

17. J. P. Vacanti, R. Langer, Tissue engineering: the design and fabrication of living replacement devices for surgical reconstruction and transplantation., *Lancet* **354 Suppl** , SI32–4 (1999).

18. E. Lavik, R. Langer, Tissue engineering: current state and perspectives., *Applied microbiology and biotechnology* **65**, 1–8 (2004).

19. R. M. Nerem, Tissue engineering: the hope, the hype, and the future., *Tissue engineering* **12**, 1143–50 (2006).

20. R. M. Nerem, Regenerative medicine: the emergence of an industry., *Journal of the Royal Society, Interface* **7 Suppl 6**, S771–5 (2010).

21. A. Jaklenec, A. Stamp, E. Deweerd, A. Sherwin, R. Langer, Progress in the Tissue Engineering and Stem Cell Industry "Are we there yet?"., *Tissue engineering.*

Part B, Reviews **18**, 155–66 (2012).

22. M. J. Lysaght, A. L. Hazlehurst, Tissue engineering: the end of the beginning., *Tissue engineering* **10**, 309–20 (2004).

23. M. J. Lysaght, N. A. Nguy, K. Sullivan, An economic survey of the emerging tissue engineering industry., *Tissue engineering* **4**, 231–8 (1998).

24. M. J. Lysaght, J. Reyes, The Growth of Tissue Engineering, *Tissue Engineering* **7**, 485–494 (2001).

25. M. J. Lysaght, A. Jaklenec, E. Deweerd, Great expectations: private sector activity in tissue engineering, regenerative medicine, and stem cell therapeutics., *Tissue engineering. Part A* **14**, 305–15 (2008).

26. N. Parenteau, Skin: The first tissue-engineered products, *Scientific American* **280**, 83–84 (1999).

27. B. Guillotin, F. Guillemot, Cell patterning technologies for organotypic tissue fabrication., *Trends in biotechnology* **29**, 183–190 (2011).

28. A. G. Mikos et al., Engineering complex tissues., *Tissue engineering* **12**, 3307–39 (2006).

29. A. I. Caplan, S. P. Bruder, Mesenchymal stem cells: building blocks for molecular medicine in the 21st century., *Trends in molecular medicine* **7**, 259–64 (2001).

30. J. M. Gimble, A. J. Katz, B. A. Bunnell, Adipose-derived stem cells for regenerative medicine., *Circulation research* **100**, 1249–60 (2007).

31. J. Hipp, A. Atala, Sources of stem cells for regenerative medicine., *Stem cell reviews* **4**, 3–11 (2008).

32. G. Chan, D. J. Mooney, New materials for tissue engineering: towards greater control over the biological response., *Trends in biotechnology* **26**, 382–92 (2008).

33. L. Zhang, T. J. Webster, Nanotechnology and nanomaterials: Promises for improved tissue regeneration, *Nano Today* **4**, 66–80 (2009).

34. V. Mironov et al., Biofabrication: a 21st century manufacturing paradigm., *Biofabrication* **1**, 022001 (2009).

35. W.-Y. Yeong, C.-K. Chua, K.-F. Leong, M. Chandrasekaran, Rapid prototyping in tissue engineering: challenges and potential., *Trends in biotechnology* **22**, 643–52 (2004).

36. K. F. Leong, C. M. Cheah, C. K. Chua, Solid freeform fabrication of three-dimensional scaffolds for engineering replacement tissues and organs, *Biomaterials* **24**, 2363–2378 (2003).

37. Q. P. Pham, U. Sharma, A. G. Mikos, Electrospinning of polymeric nanofibers for tissue engineering applications: a review., *Tissue engineering* **12**, 1197–211 (2006).

38. T. Kaully, K. Kaufman-Francis, A. Lesman, S. Levenberg, Vascularization-the conduit to viable engineered tissues., *Tissue engineering. Part B, Reviews* **15**, 159–69 (2009).

39. M. Lovett, K. Lee, A. Edwards, D. L. Kaplan, Vascularization strategies for tissue engineering., *Tissue engineering. Part B, Reviews* **15**, 353–70 (2009).

40. E. C. Novosel, C. Kleinhans, P. J. Kluger, Vascularization is the key challenge in tissue engineering., *Advanced drug delivery reviews* **63**, 300–11 (2011).

41. J. Rouwkema, N. C. Rivron, C. A. van Blitterswijk, Vascularization in tissue

engineering., *Trends in biotechnology* **26**, 434–41 (2008).

42. S. Hurtley, Location , location, location, *Science* **326**, 1205 (2009).

43. The third industrial revolution*The Economist* (2012).

44. S. M. Peltola, F. P. W. Melchels, D. W. Grijpma, M. Kellomäki, A review of rapid prototyping techniques for tissue engineering purposes., *Annals of medicine* **40**, 268–80 (2008).

45. V. L. Tsang, S. N. Bhatia, Three-dimensional tissue fabrication., *Advanced drug delivery reviews* **56**, 1635–47 (2004).

46. D. W. Hutmacher, M. Sittinger, M. V Risbud, Scaffold-based tissue engineering: rationale for computer-aided design and solid free-form fabrication systems., *Trends in biotechnology* **22**, 354–62 (2004).

47. J. S. Miller et al., Rapid casting of patterned vascular networks for perfusable engineered three-dimensional tissues., *Nature materials* **11**, 1–7 (2012).

48. W. Sun, A. Darling, B. Starly, J. Nam, Computer-aided tissue engineering: overview, scope and challenges., *Biotechnology and applied biochemistry* **39**, 29–47 (2004).

49. N. Matsuda, T. Shimizu, M. Yamato, T. Okano, Tissue Engineering Based on Cell Sheet Technology, *Advanced materials* **19**, 3089–3099 (2007).

50. J. Yang et al., Reconstruction of functional tissues with cell sheet engineering., *Biomaterials* **28**, 5033–43 (2007).

51. I. E. Hannachi, M. Yamato, T. Okano, Cell sheet technology and cell patterning for biofabrication., *Biofabrication* **1**, 022002 (2009).

52. D. Seliktar, Designing Cell-Compatible Hydrogels for Biomedical Applications, *Science* **336**, 1124–1128 (2012).

53. K. Y. Lee, D. J. Mooney, Hydrogels for Tissue Engineering, *Chemical Reviews* **101**, 1869–1880 (2001).

54. J. L. Drury, D. J. Mooney, Hydrogels for tissue engineering: scaffold design variables and applications, *Biomaterials* **24**, 4337–4351 (2003).

55. F. Brandl, F. Sommer, A. Goepferich, Rational design of hydrogels for tissue engineering: impact of physical factors on cell behavior., *Biomaterials* **28**, 134–46 (2007).

56. N. C. Hunt, L. M. Grover, Cell encapsulation using biopolymer gels for regenerative medicine, *Biotechnology Letters* **32**, 733–742 (2010).

57. G. D. Nicodemus, S. J. Bryant, Cell encapsulation in biodegradable hydrogels for tissue engineering applications., *Tissue engineering. Part B, Reviews* **14**, 149–65 (2008).

58. B. V Slaughter, S. S. Khurshid, O. Z. Fisher, A. Khademhosseini, N. a Peppas, Hydrogels in regenerative medicine., *Advanced materials* **21**, 3307–29 (2009).

59. R. V Ulijn et al., Bioresponsive hydrogels, *Materials Today* **10**, 40–48 (2007).

60. G. D. Nicodemus, S. J. Bryant, Cell encapsulation in biodegradable hydrogels for tissue engineering applications., *Tissue engineering. Part B, Reviews* **14**, 149–165 (2008).

61. J. F. Mano et al., Natural origin biodegradable systems in tissue engineering and regenerative medicine: present status and some moving trends., *Journal of the Royal Society, Interface* **4**, 999–1030 (2007).

62. P. B. Malafaya, G. A. Silva, R. L. Reis, Natural-origin polymers as carriers and

scaffolds for biomolecules and cell delivery in tissue engineering applications., *Advanced drug delivery reviews* **59**, 207–33 (2007).

63. H. Geckil, F. Xu, X. Zhang, S. Moon, U. Demirci, Engineering hydrogels as extracellular matrix mimics., *Nanomedicine* **5**, 469–84 (2010).

64. J. Zhu, Bioactive modification of poly(ethylene glycol) hydrogels for tissue engineering., *Biomaterials* **31**, 4639–56 (2010).

65. A. D. Augst, H. J. Kong, D. J. Mooney, Alginate Hydrogels as Biomaterials, *Macromolecular bioscience* **6**, 623–633 (2006).

66. S. N. Pawar, K. J. Edgar, Alginate derivatization: A review of chemistry, properties and applications., *Biomaterials* **33**, 3279–305 (2012).

67. N. Annabi et al., Controlling the porosity and microarchitecture of hydrogels for tissue engineering., *Tissue engineering. Part B, Reviews* **16**, 371–83 (2010).

68. J. W. Nichol, A. Khademhosseini, Modular Tissue Engineering: Engineering Biological Tissues from the Bottom Up., *Soft matter* **5**, 1312–1319 (2009).

69. A. Khademhosseini, R. Langer, Microengineered hydrogels for tissue engineering., *Biomaterials* **28**, 5087–92 (2007).

70. U. A. Gurkan, S. Tasoglu, D. Kavaz, M. C. Demirel, U. Demirci, Emerging Technologies for Assembly of Microscale Hydrogels, *Advanced healthcare materials* **1**, 149–158 (2012).

71. N. W. Choi et al., Microfluidic scaffolds for tissue engineering., *Nature materials* **6**, 908–15 (2007).

72. H. Andersson, A. van den Berg, Microfabrication and microfluidics for tissue engineering: state of the art and future opportunities., *Lab on a chip* **4**, 98–103 (2004).

73. J. Voldman, Electrical forces for microscale cell manipulation., *Annual review of biomedical engineering* **8**, 425–54 (2006).

74. T. G. Fernandes, M. M. Diogo, D. S. Clark, J. S. Dordick, J. M. S. Cabral, High-throughput cellular microarray platforms: applications in drug discovery, toxicology and stem cell research., *Trends in biotechnology* **27**, 342–9 (2009).

75. M. L. Yarmush, K. R. King, Living-cell microarrays., *Annual review of biomedical engineering* **11**, 235–57 (2009).

76. D. S. Chen, M. M. Davis, Molecular and functional analysis using live cell microarrays., *Current opinion in chemical biology* **10**, 28–34 (2006).

77. X. Gidrol et al., 2D and 3D cell microarrays in pharmacology., *Current opinion in pharmacology* **9**, 664–8 (2009).

78. D. Castel, A. Pitaval, M. A. Debily, X. Gidrol, Cell microarrays in drug discovery., *Drug discovery today* **11**, 616–22 (2006).

79. M. A. Walling, J. R. E. Shepard, Cellular heterogeneity and live cell arrays., *Chemical Society reviews* **40**, 4049–76 (2011).

80. I. Barbulovic-Nad et al., Bio-microarray fabrication techniques - a review., *Critical reviews in biotechnology* **26**, 237–59 (2006).

81. H.-C. Moeller, M. K. Mian, S. Shrivastava, B. G. Chung, A. Khademhosseini, A microwell array system for stem cell culture., *Biomaterials* **29**, 752–63 (2008).

82. T. Billiet, M. Vandenhaute, J. Schelfhout, S. Van Vlierberghe, P. Dubruel, A review of trends and limitations in hydrogel-rapid prototyping for tissue engineering., *Biomaterials* **33**, 6020–41 (2012).

83. V. Mironov, N. Reis, B. Derby, Bioprinting : A Beginning, *Tissue engineering* **12**, 631–634 (2006).

84. R. J. Klebe, Cytoscribing: a method for micropositioning cells and the construction of two- and three-dimensional synthetic tissues., *Experimental cell research* **179**, 362–73 (1988).

85. F. Xu et al., Microengineering methods for cell-based microarrays and high-throughput drug-screening applications., *Biofabrication* **3**, 034101 (2011).

86. P. Calvert, Printing cells., *Science* **318**, 208–9 (2007).

87. K. W. Binder, A. J. Allen, J. J. Yoo, A. Atala, Drop-on-Demand Inkjet Bioprinting: a Primer, *Gene therapy and regulation* **06**, 33 (2011).

88. P. G. Campbell, L. E. Weiss, Tissue engineering with the aid of inkjet printers., *Expert opinion on biological therapy* **7**, 1123–7 (2007).

89. B. Derby, Printing and Prototyping of Tissues and Scaffolds, *Science* **338**, 921–926 (2012).

90. K. J. Burg, T. Boland, Minimally invasive tissue engineering composites and cell printing., *IEEE engineering in medicine and biology magazine : the quarterly magazine of the Engineering in Medicine & Biology Society* **22**, 84–91 (2003).

91. S. Wüst, R. Müller, S. Hofmann, Controlled Positioning of Cells in Biomaterials—Approaches Towards 3D Tissue Printing, *Journal of functional biomaterials* **2**, 119–154 (2011).

92. F. Guillemot, V. Mironov, M. Nakamura, Bioprinting is coming of age: report from the International Conference on Bioprinting and Biofabrication in Bordeaux (3B'09), *Biofabrication* **2**, 010201 (2010).

93. V. Mironov, T. Boland, T. Trusk, G. Forgacs, R. R. Markwald, Organ printing: computer-aided jet-based 3D tissue engineering, *Trends in biotechnology* **21**, 157–161 (2003).

94. N. E. Fedorovich et al., Hydrogels as extracellular matrices for skeletal tissue engineering: State-of-the-Art and Novel Application in Organ Printing, *Tissue engineering* **13**, 1905–1925 (2007).

95. C. C. Chang, E. D. Boland, S. K. Williams, J. B. Hoying, Direct-write bioprinting three-dimensional biohybrid systems for future regenerative therapies., *Journal of biomedical materials research. Part B, Applied biomaterials* **98**, 160–70 (2011).

96. X. Wang, Y. Yan, R. Zhang, Recent trends and challenges in complex organ manufacturing., *Tissue engineering. Part B, Reviews* **16**, 189–97 (2010).

97. N. E. Fedorovich, J. Alblas, W. E. Hennink, F. C. Oner, W. J. A. Dhert, Organ printing: the future of bone regeneration?, *Trends in biotechnology* **29**, 601–6 (2011).

98. C. M. Smith et al., Three-dimensional bioassembly tool for generating viable tissue-engineered constructs., *Tissue engineering* **10**, 1566–76 (2004).

99. C. M. Smith, J. J. Christian, W. L. Warren, S. K. Williams, Characterizing environmental factors that impact the viability of tissue-engineered constructs fabricated by a direct-write bioassembly tool., *Tissue engineering* **13**, 373–83 (2007).

100. X. Wang, Y. Yan, R. Zhang, Rapid prototyping as a tool for manufacturing bioartificial livers., *Trends in biotechnology* **25**, 505–13 (2007).

101. X. Wang et al., Generation of three-dimensional hepatocyte/gelatin structures with rapid prototyping system., *Tissue engineering* **12**, 83–90 (2006).

102. Y. Yan et al., Fabrication of viable tissue-engineered constructs with 3D cell-

assembly technique., *Biomaterials* **26**, 5864–71 (2005).

103. J. Cheng et al., Rheological Properties of Cell-Hydrogel Composites Extruding Through Small-Diameter Tips, *Journal of manufacturing science and engineering* **130**, 021014 (2008).

104. Y. Yan, Direct Construction of a Three-dimensional Structure with Cells and Hydrogel, *Journal of bioactive and compatible polymers* **20**, 259–269 (2005).

105. W. Xu et al., Rapid Prototyping Three-Dimensional Cell/Gelatin/Fibrinogen Constructs for Medical Regeneration, *Journal of bioactive and compatible polymers* **22**, 363–377 (2007).

106. M. Xu, Y. Yan, H. Liu, R. Yao, X. Wang, Controlled Adipose-derived Stromal Cells Differentiation into Adipose and Endothelial Cells in a 3D Structure Established by Cell-assembly Technique, *Journal of bioactive and compatible polymers* **24**, 31–47 (2009).

107. S. Li et al., Direct Fabrication of a Hybrid Cell/Hydrogel Construct by a Double-nozzle Assembling Technology, *Journal of bioactive and compatible polymers* **24**, 249–265 (2009).

108. R. Landers, R. Mülhaupt, Desktop manufacturing of complex objects, prototypes and biomedical scaffolds by means of computer-assisted design combined with computer-guided 3D plotting of polymers and reactive oligomers, *Macromolecular materials and engineering* **282**, 17–21 (2000).

109. R. Landers, U. Hübner, R. Schmelzeisen, R. Mülhaupt, Rapid prototyping of scaffolds derived from thermoreversible hydrogels and tailored for applications in tissue engineering., *Biomaterials* **23**, 4437–47 (2002).

110. A. Pfister et al., Biofunctional Rapid Prototyping for Tissue-Engineering Applications : 3D Bioplotting versus 3D Printing, *Biofunctional rapid prototyping* , 624–638 (2003).

111. N. E. Fedorovich, J. R. De Wijn, A. J. Verbout, J. Alblas, W. J. A. Dhert, Three-dimensional fiber deposition of cell-laden, viable, patterned constructs for bone tissue printing., *Tissue engineering. Part A* **14**, 127–33 (2008).

112. N. E. Fedorovich, E. Kuipers, D. Gawlitta, W. J. A. Dhert, J. Alblas, Scaffold porosity and oxygenation of printed hydrogel constructs affect functionality of embedded osteogenic progenitors., *Tissue engineering. Part A* **17**, 2473–86 (2011).

113. N. E. Fedorovich, H. M. Wijnberg, W. J. A. Dhert, J. Alblas, Distinct tissue formation by heterogeneous printing of osteo- and endothelial progenitor cells., *Tissue engineering. Part A* **17**, 2113–21 (2011).

114. N. E. Fedorovich et al., Biofabrication of osteochondral tissue equivalents by printing topologically defined, cell-laden hydrogel scaffolds., *Tissue engineering. Part C, Methods* **18**, 33–44 (2012).

115. R. Gaetani et al., Cardiac tissue engineering using tissue printing technology and human cardiac progenitor cells., *Biomaterials* **33**, 1782–90 (2012).

116. W. Schuurman et al., Bioprinting of hybrid tissue constructs with tailorable mechanical properties., *Biofabrication* **3**, 021001 (2011).

117. J. Y. Kim, D.-W. Cho, Blended PCL/PLGA scaffold fabrication using multi-head deposition system, *Microelectronic engineering* **86**, 1447–1450 (2009).

118. J.-H. Shim, J. Y. Kim, M. Park, J. Park, D.-W. Cho, Development of a hybrid scaffold with synthetic biomaterials and hydrogel using solid freeform fabrication

technology., *Biofabrication* **3**, 034102 (2011).

119. K. He, X. Wang, Rapid prototyping of tubular polyurethane and cell/hydrogel constructs, *Journal of bioactive and compatible polymers* **26**, 363–374 (2011).

120. E. Malone, H. Lipson, Fab@Home: the personal desktop fabricator kit, *Rapid prototyping journal* **13**, 245–255 (2007).

121. D. L. Cohen, E. Malone, H. Lipson, L. J. Bonassar, Direct freeform fabrication of seeded hydrogels in arbitrary geometries., *Tissue engineering* **12**, 1325–35 (2006).

122. D. L. Cohen et al., Increased mixing improves hydrogel homogeneity and quality of three-dimensional printed constructs., *Tissue engineering. Part C, Methods* **17**, 239–48 (2011).

123. D. L. Cohen, J. I. Lipton, L. J. Bonassar, H. Lipson, Additive manufacturing for in situ repair of osteochondral defects., *Biofabrication* **2**, 035004 (2010).

124. A. Skardal, J. Zhang, G. D. Prestwich, Bioprinting vessel-like constructs using hyaluronan hydrogels crosslinked with tetrahedral polyethylene glycol tetracrylates., *Biomaterials* **31**, 6173–81 (2010).

125. A. Skardal et al., Photocrosslinkable hyaluronan-gelatin hydrogels for two-step bioprinting., *Tissue engineering. Part A* **16**, 2675–85 (2010).

126. S. Khalil, J. Nam, W. Sun, Multi-nozzle deposition for construction of 3D biopolymer tissue scaffolds, *Rapid prototyping journal* **11**, 9–17 (2005).

127. S. Khalil, W. Sun, Biopolymer deposition for freeform fabrication of hydrogel tissue constructs, *Materials science and engineering: C* **27**, 469–478 (2007).

128. S. Khalil, W. Sun, Bioprinting endothelial cells with alginate for 3D tissue constructs., *Journal of biomechanical engineering* **131**, 111002 (2009).

129. K. C. Yan, K. Nair, W. Sun, Three dimensional multi-scale modelling and analysis of cell damage in cell-encapsulated alginate constructs., *Journal of biomechanics* **43**, 1031–8 (2010).

130. R. Chang, J. Nam, W. Sun, Effects of dispensing pressure and nozzle diameter on cell survival from solid freeform fabrication-based direct cell writing., *Tissue engineering. Part A* **14**, 41–8 (2008).

131. K. Nair et al., Characterization of cell viability during bioprinting processes., *Biotechnology journal* **4**, 1168–77 (2009).

132. G. Forgacs, R. A. Foty, Y. Shafrir, M. S. Steinberg, Viscoelastic properties of living embryonic tissues: a quantitative study., *Biophysical journal* **74**, 2227–34 (1998).

133. V. Mironov, G. Prestwich, G. Forgacs, Bioprinting living structures, *Journal of materials chemistry* **17**, 2054 (2007).

134. V. Mironov et al., Organ printing: tissue spheroids as building blocks., *Biomaterials* **30**, 2164–74 (2009).

135. K. Jakab et al., Tissue engineering by self-assembly and bio-printing of living cells., *Biofabrication* **2**, 022001 (2010).

136. F. Marga et al., Toward engineering functional organ modules by additive manufacturing., *Biofabrication* **4**, 022001 (2012).

137. T. Boland, V. Mironov, A. Gutowska, E. A. Roth, R. R. Markwald, Cell and organ printing 2: fusion of cell aggregates in three-dimensional gels., *The anatomical record. Part A, Discoveries in molecular, cellular, and evolutionary biology* **272**, 497–502 (2003).

138. K. Jakab, A. Neagu, V. Mironov, R. R. Markwald, G. Forgacs, Engineering biological structures of prescribed shape using self-assembling multicellular systems., *Proceedings of the National Academy of Sciences of the United States of America* **101**, 2864–9 (2004).

139. K. Jakab, A. Neagu, V. Mironov, G. Forgacs, Organ printing : Fiction or science, *Biorheology* **41**, 371–375 (2004).

140. K. Jakab et al., Tissue engineering by self-assembly of cells printed into topologically defined structures., *Tissue engineering. Part A* **14**, 413–21 (2008).

141. C. Norotte, F. S. Marga, L. E. Niklason, G. Forgacs, Scaffold-free vascular tissue engineering using bioprinting., *Biomaterials* **30**, 5910–7 (2009).

142. D. J. Odde, M. J. Renn, Laser-guided direct writing for applications in biotechnology., *Trends in biotechnology* **17**, 385–9 (1999).

143. D. J. Odde, M. J. Renn, Laser-guided direct writing of living cells., *Biotechnology and bioengineering* **67**, 312–8 (2000).

144. Y. Nahmias, R. E. Schwartz, C. M. Verfaillie, D. J. Odde, Laser-guided direct writing for three-dimensional tissue engineering., *Biotechnology and bioengineering* **92**, 129–36 (2005).

145. Z. Ma et al., Laser-guidance-based cell deposition microscope for heterotypic single-cell micropatterning., *Biofabrication* **3**, 034107 (2011).

146. J. Bohandy, B. F. Kim, F. J. Adrian, Metal deposition from a supported metal film using an excimer laser, *Journal of applied physics* **60**, 1538 (1986).

147. N. R. Schiele et al., Laser-based direct-write techniques for cell printing., *Biofabrication* **2**, 032001 (2010).

148. F. Guillemot et al., Laser-assisted bioprinting to deal with tissue complexity in regenerative medicine, *MRS Bulletin* **36**, 1015–1019 (2011).

149. D. Young, R. C. . Auyeung, A. Piqué, D. . Chrisey, D. D. Dlott, Plume and jetting regimes in a laser based forward transfer process as observed by time-resolved optical microscopy, *Applied surface science* **197-198**, 181–187 (2002).

150. P. K. Wu et al., The deposition, structure, pattern deposition, and activity of biomaterial thin-films by matrix-assisted pulsed-laser evaporation (MAPLE) and MAPLE direct write, *Thin solid films* **398-399**, 607–614 (2001).

151. B. R. Ringeisen et al., Generation of mesoscopic patterns of viable Escherichia coli by ambient laser transfer., *Biomaterials* **23**, 161–6 (2002).

152. J. A. Barron, B. R. Ringeisen, H. Kim, B. J. Spargo, D. B. Chrisey, Application of laser printing to mammalian cells, *Thin solid films* **453-454**, 383–387 (2004).

153. B. R. Ringeisen et al., Laser printing of pluripotent embryonal carcinoma cells., *Tissue engineering* **10**, 483–91 (2004).

154. J. A. Barron, P. Wu, H. D. Ladouceur, B. R. Ringeisen, Biological laser printing: a novel technique for creating heterogeneous 3-dimensional cell patterns., *Biomedical microdevices* **6**, 139–47 (2004).

155. J. A. Barron, D. B. Krizman, B. R. Ringeisen, Laser Printing of Single Cells: Statistical Analysis, Cell Viability, and Stress, *Annals of biomedical engineering* **33**, 121–130 (2005).

156. C. M. Othon, X. Wu, J. J. Anders, B. R. Ringeisen, Single-cell printing to form three-dimensional lines of olfactory ensheathing cells., *Biomedical materials* **3**, 034101 (2008).

157. F. Guillemot et al., High-throughput laser printing of cells and biomaterials for tissue engineering., *Acta biomaterialia* **6**, 2494–500 (2010).

158. S. Catros et al., Laser-assisted bioprinting for creating on-demand patterns of human osteoprogenitor cells and nano-hydroxyapatite., *Biofabrication* **3**, 025001 (2011).

159. A. Doraiswamy et al., Laser microfabrication of hydroxyapatite-osteoblast-like cell composites., *Journal of biomedical materials research. Part A* **80**, 635–43 (2007).

160. M. Gruene et al., Laser printing of three-dimensional multicellular arrays for studies of cell-cell and cell-environment interactions., *Tissue engineering. Part C, Methods* **17**, 973–82 (2011).

161. M. Gruene et al., Laser Printing of Stem Cells for Biofabrication of Scaffold-Free Autologous Grafts., *Tissue engineering. Part C, Methods* **17**, 79–87 (2011).

162. L. Koch et al., Skin tissue generation by laser cell printing., *Biotechnology and bioengineering* **109**, 1855–1863 (2012).

163. A. Ovsianikov et al., Laser printing of cells into 3D scaffolds., *Biofabrication* **2**, 014104 (2010).

164. R. Gaebel et al., Patterning human stem cells and endothelial cells with laser printing for cardiac regeneration., *Biomaterials* **32**, 9218–30 (2011).

165. S. Catros et al., Layer-by-Layer Tissue Microfabrication Supports Cell Proliferation in Vitro and in Vivo., *Tissue engineering. Part C, Methods* **18**, 62–70 (2012).

166. R. K. Pirlo, P. Wu, J. Liu, B. Ringeisen, PLGA/hydrogel biopapers as a stackable substrate for printing HUVEC networks via BioLP., *Biotechnology and bioengineering* **109**, 262–73 (2012).

167. N. R. Schiele, D. B. Chrisey, D. T. Corr, Gelatin-based laser direct-write technique for the precise spatial patterning of cells., *Tissue engineering. Part C, Methods* **17**, 289–98 (2011).

168. N. A. Raof, N. R. Schiele, Y. Xie, D. B. Chrisey, D. T. Corr, The maintenance of pluripotency following laser direct-write of mouse embryonic stem cells., *Biomaterials* **32**, 1802–8 (2011).

169. S. J. Moon et al., Layer by layer three-dimensional tissue epitaxy by cell-laden hydrogel droplets., *Tissue engineering. Part C, Methods* **16**, 157–66 (2010).

170. U. Demirci, G. Montesano, Cell encapsulating droplet vitrification., *Lab on a chip* **7**, 1428–33 (2007).

171. W. Lee et al., Multi-layered culture of human skin fibroblasts and keratinocytes through three-dimensional freeform fabrication., *Biomaterials* **30**, 1587–95 (2009).

172. W. Lee et al., Three-dimensional bioprinting of rat embryonic neural cells., *Neuroreport* **20**, 798–803 (2009).

173. W. Lee et al., On-Demand Three-Dimensional Freeform Fabrication of Multi-Layered Hydrogel Scaffold With Fluidic Channels, *Biotechnology* **105**, 1178–1186 (2010).

174. F. Xu et al., A droplet-based building block approach for bladder smooth muscle cell (SMC) proliferation., *Biofabrication* **2**, 014105 (2010).

175. F. Xu et al., A three-dimensional in vitro ovarian cancer coculture model using a high-throughput cell patterning platform., *Biotechnology journal* **6**, 204–12 (2011).

176. S. Moon et al., Drop-on-demand single cell isolation and total RNA analysis., *PloS one* **6**, e17455 (2011).

177. C. J. Flaim, S. Chien, S. N. Bhatia, An extracellular matrix microarray for probing cellular differentiation., *Nature methods* **2**, 119–25 (2005).

178. D. G. Anderson, S. Levenberg, R. Langer, Nanoliter-scale synthesis of arrayed biomaterials and application to human embryonic stem cells., *Nature biotechnology* **22**, 863–6 (2004).

179. D. G. Anderson, D. Putnam, E. B. Lavik, T. A. Mahmood, R. Langer, Biomaterial microarrays: rapid, microscale screening of polymer-cell interaction., *Biomaterials* **26**, 4892–7 (2005).

180. T. Hart, A. Zhao, A. Garg, S. Bolusani, E. M. Marcotte, Human cell chips: adapting DNA microarray spotting technology to cell-based imaging assays., *PloS one* **4**, e7088 (2009).

181. M. Lee et al., Three-dimensional cellular microarray for high-throughput toxicology assays., *Proceedings of the National Academy of Sciences of the United States of America* **105**, 59–63 (2008).

182. T. G. Fernandes et al., On-chip, cell-based microarray immunofluorescence assay for high-throughput analysis of target proteins., *Analytical chemistry* **80**, 6633–9 (2008).

183. T. G. Fernandes et al., Three-dimensional cell culture microarray for high-throughput studies of stem cell fate., *Biotechnology and bioengineering* **106**, 106–18 (2010).

184. H. Sirringhaus, High-Resolution Inkjet Printing of All-Polymer Transistor Circuits, *Science* **290**, 2123–2126 (2000).

185. B. Derby, Inkjet Printing of Functional and Structural Materials: Fluid Property Requirements, Feature Stability, and Resolution, *Annual review of materials research* **40**, 395–414 (2010).

186. F. G. Zaugg, P. Wagner, Drop-on-Demand Printing of Protein Biochip Arrays, *MRS Bulletin* **28**, 837–842 (2003).

187. A. V Lemmo, D. J. Rose, T. C. Tisone, Inkjet dispensing technology: applications in drug discovery., *Current opinion in biotechnology* **9**, 615–7 (1998).

188. J. Sumerel et al., Piezoelectric ink jet processing of materials for medical and biological applications., *Biotechnology journal* **1**, 976–87 (2006).

189. T. Boland, T. Xu, B. Damon, X. Cui, Application of inkjet printing to tissue engineering., *Biotechnology journal* **1**, 910–7 (2006).

190. T. C. Burg, C. A. P. Cass, R. Groff, M. E. Pepper, K. J. L. Burg, Building off-the-shelf tissue-engineered composites., *Philosophical transactions. Series A, Mathematical, physical, and engineering sciences* **368**, 1839–62 (2010).

191. B. Derby, Bioprinting: inkjet printing proteins and hybrid cell-containing materials and structures, *Journal of materials chemistry* **18**, 5717 (2008).

192. B. Derby, Applications for Ink Jet Printing in Biology and Medicine, *NIP25 and digital fabrication* , 2–3 (2009).

193. W. C. Wilson, T. Boland, Cell and organ printing 1: protein and cell printers., *The anatomical record. Part A, Discoveries in molecular, cellular, and evolutionary biology* **272**, 491–6 (2003).

194. T. Xu et al., Construction of high-density bacterial colony arrays and patterns by

the ink-jet method., *Biotechnology and bioengineering* **85**, 29–33 (2004).

195. L. Pardo, W. C. Wilson, T. Boland, Characterization of Patterned Self-Assembled Monolayers and Protein Arrays Generated by the Ink-Jet Method, *Langmuir* **19**, 1462–1466 (2003).

196. E. A. Roth et al., Inkjet printing for high-throughput cell patterning., *Biomaterials* **25**, 3707–15 (2004).

197. T. Xu, J. Jin, C. Gregory, J. J. Hickman, T. Boland, Inkjet printing of viable mammalian cells., *Biomaterials* **26**, 93–9 (2005).

198. T. Xu et al., Viability and electrophysiology of neural cell structures generated by the inkjet printing method., *Biomaterials* **27**, 3580–8 (2006).

199. X. Cui, D. Dean, Z. M. Ruggeri, T. Boland, Cell damage evaluation of thermal inkjet printed Chinese hamster ovary cells., *Biotechnology and bioengineering* **106**, 963–9 (2010).

200. T. Xu et al., Inkjet-mediated gene transfection into living cells combined with targeted delivery., *Tissue engineering. Part A* **15**, 95–101 (2009).

201. X. Cui, T. Boland, Human microvasculature fabrication using thermal inkjet printing technology., *Biomaterials* **30**, 6221–7 (2009).

202. T. Boland et al., Drop-on-demand printing of cells and materials for designer tissue constructs, *Materials science and engineering: C* **27**, 372–376 (2007).

203. T. Xu, C. Baicu, M. Aho, M. Zile, T. Boland, Fabrication and characterization of bio-engineered cardiac pseudo tissues, *Biofabrication* **1**, 035001 (2009).

204. T. Xu, W. Zhao, A. Atala, J. J. Yoo, Bio-printing of living organized tissues using an inkjet technology, *Digital fabrication 2006* , 131–134 (2006).

205. T. Xu et al., Characterization of Cell Constructs Generated With Inkjet Printing Technology Using In Vivo Magnetic Resonance Imaging, *Journal of manufacturing science and engineering* **130**, 021013 (2008).

206. T. Xu et al., Complex heterogeneous tissue constructs containing multiple cell types prepared by inkjet printing technology., *Biomaterials* **34**, 130–9 (2013).

207. T. Xu, H. Kincaid, A. Atala, J. J. Yoo, High-Throughput Production of Single-Cell Microparticles Using an Inkjet Printing Technology, *Journal of manufacturing science and engineering* **130**, 021017 (2008).

208. M. Nakamura et al., Biocompatible inkjet printing technique for designed seeding of individual living cells., *Tissue engineering* **11**, 1658–66 (2005).

209. M. Nakamura, Y. Nishiyama, C. Henmi, K. Yamaguchi, Inkjet bioprinting as an effective tool for tissue fabrication, *Science And technology* , 89–92 (2006).

210. Y. Nishiyama et al., Development of a three-dimensional bioprinter: construction of cell supporting structures using hydrogel and state-of-the-art inkjet technology., *Journal of biomechanical engineering* **131**, 035001 (2009).

211. K. Arai et al., Three-dimensional inkjet biofabrication based on designed images, *Biofabrication* **3**, 034113 (2011).

212. R. E. Saunders, J. E. Gough, B. Derby, Delivery of human fibroblast cells by piezoelectric drop-on-demand inkjet printing., *Biomaterials* **29**, 193–203 (2008).

213. M. Di Biase, R. E. Saunders, N. Tirelli, B. Derby, Inkjet printing and cell seeding thermoreversible photocurable gel structures, *Soft matter* **7**, 2639 (2011).

214. S. Parsa, M. Gupta, F. Loizeau, K. C. Cheung, Effects of surfactant and gentle agitation on inkjet dispensing of living cells, *Biofabrication* **2**, 025003 (2010).

215. A. R. Liberski, J. T. Delaney, U. S. Schubert, “One cell-one well”: a new approach to inkjet printing single cell microarrays., *ACS combinatorial science* **13**, 190–5 (2011).

216. C. A. Parzel, M. E. Pepper, T. C. Burg, R. E. Groff, K. J. L. Burg, EDTA enhances high-throughput two-dimensional bioprinting by inhibiting salt scaling and cell aggregation at the nozzle surface., *Journal of tissue engineering and regenerative medicine* **3**, 260–8 (2009).

217. M. E. Pepper et al., in *Annual International Conference of the IEEE Engineering in Medicine and Biology Society*, (2011), pp. 3609–12.

218. M. E. Pepper, V. Seshadri, T. C. Burg, K. J. L. Burg, R. E. Groff, Characterizing the effects of cell settling on bioprinter output., *Biofabrication* **4**, 011001 (2012).

219. M. E. Pepper et al., in *Conference of the IEEE Engineering in Medicine and Biology Society*, (2010), vol. 2010, pp. 259–62.

220. M. E. Pepper et al., A quantitative metric for pattern fidelity of bioprinted cocultures., *Artificial organs* **36**, E151–62 (2012).

221. M. S. Brown, N. T. Kattamis, C. B. Arnold, Time-resolved study of polyimide absorption layers for blister-actuated laser-induced forward transfer, *Journal of applied physics* **107**, 083103 (2010).

222. D. Chahal, A. Ahmadi, K. C. Cheung, Improving piezoelectric cell printing accuracy and reliability through neutral buoyancy of suspensions., *Biotechnology and bioengineering* **109**, 2932–40 (2012).

223. T. J. Pollock, Gellan-related polysaccharides and the genus Sphingomonas, *Journal of general microbiology* **139**, 1939–1945 (1993).

224. P. Jansson, B. Lindberg, Structural studies of gellan gum, an extracellular polysaccharide elaborated by Pseudomonas elodea, *Carbohydrate research* **124**, 135–139 (1983).

225. A. J. Jay et al., Analysis of structure and function of gellans with different substitution patterns, *Carbohydrate polymers* **35**, 179–188 (1998).

226. E. R. Morris, K. Nishinari, M. Rinaudo, Gelation of gellan – A review, *Food hydrocolloids* **28**, 373–411 (2012).

227. I. Giavasis, L. M. Harvey, B. McNeil, Gellan gum., *Critical reviews in biotechnology* **20**, 177–211 (2000).

228. A. M. Fialho et al., Occurrence, production, and applications of gellan: current state and perspectives, *Applied microbiology and biotechnology* **79**, 889–900 (2008).

229. R. Chandrasekaran, A. Radha, Molecular architectures and functional properties of gellan gum and related polysaccharides, *Trends in food science & technology* **6**, 143–148 (1995).

230. E. Miyoshi, Rheological and thermal studies of gel-sol transition in gellan gum aqueous solutions, *Carbohydrate polymers* **30**, 109–119 (1996).

231. M. Milas, X. Shi, M. Rinaudo, On the physicochemical properties of gellan gum., *Biopolymers* **30**, 451–64 (1990).

232. E. Ogawa, Conformational Transition of Polysaccharide Sodium-Gellan Gum in Aqueous Solutions, *Macromolecules* **29**, 5178–5182 (1996).

233. E. Ogawa, H. Matsuzawa, M. Iwahashi, Conformational transition of gellan gum of sodium, lithium, and potassium types in aqueous solutions, *Food*

hydrocolloids **16**, 1–9 (2002).

234. M. Bosco, S. Miertus, M. Dentini, A. L. Segre, The structure of gellan in dilute aqueous solution., *Biopolymers* **54**, 115–26 (2000).

235. M. Milas, The gellan sol-gel transition, *Carbohydrate Polymers* **30**, 177–184 (1996).

236. E. Ogawa, R. Takahashi, H. Yajima, K. Nishinari, Thermally induced coil-to-helix transition of sodium gellan gum with different molar masses in aqueous salt solutions., *Biopolymers* **79**, 207–17 (2005).

237. E. Ogawa, R. Takahashi, H. Yajima, K. Nishinari, Effects of molar mass on the coil to helix transition of sodium-type gellan gums in aqueous solutions, *Food hydrocolloids* **20**, 378–385 (2006).

238. J. Horinaka, K. Kani, Y. Itokawa, E. Ogawa, Y. Shindo, Gelation of gellan gum aqueous solutions studied by polarization modulation spectroscopy., *Biopolymers* **75**, 376–83 (2004).

239. K. Kani, J. Horinaka, S. Maeda, Effects of monovalent cation and anion species on the conformation of gellan chains in aqueous systems, *Carbohydrate polymers* **61**, 168–173 (2005).

240. J. Horinaka, K. Kani, Y. Hori, S. Maeda, Effect of pH on the conformation of gellan chains in aqueous systems., *Biophysical chemistry* **111**, 223–7 (2004).

241. V. Crescenzi, M. Dentini, T. Coviello, R. Rizzo, Comparative analysis of the behavior of gellan gum (S-60) and welan gum (S-130) in dilute aqueous solution, *Carbohydrate research* **149**, 425–432 (1986).

242. H. Grasdalen, O. Smidsrod, Gelation of gellan gum, *Carbohydrate polymers* **7**, 371–393 (1987).

243. E. Morris, Conformational and rheological transitions of welan, rhamsan and acylated gellan, *Carbohydrate polymers* **30**, 165–175 (1996).

244. S. A. Agnihotri, S. S. Jawalkar, T. M. Aminabhavi, Controlled release of cephalexin through gellan gum beads: effect of formulation parameters on entrapment efficiency, size, and drug release., *European journal of pharmaceutics and biopharmaceutics* **63**, 249–61 (2006).

245. B. Jansson, H. Hägerström, N. Fransén, K. Edsman, E. Björk, The influence of gellan gum on the transfer of fluorescein dextran across rat nasal epithelium in vivo., *European journal of pharmaceutics and biopharmaceutics* **59**, 557–64 (2005).

246. Y. Sultana, M. Aqil, A. Ali, Ion-activated, Gelrite-based in situ ophthalmic gels of pefloxacin mesylate: comparison with conventional eye drops., *Drug delivery* **13**, 215–9 (2006).

247. F. Kedzierewicz, C. Lombry, R. Rios, M. Hoffman, P. Maincent, Effect of the formulation on the in-vitro release of propranolol from gellan beads., *International journal of pharmaceutics* **178**, 129–36 (1999).

248. A. Gal, A. Nussinovitch, Hydrocolloid carriers with filler inclusion for diltiazem hydrochloride release., *Journal of pharmaceutical sciences* **96**, 168–78 (2007).

249. S. C. Kumar, C. S. Satish, H. G. Shivakumar, Formulation and Evaluation of Chitosan-Gellan Based Methotrexate Implants, *Journal of macromolecular science, Part A* **45**, 643–649 (2008).

250. J. Li, K. Kamath, C. Dwivedi, Gellan Film as an Implant for Insulin Delivery,

Journal of biomaterials applications **15**, 321–343 (2001).

251. K. Klimaszewska, Plantlet development from immature zygotic embryos of hybrid larch through somatic embryogenesis, *Plant science* **63**, 95–103 (1989).

252. P. L. Rule, A. D. Alexander, Gellan gum as a substitute for agar in leptospiral media., *Journal of clinical microbiology* **23**, 500–4 (1986).

253. G. Ciardelli et al., Blends of poly-(e-caprolactone) and polysaccharides in tissue engineering applications., *Biomacromolecules* **6**, 1961–76 (2005).

254. M. G. Cascone, N. Barbani, C. C. P.Giusti, G. Ciardelli, L. Lazzeri, Bioartificial polymeric materials based on polysaccharides, *Journal of biomaterials science, Polymer edition* **12**, 267–281 (2001).

255. A. M. Smith, R. M. Shelton, Y. Perrie, J. J. Harris, An initial evaluation of gellan gum as a material for tissue engineering applications., *Journal of biomaterials applications* **22**, 241–54 (2007).

256. J. T. Oliveira et al., Gellan gum: A new biomaterial for cartilage tissue engineering applications, *Journal of biomedical materials research Part A* **93A**, 852–863 (2010).

257. J. T. Oliveira et al., Performance of new gellan gum hydrogels combined with human articular chondrocytes for cartilage regeneration when subcutaneously implanted in nude mice., *Journal of tissue engineering and regenerative medicine* **3**, 493–500 (2009).

258. J. T. Oliveira et al., Gellan gum injectable hydrogels for cartilage tissue engineering applications: in vitro studies and preliminary in vivo evaluation., *Tissue engineering. Part A* **16**, 343–53 (2010).

259. N. A. Silva et al., Development and characterization of a novel hybrid tissue engineering-based scaffold for spinal cord injury repair., *Tissue engineering. Part A* **16**, 45–54 (2010).

260. D. F. Coutinho et al., Modified Gellan Gum hydrogels with tunable physical and mechanical properties., *Biomaterials* **31**, 7494–502 (2010).

261. J. Silva-Correia et al., Gellan gum-based hydrogels for intervertebral disc tissue-engineering applications., *Journal of tissue engineering and regenerative medicine* **5**, e97–107 (2011).

262. J. Silva-Correia et al., Angiogenic potential of gellan-gum-based hydrogels for application in nucleus pulposus regeneration: in vivo study., *Tissue engineering. Part A* **18**, 1203–12 (2012).

263. D. R. Pereira et al., Development of gellan gum-based microparticles/hydrogel matrices for application in the intervertebral disc regeneration., *Tissue engineering. Part C, Methods* **17**, 961–72 (2011).

264. H. Du, P. Hamilton, M. Reilly, N. Ravi, Injectable in situ Physically and Chemically Crosslinkable Gellan Hydrogel., *Macromolecular bioscience* **12**, 952–61 (2012).

265. Y. Gong et al., An improved injectable polysaccharide hydrogel: modified gellan gum for long-term cartilage regeneration in vitro, *Journal of materials chemistry* **19**, 1968 (2009).

266. J. Fan et al., In vitro engineered cartilage using synovium-derived mesenchymal stem cells with injectable gellan hydrogels., *Acta biomaterialia* **6**, 1178–85 (2010).

267. H. Lee, S. Fisher, M. S. Kallos, C. J. Hunter, Optimizing gelling parameters of

gellan gum for fibrocartilage tissue engineering., *Journal of biomedical materials research. Part B, Applied biomaterials* **98B**, 238–45 (2011).

268. C. Wang, Y. Gong, Y. Lin, J. Shen, D.-A. Wang, A novel gellan gel-based microcarrier for anchorage-dependent cell delivery., *Acta biomaterialia* **4**, 1226–34 (2008).

269. H. Shin, B. D. Olsen, A. Khademhosseini, The mechanical properties and cytotoxicity of cell-laden double-network hydrogels based on photocrosslinkable gelatin and gellan gum biomacromolecules., *Biomaterials* **33**, 3143–52 (2012).

270. N. A. Silva et al., The effects of peptide modified gellan gum and olfactory ensheathing glia cells on neural stem/progenitor cell fate., *Biomaterials* **33**, 6345–54 (2012).

271. C. J. Ferris, M. in het Panhuis, Gel–carbon nanotube composites: the effect of carbon nanotubes on gelation and conductivity behaviour, *Soft matter* **5**, 1466 (2009).

272. N. Songmee, P. Singjai, M. in het Panhuis, Gel-carbon nanotube materials: the relationship between nanotube network connectivity and conductivity., *Nanoscale* **2**, 1740–5 (2010).

273. J. Boge, L. J. Sweetman, M. in het Panhuis, S. F. Ralph, The effect of preparation conditions and biopolymer dispersants on the properties of SWNT buckypapers, *Journal of materials chemistry* **19**, 9131 (2009).

274. M. in het Panhuis, A. Heurtematte, W. R. Small, V. N. Paunov, Inkjet printed water sensitive transparent films from natural gum-carbon nanotube composites, *Soft Matter* **3**, 840 (2007).

275. G. C. Pidcock, M. in het Panhuis, Extrusion Printing of Flexible Electrically Conducting Carbon Nanotube Networks, *Advanced Functional Materials* (2012), doi:10.1002/adfm.201200724.

276. A. J. Granero, J. M. Razal, G. G. Wallace, M. in het Panhuis, Mechanical reinforcement of continuous flow spun polyelectrolyte complex fibers., *Macromolecular bioscience* **9**, 354–60 (2009).

277. K. A. Mat Amin, M. in het Panhuis, Polyelectrolyte complex materials from chitosan and gellan gum, *Carbohydrate polymers* **86**, 352–358 (2011).

278. K. A. Mat Amin et al., Polyelectrolyte complex materials consisting of antibacterial and cell-supporting layers., *Macromolecular bioscience* **12**, 374–82 (2012).

279. T. M. Higgins, S. E. Moulton, K. J. Gilmore, G. G. Wallace, M. in het Panhuis, Gellan gum doped polypyrrole neural prosthetic electrode coatings, *Soft matter* **7**, 4690 (2011).

280. C. J. Ferris, M. in Het Panhuis, Conducting bio-materials based on gellan gum hydrogels, *Soft matter* **5**, 3430–3437 (2009).

281. C. J. Ferris, M. in het Panhuis, Conducting bio-materials based on gellan gum hydrogels, *Soft matter* **5**, 3430–3437 (2009).

282. K. Y. Lee, D. J. Mooney, Alginate: properties and biomedical applications., *Progress in polymer science* **37**, 106–126 (2012).

283. P. Sikorski, F. Mo, G. Skjåk-Braek, B. T. Stokke, Evidence for egg-box-compatible interactions in calcium-alginate gels from fiber X-ray diffraction., *Biomacromolecules* **8**, 2098–103 (2007).

284. M. T. Nickerson, A. T. Paulson, Rheological properties of gellan, κ-carrageenan and alginate polysaccharides: effect of potassium and calcium ions on macrostructure assemblages, *Carbohydrate polymers* **58**, 15–24 (2004).

285. I. D. Rupenthal, C. R. Green, R. G. Alany, Comparison of ion-activated in situ gelling systems for ocular drug delivery. Part 1: physicochemical characterisation and in vitro release., *International journal of pharmaceutics* **411**, 69–77 (2011).

286. D. A. De Silva, L. A. Poole-Warren, P. J. Martens, M. in het Panhuis, Mechanical characteristics of swollen gellan gum hydrogels, *Journal of applied polymer science*, accepted (2013).

287. P. M. Rath, D. Schmidt, Gellan gum as a suitable gelling agent in microbiological media for PCR applications., *Journal of medical microbiology* **50**, 108–9 (2001).

288. R. M. Wadowsky, S. Laus, T. Libert, S. J. States, G. D. Ehrlich, Inhibition of PCR-based assay for Bordetella pertussis by using calcium alginate fiber and aluminum shaft components of a nasopharyngeal swab., *Journal of clinical microbiology* **32**, 1054–7 (1994).

289. M. C. García, M. C. Alfaro, N. Calero, J. Muñoz, Influence of gellan gum concentration on the dynamic viscoelasticity and transient flow of fluid gels, *Biochemical engineering journal* **55**, 73–81 (2011).

290. C. L. A. Berli, D. Quemada, Rheological Modeling of Microgel Suspensions Involving Solid−Liquid Transition, *Langmuir* **16**, 7968–7974 (2000).

291. J. B. Thorne, G. J. Vine, M. J. Snowden, Microgel applications and commercial considerations, *Colloid and polymer science* **289**, 625–646 (2011).

292. L. H. Gracia, M. J. Snowden, in *Handbook of Industrial Water Soluble Polymers*, (2007), pp. 282–311.

293. W. Carvalho, M. Djabourov, Physical gelation under shear for gelatin gels, *Rheologica acta* **36**, 591–609 (1997).

294. I. T. Norton, D. A. Jarvis, T. J. Foster, A molecular model for the formation and properties of fluid gels., *International journal of biological macromolecules* **26**, 255–61 (1999).

295. N. Altmann, J. J. Cooper-White, D. E. Dunstan, J. R. Stokes, Strong through to weak "sheared" gels, *Journal of non-Newtonian fluid mechanics* **124**, 129–136 (2004).

296. G. Sworn, G. R. Sanderson, W. Gibson, Gellan gum fluid gels, *Food hydrocolloids* **9**, 265–271 (1995).

297. A. I. Rodríguez-Hernández, S. Durand, C. Garnier, A. Tecante, J. L. Doublier, Rheology-structure properties of gellan systems: evidence of network formation at low gellan concentrations, *Food hydrocolloids* **17**, 621–628 (2003).

298. M. Caggioni, P. T. Spicer, D. L. Blair, S. E. Lindberg, D. A. Weitz, Rheology and microrheology of a microstructured fluid: The gellan gum case, *Journal of rheology* **51**, 851–865 (2007).

299. W. J. Frith, X. Garijo, T. J. Foster, in *Gums and Stabilisers for the Food Industry 11*, P. A. Williams, G. O. Phillips, Eds. (Royal Society of Chemistry, Cambridge, 2002), vol. 11, pp. 95–103.

300. H. Kiani, M. E. Mousavi, Z. E. Mousavi, Particle stability in dilute fermented dairy drinks: formation of fluid gel and impact on rheological properties., *Food*

science and technology international **16**, 543–51 (2010).

301. H. M. Blau et al., Plasticity of the differentiated state., *Science* **230**, 758–66 (1985).

302. D. Yaffe, O. Saxel, Serial passaging and differentiation of myogenic cells isolated from dystrophic mouse muscle, *Nature* **270**, 725–727 (1977).

303. L. A. Greene, A. S. Tischler, Establishment of a noradrenergic clonal line of rat adrenal pheochromocytoma cells which respond to nerve growth factor., *Proceedings of the National Academy of Sciences of the United States of America* **73**, 2424–8 (1976).

304. K. K. Sanford, W. R. Earle, G. D. Likely, The growth in vitro of single isolated tissue cells, *Journal of the National Cancer Institute* **9**, 229–246 (1948).

305. F. K. Hansen, G. Rødsrud, Surface tension by pendant drop, *Journal of colloid and interface science* **141**, 1–9 (1991).

306. A. J. M. Yang, Molecular theory of surface tension, *The journal of chemical physics* **64**, 3732 (1976).

307. L. P. Martínez-Padilla, F. López-Araiza, A. Tecante, Steady and oscillatory shear behavior of fluid gels formed by binary mixtures of xanthan and gellan, *Food hydrocolloids* **18**, 471–481 (2004).

308. S. R. Ellis et al., Direct lipid profiling of single cells from inkjet printed microarrays., *Analytical chemistry* **84**, 9679–83 (2012).

309. T. N. Schumacher, T. J. Tsomides, In vitro radiolabeling of peptides and proteins., *Current protocols in protein science* **Chapter 3**, Unit 3.3 (2001).

310. L. W. Doner, D. D. Douds, Purification of commercial gellan to monovalent cation salts results in acute modification of solution and gel-forming properties., *Carbohydrate research* **273**, 225–33 (1995).

311. L. W. Doner, Rapid purification of commercial gellan gum to highly soluble and gellable monovalent cation salts, *Carbohydrate polymers* **32**, 245–247 (1997).

312. U. Hersel, C. Dahmen, H. Kessler, RGD modified polymers: biomaterials for stimulated cell adhesion and beyond, *Biomaterials* **24**, 4385–4415 (2003).

313. J. A. Rowley, G. Madlambayan, D. J. Mooney, Alginate hydrogels as synthetic extracellular matrix materials., *Biomaterials* **20**, 45–53 (1999).

314. S. J. Bidarra et al., Injectable in situ crosslinkable RGD-modified alginate matrix for endothelial cells delivery., *Biomaterials* **32**, 7897–904 (2011).

315. N. O. Dhoot, C. A. Tobias, I. Fischer, M. A. Wheatley, Peptide-modified alginate surfaces as a growth permissive substrate for neurite outgrowth, *Journal of biomedical materials research Part A* **71A**, 191–200 (2004).

316. S.-W. Kang et al., The Effect of Conjugating RGD into 3D Alginate Hydrogels on Adipogenic Differentiation of Human Adipose-Derived Stromal Cells., *Macromolecular bioscience* **11**, 673–9 (2011).

317. J. W. Lee, Y. J. Park, S. J. Lee, S. K. Lee, K. Y. Lee, The effect of spacer arm length of an adhesion ligand coupled to an alginate gel on the control of fibroblast phenotype., *Biomaterials* **31**, 5545–51 (2010).

318. A. Loebsack et al., In vivo characterization of a porous hydrogel material for use as a tissue bulking agent, *Journal of biomedical materials research* **57**, 575–581 (2001).

319. S. Wold, K. Esbensen, P. Geladi, Principal component analysis, *Chemometrics*

and intelligent laboratory systems **2**, 37–52 (1987).

320. A. S. Kabalnov, E. A. Fellner, D. W. Jenkins, K. G. Miller, Inkjet ink and method of making the same, US Patent, US 2011/0169887 (2011).

321. D. C. Vadillo, T. R. Tuladhar, a. C. Mulji, M. R. Mackley, The rheological characterization of linear viscoelasticity for ink jet fluids using piezo axial vibrator and torsion resonator rheometers, *Journal of Rheology* **54**, 781 (2010).

322. R. P. Chhabra, in *Rheology of Complex Fluids*, J. M. Krishnan, A. P. Deshpande, P. B. S. Kumar, Eds. (Springer, New York, 2010), pp. 3–34.

323. M. R. R. Niño, J. M. R. Patino, Surface tension of bovine serum albumin and tween 20 at the air-aqueous interface, *Journal of the American Oil Chemists' Society* **75**, 1241–1248 (1998).

324. E. T. Papoutsakis, Media additives for protecting freely suspended animal cells against agitation and aeration damage., *Trends in biotechnology* **9**, 316–24 (1991).

325. K. A. Barbee, Mechanical cell injury., *Annals of the New York Academy of Sciences* **1066**, 67–84 (2005).

326. S. A. Maskarinec, G. Wu, K. Y. C. Lee, Membrane sealing by polymers., *Annals of the New York Academy of Sciences* **1066**, 310–20 (2005).

327. T. Tharmalingam, H. Ghebeh, T. Wuerz, M. Butler, Pluronic enhances the robustness and reduces the cell attachment of mammalian cells., *Molecular biotechnology* **39**, 167–77 (2008).

328. J. M. Collins, F. Despa, R. C. Lee, Structural and functional recovery of electropermeabilized skeletal muscle in-vivo after treatment with surfactant poloxamer 188., *Biochimica et biophysica acta* **1768**, 1238–46 (2007).

329. B. Greenebaum et al., Poloxamer 188 prevents acute necrosis of adult skeletal muscle cells following high-dose irradiation., *Burns : journal of the International Society for Burn Injuries* **30**, 539–47 (2004).

330. G. Serbest, J. Horwitz, K. Barbee, The effect of poloxamer-188 on neuronal cell recovery from mechanical injury., *Journal of neurotrauma* **22**, 119–32 (2005).

331. N. Quinete et al., Degradation studies of new substitutes for perfluorinated surfactants., *Archives of environmental contamination and toxicology* **59**, 20–30 (2010).

332. R. G. A. Wills, M. J. Watt-Smith, F. C. Walsh, The Use of Fluorocarbon Surfactants to Improve the Manufacture of PEM Fuel Cell Electrodes, *Fuel cells* **9**, 148–156 (2009).

333. M. Krafft, Fluorocarbons and fluorinated amphiphiles in drug delivery and biomedical research, *Advanced drug delivery reviews* **47**, 209–228 (2001).

334. X. Li et al., Hydrophobic tail length, degree of fluorination and headgroup stereochemistry are determinants of the biocompatibility of (fluorinated) carbohydrate surfactants., *Colloids and surfaces. B, Biointerfaces* **73**, 65–74 (2009).

335. J. G. Riess, J. Greiner, Carbohydrate- and related polyol-derived fluorosurfactants: an update., *Carbohydrate research* **327**, 147–68 (2000).

336. C. C. Larsen, F. Kligman, C. Tang, K. Kottke-Marchant, R. E. Marchant, A biomimetic peptide fluorosurfactant polymer for endothelialization of ePTFE with limited platelet adhesion., *Biomaterials* **28**, 3537–48 (2007).

337. C. Tang, F. Kligman, C. C. Larsen, K. Kottke-Marchant, R. E. Marchant, Platelet and endothelial adhesion on fluorosurfactant polymers designed for vascular

graft modification., *Journal of biomedical materials research. Part A* **88**, 348–58 (2009).

338. E. Brouzes et al., Droplet microfluidic technology for single-cell high-throughput screening., *Proceedings of the National Academy of Sciences of the United States of America* **106**, 14195–200 (2009).

339. J. Clausell-Tormos et al., Droplet-based microfluidic platforms for the encapsulation and screening of Mammalian cells and multicellular organisms., *Chemistry & biology* **15**, 427–37 (2008).

340. S. A. Maskarinec, J. Hannig, R. C. Lee, K. Y. C. Lee, Direct observation of poloxamer 188 insertion into lipid monolayers., *Biophysical journal* **82**, 1453–9 (2002).

341. N. F. Morrison, O. G. Harlen, Viscoelasticity in inkjet printing, *Rheologica acta* **49**, 619–632 (2010).

342. S. D. Hoath et al., Links Between Ink Rheology, Drop-on-Demand Jet Formation, and Printability, *Journal of imaging science and technology* **53**, 041208 (2009).

343. K. K. Parker, D. E. Ingber, Extracellular matrix, mechanotransduction and structural hierarchies in heart tissue engineering., *Philosophical transactions of the Royal Society of London. Series B, Biological sciences* **362**, 1267–79 (2007).

344. U. Demirci, G. Montesano, Single cell epitaxy by acoustic picolitre droplets., *Lab on a chip* **7**, 1139–45 (2007).

345. S. Kapur, D. J. Baylink, K.-H. William Lau, Fluid flow shear stress stimulates human osteoblast proliferation and differentiation through multiple interacting and competing signal transduction pathways, *Bone* **32**, 241–251 (2003).

346. P. Malaviya, R. M. Nerem, Fluid-induced shear stress stimulates chondrocyte proliferation partially mediated via TGF-beta1., *Tissue engineering* **8**, 581–90 (2002).

347. S. Yano, M. Komine, M. Fujimoto, H. Okochi, K. Tamaki, Mechanical stretching in vitro regulates signal transduction pathways and cellular proliferation in human epidermal keratinocytes., *The Journal of investigative dermatology* **122**, 783–90 (2004).

348. S. Akimoto, M. Mitsumata, T. Sasaguri, Y. Yoshida, Laminar Shear Stress Inhibits Vascular Endothelial Cell Proliferation by Inducing Cyclin-Dependent Kinase Inhibitor p21Sdi1/Cip1/Waf1, *Circulation research* **86**, 185–190 (2000).

349. H. H. Vandenburgh, S. Hatfalufy, P. Karlisch, J. Shansky, Skeletal muscle growth is stimulated by intermittent stretch-relaxation in tissue culture, *American journal of physiology* **256**, C674–C682 (1989).

350. Y.-E. Kuo et al., Local stimulation of cultured myocyte cells by femtosecond laser-induced stress wave, *Applied physics A* **101**, 597–600 (2010).

351. P. S. Maher, R. P. Keatch, K. Donnelly, R. E. Mackay, J. Z. Paxton, Construction of 3D biological matrices using rapid prototyping technology, *Rapid prototyping journal* **3**, 204– 210 (2009).

352. N. Reis, C. Ainsley, B. Derby, Ink-jet delivery of particle suspensions by piezoelectric droplet ejectors, *Journal of applied physics* **97**, 094903 (2005).

353. X. Cui, K. Breitenkamp, M. G. Finn, M. Lotz, D. D. D'Lima, Direct Human Cartilage Repair Using Three-Dimensional Bioprinting Technology., *Tissue*

engineering. Part A **18**, 1304–12 (2012).

354. X. Lu, Recent developments in single-cell analysis, *Analytica chimica acta* **510**, 127–138 (2004).

355. Y. Lin, R. Trouillon, G. Safina, A. G. Ewing, Chemical analysis of single cells., *Analytical chemistry* **83**, 4369–92 (2011).

356. A. Svatoš, Single-cell metabolomics comes of age: new developments in mass spectrometry profiling and imaging., *Analytical chemistry* **83**, 5037–44 (2011).

357. T. Masujima, Live Single-cell Mass Spectrometry, *Analytical sciences* **25**, 953–960 (2009).

358. B. Shrestha, A. Vertes, In situ metabolic profiling of single cells by laser ablation electrospray ionization mass spectrometry., *Analytical chemistry* **81**, 8265–71 (2009).

359. I. Lanekoff et al., An in situ fracture device to image lipids in single cells using ToF-SIMS, *Surface and interface analysis* **43**, 257–260 (2011).

360. V. Kertesz, G. J. Van Berkel, Fully automated liquid extraction-based surface sampling and ionization using a chip-based robotic nanoelectrospray platform., *Journal of mass spectrometry : JMS* **45**, 252–60 (2010).

361. D. Eikel et al., Liquid extraction surface analysis mass spectrometry (LESA-MS) as a novel profiling tool for drug distribution and metabolism analysis: the terfenadine example., *Rapid communications in mass spectrometry : RCM* **25**, 3587–96 (2011).

362. S. J. Blanksby, T. W. Mitchell, Advances in mass spectrometry for lipidomics., *Annual review of analytical chemistry* **3**, 433–65 (2010).

363. M. R. Wenk, Lipidomics: new tools and applications., *Cell* **143**, 888–95 (2010).

364. A. Yusof et al., Inkjet-like printing of single-cells., *Lab on a chip* , 2447–2454 (2011).

365. L. Stoll, A. Spector, Changes in serum influence the fatty-acid composition of established cell-lines, *In vitro - Journal of the Tissue Culture Association* **20**, 732–738 (1984).

366. W. Bian, N. Bursac, Engineered skeletal muscle tissue networks with controllable architecture, *Biomaterials* **30**, 1401–1412 (2009).

367. H. Liao, G.-Q. Zhou, Development and progress of engineering of skeletal muscle tissue., *Tissue engineering. Part B, Reviews* **15**, 319–31 (2009).

368. A. Khademhosseini, R. Langer, J. Borenstein, J. P. Vacanti, Microscale technologies for tissue engineering and biology., *Proceedings of the National Academy of Sciences of the United States of America* **103**, 2480–7 (2006).

369. A. P. Gilmore, Anoikis., *Cell death and differentiation* **12 Suppl 2**, 1473–7 (2005).

370. F. Rask et al., Hydrogels modified with QHREDGS peptide support cardiomyocyte survival in vitro and after sub-cutaneous implantation, *Soft matter* , 5089–5099 (2010).

371. T. Boontheekul, E. E. Hill, H.-J. Kong, D. J. Mooney, Regulating myoblast phenotype through controlled gel stiffness and degradation., *Tissue engineering* **13**, 1431–42 (2007).

372. M. Grellier et al., The effect of the co-immobilization of human osteoprogenitors and endothelial cells within alginate microspheres on mineralization

in a bone defect., *Biomaterials* **30**, 3271–8 (2009).

373. D. E. Discher, P. Janmey, Y.-L. Wang, Tissue cells feel and respond to the stiffness of their substrate., *Science* **310**, 1139–43 (2005).

374. A. J. Engler, S. Sen, H. L. Sweeney, D. E. Discher, Matrix elasticity directs stem cell lineage specification., *Cell* **126**, 677–89 (2006).

375. V. Vogel, M. Sheetz, Local force and geometry sensing regulate cell functions., *Nature reviews. Molecular cell biology* **7**, 265–75 (2006).

376. J. L. Charest, A. J. García, W. P. King, Myoblast alignment and differentiation on cell culture substrates with microscale topography and model chemistries., *Biomaterials* **28**, 2202–10 (2007).

377. J. Y. Park, D. H. Lee, E. J. Lee, S.-H. Lee, Study of cellular behaviors on concave and convex microstructures fabricated from elastic PDMS membranes., *Lab on a chip* **9**, 2043–9 (2009).

378. P.-Y. Wang, H. Thissen, W.-B. Tsai, The roles of RGD and grooved topography in the adhesion, morphology, and differentiation of C2C12 skeletal myoblasts., *Biotechnology and bioengineering* **109**, 2104–15 (2012).

379. T. Neumann, S. D. Hauschka, J. E. Sanders, Tissue engineering of skeletal muscle using polymer fiber arrays., *Tissue engineering* **9**, 995–1003 (2003).

380. M. Rumpler, A. Woesz, J. W. C. Dunlop, J. T. van Dongen, P. Fratzl, The effect of geometry on three-dimensional tissue growth., *Journal of the Royal Society, Interface* **5**, 1173–80 (2008).

381. C. M. Bidan et al., How linear tension converts to curvature: geometric control of bone tissue growth., *PloS one* **7**, e36336 (2012).

382. C. M. Nelson et al., Emergent patterns of growth controlled by multicellular form and mechanics., *Proceedings of the National Academy of Sciences of the United States of America* **102**, 11594–9 (2005).

383. J. Sun, W. Xiao, Y. Tang, K. Li, H. Fan, Biomimetic interpenetrating polymer network hydrogels based on methacrylated alginate and collagen for 3D pre-osteoblast spreading and osteogenic differentiation, *Soft matter* **8**, 2398 (2012).

384. L. A. Reis et al., A peptide-modified chitosan-collagen hydrogel for cardiac cell culture and delivery., *Acta biomaterialia* **8**, 1022–36 (2012).

385. S. Suri, C. E. Schmidt, Cell-laden hydrogel constructs of hyaluronic acid, collagen, and laminin for neural tissue engineering., *Tissue engineering. Part A* **16**, 1703–16 (2010).

386. L. Almany, D. Seliktar, Biosynthetic hydrogel scaffolds made from fibrinogen and polyethylene glycol for 3D cell cultures., *Biomaterials* **26**, 2467–77 (2005).

387. K. Shapira-Schweitzer, D. Seliktar, Matrix stiffness affects spontaneous contraction of cardiomyocytes cultured within a PEGylated fibrinogen biomaterial., *Acta biomaterialia* **3**, 33–41 (2007).

388. V. Ottani, M. Raspanti, A. Ruggeri, Collagen structure and functional implications, *Micron* **32**, 251–260 (2001).

389. E. Ruoslahti, RGD and other recognition sequences for integrins, *Annual review of cell and developmental biology* **12**, 697–715 (1996).

390. E. Ruoslahti, M. D. Pierschbacher, New Perspectives in Cell Adhesion : RGD and Integrins, *Science* **238**, 491–497 (1987).

391. D. F. Williams, The role of short synthetic adhesion peptides in regenerative

medicine; the debate., *Biomaterials* **32**, 4195–7 (2011).

392. D. L. Taylor et al., Characterization of Gellan Gum by Capillary Electrophoresis, *Australian journal of chemistry* **65**, 1156 (2012).

393. H. J. Kong, T. Boontheekul, D. J. Mooney, Quantifying the relation between adhesion ligand-receptor bond formation and cell phenotype., *Proceedings of the National Academy of Sciences of the United States of America* **103**, 18534–9 (2006).

394. S. P. Massia, J. A. Hubbell, An RGD Spacing of 440 nm Is Sufficient for Integrin a,ß 3 -mediated Fibroblast Spreading and 140 nm for Focal Contact and Stress Fiber Formation, *The journal of cell biology* **114**, 1089–1100 (1991).

395. J. A. Rowley, D. J. Mooney, Alginate type and RGD density control myoblast phenotype, *Journal of biomedical materials research* **60**, 217–223 (2001).

396. R. Timkovich, Detection of the Stable Addition of Carbodiimide to Proteins, *Analytical biochemistry* **143**, 135–143 (1977).

397. A. Williams, I. T. Ibrahim, A new mechanism involving cyclic tautomers for the reaction with nucleophiles of the water-soluble peptide coupling reagent 1-ethyl-3-(3’-(dimethylamino)propyl)carbodiimide (EDC), *Journal of the American Chemical Society* **103**, 7090–7095 (1981).

398. M. D. Pierschbacher, E. Ruoslahti, Influence of stereochemistry of the sequence Arg-Gly-Asp-Xaa on binding specificity in cell adhesion., *The journal of biological chemistry* **262**, 17294–8 (1987).

399. A. J. Engler et al., Myotubes differentiate optimally on substrates with tissue-like stiffness: pathological implications for soft or stiff microenvironments., *The journal of cell biology* **166**, 877–87 (2004).

400. U. Cheema, S.-Y. Yang, V. Mudera, G. G. Goldspink, R. A. Brown, 3-D in vitro model of early skeletal muscle development., *Cell motility and the cytoskeleton* **54**, 226–36 (2003).

401. Y. Nagai, H. Yokoi, K. Kaihara, K. Naruse, The mechanical stimulation of cells in 3D culture within a self-assembling peptide hydrogel., *Biomaterials* **33**, 1044–1051 (2011).